Computational methods for assessment of solar energy potential in present and future climates

Christopher James Smith

Submitted in accordance with the requirements for the degree of
Doctor of Philosophy

The University of Leeds

School of Chemical and Process Engineering

Energy Research Institute

November 2015

The candidate confirms that the work submitted is his own, except where work which has formed part of jointly-authored publications has been included. The contribution of the candidate and the other authors to this work has been explicitly indicated below. The candidate confirms that appropriate credit has been given within the thesis where reference has been made to the work of others.

Chapter 3: Smith, C.J., Forster, P.M., Crook, R., 2014. *Global analysis of photovoltaic energy output enhanced by phase change material cooling*. Applied Energy **126**, 21–28. Manuscript and computations performed by candidate.

Chapter 4: Bright, J.M., Smith, C.J., Taylor, P.G., Crook, R., 2015. *Stochastic generation of synthetic minutely irradiance time series derived from mean hourly weather observation data*. Solar Energy **115**, 229–242. Candidate performed work and wrote the first draft of section 2.4 of this paper, subsequently revised by J.M. Bright. The candidate also assisted with the computational model described by the paper.

Chapter 5: Smith, C.J., Forster, P.M., Crook, R. *An all-sky radiative transfer method to predict optimal tilt and azimuth angle of a solar collector*. Accepted for publication in Solar Energy. Manuscript written and computations performed by candidate.

Chapter 6: Smith, C.J., Crook, R., Forster, P.M., 2015. *Changes in solar PV output due to water vapour loading in a future climate scenario*. 31st European Photovoltaic Solar Energy Conference 2015, Hamburg, 14–18 September. EU-PVSEC Proceedings 2102–2105. Manuscript and computations performed by candidate.

In addition, the following chapters contain elements of unpublished joint work.

Chapter 7: Climate change simulations performed by S. Osprey, L. Jackson and J. Crook. Manuscript and computations performed by candidate.

Acknowledgements

This work could not have been completed without the considerable help of others, for which I am exceptionally grateful. Firstly I would like to thank my supervisors Dr Rolf Crook and Professor Piers Forster for their advice and guidance throughout the last few years. Thanks also to the solar energy research group: Ross, Dave, Niamh and Pip for being greatly helpful in my brief forays into the lab, and Jamie and James G. for some very interesting and fruitful collaborations. A particular thanks to the University of Leeds Cross Country Club and their coach Greg Hull for the cold winter training sessions and shared appreciation of hills, mud and real ale. I'd like to thank my colleagues on the Doctoral Training Centre for making the office a better place to be, and to James, Emily and David for keeping it all ticking over. I am grateful to EPSRC for financial support.

For more technical matters, in no particular order, I would like to thank the makers of the libRadtran software, from which many results in this thesis are calculated, and to one of the authors Arve Kylling for the application of radiation to tilted planes which provided the inspiration for chapter 5. Thanks to Miroslav Kocifaj for detailed discussions in relation to his UniSky simulator tool, which enabled a useful comparison with the tilt model presented in chapter 5. I am grateful to Catherine Scott who provided a model run of the GLOMAP aerosol dataset which has been used extensively in the work, Scott Osprey and Lawrence Jackson who produced 3-hourly runs of the HadGEM2-CCS climate model for the scenarios considered in chapter 7, without which this work would not have been possible, and Julia Crook for her suggestions of analysing uncertainty as well as having the original idea to consider effects of geoengineering. Finally, the helpful suggestions of several peer-reviewers have improved the quality of those chapters with associated papers.

I would like to thank the students and staff of the Madhav Institute of Technology and Science, Gwalior, India, for their kind hospitality, in particular Dr C.S. Malvi and Ankit Pandey, both of whom I am especially grateful to for making my experience in India a pleasant one.

Finally I would like to thank my family for their encouragement, and my partner Heather, for the cups of tea, support and understanding.

Abstract

Climate change has motivated the need to produce energy from non-fossil sources such as solar photovoltaics (PV) and concentrating solar power (CSP). As solar power output depends on both the incident irradiance and the ambient temperature, climate change could affect solar energy production. In the last few years, a handful of studies have investigated the interactions between global climate and solar energy output. The aims of this thesis are to build on this previous work by both introducing a tilted solar collector alignment, such as would be seen in the real world, and also to include the spectral response of different PV semiconductor materials. A method to mitigate the effects of global temperature increase on solar PV is also explored. These simulations are performed with a number of radiative transfer, heat transfer and energy balance models. It is shown that the solar resource at the end of the 21st Century is expected to differ by more than ±5% compared to today in many regions of the world, and in some places up to ±20%. PV semiconductors with bandgaps in the range of 1.4–1.7 eV perform relatively better in a future climate scenario compared to the commonly-used crystalline silicon (1.1 eV), due to changes in atmospheric absorption characteristics. A further extension to a geoengineering scenario, in which humans deliberately inject aerosols into the atmosphere to lower global temperatures, shows that tracking PV and CSP energy outputs could decline by up to 15% compared to present-day values. Solar PV output can be increased by up to 6% by passive cooling of solar modules with phase change materials. As solar energy investment decisions are often made on the long-term annual mean energy output being known to within a few percent, changes in solar resource estimates of this magnitude are of importance.

Contents

List of Tables

List of Figures

Abbreviations

AERONET	Aerosol Robotic Network
AFGL	United States Air Force Geophysics Laboratory
AM	air mass
APE	average photon energy
AR4	Fourth Assessment Report
AR5	Fifth Assessment Report
ASTM	American Society for Testing and Materials
BRDF	bi-directional reflectance distribution function
BSRN	Baseline Surface Radiation Network
CDF	cumulative distribution function
CfD	contract for difference
CLASSIC	Coupled Large-scale Aerosol Simulator for Studies in Climate
CMIP	Coupled Model Intercomparison Project
CMIP5	Coupled Model Intercomparison Project, Phase 5
CPI	consumer price index
CPV	concentrating PV
CSP	concentrating solar power
CV	coefficient of variation
c-Si	crystalline silicon
DHG	double Henyey-Greenstein
DHI	diffuse horizontal irradiance
DISORT	Discrete Ordinates Radiative Transfer solver
DNI	direct normal irradiance
ECMWF	European Centre for Medium-range Weather Forecasts
eV	electron volt
EVA	ethylene vinyl acetate
FiT	feed-in tariff
GCM	global climate model
GeoMIP	Geoengineering Model Intercomparison Project
GHG	greenhouse gas
GHI	global horizontal irradiance

GLOMAP	Global Model of Aerosol Processes
HG	Henyey-Greenstein
IEA	International Energy Agency
IGBP	International Geosphere-Biosphere Programme
IPCC	Intergovernmental Panel on Climate Change
ISCCP	International Satellite Cloud Climatology Project
LCOE	levelised cost of electricity
MBD	mean bias difference
MACC	Monitoring Atmosphere Composition and Climate
MIDAS	Met Office Integrated Data Archive System
MODIS	Moderate Resolution Imaging Spectroradiometer
NOCT	Nominal Operating Cell Temperature
NREL	National Renewable Energy Laboratory
PCM	phase change material
PDF	probability density function
ppm	parts per million
PV	photovoltaic
PVGIS	Photovoltaic Geographical Information System
PV/PCM	PV with integrated PCM
PV/T	PV/thermal
QC	quality control
RCP	Representative Concentration Pathway
RCM	regional climate model
RMSD	root-mean-square difference
RO	Renewables Obligation
ROC	Renewables Obligation Certificate
rsds	Surface downwelling shortwave radiation
SCC	spectral climate change factor
SMM	spectral mismatch factor
SRES	Special Report on Emissions Scenarios
SRM	solar radiation management
SSI	stratospheric sulphate injection
STC	standard testing conditions
UF	useful fraction
UTC	Coordinated Universal Time
WMO	World Meteorological Organization

Nomenclature

A	Module/solar cell area
A	Projected area of ice particle
a	Fitting constant
a	Generalised gamma distribution parameter
$a_{0,1,2,3}$	Fitting constants
$b_{1,2}$	Fitting constants
C	Heat capacity
c_1	Temperature coefficient for solar cell efficiency
c_2	Radiation coefficient for solar cell efficiency
c_8	okta, number of eighths of the sky obscured by cloud
C_l	Cloud liquid water content
c_p	Specific heat capacity
C_{pcml}	Heat capacity of PCM in liquid state
c_{pcml}	Specific heat capacity of PCM in liquid state
C_{pcms}	Heat capacity of PCM in solid state
c_{pcms}	Specific heat capacity of PCM in solid state
d	Generalised gamma distribution parameter
D_{max}	Maximum diameter of ice particle
E	Energy
e	Model estimated value
E_g	Solar cell bandgap energy
F	Modulating factor for diffuse to global ratio in Klucher tilt model
f_c	Cloud fraction
f_{SCC}	Spectral climate change factor
f_{SMM}	Spectral mismatch factor
f_{UF}	Useful fraction
G	Global horizontal irradiance
g	Asymmetry parameter
G_0	Top of atmosphere direct normal irradiance
G_B	Direct normal irradiance
G_D	Diffuse horizontal irradiance

G_S	Solar constant
G_T	Plane-of-array radiation
G_λ	Spectral irradiance
G_{cs}	Clear-sky global irradiance
$G_{B,\mathrm{cs}}$	Clear-sky direct normal irradiance
G_{BT}	Direct plane-of-array irradiance
$G_{D,\mathrm{cs}}$	Clear-sky diffuse horizontal irradiance
H	Enthalpy
h	Hour angle
h_0	Atmospheric scale height
h_a	Convective heat transfer coefficient
h_c	Cloud geometric height
h_s	Sunset hour angle
h_t	Cloud top height
I	Radiance/radiative intensity
I_B	Direct contribution to radiance or incident ray
I_D	Diffuse contribution to radiance or incident ray
I_m	mth azimuthal intensity
J	Current density
j	Day number of year
j	Index variable
J_0	Reverse saturation current density
J_{ph}	Photocurrent density
J_{sc}	Short circuit current density
k	Boltzmann constant
k	Extinction coefficient
k	Thermal conductivity
k_t'	Airmass-scaled clearness index
k_0	Constant for CSP efficiency relationship
k_1	Linear variation of CSP efficiency with fluid inlet temperature
k_t	Clearness index
k_{pcml}	Thermal conductivity of PCM in liquid state
k_{pcms}	Thermal conductivity of PCM in solid state
L	Fitting constant
L	Latent heat of PCM
L	Longitude
l	Latitude
l	Number of PCM layers

m_a	Air mass
N	Number of observations or datapoints
n	Number distribution of cloud droplets
$N(\lambda)$	Number of photons of wavelength λ
o	Observed value
P	Output power
p	Condensed cloud path, liquid plus ice
p	Generalised gamma distribution parameter
p	Heat transfer enhancement factor
p	Phase function
p_0	Air pressure at sea level
p_i	Ice water path
P_j	jth Legendre polynomial
p_l	Cloud liquid water path
p_t	Cloud top pressure
P_{25}	Power output at cell temperature of 25°C
q	Elementary charge, 1 eV
q	Heat flow quantity
$Q(\lambda)$	External quantum efficiency
Q_{liq}	Cumulative heat required to melt PCM
r	Radial coordinate
r	Radius of cloud droplets
r_{eff}	Effective radius of cloud droplets
R_D	Diffuse transposition factor
R_R	Reflected transposition factor
s	Distance coordinate for intensity
s	Scale factor describing steepness of phase change region of enthalpy function
$S(\lambda)$	Spectral response
s^2	Sample variance
s_f	Sunshine fraction
S_m	mth azimuthal source function
t	Time
$T(\cdot)$	CDF of Student t distribution
T_a	Ambient air temperature
T_c	Solar cell temperature
T_i	Fluid inlet temperature for CSP
T_L	Linke turbidity factor

t_z	Time zone adjustment to hour angle
T_{alu}	Temperature of back aluminium layer of solar module
T_{glass}	Temperature of front glass layer of solar module
$T_{\max}$	Daily maximum air temperature
T_{melt}	Melting temperature of phase change material
$T_{\min}$	Daily minimum air temperature
T_{NOCT}	Nominal operating cell temperature
T_{pcm}	Temperature of phase change material
T_{sky}	Sky temperature
U	Eastward component of 10 m wind speed
V	Northward component of 10 m wind speed
V	Projected volume of ice particle
V	Voltage
V_{mp}	Voltage at maximum power point
V_{oc}	Open circuit voltage
W	Magnitude of 10 m wind speed
W	Weighting factor for discretisation of integrated radiance method
w	Precipitible water vapour column depth
z	Material thickness
z	Vertical coordinate
α	Absorptance
α	Angstrom exponent
α	Skew-*t* distribution skewness parameter
β	Tilt angle of solar module
β_{opt}	Optimal tilt angle of solar module
γ	Solar module azimuth (orientation) angle
$\Gamma(\cdot)$	Gamma function
δ	Solar declination
δ_R	Rayleigh scattering optical depth
$\Delta\theta_j$	Discrete polar angle bin for integrated radiance method
$\Delta\phi_k$	Discrete azimuthal angle bin for integrated radiance method
ε	Emissivity
η	Solar PV cell efficiency
η_{CSP}	Electrical efficiency of CSP
η_{ref}	Reference solar cell efficiency
Θ	Scattering angle
θ	Polar angle in spherical coordinates
θ	Polar angle of incident ray

θ'	Polar angle of scattered ray
θ_d	Angle between normal of tilted module and incident ray
θ_e	Solar elevation angle
θ_i	Incidence angle between solar beam and normal to plane
θ_j	jth discrete polar angle for evaluation of radiative transfer equation using discrete ordinates method
θ_m	Bound of integration in integrated radiance method, perpendicular to the normal of the solar module
θ_z	Solar zenith angle
κ	Thermal conductance
κ_{pcml}	Thermal conductance of PCM in liquid state
κ_{pcms}	Thermal conductance of PCM in solid state
λ	Wavelength in nanometres
λ_s	Bandgap wavelength
μ	Cosine of scattering angle or polar angle
μ	Skew-*t* distribution location parameter
ν	Skew-*t* distribution degrees of freedom parameter
ρ	Material density
ρ	Surface albedo
ρ_l	Density of liquid water
ρ_{pcml}	Density of PCM in liquid state
ρ_{pcms}	Density heat capacity of PCM in solid state
σ	Skew-*t* distribution scale parameter
σ	Stefan-Boltzmann constant
τ	Optical depth (usually defined in vertical direction)
τ	Transmissivity
τ_a	Aerosol optical depth
τ_c	Optical depth of cloud (phase unspecified)
τ_i	Ice cloud optical depth
τ_l	Liquid water cloud optical depth
τ_R	Optical depth of clean, clear, dry "Rayleigh" atmosphere
τ_s	Slant-path optical depth
$\tau_{\text{a}\lambda}$	Aerosol optical depth at wavelength λ, in nanometres
ϕ	Azimuth angle of incident ray
ϕ	Azimuthal angle in spherical coordinates
ϕ'	Azimuth angle of scattered ray
ϕ_a	Solar azimuth angle
χ_j	jth moment of scattering phase function

ω	Single scattering albedo

Chapter 1

Introduction

1.1 The sun as an energy source

Solar energy is arguably mankind's earliest and most versatile fuel resource. It is the precursor for the vast majority of energy technologies that are currently being exploited. Clearly the sun is the source of energy for solar photovoltaics (PV), the main focus of this thesis, and concentrating solar power (CSP). Solar heating over land creates convection which is the source of wind. Evaporative heating from the sun is the driver of the hydrological cycle, enabling hydroelectricity. The sun is an important component of photosynthesis needed for plants to grow, and this energy is released when biomass is burned. Fossil fuels, which make up the large majority of primary energy supply, were formed from the subsurface compression of prehistoric organisms, whose energy was originally derived from photosynthesis directly (coal) or indirectly (oil and gas) from the sun.

Solar energy is renewable, and on the timescales of human civilisations inexhaustible. This is in contrast to fossil fuel reserves which are finite. Precise estimates of the global stock of fossil fuels are continually being revised with changes in extraction methods, discovery of new and unconventional reserves, and economics of extraction. Nevertheless, the current proven reserves are projected to last far beyond the next 50 years for oil and gas and 100 years for coal (BP, 2015).

In one year, about 3×10^{24} J of energy from the sun reaches the earth's surface[1]. The global total primary energy demand in 2013 was around[2] 6×10^{20} J, or 0.02% of the solar resource. The challenge is the conversion of this vast energy resource into a usable form, in an efficient and cost-effective manner.

---

[1] calculated from the 2013 ECMWF solar resource map in fig. 1.1, summing up the irradiation contribution from each grid cell multiplied by the area of the cell.

[2] calculated as 13555 million tonnes oil equivalent (mtoe) (IEA, 2015b) multiplied by the conversion factor of 1 mtoe = 41868 TJ (IEA, 2014a).

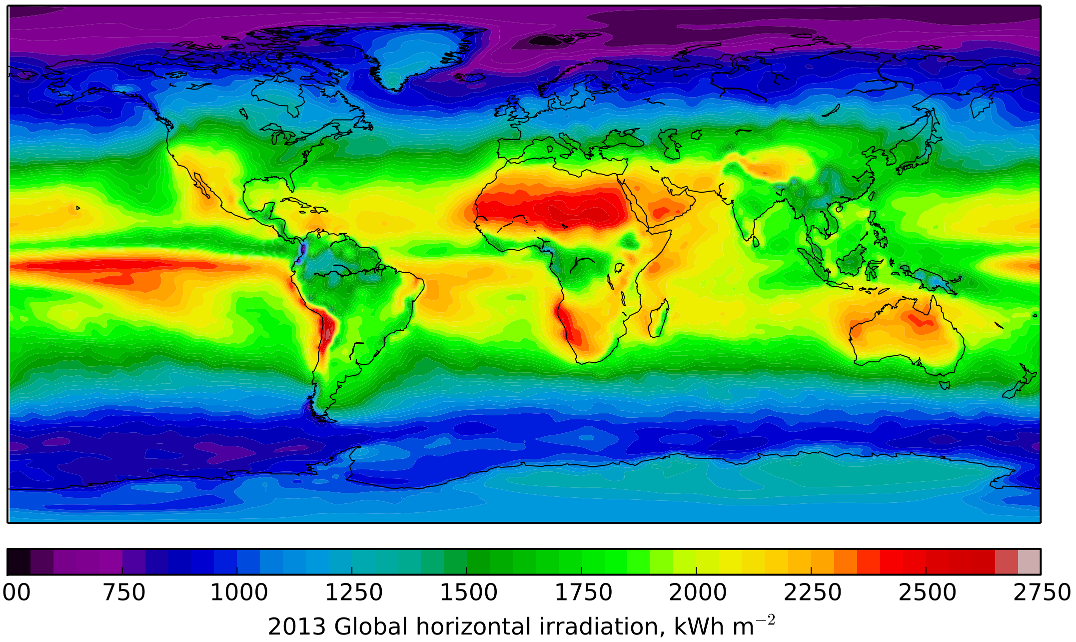

Figure 1.1: The annual horizontal solar resource. Data source: ECMWF reanalysis for 2013.

1.2 Energy and climate change

As is now well-known, the burning of fossil fuels to generate energy emits carbon dioxide (CO_2) into the atmosphere. CO_2 is a greenhouse gas (GHG), meaning that it is effective in absorbing and re-radiating thermal radiation that is emitted by the surface of the Earth in the lower atmosphere. Greenhouse gases are important, as the average Earth surface temperature would be −18°C in their absence (Thomas & Stamnes, 2002, page 441), conditions which would not be suitable for the evolution of complex life. However, increases in the atmospheric concentration of GHGs allow for more heat to be retained in the atmosphere, causing global average temperatures to increase. This effect has been observed since the beginning of the Industrial Revolution, where the best estimate of global mean temperature rise is 0.85°C (IPCC, 2013). Over the period 1880–2014, the concentration of CO_2 in the atmosphere has increased from 280 to 399 parts per million (ppm) (IPCC, 2013; Dlugokencky & Tans, 2015). Including the radiative effects of non-CO_2 GHGs (primarily CH_4 and N_2O), the best estimate of CO_2-equivalent GHG concentration was 430 ppm in 2011 (IPCC, 2013). While there is evidence to suggest that throughout the history of the earth the climate has been several degrees warmer than today, the speed at which global temperatures are rising is putting pressure on the ability of ecosystems to adapt. Increases in global average temperatures are likely to affect the climate in extreme and unpredictable ways, including heatwaves, droughts, extreme precipitation events and changes to monsoon patterns. The dual effect of thermal expansion of warmer oceans and melting of polar ice caps is expected to cause global sea levels to rise, putting coastal areas and island nations at risk. Uptake of CO_2 by the oceans causes them to become more acidic, which can be detrimental to marine life.

At the 2009 UN Conference of the Parties in Copenhagen, it was agreed that the maximum global temperature rise should be limited to 2°C from pre-industrial times (UNFCCC, 2009). Incidentally, there is no scientific reason why 2°C is an appropriate limit, but has been interpreted to be the threshold at which the worst effects of "dangerous" climate change occur can be avoided (Jaeger & Jaeger, 2010). In order to stay under the 2°C threshold, significant cuts to GHG emissions will be required over the coming decades: a long term atmospheric CO_2-equivalent level of 500 ppm will give around a 50% chance of global temperature rise remaining within 2°C (IPCC, 2014). However, there is currently no globally-agreed pathway to facilitate a reduction in GHG emissions. The Kyoto Protocol, which set advisory targets for some of the world's most developed countries, expired in 2012; the Doha Amendment is an extension to the period 2013–2020, but the only non-European nations to take on emissions targets to date are Kazakhstan and Australia (UNFCCC, 2012). With no legally-binding framework and the non-committal of some of the world's largest GHG-emitting countries, notably the US, China, India, Japan and Russia, there is little disincentive for missing these advisory targets. The objective of the 2015 Conference in Paris is to set out a legally-binding global agreement for emissions reduction in the context of limiting total global temperature rise to 2°C.

Owing to the long atmospheric lifetime of CO_2, there is a roughly one-to-one relationship between the atmospheric concentration of CO_2 and total anthropogenic emissions since the Industrial Revolution. In order to have a 50% chance of meeting the 2°C limit, the cumulative emissions of CO_2 since the Industrial Revolution would need to stay below approximately 1100 gigatonnes (Meinshausen *et al.*, 2009). This would involve leaving two-thirds of current proven fossil fuel reserves in the ground. Split out by technology this equates to one-third of oil, half of gas, and 80% of coal (McGlade & Ekins, 2015). Indeed, scarcity of fossil fuel reserves and "peak oil" worries of the late 20th and early 21st centuries have become a secondary concern to the climate impact of releasing the embodied carbon within those fuels.

The energy sector is responsible for about two-thirds of global GHG emissions (IEA, 2015a). Solar energy can help mitigate climate change by displacing energy generation by fossil fuels. Solar energy is not zero-emission, as energy is required to extract raw materials and manufacture solar energy devices as well as in the transportation, installation and decommissioning stages of a solar collector's life. However, it produces far fewer greenhouse gases than fossil fuel generation per unit of electricity generated. Estimates of lifecycle emissions are 35–58 g CO_2 kWh^{-1} for silicon PV modules (Liu *et al.*, 2015) and 14 g CO_2 kWh^{-1} for solar thermal collectors (Pehnt, 2006), compared to

443 g CO_2 kWh^{-1} for gas and 960–1050 g CO_2 kWh^{-1} for coal (Gagnon *et al.*, 2002)[3]. If global energy supply becomes less carbon-intensive by substitution with renewables, the lifecycle CO_2 figure for solar energy will become lower.

Domestically, the UK Climate Change Act 2008 legislated for an 80% reduction in total greenhouse gas emissions by 2050 compared to 1990 levels, which includes a 34% reduction by 2020 (HM Government, 2008). Providing the pathway to an 80% cut is steady, this is consistent with a global 2°C target.

1.3 Economic and policy background

Solar energy has traditionally been perceived as expensive when compared to fossil fuel generation. However, solar PV has become increasingly attractive in recent years due to a fall in raw material costs, increases in module efficiencies, and cost efficiencies generated from learning and economies of scale (Labouret & Villoz, 2010; Wand & Leuthold, 2011; Cherrington *et al.*, 2013). In many countries solar energy has now achieved grid parity (IRENA, 2014), meaning the levelised cost of electricity (LCOE) or lifecycle costs from PV are equal to or cheaper than the grid electricity price (Branker *et al.*, 2011).

In most countries it has required a measure of financial support in order to make solar energy competitive with other energy generation technology. The UK is one of them, due to a fairly low annual solar resource. The UK, along with many other countries, has a feed-in tariff (FiT) which pays generators of solar energy for the power they produce. FiTs in the UK are available to owners of small ($<$ 250 kW) and medium (250 kW–5 MW) sized installations, generally rooftop systems and small solar farms. FiT payments are guaranteed at a constant rate per kWh of electricity produced depending on the size of the installation, with an additional export rate of 4.85p/kWh which pays producers for the amount of electricity exported back to the grid (deemed to be 50% of the electricity generated, unless this is specifically metered). The FiT rate was always planned to reduce gradually, approximately once every three months, as the price of solar energy and grid electricity converged. However, since its inception in April 2010, the FiT rate has gone through a number of abrupt changes due to policy shifts. In March 2012, a drastic drop in FiT rate for the smallest ($<$ 4 kW) installations from 43.3p/kWh to 21p/kWh was implemented, which was delayed from the intended December 2011 start date due to a successful High Court appeal from several groups (Muhammad-Sukki *et al.*, 2013). The Government announced in August 2015 that a further large reduction in FiTs from

---

[3] It is appreciated that the latter references are rather old, but since for fossil fuels the majority of lifecycle emissions arise from the energy generation phase, the uncertainties for fossil-fuel generation are lower in relative terms than for solar energy. In particular, as gas and coal are carbon-rich fuels, there is an unbreachable lower limit for CO_2 emissions per kWh for fossil fuels even if power plants were 100% thermodynamically efficient.

12.47p/kWh to 1.63p/kWh was planned (DECC, 2015b). Following a consultation period the new FiT rate was set at 4.39p/kWh for the period from 15 January to 31 March 2016, with small quarterly reductions from then on (Ofgem, 2016). It is argued that such uncertainty harms investor and consumer confidence with negative effects for the UK solar industry (Cherrington *et al.*, 2013).

For large scale (> 5 MW) generators, the Renewables Obligation (RO) exists to create a market adjustment that enables renewables to achieve grid parity. Owners of medium-scale installations between 250 kW and 5 MW capacity can choose whether they would prefer to be assessed under the RO or FiT schemes. When the scheme was introduced, one Renewables Obligation Certificate (ROC) would be awarded to a generator for each MWh of renewable electricity generated. At the end of the year the generator had to present a sufficient number of ROCs to cover their total (renewable plus non-renewable) generation. This has the effect of fixing a certain percentage, which increased annually, of electricity which had to come from renewables. This changed in 2009 when ROCs were banded by technology and a different number of ROCs for each technology were awarded (Woodman & Mitchell, 2011). From then on, each generator has to present a specific number of ROCs for each MWh generated. For 2015/16 this is 0.29 ROCs per MWh (Ofgem, 2015). The banding structure is to encourage marginal technologies to develop more. The level of support is slightly different for building-mounted (1.5 ROC/MWh) or ground-mounted (1.3 ROC/MWh) solar PV (DECC, 2013). Therefore, a large utility company that generates 22.3% of its electricity (0.29 ROC/MWh divided by 1.3 ROC/MWh) from ground-mounted PV and the rest from fossil fuels would meet its obligation for 2015/16. When a generator does not meet the required level of renewable energy generation, the utility company must purchase ROCs or contribute to a buyout fund to make up the shortfall. Conversely, utilities that exceed the renewable percentage limit generate ROCs for their excess capacity which can be sold to companies that do not meet the target. The RO was implemented in April 2002 and will run until March 2037 but closed to new entrants from April 2017 (DECC, 2015a). This was always the intention. However, for solar PV from April 2015 there is no RO support for new installations above 5 MW, and the Government have recently run a consultation period for closing the scheme from April 2016 for systems between 250 kW–5 MW.

The RO is in the process of being replaced by a FiT with a contract for difference (CfD). The CfD guarantees a set price (the "strike price") per MWh of renewable generation. When market electricity prices are lower than the strike price, the generator receives a payment of the difference between the strike price and the market price. On the other hand, if market prices rise above the strike price, the generator has to pay back the excess of market price minus strike price to the Government (DECC, 2011). The CfD is running concurrently with the RO during the latter years of the RO availability. The first CfDs have been agreed as of February 2015 (DECC, 2015c).

The EU has set the UK a target of achieving 15% of energy from renewables by 2020, as part of an EU-wide target of 20%, which means that to balance the fossil-fuel heavy contributions from transport and heat, 30% of electricity should be from renewables by 2020.

Even despite a challenging policy environment domestically, solar energy has a role to play in the future. Solar PV exceeded 1% of global electricity supply for the first time in 2014 (IEA-PVPS, 2014). By 2050, PV and CSP have the potential to provide respectively 11% and 16% of global electricity supply (IEA, 2014b,c) under the International Energy Agency (IEA)'s high renewable deployment scenario. Even under the most pessimistic outlook, global solar PV capacity will be several times larger than it is today. The majority of this capacity is likely to be in the tropics and lower mid-latitudes which are currently most favourable (fig. 1.1), but several northern European countries including the UK have seen a huge increase in capacity in recent years. Therefore, estimates of PV yield for various regions of the world is likely to become increasingly important.

1.4 Layout of the thesis

The content of this thesis is comprised of a series of studies which are linked by the theme of solar energy output estimation and forecasting in current and future climates. Accurate resource assessment is essential for prediction of solar energy yields, which in turn feed into economic forecasts that underlie the above ideas. The following chapters are set out as follows.

Chapter 2 provides a more technical introduction to solar energy, including calculation of irradiance and the solar spectrum. Radiative transfer theory and how it relates to solar energy, a concept which underpins much of the work in this thesis, is introduced. Data sources which are used in future chapters are described as are future climate scenarios that are used by the Intergovernmental Panel on Climate Change (IPCC), which drives the atmospheric state for solar energy simulations in chapters 6 and 7. Finally, an introduction to solar photovoltaic efficiency and temperature relationships, which are referred to consistently throughout this thesis, is presented.

Chapter 3 builds on the temperature-efficiency relationship of solar cells, and considers a method to passively cool solar cells using phase change materials in order to improve efficiency, using a global model. European Centre for Medium-range Weather Forecasts (ECMWF) ERA-Interim meteorological reanalysis data is used to provide 3-

hourly values of radiation, temperature and wind speed that feeds the heat transfer model of solar modules with and without an attached phase change material reservoir. The technical potential and cost-effectiveness of using phase change materials to improve solar PV output power in current climate conditions globally is explored.

Chapter 4 analyses the statistics of hourly solar energy transmission for the UK based on cloud fraction. These statistics are used to generate a stochastic 1-minutely irradiance time series that can be used in demand-side modelling. This chapter is the first in the thesis to include a radiative transfer method to simulate solar radiation, where it is used to generate estimates for the theoretical clear-sky irradiation given inputs of the atmospheric state from the ECMWF data. The ratio of observed solar irradiation values, taken from the Met Office Integrated Data Archive System (MIDAS), to the theoretical clear-sky values calculated from the radiative transfer model is known as the clear-sky index. The distributions of clear-sky index for each discrete cloud fraction bin (measured in oktas, or eighths of the sky obscured) are analysed in detail. The aim of this chapter is to demonstrate that the transmission of solar radiation due to clouds can take on a wide distribution of values, and is more accurately described by a distribution than a single value for each cloud fraction than has been performed in previous studies (e.g. Kasten & Czeplak (1980); Nielsen *et al.* (1981); Matszuko (2012)).

The radiative transfer modelling procedure is extended to include clouds in **chapter 5**. Inputs for the radiative transfer model, namely the state of the atmosphere, surface, and clouds, are taken from MODIS satellite observations. This method of obtaining estimates for solar radiation data is validated against high-quality observations for horizontal radiation. Following this, a method to derive tilted radiation estimates from the radiative transfer method is described. As most climate and meteorological datasets only provide horizontal radiation values, a method to estimate tilted radiation is useful for solar energy engineering purposes where solar panel angle is usually optimised to maximise incident irradiance.

In section 1.2 above, it is described how solar energy can offset some of the negative effects of climate change. An idea that has gained traction in recent years (e.g. Crook *et al.* (2011); Burnett *et al.* (2014); Wild *et al.* (2015)), but that is still relatively little-researched, is how changes in the climate itself can influence the solar resource available. In **chapter 6**, the radiative transfer method to model solar PV output is applied to future climate scenarios. Input states of the present and future atmosphere under a high radiative forcing scenario (RCP8.5) are used with a radiative transfer model to produce the spectrally resolved radiation. A simple model is used to optimise PV module tilt. Using an optimally-aligned tilt angle for solar modules is an improvement over many studies that consider climate changes on PV assuming a horizontal module alignment. As different atmospheric constituents absorb and scatter different wavelengths of solar radiation with varying strengths, the solar spectral quality of surface radiation is affected by the atmosphere as well as the total (broadband) radiation. The spectral radiation is convoluted with the spectral responses of six different solar PV semiconductor materials for past and future climates. The extension to spectrally-resolved radiation is a further development on previous work.

Chapter 7 extends the future climate scenario modelling by considering the impacts to solar PV energy if the climate is deliberately *geoengineered* with sulphate aerosol particles that are designed to offset some of the global temperature increase expected under climate change. The impacts on another solar energy technology, concentrating solar power (CSP), which uses direct sunlight to operate, are also considered.

Finally, **chapter 8** provides a summary and conclusion, and describes ideas for further work.

1.5 Notes on terminology and nomenclature

The following terms for solar radiation are used. *Intensity* or *radiance* is the radiation flow in a specific direction and has units of [W m^{-2} sr^{-1}] *Irradiance* represents the instantaneous flux of radiation incident on a surface [W m^{-2}], and is the integral of radiances over the hemisphere of interest. *Spectral irradiance* is the irradiance per unit wavelength and is measured in [W m^{-3}] in SI units, or more commonly in [W m^{-2} nm^{-1}]. *Spectral radiance*, which is not called upon specifically in this thesis, is the analogous directional value [W m^{-2} nm^{-1} sr^{-1}]. *Irradiation* is a measure of energy, and is the irradiance summed or integrated over a period of time (units of [J m^{-2}] or [kW h m^{-2}], for instance). *Insolation* is the time-averaged solar irradiance, useful for comparing long-term data from different sites. The units of insolation are also [W m^{-2}]. Finally, *radiation* is a general term used to encompass all of these definitions.

In terms of nomenclature, consistency between chapters has been imposed and where possible conventions that prevail in literature have been used. To prevent a barrage of subscripts and to keep equations as readable as possible there will be occasional clashes in terms: for example s is used in chapter 2 to describe the path length of a beam of radiation and in chapter 3 to describe the width of a phase-change region for a non-isothermal phase change material. The meaning should be clear by context and care has been taken to ensure that these cases do not overlap and terms are fully defined when first used. A nomenclature list is provided in the thesis preamble.

Chapter 2

Fundamentals, methods and concepts

This chapter provides a technical introduction to the concepts that are referred to repeatedly later in the thesis. Firstly the fundamentals of solar resource are introduced. Then, a summary of radiative transfer theory is provided, including useful parameterisations that are encountered in later chapters. Data sources that comprise the inputs to simulations are introduced next, followed by a description of climate change scenarios used by the IPCC. Finally, the concepts that apply specifically to solar photovoltaics are described. The last section rounds up computational methods utilised in the study chapters.

2.1 The solar resource

The solar radiation incident on a plane normal to the sun's solar beam at the top of the earth's atmosphere, or solar constant G_S, at the mean earth-sun distance is about 1367 W m^{-2}. The earth's orbit is slightly eccentric which brings it closer to or further from the sun at different times of year. Taking this into account the top of atmosphere normal irradiance G_0 is approximately (Šúri & Hofierka, 2004)

$$G_0 = G_S \left(1 + 0.03344 \cos \left(\frac{360 j}{N_{\mathrm{YL}}} - 0.048869 \right) \right) \tag{2.1}$$

with j being the day number since the start of the year and N_{YL} being the number of days in the year. The argument of the cosine function is in degrees. $N_{\mathrm{YL}} = 360$ in some climate models, for example the HadGEM2 family (Jones *et al.*, 2010) used in chapters 6 and 7 in this thesis. The small angular differences between 360 and 365–366 day years are not considered critical except where a very accurate representation of solar position is required.

2.1.1 Solar position

The position of the sun in the sky as viewed from a point on the Earth's surface is the starting point for solar resource calculations. It can be expressed by two coordinates, the

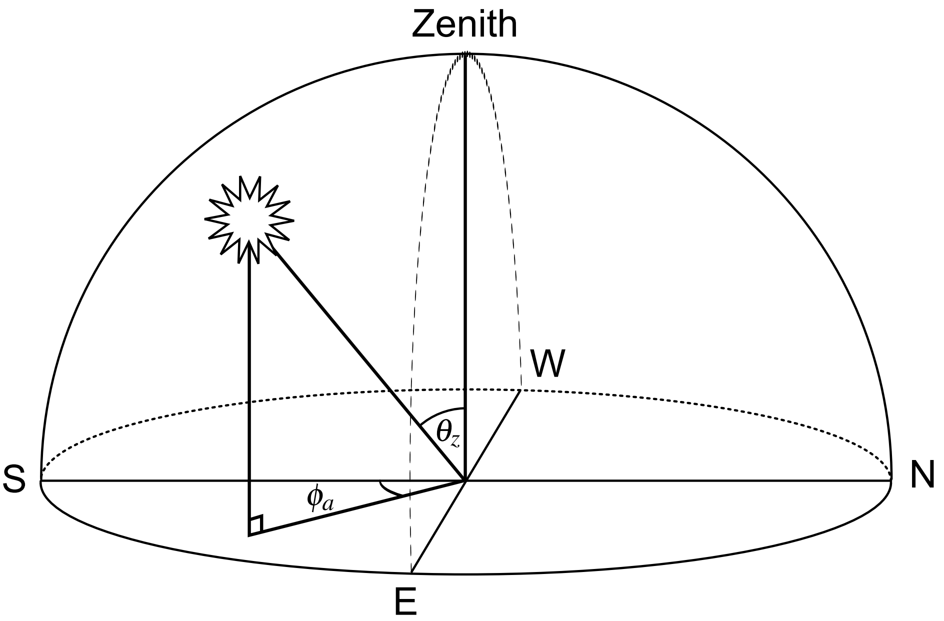

Figure 2.1: Diagram of the sky dome showing the zenith angle θ_z made between the local vertical and the solar beam, and azimuth angle ϕ_a made between the south-facing meridian and the solar beam (in this example, ϕ_a is negative).

zenith angle θ_z and azimuth ϕ_a (fig. 2.1).

Zenith angle

θ_z describes the angular distance of the sun from the vertical and is dependent on latitude l, time of day, and solar declination δ (Hottel & Woertz, 1942):

$$\cos\theta_z = \sin\delta\sin l + \cos\delta\cos l\cos h. \tag{2.2}$$

δ is the solar declination, or angular position of the sun at noon relative to latitude. It is given by (Lorenzo, 2003)

$$\delta = -23.45\cos\left(\frac{360(j+10.25)}{N_{\mathrm{YL}}}\right) \tag{2.3}$$

where j is day number and both the cosine argument and δ are in degrees. The other variable in eq. (2.2) is h, the hour angle. h ranges from -180° at solar midnight, through 0° at solar noon and approaches 180° towards the next solar midnight. h (in degrees) can be calculated using

$$h = (15(t - t_z) + L - 180) \tag{2.4}$$

where t is the local time on a 24 hour clock converted to a decimal (e.g. 15.5 representing 3:30pm), t_z is the local time zone adjustment in hours relative to Coordinated Universal Time (UTC) (positive for timezones ahead of UTC and negative for those behind), and L is the location's longitude. In many climatological datasets, time is always given in UTC and $t_z = 0$. The hour angle of sunset follows from eq. (2.2) with $\cos\theta_z = 0$ so that

$$h_s = \arccos(-\tan\delta\tan l). \tag{2.5}$$

Equation (2.5) has real solutions when $-1 \leq \tan\delta\tan l \leq 1$. Values outside of this range relate to polar summer and winter where the sun does not set or rise on a daily basis.

An alternative positional measure is the elevation angle θ_e which describes the angle above a level horizon made by the sun:

$$\theta_e = 90 - \theta_z. \tag{2.6}$$

In some contexts, using the elevation angle creates a clearer mental picture than zenith angle, because a high elevation angle corresponds to the sun being positionally "high" in the sky.

Azimuth angle

The solar azimuth angle ϕ_a gives the horizontal position of the sun compared to the south-facing meridian:

$$\cos\phi_a = \frac{\sin\delta\cos l - \cos h\cos\delta\sin l}{\cos\theta_z}. \tag{2.7}$$

The convention used in this thesis is to define sun in the south as $\phi_a = 0°$ increasing clockwise so that west is 90°, north is 180° and east is 270°. This definition means that the solar azimuth has an analogy with the hour angle, although the two are not the same in general.

The relationships given above are first-order approximations based on periodic sun-earth geometry that are sufficient for a wide range of applications. Occasionally, as in chapter 4, a very precise representation of solar zenith and azimuth that takes into account other extraterrestrial factors is required, such as the algorithm of Blanco-Muriel *et al.* (2001).

2.1.2 Direct and diffuse radiation

To a very good approximation, the radiation that reaches the top of the earth's atmosphere from the sun has travelled unobstructed through about 1.5×10^8 km of space to reach the earth. The relatively short journey from the top of the atmosphere to the earth's surface is the most difficult and interesting part to resolve. As the sun's radiation travels through the atmosphere, some of this energy is absorbed or scattered by gas molecules, clouds, and aerosols. Any radiation that reaches the surface unobstructed is termed direct radiation (Labouret & Villoz, 2010).

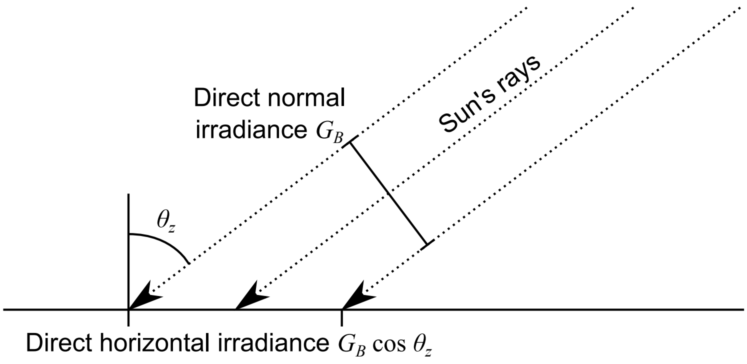

Figure 2.2: Direct normal irradiance and direct horizontal irradiance

The intensity of the direct radiation depends on the plane it is measured in. The quantity of most interest in solar energy applications is the direct normal irradiance (DNI) G_B (B for beam), which is the direct radiation intensity normal to the solar beam (fig. 2.2). If the solar zenith angle is greater than zero, the direct radiation intensity on a horizontal plane on the earth's surface is spread across to the projected area of the sun beam (fig. 2.2) (Labouret & Villoz, 2010). The projected area relationship for the direct beam is $G_B \cos\theta_z$. This is known as the direct horizontal irradiance.

When solar photons do collide with particles in the atmosphere, they could be absorbed or scattered. If they are absorbed they are lost from the solar beam completely. If scattered, the photon trajectory usually changes and the new direction could be anywhere in the 4π steradian field (defined much more formally in section 2.2). This scattering is the source of diffuse radiation. Unlike in the direct case, there is no simple geometrical relationship to determine the diffuse radiation except where it is assumed to emanate from all directions equally, which is approximately true in overcast situations but not otherwise (Gueymard, 2009). Therefore, diffuse radiation, G_D, is usually reported on the horizontal plane irrespective of the direction of solar incidence.

The sum of direct horizontal irradiance and diffuse horizontal irradiance is termed the global horizontal irradiance (GHI), G:

$$G = G_B \cos\theta_z + G_D. \tag{2.8}$$

2.1.3 Air mass

The energy emitted by the sun closely approximates that of a blackbody at 5778 K (Thomas & Stamnes, 2002), emitting across the spectral range of approximately 250–4000 nm. Alongside being a key parameter in solar geometry, the solar zenith angle determines the path length through the atmosphere that the solar beam takes before reaching the earth's surface. The longer the atmospheric path length, the more opportunities for the direct beam to be absorbed or scattered.

When the sun is directly overhead at $\theta_z = 0°$, the sun's beam travels through one atmosphere to reach the surface, at sea level pressure. This is represented by an air mass (AM) number of 1. The AM number describes how many atmospheres the solar beam travels before reaching the earth's surface. Up to about $\theta_z = 70°$ the atmosphere can be considered *plane-parallel* and the air mass m_a is close to $\sec\theta_z = 1/\cos\theta_z$. At higher zenith angles the curvature of the atmosphere becomes important and instead of diverging to infinity with the secant function, $m_a \approx 38$ at $\theta_z = 90°$ (Kasten & Young, 1989). The Kasten & Young (1989) formula between air mass and zenith angle is

$$m_a = \frac{\exp(-z/h_0)}{\cos\theta_z + 0.50572(90 - \theta_z + 6.07995)^{-1.6364}} \tag{2.9}$$

with θ_z in degrees, z altitude in metres, and h_0 atmospheric scale height ($\approx$ 8.5 km), which describes the height at which air pressure falls to 1/e of its sea-level value.

Air mass affects both the global irradiance G and the spectral irradiance G_λ. Clearly the possibility of greater absorption across all wavelengths affects G. The absorption and scattering of the atmosphere has different efficiencies at different wavelengths. The spectral absorption depends on the loadings (and types) of aerosols, water vapour and ozone. Furthermore, the direct and diffuse components of radiation are affected differently. At high air masses, the direct beam is extinguished efficiently in the short wavelengths whereas the ratio of the direct beam that is transmitted is greater in the long wavelengths (fig. 2.3a). This is due to Rayleigh scattering effects being more effective at shorter wavelengths. Effectively this changes the colour spectrum of the direct beam. In fig. 2.3b the peak of the diffuse radiation spectrum is nearer the blue end of the spectrum for all air masses than for direct radiation. For global horizontal radiation in fig. 2.3c, increasing air mass tends to result in a flatter spectrum owing to the greater contributions from shorter wavelengths in the diffuse and longer wavelengths in the direct. These spectral effects are investigated in more detail in chapter 6.

2.1.4 Atmospheric transmission

Linke turbidity factor

If atmospheric constituents do not vary, the air mass dictates the solar transmission. A quantity called the Linke turbidity factor T_L is a popular measure for clear-sky measurements and has been provided here for background as it demonstrates the effect of increasing air mass on solar radiation. T_L specifies how many atmospheres containing just Rayleigh scattering and absorption by O_2, CO_2 and O_3 ("clean, dry" atmospheres)

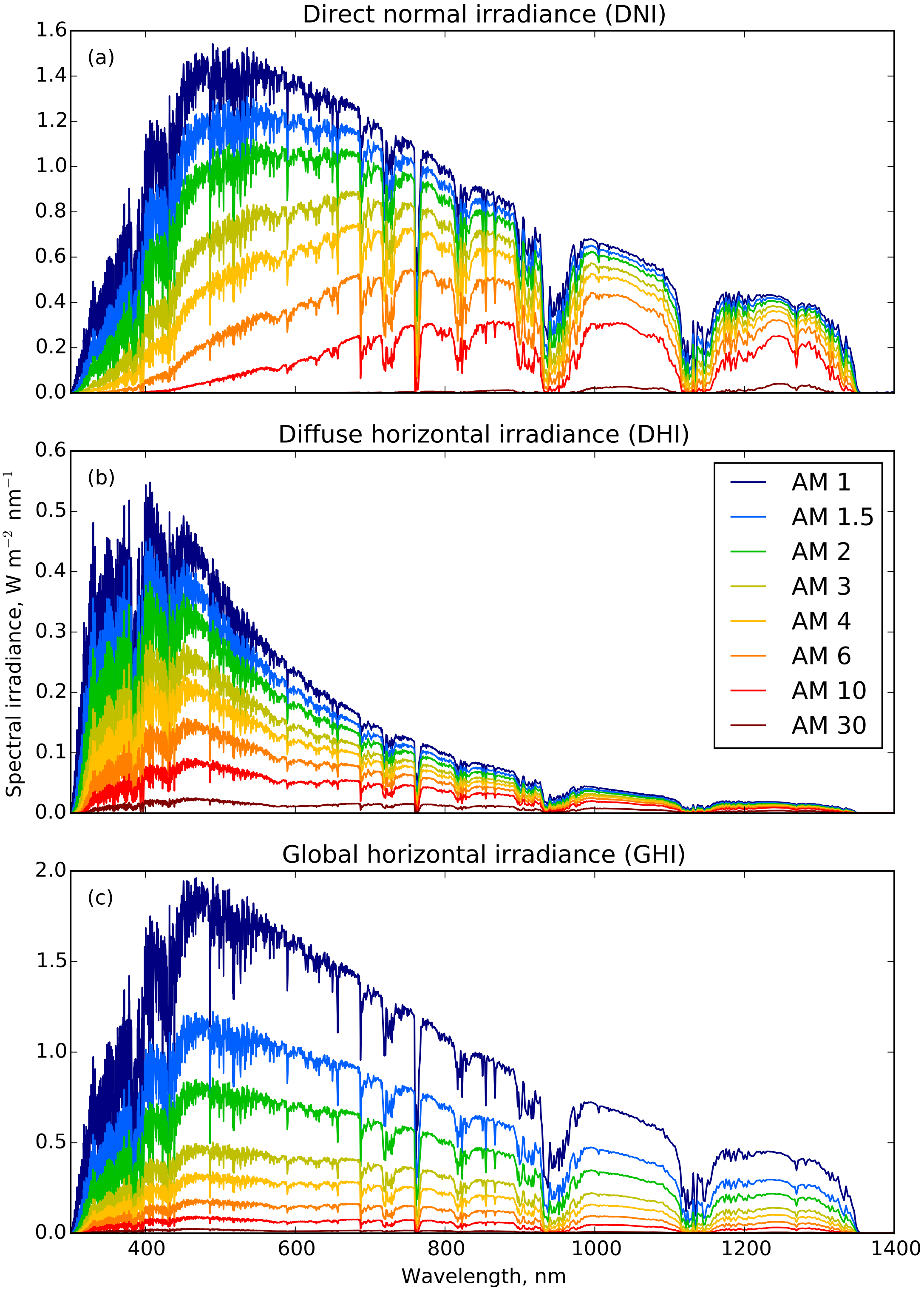

Figure 2.3: The (a) DNI, (b) DHI and (c) GHI at a variety of air masses. Spectrum produced from the REPTRAN coarse (15 cm^{-1}) solar spectrum, with default rural aerosol and US standard atmosphere in libRadtran.

Type of air	Linke turbidity factor
Arctic air	2.0–3.5
Sub-Arctic air	3.0–4.0
Sub-tropical air	3.5–4.5
Tropical air	4.0–5.0
Polluted air	> 6.0

Table 2.1: Typical values of Linke turbidity factor (Scharmer & Greif, 2000; Becker, 2001)

provides the same attenuation of radiation as the observed cloudless-sky atmosphere that contains water vapour and aerosols in addition (Louche *et al.*, 1986). The Linke turbidity factor is given by

$$T_L = \tau / \tau_R, \tag{2.10}$$

for which τ is the total clear-sky (vertical) optical depth, including water vapour, ozone and mixed gas absorption, aerosol absorption and scattering and Rayleigh scattering, and τ_R is optical depth due to Rayleigh scattering plus absorption from ozone and mixed gases (the "clean, dry") atmosphere. Optical depth is defined formally in section 2.2; as its name suggests it is related to the amount of an optically active substance in the atmosphere. τ and τ_R are air mass dependent, so they are usually normalised to AM 2 (Ineichen & Perez, 2002).

Conditions for which $T_L = 1$ are almost never encountered in reality. T_L is greater in the tropics than at the poles, higher in summer than in winter, and higher in urban areas compared to rural (table 2.1). For a specific site of interest, values of the monthly Linke turbidity factor have been interpolated from global observations at a resolution of $\frac{1}{12}^\circ \times \frac{1}{12}^\circ$ by Remund *et al.* (2003) and are available from `http://www.soda-is.com`.

Scharmer & Greif (2000) give the clear sky direct irradiance normal to the solar beam as a function of Linke turbidity, air mass and Rayleigh optical depth:

$$G_{B,\mathrm{cs}} = G_0 \exp\left(-0.8662 m_a T_L \delta_R\right). \tag{2.11}$$

where δ_R is an empirical relationship for Rayleigh optical depth as a function of air mass:

$$\delta_R = \begin{cases} 1/\left(6.6296 + 1.7513 m_a - 0.1202 m_a^2 + 0.0065 m_a^3 - 0.00013 m_a^4\right) & m_a \leq 20, \\ 1/\left(10.4 + 0.718 m_a\right) & m_a > 20. \end{cases} \tag{2.12}$$

The formulation for the clear-sky diffuse irradiance $G_{D,\mathrm{cs}}$ is complex and not repeated here but can be found in Rigollier *et al.* (2000).

In fig. 2.4, the clear-sky irradiance for Linke turbidity values from 1 to 6 is shown along

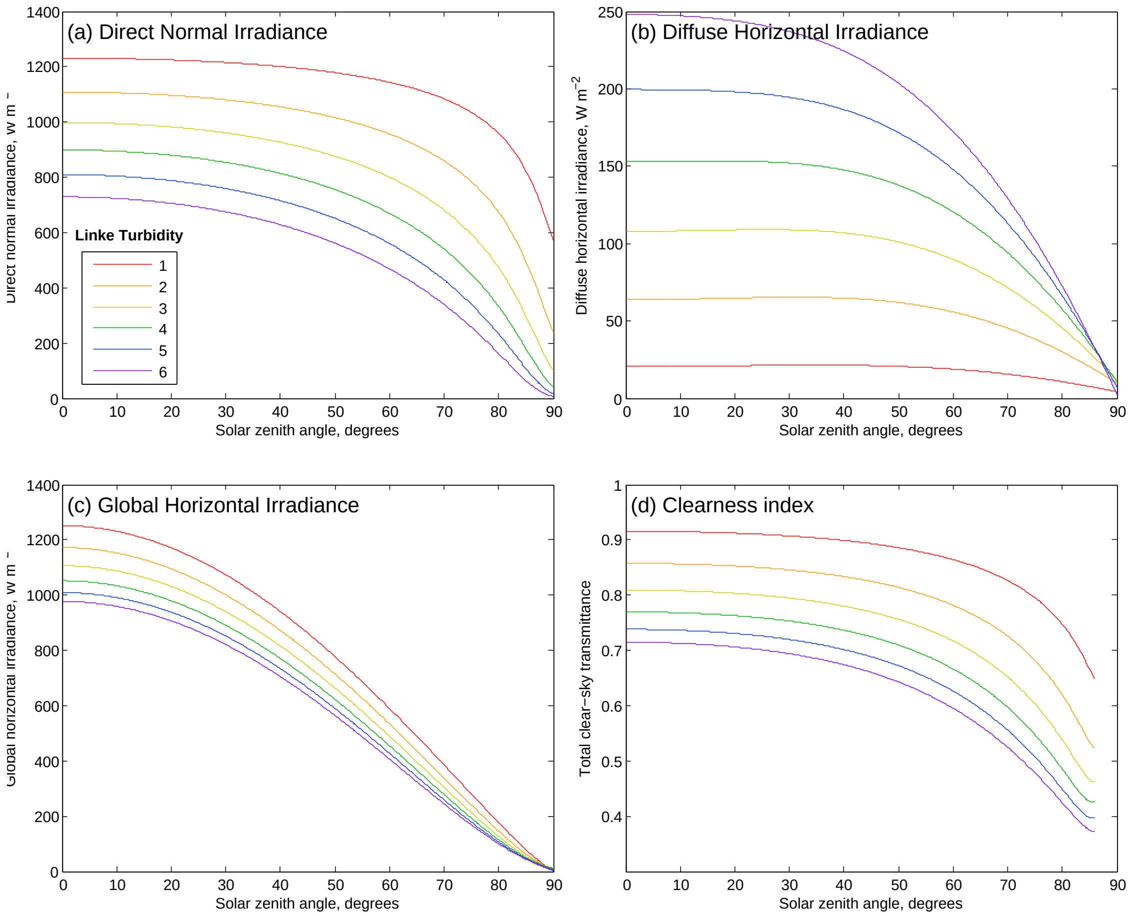

Figure 2.4: (a) Direct horizontal irradiance; (b) diffuse horizontal irradiance; (c) global horizontal irradiance and (d) atmospheric transmittance (clearness index) for Linke turbidity factors 1–6.

with the atmospheric transmittance (clearness index). As expected from eq. (2.11), the direct beam is attenuated according to an increase in air mass (function of θ_z) and Linke turbidity (fig. 2.4a). Some of the direct radiation is scattered, which is seen by the increase in diffuse radiation with increasing Linke turbidity factor (fig. 2.4b). However this is not enough to compensate for the absorption, as is seen by the decrease of global horizontal radiation with increasing T_L (fig. 2.4c). The final figure (fig. 2.4d) is of interest, as it suggests that with the clear-sky atmospheric conditions being equal, the atmospheric transmissivity decreases for increasing airmass or zenith angle. This is the subject of the rest of this section.

Clearness index

Clearness index k_t is defined as the ratio of GHI to horizontal irradiance at the top of the atmosphere:

$$k_t = \frac{G}{G_0 \cos\theta_z}. \tag{2.13}$$

Clearness index is often used to parameterise the transmission of the atmosphere as a result of all constituents and is not just limited to clear-sky observations. In the literature, a notation tendency is to use k_t for fairly short-term (minutely to hourly) observations and K_t for longer-term observations (daily or monthly), and averages of these observations by $\overline{k_t}$ or $\overline{K_t}$ (Vignola *et al.*, 2012, Appendix A). In this thesis, k_t will be used regardless of the time period in question for consistency, and $\overline{k_t}$ will represent the average of these observations. Similarly, no temporal distinction is made for G and G_0, which can represent instantaneous, averaged or summed quantities (i.e. irradiance, insolation or irradiation) depending on the context.

It is shown in fig. 2.4d that k_t is dependent on airmass in clear skies. There are several ways to attempt to reduce or eliminate airmass dependence.

Normalised clearness index

As k_t increases with increasing solar elevation angle, it is not possible to tell from a moderate value of clearness index alone whether an observation is from a cloudless atmosphere at low solar elevation angle, or a cloudy or turbid atmosphere at high solar elevation angle. One solution is to use an airmass-scaled k_t, denoted k_t'. This can be done by normalising k_t to a range based on the likely maximum value for a particular solar elevation based on observations (Olseth & Skartveit, 1987), or to eliminate air mass dependency by normalising to AM1 conditions as proposed by Perez *et al.* (1990a) such that

$$k_t' = \frac{k_t}{1.031 \exp(-1.4/[0.9 + 9.4m_a]) + 0.1}. \tag{2.14}$$

Unless otherwise stated explicitly, in this thesis k_t' will refer to the Perez *et al.* (1990a) normalisation of eq. (2.14).

Clear-sky index

Another normalisation that is used extensively in chapter 4 is the "clear-sky" index k_c, which relates the surface-received radiation to the theoretical amount expected under a cloudless sky:

$$k_c = \frac{G}{G_{\mathrm{cs}}}. \tag{2.15}$$

The clear-sky index is designed to be airmass independent, and measures the transmissivity of the atmosphere due to clouds alone. It requires a theoretical way of calculating the clear-sky radiation, which can be done using the Linke Turbidity formulation from the global maps provided by Remund *et al.* (2003) or from radiative transfer simulations. The main differences between k_t, k_t' and k_c are described in table 2.2.

Relationship	Describes	Air-mass dependent
Clearness index k_t	All atmospheric extinction	Yes
Normalised clearness index k_t'	All atmospheric extinction normalised to AM1 or range of possible values	Somewhat
Clear-sky index k_c	Extinction due to clouds only	No for cloudless sky; somewhat for clouds

Table 2.2: Summary of the differences between atmospheric transmission indices. In theory k_t' and k_c should be airmass independent, but due to errors at low elevation angles this is not quite the case for k_t'. k_c is airmass independent for clear skies, but since the transmission path lengths through clouds increase at lower solar elevations there is still an airmass dependency. The implications for k_c are discussed later in this chapter.

2.2 The radiative transfer equation

This thesis uses radiative transfer simulations in chapters 4 to 6 and so a review of the theory is provided in this section. Radiative transfer simulations provide a method to calculate solar radiation given a particular atmospheric state. For example, the spectra in fig. 2.3 were produced from radiative transfer models.

Much of the theory of radiative transfer was developed by Chandrasekhar (1960). The most important and relevant parts of the theory to this thesis are covered in this section as the full background and derivations are fairly involved. A complete and comprehensive modern reference is provided by Thomas & Stamnes (2002).

The equation of radiative transfer in the shortwave, including scattering but neglecting thermal emission, is

$$\frac{1}{k}\frac{\mathrm{d}I}{\mathrm{d}s} = -I + \frac{\omega}{4\pi}\int_0^{2\pi}\int_0^{\pi} p(\theta,\phi,\theta',\phi')I(\theta',\phi')\sin\theta'\,\mathrm{d}\theta'\,\mathrm{d}\phi'. \tag{2.16}$$

The various terms and notation in eq. (2.16) require definition and justification. The physical description of eq. (2.16) is that as a beam of radiation with intensity I [W m^{-2} sr^{-1}, a radiance quantity], travels through an optically active medium, it may be scattered or absorbed by species in the medium at a rate proportional to the original intensity, plus, it may gain or lose any scattered radiation scattered into or out of the direction of interest. The extinction coefficient k, which has units [m^{-1}], determines the rate of attenuation of the radiation.

The extinction coefficient is related to the dimensionless path optical depth τ_s for a ray travelling a distance s by

$$\int_0^s k(s')\,\mathrm{d}s' = \tau_s. \tag{2.17}$$

The components of the scattering term are the single-scattering albedo ω and phase function $p(\theta,\phi,\theta',\phi')$. The phase function describes the probability density of scattered light on collision with a particle for a ray coming from the direction (θ,ϕ) into the direction (θ',ϕ'). As the double integral is over the surface area of a sphere representing all possible angles (θ',ϕ'), the $\sin\theta'$ term is necessary to perform the integration in a spherical coordinate system and $1/4\pi$, the reciprocal of the surface area of a sphere, is a normalising constant. The single-scattering albedo ω represents the probability that a photon is scattered rather than absorbed. If absorbed, it is lost from the beam, and does not participate in the scattered radiance quantity. For clouds, typically $\omega > 0.99$ in solar wavelengths (Hu & Stamnes, 1993) whereas for aerosols ω ranges from approximately 0.5–0.9 (Lacis & Mishchenko, 1995).

2.2.1 Direct radiation from a radiative transfer perspective

For solar energy radiative transfer modelling, it makes sense to split out the direct and diffuse contributions to the radiation such that $I = I_B + I_D$. For the direct case, the scattering term is zero. Therefore solving eq. (2.16) for the direct beam gives

$$I_B = I_0 \exp(-\tau_s) \tag{2.18}$$

for some incident beam intensity I_0. This is the Beer-Lambert law. In plane-parallel geometry, the optical depth is typically referred to with respect to the vertical direction, such that $\tau = \tau_s \cos\theta_z$. If τ describes the vertical extinction of the whole atmosphere and the intensity I_0 is equal to the solar intensity G_0, then the beam irradiance is

$$G_B = G_0 \exp(-m_a \tau). \tag{2.19}$$

By determining empirical relationships for τ as a function of Linke turbidity and Rayleigh scattering efficiency, this formulation is used to calculate clear-sky beam irradiance in eq. (2.11). The diffuse component, which is more difficult to solve, is recovered from subtracting out the contribution from the direct beam in eq. (2.16).

2.2.2 Phase function and its relationship to diffuse radiation

It is typically assumed that the scattering phase function is azimuthally symmetric. Then, the phase function can be reduced from a function of two angles to a function of one angle

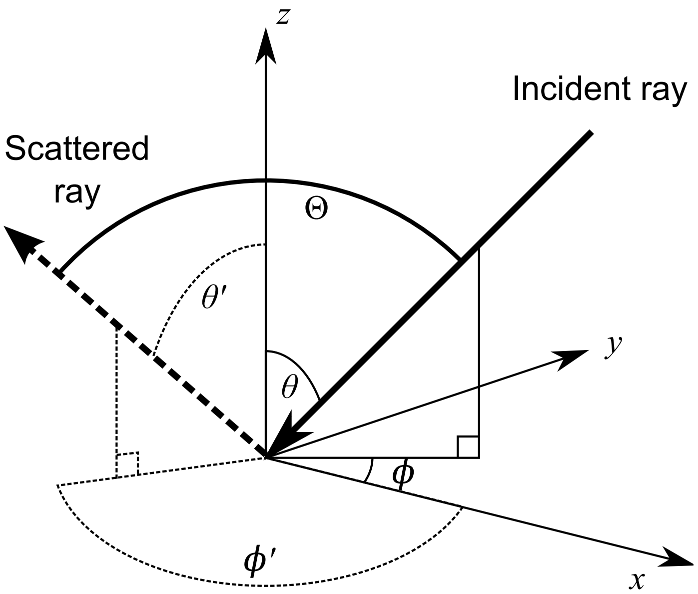

Figure 2.5: Schematic of particle scattering, where the particle is at the origin.

by the cosine law of spherical geometry:

$$\cos\Theta = \cos\theta\cos\theta' + \sin\theta\sin\theta'\cos(\phi - \phi') \tag{2.20}$$

A schematic diagram is shown in fig. 2.5.

Radiation is forward-scattered if $\cos\Theta > 0$ and back-scattered if $\cos\Theta < 0$. The phase function satisfies the normalisation property of a probability distribution, such that

$$\frac{1}{4\pi}\int_0^{2\pi}\int_0^{\pi} p(\cos\Theta)\sin\theta\,\mathrm{d}\theta\,\mathrm{d}\phi = 1. \tag{2.21}$$

The moments of the phase function are introduced as follows. The jth moment of the scattering phase function χ_j is derived as a consequence of the jth Legendre polynomial P_j such that

$$\chi_j = \frac{1}{2}\int_{-1}^{1} P_j(\mu)p(\mu)\,\mathrm{d}\mu. \tag{2.22}$$

The substitution $\mu = \cos\Theta$ has been made in eq. (2.22) (this highlights a common convention in radiative transfer literature). The first two Legendre polynomials are $P_0(x) = 1$ and $P_1(x) = x$ with higher polynomials defined by the recurrence relation

$$(j+1)P_{j+1}(x) = (2j+1)xP_j(x) - jP_{j_1}(x). \tag{2.23}$$

The first moment of the phase function p is the mean direction of scattering, more commonly known as the asymmetry parameter g, which is

$$g = \chi_1 = \frac{1}{2}\int_{-1}^{1} \mu p(\mu)\,\mathrm{d}\mu. \tag{2.24}$$

g is an important value as it determines the proportion of radiation scattered into the forward hemisphere; $g = 1$ if all radiation is forward-scattered, $g = 0$ if forward-scattering equals backscattering, and $g = -1$ where all radiation is scattered backwards. Therefore, the value of g can have a large influence on the amount of scattered light that reaches the earth from the sun. For clouds, g is often very close to 1; for aerosols, values ranging from 0.6–0.9 are common depending on the size and composition of the aerosol.

Higher moments of the phase function are useful in the numerical approximations of the radiative transfer equation, as described further on in this chapter. Phase functions that are used at various points in this thesis are introduced below.

Rayleigh scattering

For molecules that are much smaller than the incident wavelength, the Rayleigh scattering phase function describes the distribution of scattered radiation such that

$$p_{\mathrm{R}}(\cos\Theta) = \frac{3}{4}(1 + \cos^2\Theta). \tag{2.25}$$

The Rayleigh scattering phase function is appropriate for gas molecules in the shortwave part of the spectrum. It can be shown that $g = 0$ by application of eq. (2.24), hence the Rayleigh phase function scatters photons forwards or backwards with equal probability.

Mie scattering

For larger particles such as cloud droplets and aerosols, the wavelength of light is comparable or smaller to the size of the particle and the Rayleigh scattering model is no longer appropriate. Scattering for these larger particles is described by Mie theory and relies on the complex refractive indices of the particles. For spherical particles, the method is well-defined but not straightforward.

Because a simple representation like eq. (2.25) does not usually present itself, the phase function must be expanded by its moments. If g is close to 1, as is often the case in clouds, the phase function converges very slowly in its moment expansion and hundreds of terms can be required to calculate an accurate phase function. This can make Mie scattering computationally too intense for multiple calculations. Additionally, for ice clouds which are made of particles that are not spherical, Mie theory is in general not appropriate. Therefore, some simpler asymmetric ($g \neq 0$) phase functions for modelling aerosols and clouds can be used, for example the Henyey-Greenstein and double Henyey-Greenstein described below.

Henyey-Greenstein (HG) phase function

The Henyey-Greenstein (HG) phase function was originally devised for astrophysical use, but has found popularity in atmospheric radiative transfer. The HG phase function is

$$p_{\mathrm{HG}}(\cos\Theta) = \frac{1-g^2}{(1+g^2-2g\cos\Theta)^{3/2}}. \tag{2.26}$$

It is a mathematical convenience that is not based in physical reality. However, it possesses a number of desirable properties. Firstly, it can model the strong forward-scattering peak apparent in many real scattering processes such as in aerosol and liquid water cloud phase functions. Secondly, the entire phase function is parameterised by powers of g such that $\chi_j = g^j$, which is a very convenient computational advantage. Thirdly, the forward/isotropic/backward scattering when $g = 1$, $g = 0$ and $g = -1$ is recovered as expected.

Double Henyey-Greenstein (DHG) phase function

The last property above can be exploited to better model the backscattering peak present in some ice cloud phase functions. A linear combination of two HG phase functions can be combined into a double Henyey-Greenstein (DHG) phase function such that (Key *et al.*, 2002)

$$p_{\mathrm{DHG}}(\cos\Theta) = f p_{\mathrm{HG}}(g_1,\cos\Theta) + (1-f)p_{\mathrm{HG}}(g_2,\cos\Theta) \tag{2.27}$$

where f lies between 0 and 1. Usually, g_1 is positive and g_2 is negative.

2.2.3 Cloud parameterisations

Liquid clouds

Liquid water clouds are observed to contain a distribution of water droplet sizes. Common distributions used to describe these include the gamma, generalised gamma and lognormal distributions (Hu & Stamnes, 1993; Rossow *et al.*, 1996). Calculating the optical properties for each droplet size in a distribution is a laborious task. Fortunately, the shape of the distribution can be described adequately with a single parameter, the effective radius r_{eff}, which describes the ratio of the distribution of droplet volumes to surface areas:

$$r_{\mathrm{eff}} = \frac{\displaystyle\int_0^\infty n(r)r^3dr}{\displaystyle\int_0^\infty n(r)r^2dr}. \tag{2.28}$$

where r represents actual radii and $n(r)$ is the number of cloud droplets of radius r present. Then, at visible wavelengths, the liquid cloud optical depth τ_l is approximately

$$\tau_l = \frac{3p_l}{2\rho_l r_{\mathrm{eff},l}} \tag{2.29}$$

where p_l is the column-integrated cloud water path [kg m^{-2}], ρ_l is the density of water of 1000 kg m^{-3} and $r_{\mathrm{eff},l}$ is in µm. An alternative definition is to specify the liquid cloud water content C_l, which describes the amount of cloud water in a given volume [kg m^{-3}], in which case $p_l = C_l h_c$ where h_c is cloud geometric height.

By assuming an effective radius of 10 µm (10^{-5} m), an effective rule-of-thumb for determining the optical depth from cloud water path is (Stephens, 1976)

$$\tau_l = 150p_l = 0.15C_l h_c. \tag{2.30}$$

The International Satellite Cloud Climatology Project (ISCCP) use a slightly different definition owing to a more precise calculation of the Mie extinction efficiency (the factor of 3 in the numerator of eq. (2.29) is replaced by 3.1785) at 600 nm incident wavelength (Rossow *et al.*, 1996), which is

$$\tau_l = 158.925p_l. \tag{2.31}$$

Hu & Stamnes (1993) provided a convenient approximation to the full Mie solution for water clouds by fitting curves of the form

$$\begin{aligned} \tau_l/p_l &= a_1 r_{\mathrm{eff}}^{b_1} + c_1 && (2.32) \\ 1-\omega &= a_2 r_{\mathrm{eff}}^{b_2} + c_2 && (2.33) \\ g &= a_3 r_{\mathrm{eff}}^{b_3} + c_3 && (2.34) \end{aligned}$$

where a, b and c are functions of wavelength.

Ice clouds

Ice clouds pose a particular complexity as ice crystals form in a variety of habits (shapes), on which the scattering phase function is strongly dependent. Additional morphological features such as surface roughness and trapped air bubbles also affect the phase function (Xie *et al.*, 2006, 2012). In order to correctly model ice cloud scattering a full phase matrix scattering code should be used (e.g. Baum *et al.* (2014)), however the number of Legendre coefficients that need to be calculated for each scattering phase function make its use computationally prohibitive for multiple calculations. The situation is further complicated by the fact there is no unique choice of effective radius for ice particles as they are not generally symmetric. Following Key *et al.* (2002), the effective radius for ice clouds can be defined as

$$r_{\mathrm{eff},i} = \frac{3\displaystyle\int n(D_{\mathrm{max}})V(D_{\mathrm{max}})\,\mathrm{d}D_{\mathrm{max}}}{4\displaystyle\int n(D_{\mathrm{max}})A(D_{\mathrm{max}})\,\mathrm{d}D_{\mathrm{max}}} \tag{2.35}$$

where D_{max} is the length of the maximum diameter of an ice particle and V and A are projected volumes and areas of the ice particle assuming that the equivalent volume and area of a sphere is used. This is the convention used in Key's parameterisation for ice clouds which has been used in chapter 5. The Key *et al.* (2002) formula provides τ_i, g and ω as a function of r_{eff} and wavelength. Assuming an effective radius of 30 µm, at 600 nm wavelength, the ice cloud optical depth can be represented in the same way as eq. (2.29) with the density of ice as 525 kg m^{-3}, so that (Rossow *et al.*, 1996)

$$\tau_i = 95.238 p_i. \tag{2.36}$$

2.2.4 Plane parallel and pseudo-spherical geometry

For atmospheric radiative transfer modelling, the simplest assumption is that there is a plane-parallel, vertically stratified atmosphere that does not vary in the horizontal direction. Then, the left-hand side of eq. (2.16) becomes

$$\frac{1}{k}\frac{\mathrm{d}I}{\mathrm{d}s} = \frac{\cos\theta}{k}\frac{\mathrm{d}I}{\mathrm{d}z} \tag{2.37}$$

where θ is polar angle, meaning that $\cos\theta$ is the zenith angle of the incident ray. This geometry is appropriate when the solar elevation angle is not too low. At low elevations, the curvature of the atmosphere becomes important, as seen in the air mass calculation. In this case, spherical geometry must be used. The left-hand side of eq. (2.16) in spherical geometry is complex and involves angular derivatives (Thomas & Stamnes, 2002). It can be simplified if the direct beam is treated separately from the diffuse radiation. The problem is then reduced to the "spherical shell", assuming no variation in the azimuth direction, and then

$$\frac{\mathrm{d}I}{\mathrm{d}s} = \cos\theta\frac{\partial I}{\partial r} - \frac{\sin\theta}{r}\frac{\partial I}{\partial\theta}. \tag{2.38}$$

However, it has been shown by Dahlback & Stamnes (1991) that for zenith angles less than 90° the second term in eq. (2.38) can be considered small and

$$\frac{\mathrm{d}I}{\mathrm{d}s} \approx \frac{\mathrm{d}I}{\mathrm{d}r} \tag{2.39}$$

where r is the radial coordinate that has been used in place of the height coordinate z. This is the pseudo-spherical approximation (Mayer *et al.*, 2012). The air mass correction has to be applied to the direct beam in this case. For the whole atmosphere this can be approximated by eq. (2.9). For an atmosphere that has varying optical properties in each layer, the path length through each layer needs to be determined. This is given by the Chapman function (Dahlback & Stamnes, 1991).

2.2.5 Relationship between irradiance and intensity

Radiative transfer computations provide a convenient way to calculate the solar radiation. The direct beam is satisfied by eq. (2.19). If the direct beam is included in the total radiation field, the intensity can be split into a downwelling and upwelling component by choice of the integration limits:

$$G = \int_0^{2\pi} \int_{\pi/2}^{\pi} I(\theta,\phi) \sin\theta \cos\theta \, \mathrm{d}\theta \, \mathrm{d}\phi \tag{2.40}$$

and

$$G_R = \int_0^{2\pi} \int_0^{\pi/2} I(\theta,\phi) \sin\theta \cos\theta \, \mathrm{d}\theta \, \mathrm{d}\phi . \tag{2.41}$$

G is the GHI and G_R is the upwelling irradiance (in the shortwave, there is no source from the earth itself, and all upwelling radiation is reflected from the ground). In radiative transfer literature these irradiances are usually termed *half-range fluxes*, and are given the notation F^- and F^+ respectively.

In chapter 5, the extension of this concept to non-horizontal planes is introduced.

2.2.6 Numerically solving the radiative transfer equation

As can be seen, the single scattering albedo ω, phase function p (or asymmetry parameter g, if a simple phase function is assumed), and extinction coefficient k (or optical depth τ) are all that is required to completely parameterise the optical characteristics of the atmosphere. With the correct choice of geometry the equations can be formulated. However, only in certain simple situations can eq. (2.16) be solved analytically and so for most real problems a numerical method is required.

In this thesis, software containing a library of radiative transfer solvers, libRadtran (Mayer & Kylling, 2005), is used to numerically solve eq. (2.16). The choice of solver used depends on the accuracy, speed, and output requirements of the problem. The solvers used are introduced in this section.

Discrete ordinates method: DISORT

Again, the theory of solving the radiative transfer equation by this method is originally due to Chandrasekhar (1960). The Discrete Ordinates Radiative Transfer solver (DISORT) radiative transfer solver was originally a FORTRAN program written by Stamnes *et al.* (1988) and updated by Stamnes *et al.* (2000). It is implemented in libRadtran in C.

Equation (2.16) is approximated by a system of ordinary differential equations. This is performed by replacing the scattering term with a series based on the Legendre polynomial expansion of the phase function (the detail of which is omitted in this overview). Azimuthal co-dependence can be eliminated and what is left is a system of simultaneous differential equations at various choices of zenith angle, of the form

$$\cos\theta_j \frac{\mathrm{d}I_m}{\mathrm{d}\tau} = -I_m(\cos\theta_j) + S_m(\cos\theta_j), \qquad j = \pm 1, \pm 2, \dots \pm N. \tag{2.42}$$

$2 \times N$ in eq. (2.42) is known as the number of *streams*, or discrete polar angles, at which the intensity is evaluated. The subscript m relates to azimuthal dependency. S is a “source function” that characterises scattering. Depending on the boundary conditions the coefficients I_m and S_m may be azimuthally dependent, but they are not coupled. The solution for each stream is calculated by linear algebra methods in DISORT.

If radiances $I(\theta, \phi)$ are required, the results can be interpolated from eq. (2.42) for any arbitrary (θ, ϕ) pair (Stamnes *et al.*, 2000). If irradiance is required, then only one azimuthal component in eq. (2.42) needs to be calculated which represents the azimuthal average. The integrals in eqs. (2.40) and (2.41) are then calculated numerically using Gaussian quadrature.

DISORT can be implemented with or without a pseudo-spherical correction. The convention in work presented in this thesis is that the pseudo-spherical correction is implemented when the solar zenith angle $\theta_z > 75°$. Owing to slightly faster computations in plane-parallel geometry, the Cartesian system has been used for solar zenith angles less than this.

Two-stream DISORT: TWOSTR

A dedicated two-stream version of DISORT was created by Kylling *et al.* (1995) and has been implemented in libRadtran. The two-stream approximation suggests that only one angle is calculated in the upwards hemisphere and one angle in the downwards hemisphere which relate to hemispherically averaged radiances. It is possible to calculate irradiances, but not radiances at arbitrary angles. By default TWOSTR has a pseudo-spherical correction included. The obvious advantage of using fewer streams is the quicker computational time at the expense of accuracy. However, as radiative transfer calculations are themselves simulations, the concept of “accuracy” is loosely defined and the two-stream approximation can be sufficient for modelling horizontal irradiances.

Eddington approximation

The Eddington approximation is another type of two-stream solution to the radiative transfer equation in plane-parallel geometry. The intensity is defined as a linear function of polar angle such that $I = I_0 + I_1 \cos\theta$. For strongly forward-scattering phase functions, the forward peak is modelled by a Dirac delta function. This is known as the δ-Eddington approximation (Joseph *et al.*, 1976). The Eddington approximation is suggested to be suitable for optically thick atmospheres where single scattering is near to 1 (King & Harshvarhan, 1986). Testing by the author has found that computational run time is almost identical to TWOSTR.

The program RODENTS (Buras, 2011) is a δ-Eddington solver in libRadtran and has been used in chapter 6.

2.2.7 The correlated-k method

To perform a complete calculation line-by-line over the whole solar spectrum for multiple calculations, as is done to generate the spectra in fig. 2.3, is often infeasible in terms of computational time. Therefore, the correlated-*k* method (Kato *et al.*, 1999) is used to divide the solar spectrum into 32 wavelength bands with similar atmospheric absorption properties. The broadband irradiance is then obtained as the sum of the 32 wavelength bands. The comparison between the Kato *et al.* (1999) correlated-*k* spectrum and that produced by an approximate line-by-line solver for AM1 is shown in fig. 2.6. As can be seen there is some smoothing out of the spectrum by implementing this approximation.

2.3 Data sources

In later chapters a variety of data sources are used for model inputs and also for validation (table 2.3). These are introduced in more detail in this section.

2.3.1 Meteorological observations

BSRN

The Baseline Surface Radiation Network (BSRN) provides minutely measurements of horizontal irradiance from a number of sites globally. Data is provided by individual

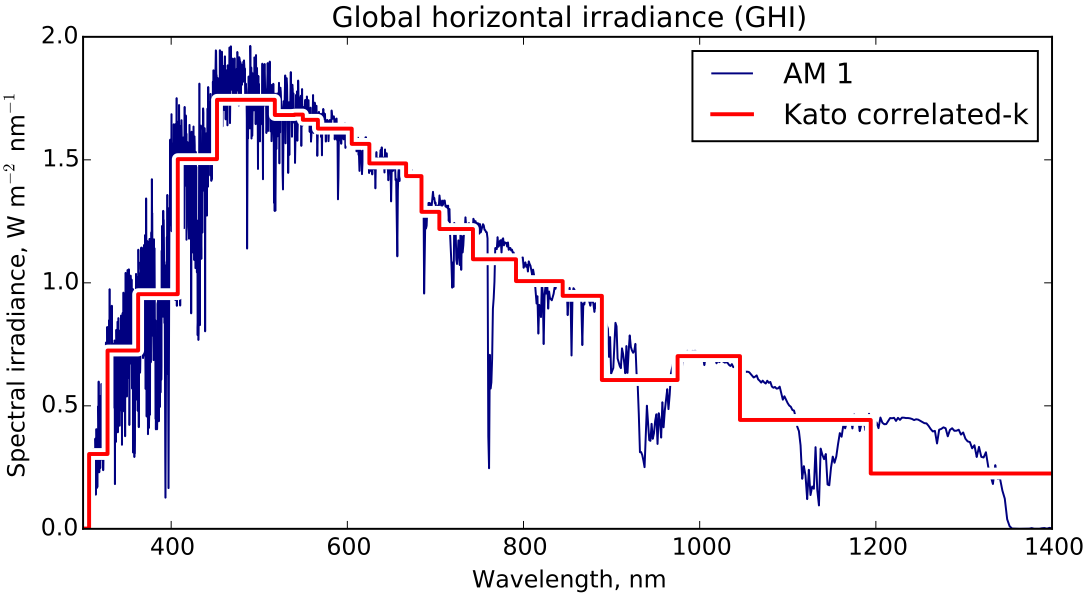

Figure 2.6: Correlated-*k* spectrum for GHI at AM1 plotted with approximate line-by-line spectrum

Dataset	Description	Chapters
BSRN	High-quality GHI measurements	3, 5
MIDAS	High-quality GHI measurements (UK)	4, 5
	Cloud fraction	4
ECMWF	Solar radiation	3
	Atmospheric state	4
MODIS	Atmospheric state, clouds, albedo	5
GLOMAP	Aerosol properties	4, 5
IGBP	Albedo	4–6
HadGEM2-ES	Atmospheric state, clouds, aerosol	6
HadGEM2-CCS	Atmospheric state, clouds, aerosol	7

Table 2.3: Datasets used in this thesis

national meteorological offices and is collected by the BSRN, available from `http://bsrn.awi.de`. Solar irradiance at BSRN sites is measured with a Kipp & Zonen CMP21 or CMP22 pyranometer with the exception of Tamanrasset which uses the Eppley PSP, all of which are World Meteorological Organisation (WMO) High Quality certified.

The BSRN data contains instances of missing or suspicious records. Data gaps range from one minute to several days. In this thesis, a quality control (QC) procedure was applied to the BSRN data to fill in missing or suspect data following the M7 method recommended by Roesch *et al.* (2011). The M7 method calculates monthly 15-minute means from data where at least 3 minutes per 15-minute period exist and are within the "physically possible" limit for GHI of $1.5G_0\cos^{1.2}\theta_z + 100$ W m^{-2} where G_0 is as in eq. (2.1). The monthly mean is only valid if all 96 15-minute bins contain valid values.

Code	Station name	Country	Lat.	Lon.	Alt. (m)
LAU	Lauder	New Zealand	45.045°S	169.689°E	350
SMS	São Martinho	Brazil	29.443°S	53.823°W	489
GOB	Gobabeb	Namibia	23.561°S	15.042°E	407
BRB	Brasilia	Brazil	15.601°S	47.713°W	1023
DAR	Darwin	Australia	12.420°S	130.891°E	350
PTR	Petrolina	Brazil	9.068°S	40.319°W	387
TAM	Tamanrasset	Algeria	22.780°N	5.510°E	1366
MNM	Minamitorishima	Japan	24.288°N	153.983°E	7
ISH	Ishigakijima	Japan	24.337°N	124.163°E	6
IZA	Izaña	Tenerife	28.309°N	16.499°W	2373
FUA	Fukuoka	Japan	33.582°N	130.375°E	3
TAT	Tateno	Japan	36.050°N	140.133°E	25
CLH	Chesapeake Light	USA	36.905°N	75.713°W	37
BOU	Boulder	USA	40.050°N	105.007°W	1577
SAP	Sapporo	Japan	43.060°N	141.329°E	17
CAR	Carpentras	France	44.083°N	5.059°E	100
SON	Sonnblick	Austria	47.054°N	12.958°E	3109
PAL	Palaiseau	France	48.713°N	2.208°E	156
CAB	Cabauw	Netherlands	51.971°N	4.927°E	0
TOR	Toravere	Estonia	58.254°N	26.462°E	70
NYA	Ny-Ålesund	Svalbard	78.925°N	11.930°E	11
ALE	Alert	Canada	82.490°N	62.420°W	127

Table 2.4: List of BSRN stations used in this thesis

Since inception in 1992, there have been 59 BSRN sites globally. Of these, 22 provide data for every month of 2013, and these stations have been used. Stations on the Antarctic continent have not been included. These stations are given in table 2.4 and are used to check the validity of the insolation data in chapter 3 and to validate the tilt model in chapter 5.

MIDAS

MIDAS provides pyranometer measurements of hourly GHI for approximately 90 sites in the UK. The MIDAS data has passed a QC procedure run by the UK Met Office. 64 of these sites also report cloud fraction. The sites that report both irradiation and cloud fraction are used to create the clear-sky statistics in chapter 4. In chapter 5, five MIDAS sites with good data coverage for 2013 are used to validate the tilted irradiance model.

The convention in this thesis is to use the three-letter BSRN station codes in upper case for BSRN stations and an upper- and lower-case abbreviation or the source ID number for MIDAS stations.

2.3.2 Meteorological reanalyses

High-quality irradiance data from outside the UK is generally only available from BSRN or from research institutes. Even if observations from overseas meteorological offices were generally available, large areas of the world would be very sparsely covered by weather stations. For example, there were no BSRN stations with valid irradiance data in Asia outside of Japan for the year of 2013.

The ECMWF meteorological reanalysis data provides even global spatial coverage from a combination of observations, numerical weather models and forecasts (Dee *et al.*, 2011b). This modelled data is available every 3 hours from 1979 onwards from the ERA-Interim dataset on a horizontal grid of about $0.7^\circ \times 0.7^\circ$. For the studies introduced in later chapters a resolution of $1.5^\circ \times 1.5^\circ$ is used. In addition to solar radiation estimates, ECMWF provides several datasets relating to the atmospheric state on 60 vertical levels. Such examples of the multi-level data are cloud fraction, cloud liquid water content, temperature, water vapour, and ozone. The ECMWF radiation estimates are derived from a dedicated ECMWF radiative transfer model (Morcrette *et al.*, 2008). Data is available from `http://www.ecmwf.int`.

As ERA-Interim data is reanalysed from observations, uncertainty can be present in both the observations that feed the model (in terms of data availability, measurement techniques and instrumental uncertainty) and the model physics and parameterisations that produce the reanalysed climate state from the inputs (Thorne & Vose, 2010). It is suggested that the errors in clear-sky radiation as predicted in the ECMWF (and other) radiative transfer models are small, on the order of 1 W m^{-2} for errors in the absorption properties of atmospheric species (Pincus, 2011) and another 1 W m^{-2} for the parameterisation of line-by-line absorption and scattering by a faster process for use in reanalysis and climate models, such as the correlated-k method (section 2.2.7, Pincus *et al.* (2015)). Notwithstanding the fact that these errors may be of opposite sign and partially cancel, the maximum expected error from clear-sky radiation is a little over 1% based on the global average downwelling insolation of 184 W m^{-2} (Trenberth *et al.*, 2009). Likewise, surface temperatures from the ERA-interim dataset are found to closely match those of observation (Dee *et al.*, 2011a). Near-surface wind speed may be subject to larger errors due to the imposition of a single value for a large area, and the changes in orography and surface roughness over the area of a grid cell in addition to sub-timestep variations and nonlinearities in wind speed, however the impact of these errors in the present work is small as they only affect the convective heat transfer away from a solar PV system.

The largest and most important uncertainties for the purposes of this thesis in the ECMWF data are due to the radiative effects of clouds, and how they attenuate the incoming so-

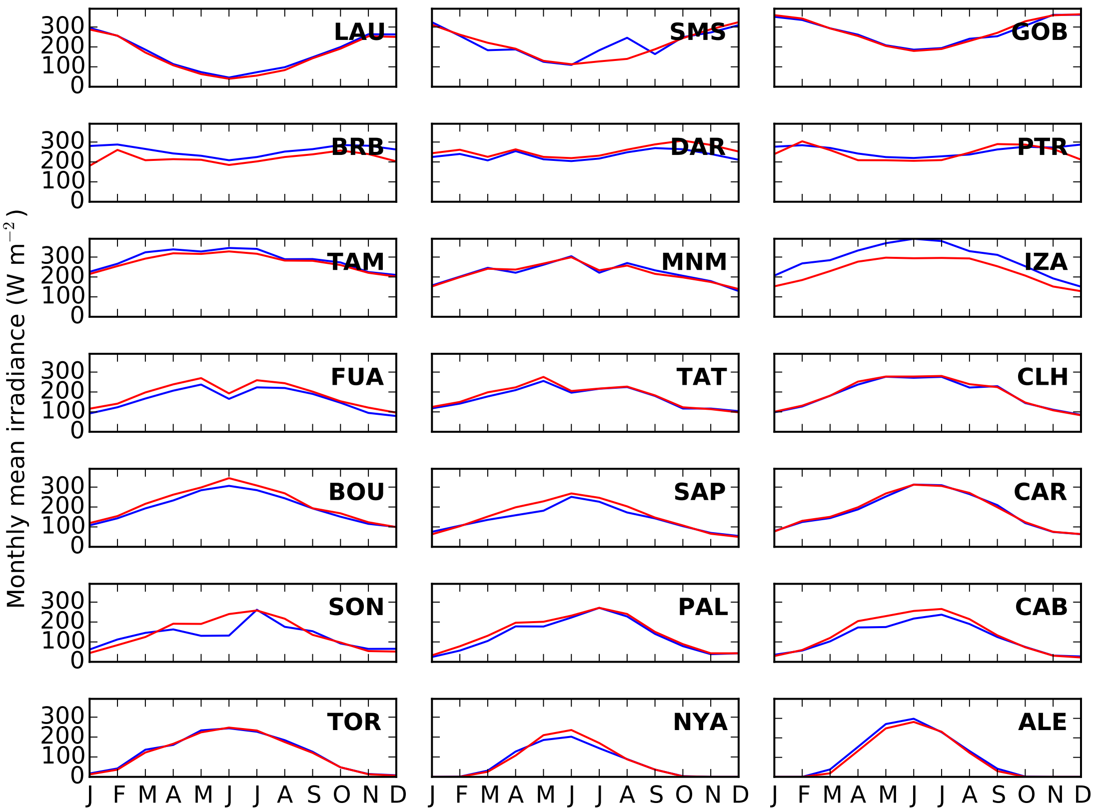

Figure 2.7: Monthly mean irradiances for 21 BSRN sites and the ECMWF reanalysis data. BSRN data is in blue and ECMWF is in red. The year of comparison for this figure is 2013. Table 2.4 contains station names and locations.

lar radiation. Cloud fraction predicted by the ERA-Interim reanalysis has been shown to be overestimated compared to observation for Arctic BSRN sites, however the ECMWF ERA-interim reanalysis is one of the better performing models for global radiation, estimating the long-term annual average within 2.5% of the observed value at these sites (Zib *et al.*, 2012).

To extend the Zib *et al.* (2012) analysis to all BSRN stations used in this thesis, the monthly mean irradiance from ECMWF is compared to the monthly mean ground measurements from BSRN with the Roesch *et al.* (2011) QC procedure applied. For the 21 sites that contain data for 2013, good agreement is seen between the reanalysis data and the ground measurements (fig. 2.7). The only serious disagreements are seen annually at Izaña (IZA) and for certain months at Sonnblick (SON) and São Martinho (SMS). IZA and SON are both high-latitude locations that other models also replicate poorly and the implications of this are discussed further in chapter 5. In general the ECMWF radiation data is a satisfactory dataset to use for modelling simulations.

2.3.3 Satellite observations

For the work in chapter 5, observations of the atmosphere, clouds and surface albedo were provided by the Moderate Resolution Imaging Spectroradiometer (MODIS) instrument on board the Terra and Aqua satellites. The Terra satellite overpasses the equator at approximately 10:30 local solar time daily and the Aqua satellite overpasses at approximately 13:30 daily. Therefore, synoptic diurnal differences between the morning and afternoon can be partially captured. Each satellite has 36 spectral bands and a nadir resolution of 250 m, 500 m or 1000 m depending on the band.

There are different stages of MODIS data processing (Hubanks *et al.*, 2008). Level 1 is the raw radiances that are returned from the satellites which are calibrated and then geolocated. From the Level 1 data, algorithms are used to infer the aerosol, water vapour, ozone and cloud properties on grids of 1 km, 5 km or 10 km at nadir. This is Level 2 data. Level 1 and 2 data relate to the satellite overpasses ("swaths"). A further level of processing aggregates Level 2 observations into a regular grid, which is Level 3. These Level 3 inputs are available as daily, 8-day, 16-day and monthly averages on grid sizes of $1^\circ \times 1^\circ$ for atmosphere products and $0.05^\circ \times 0.05^\circ$ for albedo products. It is this $1^\circ \times 1^\circ$ that has been used in chapter 5. All data is freely available from the MODIS portal at `http://modis-atmos.gsfc.nasa.gov/`

Pre-launch experiments showed that MODIS water vapour column depth retrievals are expected to be accurate within 13%, which can be improved to 7% with the usage of additional spectral bands used to infer clouds, haze and surface temperature (Kaufman & Gao, 1992). In operation, validations against ground-based and radiosonde datasets tend to show better performance than this with typical agreement within 2–3% when bias-corrected (Diedrich *et al.*, 2015). Profiles of ozone column depth are similar to those produced from the NASA/GSFC Total Ozone Mapping Spectrometer (TOMS) on board the Earth Probe satellite, although individual retrievals can vary by up to 80% in polar regions between the two satellites (Seemann *et al.*, 2003). For TOMS, the net maximum uncertainty in measurements is not expected to exceed 5% at moderate solar zenith angles, increasing up to 8% at low sun (McPeters *et al.*, 1998). The long-term mean bias measured against ground stations for the TOMS instrument is 0.5%. Surface albedo from the MODIS satellite products is found to be within 0.05 (absolute units) of the measured surface radiation values (Liu *et al.*, 2009).

For clouds there are several MODIS products to consider, including the cloud fraction, cloud phase (whether liquid or ice), cloud height and cloud water path (the amount of cloud water in a vertical atmospheric column, in kg m^{-2} if all condensed). Instantaneous retrievals of cloud water path and cloud droplet effective radius can differ from ground-based observations by radar and lidar, with mean biases of 17.2% and 7.8% respectively for the Aqua satellite and 0.3% and −3.6% for Terra (Dong *et al.*, 2008). The standard deviation of observed differences between MODIS and ground-based observations can be large, between 23% and 33% for these variables (Dong *et al.*, 2008). Uncertainties in the retrieved ground measurements to the real variables, estimated at 10% for both cloud water path and cloud particle effective radius (Dong *et al.*, 2008), can mean that good satellite agreement with ground instruments may still not be representative. The total uncertainty is estimated to be 15% for instantaneous measurements for particle effective radius from MODIS (Platnick & Valero, 1995; Minnis *et al.*, 1998) and 17% for cloud water path (Dong *et al.*, 2008). Cloud top height retrievals from MODIS are expected to be accurate to within 140 m (Minnis *et al.*, 2003).

2.3.4 Global aerosol model

Aerosols are often the largest source of uncertainty for estimating clear sky radiation as they are highly variable in time and space, difficult to measure, and sparsely recorded (Nou *et al.*, 2015).

Aerosol data is an important input into radiative transfer simulations, especially in cloudless skies. The Aerosol Robotic Network (AERONET), operated by NASA, provides measurements of clear-sky aerosol optical depth and radiative properties at eight different wavelength bands for around 900 stations globally. For global modelling, there are two drawbacks of using the AERONET data. Firstly, the measurements can only be made in cloudless skies, and for some parts of the world there are several months without suitable measurement conditions. Secondly, even 900 point sites globally provides a fairly sparse coverage of aerosol data for some regions. And thirdly, because aerosols are so spatially dependent, conditions that are a few kilometres from a measurement site can be very different.

Therefore, when an aerosol input is required for a global model in this thesis, a run of the Global Model of Aerosol Processes (GLOMAP) model is provided to obtain a monthly aerosol climatology (Spracklen *et al.*, 2005; Scott *et al.*, 2014). GLOMAP is produced at a resolution of $2.8^\circ \times 2.8^\circ$, which specifies ω, the asymmetry parameter g, and aerosol optical depth τ_a for 6 wavelength bands in the shortwave spectrum on 31 pressure levels. The species included are sulphate, sea-salt, black carbon and particulate organic matter aerosols in four size modes. Aerosol scattering is reasonably well-described by a Henyey-Greenstein phase function, and since g is the only moment available from the GLOMAP runs, the HG phase function has been assumed.

The performance of GLOMAP has been validated against observations from AERONET

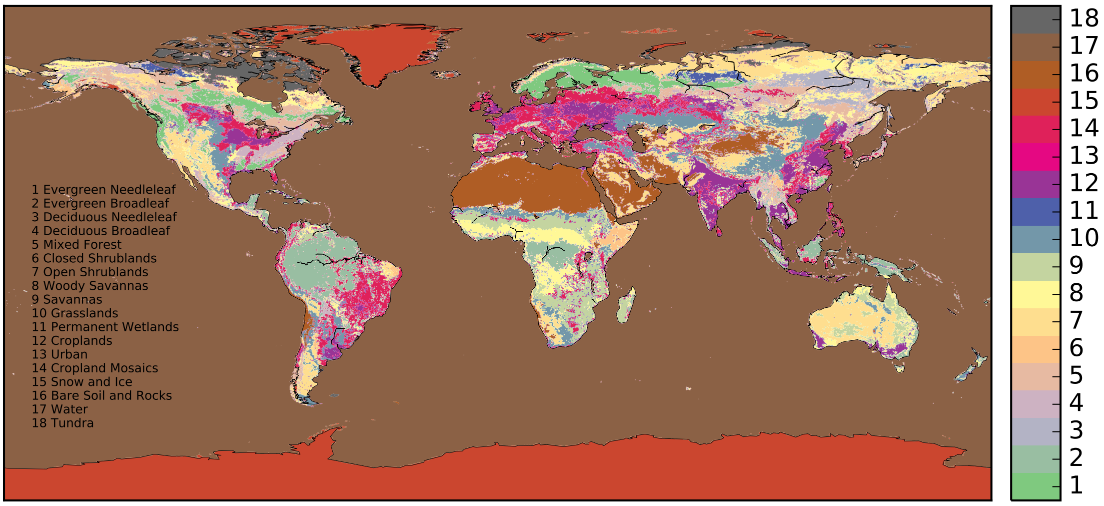

Figure 2.8: Map of IGBP surface types

sites globally. GLOMAP aerosol optical depth at 440 nm wavelength shows high correlation with the seasonal cycle and low root-mean-square difference (RMSD) across the year compared to AERONET for Europe and North America (Bellouin *et al.*, 2013). The performance of GLOMAP in replicating observations is weaker in Asia, Africa and Latin America, however, improvements over the aerosol modelling scheme used in the HadGEM2 climate model family, the Coupled Large-scale Aerosol Simulator for Studies in Climate (CLASSIC), are seen (Bellouin *et al.*, 2013). Global aerosol optical depths are around 30% lower in GLOMAP than in the ECMWF MACC aerosol reanalysis scheme (Bellouin *et al.*, 2013); however, it is seen in chapter 4 that using the GLOMAP dataset for the UK alongside the ECMWF data for the atmospheric state results in very good estimates of solar radiation in truly clear (cloud-free) skies.

2.3.5 IGBP land surface dataset

Where surface albedo data from satellites is not available or not applicable, the International Geosphere-Biosphere Programme (IGBP) library (Belward & Loveland, 1996) classifies land surface as one of 18 types at a resolution of $\frac{1}{6}^{\circ} \times \frac{1}{6}^{\circ}$ (fig. 2.8). The IGBP dataset was originally produced from satellite observations and provides spectral albedo for each type. An additional 2 surface types for temporary snow and ice covered surfaces are available but not provided in the global map. The IGBP surface type map is included in libRadtran.

2.3.6 Climate model data

Output data from the Met Office Hadley Centre family of climate models is used in chapters 6 and 7. Two models are used in this thesis: HadGEM2-ES and HadGEM2-

CCS. Both models are towards the higher end of model sophistication, including atmospheric/ocean interaction, aerosols, sea-ice, the carbon cycle, and in the case of HadGEM2-ES, tropospheric chemistry (Jones *et al.*, 2011). Different future climate scenarios are used in each study. A brief review of these follows in the next section.

2.4 Future climate scenarios

In order to make predictions about the climate of the future, an idea of possible pathways society could develop in is required. The Representative Concentration Pathways (RCPs) are a set of four climate change scenarios to the year 2100 which were used for the first time in the 2013 IPCC Fifth Assessment Report (AR5) (table 2.5). They make up one of the key experiments in the Coupled Model Intercomparison Project (CMIP) phase 5 which assesses the responses to each scenario between different climate models. In reports previous to AR5, the Special Report on Emissions Scenarios (SRES) were used (table 2.6). The RCPs are named by their radiative forcing quantities in the year 2100, where radiative forcing describes the energy imbalance of the earth climate system. Formally, radiative forcing is defined as (Ramaswamy *et al.*, 2001)

> "the change in net (down minus up) irradiance (solar plus longwave; in W m^{-2}) at the tropopause after allowing for stratospheric temperatures to readjust to radiative equilibrium, but with surface and tropospheric temperatures and state held fixed at the unperturbed values."

The RCPs were chosen to reflect the full range of plausible future development scenarios available in the literature (Moss *et al.*, 2010). An even number was preferred to avoid the central scenario being seen as the "best estimate", and the word "representative" indicates that the final scenario selected for CMIP5 is actually only one member of a set of similar scenarios available in the published literature (van Vuuren *et al.*, 2011). The RCPs also include supplementary extended concentration pathways (ECPs) which continue these scenarios to the year 2300. RCPs specify the magnitude and trajectory of radiative forcing between the present day and 2100, by specifying a time-series of concentrations of the long-lived greenhouse gases (CO_2, CH_4, N_2O, PFCs, CFCs and SF_6), aerosols, and ozone precursors (van Vuuren *et al.*, 2011).

The two pathways of most importance in this thesis are RCP8.5 and RCP4.5. RCP8.5, developed by Riahi *et al.* (2011) is baseline scenario that does not implement any mitigation policies, and is at around the 90th percentile of non-mitigation scenarios in the literature, although higher exist. Although no control is placed on future greenhouse gas emissions, air pollution reductions due to the strengthening of legislation do occur, particularly in

Name	Radiative forcing	CO_2 concentration (CO_2-eq)	Median temperature rise (1750–2100) °C
RCP8.5	> 8.5 W m^{-2} in 2100	$>$ 1370ppm in 2100	4.9
RCP6.0	~ 6.0 W m^{-2} in 2100	$\sim$ 850ppm in 2100	3.0
RCP4.5	~ 4.5 W m^{-2} in 2100	$\sim$ 650ppm in 2100	2.4
RCP2.6	~ 3.0 W m^{-2} before 2100, declining to 2.6 W m^{-2} in 2100	Peak at $\sim$ 490ppm before 2100 then decline	1.5

Table 2.5: The RCPs used for CMIP5 experiments (Moss *et al.*, 2010; Rogelj *et al.*, 2012).

urban areas in the developing world. Population growth is steady, reaching 12 billion in 2100. Economic growth, energy intensity and technology improvements are slow, leading to a largely coal-based energy system in 2100. RCP8.5 is based on the A2 SRES scenario, but is more similar in terms of overall 2100 temperature rise to A1FI (Rogelj *et al.*, 2012) table 2.6. It is used to assess maximum likely potential changes in solar energy output towards the end of the 21st Century, in chapter 6.

RCP4.5 stabilises around 2150 without overshooting, and implies a significant climate change mitigation strategy (Thomson *et al.*, 2011). Annual CO_2 emissions peak in 2050 and decline until 2080 where they remain constant until 2100. Global population peaks at 9 billion near 2070 before declining slightly towards 2100. RCP4.5 was selected as the main RCP for analysis in the Geoengineering Model Intercomparison Project (GeoMIP) (Kravitz *et al.*, 2011) and has therefore been used for analysis of geoengineering effects in chapter 7.

The SRES scenarios explored a detailed storyline behind the economic, social and technical development that underpinned emissions levels in the 21st Century, although even under the lowest emissions pathway, no efforts to mitigate climate change are assumed (van Vuuren *et al.*, 2011). The SRES scenarios are summarised briefly in table 2.6.

The RCPs are not generally compatible with the SRES pathways: RCPs 8.5, 6.0 and 4.5 have similar median and confidence interval temperature increases to SRES pathways A1FI, B2 and B1 respectively in 2100, but differing trajectories (Rogelj *et al.*, 2012). There is no equivalent SRES pathway to RCP2.6, which requires net CO_2 emissions of zero shortly after 2070 and negative emissions (i.e. capture and sequestration of atmospheric carbon) thereafter.

2.5 Photovoltaics

In this section, concepts and formulae relating to solar energy are defined.

Pathway	Description	Median temperature rise (1750–2100) °C
A1FI	A world in which global emissions continue to rise due to a development path based on fossil fuels. CO_2 emissions are 3 times the 2000 level in 2100. The global economy grows rapidly, with decreased global inequality, and global population reaches a maximum in the middle of the century with a slow decline thereafter.	5.0
A1B	Population and economic outlook the same as for A1FI. A balance of fossil and renewable technologies are used to facilitate growth. Hence, global emissions are lower than A1FI, about 1.5 times the 2000 level in 2100.	3.5
A1T	Population and economic outlook as for A1FI and A1B. Development is driven by renewable technologies. Global emissions peak around 2040, come back to the 2000 level by 2080 and continue to decline out to 2100.	3.0
A2	Population continues to rise throughout the century and economic growth is slow. Technological development is slower than for A1 scenarios. CO_2 emissions in 2100 are at a similar level to the A1FI scenario.	4.2
B1	The population scenario is the same as in the A1 scenarios with a convergent economy that is less material-intensive than A1, with global initiatives in equality and sustainability but without additional climate mitigation strategies. CO_2 emissions follow a similar trajectory to A1T.	2.5
B2	Environmental and social sustainability is focused on a regional rather than global level. Population continues to grow but at a slower rate than A2. Economic growth continues at an intermediate rate whilst technology develops slowly. CO_2 emissions are projected to be about 1.5 times those of 2000 in this scenario.	3.0

Table 2.6: SRES scenarios that were used in the IPCC Fourth Assessment Report (Nakićenović *et al.*, 2000).

2.5.1 Standard Testing Conditions

Solar cells are usually characterised by their efficiency at standard testing conditions (STC), which are conditions of 25°C cell temperature and incident irradiance of 1000 W m^{-2} under a spectrum of AM 1.5. This is a quantity reported by manufacturers for commercial modules and laboratories for research modules and cells. The solar collector is assumed to be tilted towards the sun at an angle of 37° from the horizontal, with the sun at a zenith angle of 48.2°, which corresponds to AM 1.5. In the STC spectrum, the 37° tilt reduces the incidence angle between the solar beam and the module, and ensures that the total irradiance integrates to 1000 W m^{-2}. The atmospheric concentrations of ozone, water vapour and mixed gases are provided by the United States Air Force Geophysics Laboratory (AFGL) US standard atmosphere (Anderson *et al.*, 1986). The spectrum itself is calculated by the SMARTS2 model (Gueymard, 1995) which is in fact a radiative transfer computation. It forms a standard recognised by the American Society for Testing and Materials (ASTM) and is commonly known as the ASTM-G173 spectrum (ASTM, 2003).

2.5.2 Electrical efficiency

The electrical efficiency of a solar cell with an area A is the ratio of electrical power output P to incident plane-of-array irradiance G_T (the T subscript stands for "tilted"):

$$\eta = \frac{P/A}{G_T}. \tag{2.43}$$

For multi-cell modules, the module efficiency takes into account gaps between cells in the calculation of A that do not contribute to the overall power generation. Additionally, the performance of a string of cells in series is limited by the poorest cell in the string. Therefore module efficiencies tend to be lower than single cell efficiencies.

STC provides a very idealised set of conditions that are rarely experienced in reality (Betts, 2004). The efficiency of the PV cell is a function of ambient temperature T_a and irradiance (Evans, 1981) such that

$$\eta = \eta_{\mathrm{ref}}\left[1 - c_1\,(T_c - 25) + c_2 \log_{10}(G_T)\right]. \tag{2.44}$$

In Eq. (2.44), η_{ref} is the STC efficiency, c_1 is the decline in cell efficiency with respect to an increase in in cell temperature and c_2 is an adjustment in efficiency to account for performance decline in low light conditions.

2.5.3 Nominal operating cell temperature (NOCT)

If T_c in eq. (2.44) is unknown, it can be estimated from the Nominal Operating Cell Temperature (NOCT) relationship (Lorenzo, 2003):

$$T_c = T_a + \frac{T_{\mathrm{NOCT}} - 20}{800} G_T. \tag{2.45}$$

The NOCT conditions are an ambient temperature of 20°C, irradiance of 800 W m^{-2}, and wind speed of 1 m s^{-1}. Some module manufacturers provide values of T_{NOCT}. If this is unknown, conventionally $T_{\mathrm{NOCT}} = 45$°C is used.

2.6 Computational methods

The majority of programming that appears in the thesis was conducted in Python. Python is used as a scripting language to call runs in libRadtran, a computational language (to perform some of the calculations including for tilted and spectral irradiance), and as an analysis language (to plot figures and report results). Python was chosen because of its wide scope, flexibility, and the fact that it is free and open-source. The key exception is chapter 3 where the work was performed in Matlab and world maps plotted in IDL.

Chapter 3

Passive cooling with phase change materials

The first two chapters provided an introduction and context to the thesis. In section 2.5, it was discussed how a rise in PV module operating temperature is correlated with a reduction in electrical efficiency. As only approximately 15–20% of the incident irradiance is converted to electrical power by a crystalline silicon (c-Si) PV cell, much of the excess is either reflected or is converted to heat. The decline in efficiency is typically 0.45% (relative) for every 1°C rise in cell temperature for c-Si (Skoplaki & Palyvos, 2009). Therefore, any mechanism which reduces the cell temperature, particularly at times of high irradiance, will increase cell efficiency and PV energy output. This chapter describes a global simulation to determine the increase in annual energy output attained by a PV system with an integrated phase change material (PCM) layer, which is used as a mechanism to passively cool solar modules.

A review of previous methods and models to describe passive cooling with PCMs is followed by the particular solar cell scheme used in this chapter. The application to a global setting using ECMWF climate reanalysis data shows that PCM cooling could enhance PV power output by up to 6% in some regions. The economics of using PCMs for solar PV energy improvement is discussed, and the last section summarises the chapter.

3.1 Background and literature review

PCMs in the context of this study are defined as a material that undergoes a phase transition from solid to liquid and vice versa. Starting from the solid state, when heat is applied to a PCM, it acts as a sensible heat store until the temperature of the PCM reaches its melting point T_{melt}. At this temperature, further inputs of heat are used to melt the PCM which becomes a latent heat store, and the temperature of the PCM changes very little. When fully melted, the PCM reverts to being a sensible heat store in the liquid phase and the temperature of the PCM starts to rise again on the application of additional heat. The exploitation of PCMs for solar cell cooling uses the high latent heat capacity of PCMs in the melting process as a heat sink, absorbing heat that is transferred from a PV cell while mitigating the rise of the cell temperature. In the solidifying process, this sequence happens in reverse. While the PCM layer is changing from liquid to solid, the heat is released and the solar cell is often warmer than the ambient conditions. Providing this process occurs late enough in the day or at night where solar irradiance is low, a gain in output power can be achieved by keeping the cell cooler than it would have otherwise been without PCM during peak solar hours. In an ideal system the PCM should solidify and return to a fully solid state by the next morning.

Alongside PCMs, cooling methods for PV cells include water cooling and air cooling. Water-cooled systems require a pump to circulate cold water into the PV system which adds additional capital and maintenance costs and burdens. This can be offset if the heated water is then used domestically in a PV/thermal (PV/T) system (Teo *et al.*, 2011). For domestic roof installations, water cooling may be unsuitable due to the weight of water required to deliver appropriate cooling (Krauter, 2004). In hot, dry climates where solar energy has great potential but cell temperatures are highest, water is scarce. Water cooling is unlikely to be used in utility-scale solar plants as there is little use for the warm water produced.

For open-mount PV modules, there is no need to implement additional air cooling as ambient air can flow on both the front and back of the modules. Utility-scale PV systems are likely to be open-mounted. For building-mounted PV, the reverse side of the system is close to the building surface and wind does not cool the reverse side readily, leading to higher module temperatures (Skoplaki *et al.*, 2008). For these systems, air cooling may be built into the system design and can be either active (Dubey *et al.*, 2009) or passive (Brinkworth & Sandberg, 2006), the latter relying on the buoyancy of the heated air behind the solar module to drive convection. This requires optimal choice of the duct width to maximise convective cooling. Fins may be added to the back of a PV module to increase the surface area available for air cooling. Passive air cooling may not be especially effective due to low rates of heat removal and for the potential for dust to build up inside the cooling duct (Huang *et al.*, 2006), but is a low-cost and maintenance-free solution. Active air cooling requires the use of DC fans (Dubey *et al.*, 2009) and may consume more power than is saved by the gain in photovoltaic efficiency.

PCM cooling is passive and has the potential to be more effective than air cooling. The pioneering research group for the inclusion of PCM cooling of PV was that of M.J. Huang and colleagues in Ireland. Huang *et al.* (2004) produced a 2D numerical model of the heat transfer of a PCM enclosed within two aluminium sheets which was experimentally validated. As desired, the temperature rise on the sun-facing side of the system was delayed while the PCM was melting. A later study by the same group (Huang *et al.*, 2006) compared the temperature rise of two aluminium-PCM systems to a reference aluminium plate with no PCM attached. Over the course of the 150-minute experiment at 750 W m^{-2} irradiance, the front aluminium temperature remained below the reference in both PCM systems. It was estimated that efficiency from a PV with integrated PCM (PV/PCM) system would be improved by 7.5% (relative) at peak solar hours due to the 17°C difference in aluminium plate temperatures. Two PCM regions containing different PCMs can be combined inside a container to enhance thermal conductivity through the PCMs and regulate the PV cell temperature for longer (Huang, 2011). A PV/PCM panel tested outdoors in Pakistan resulted in a PV module temperature that was 21.5°C lower than a reference at the peak time of the day (Hassan *et al.*, 2015). Two different PCMs were used: a capric-palmitic acid eutectic and a $CaCl_2.6H_2O$ salt hydrate. Over the course of the day it was calculated that PV energy output would be improved by 7.7% for the salt hydrate and 4.4% for the eutectic compared to the reference cell, estimated from the PV cell manufacturers' data of a 0.5% K^{-1} decline in efficiency and the temperature difference between the PV/PCM and reference cell. In the cooler climate of Ireland in mid-September, the power output increase was estimated to be 1.8% with the salt hydrate and 1.0% with the eutectic. No PV power data was reported for this experiment, but the open circuit voltage was higher for the PV/PCM panels during the peak solar hours which is indicative of lower cell temperatures and higher maximum power.

Other research groups have also investigated PV/PCM systems. A 1D finite-difference model of a PV/PCM module was produced and experimentally validated for an outdoor location in Italy in summer (Ciulla *et al.*, 2012). Malvi *et al.* (2011) simulated a PV/T system with PCM and showed that the combination of water cooling with PCM increased PV efficiency by 9%. Concentrating PV (CPV) cells are one area where PCM cooling may be very beneficial due to the high cell temperatures experienced with CPV. During an experiment in western India it was demonstrated that a PV/PCM system was kept at 22–25°C below a reference PV system for 3 hours at a 1.75× concentration ratio (Maiti *et al.*, 2011). A simulation conducted 12 cities also showed encouraging results for a 2× solar concentrator (Lillo Bravo *et al.*, 2011).

This chapter evaluates the global potential for PCM-assisted cooling of PV cells by modelling the increases in electrical output from a silicon solar cell using a numerical simulation. The model parameters are introduced and discussed in section 3.2 and the numerical model explained in section 3.3. The simulation is performed globally using climatological reanalysis data, which is representative of typical meteorological conditions, for each region. Global results are presented in section 3.5 along with more detailed analysis of five sites of current and future interest for solar PV. The locations where PCM-assisted

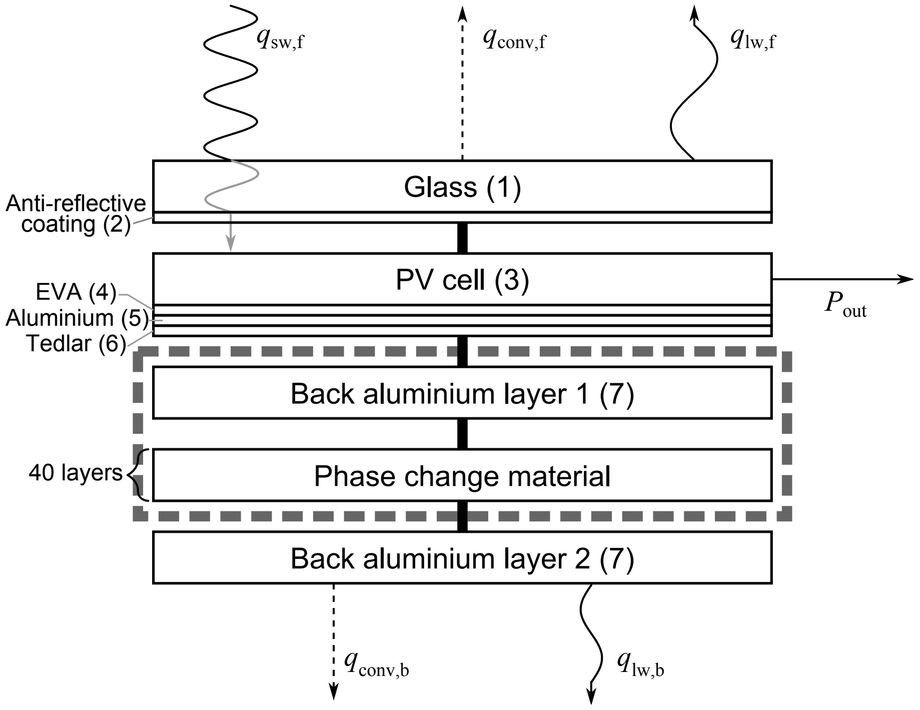

Figure 3.1: Energy balance diagram showing the energy fluxes into and out of the PV/PCM system. The thick black lines represent conductive heat exchange. Subscripts are defined as follows: sw = shortwave, lw = longwave, conv = convective, f = front, b = back. P_{out} is the electrical energy generated by the cell. The dashed grey box encompasses the components of the PV/PCM system that are omitted from the reference PV system. Numbers in brackets refer to the subscripts given to each layer in table 3.1 and eqs. (3.1) to (3.6).

cooling is likely to lead to significant energy output increases are therefore identified. A brief economic assessment is provided in section 3.6. Section 3.7 discusses the key results from the chapter and provides a conclusion.

3.2 Simulated PV/PCM module

The model PV/PCM module consists of a string of solar cells layered on top of an aluminium box containing PCM (fig. 3.1). The heat transfer through a PV/PCM cell is modelled using a one dimensional finite difference energy balance method with a one hour timestep.

The energy balance scheme consists of the incoming solar energy less the heat lost to the surroundings in the form of convection and radiation and energy extracted in the form of electricity (fig. 3.1). Conductive heat exchange occurs between each component of the PV/PCM cell.

3.2.1 PV cells

The PV module is based on that of Armstrong & Hurley (2010a) and has 6 separate layers numbered 1–6 in fig. 3.1 and table 3.1. Given the small heat capacity of some of the layers, the glass and anti-reflective coating are treated as one combined thermal mass, referred to hereafter as the *glass* layer, and the PV cell, ethylene vinyl acetate (EVA) layer, aluminium rear contact and Tedlar backing are combined into another separate thermal mass, referred to hereafter as the *cell* layer. The combining of small thermal masses improves the numerical stability of the model by avoiding division by very small numbers in the finite difference steps.

Subscript	Layer	ρ	c_p	z	k
1	Glass covering	3000	500	0.003	1.8
2	Anti-reflective coating	2400	691	1.0×10^{-7}	32
3	PV cells	2330	677	2.25×10^{-4}	148
4	EVA	960	2090	5.0×10^{-4}	0.35
5	Aluminium (cell)	2700	900	1.0×10^{-5}	237
6	Tedlar	1200	1250	0.0001	0.2

Table 3.1: Heat transfer parameters of the PV panel, from references within Armstrong & Hurley (2010a). ρ: material density (kg m^{-3}), c_p: specific heat capacity [J kg^{-1} K^{-1}], z: material thickness [m], k: thermal conductivity [W m^{-1} K^{-1}].

The total heat capacity [J K^{-1}] of the glass layer is given by

$$C_{\text{glass}} = A\left(\rho_1 c_{p1} z_1 + \rho_2 c_{p2} z_2\right) \tag{3.1}$$

and thermal conductance of the glass layer [W K^{-1}] is given by

$$\kappa_{\text{glass}} = \frac{A}{z_1/k_1 + z_2/k_2} \tag{3.2}$$

where A is the area of the cell. The heat capacity and thermal conductance of the PV cell layer is similarly given by

$$C_{\text{c}} = A\left(\rho_3 c_{p3} z_3 + \rho_4 c_{p4} z_4 + \rho_5 c_{p5} z_5 + \rho_6 c_{p6} z_6\right) \tag{3.3}$$

and

$$\kappa_{\text{c}} = \frac{A}{z_3/k_3 + z_4/k_4 + z_5/k_5 + z_6/k_6}. \tag{3.4}$$

3.2.2 Aluminium casing

The PV cell described is attached to an aluminium box which sandwiches the PCM following the experimental methods of Huang *et al.* (2004, 2006). It was shown that a highly conductive material for the PCM housing such as aluminium is more effective than an insulating housing such as Perspex (Hassan *et al.*, 2010). Heat losses through the sides of the PCM box are assumed to be negligible compared to the front and back of the box based on a module size of $A = 1$ m^2. 1 m^2 is chosen as the module size as it is a unit area. Typical commercial modules tend to be in the range of 1.5 m^2 (Green *et al.*, 2014), and since the calculations are normalised to area, this is not too great an approximation.

Both top and bottom aluminium sheets have heat capacity C_{alu} and thermal conductance G_{alu} given by

$$C_{\text{alu}} = A\rho_{\text{alu}}c_{p,\text{alu}}z_{\text{alu}} \tag{3.5}$$

and

$$\kappa_{\text{alu}} = \frac{Ak_{\text{alu}}}{z_{\text{alu}}}, \tag{3.6}$$

with $z_{\text{alu}} = 5$ mm and values of ρ, c_p and k the same as for the back contact aluminium given in Table table 3.1.

3.2.3 Phase change material

PCMs can either be isothermal or undergo a small phase change temperature range. Various materials have been exploited as PCMs, including salt hydrates, fatty acids, sugar alcohols and paraffin waxes (Zalba *et al.*, 2003; Kenisarin & Makhamov, 2007). Paraffin waxes attain their highly tunable melting points due to the varying chain lengths of their constituent hydrocarbons, and as such experience a phase change range (Heinz & Streicher, 2006).

Ideally, a PCM should have a small thermal expansion coefficient, high thermal conductivity, high latent heat of fusion and a high specific heat capacity (Malvi *et al.*, 2011). The thermal expansion of the PCM is assumed to be small in this model (Lamberg *et al.*, 2004). PCMs available commercially tend to have low coefficients of thermal conductivity, which limits the rate of heat transfer (Fan & Khodadadi, 2011). However, thermal conductivity can be improved in several ways. Examples of this include metal fins attached to the PCM aluminium layer which increase the contact surface area between the plate and PCM, inserting a metal mesh into the PCM, inserting high thermal conductivity particles into the PCM, micro-encapsulation of the PCM, or metal conductive strips interspersed within the PCM (Maiti *et al.*, 2011; Velraj *et al.*, 1999). Enhancements in thermal conductance by a factor of 10 to 20 over a plain PCM layer have been reported using a graphite powder (Öttinger, 2004; Heinz & Streicher, 2006). In this simulation, a heat transfer enhancement factor of 2 is used, following Malvi *et al.* (2011).

The PCM component is geometrically thick and has a low thermal conductance compared to the PV and aluminium components. Therefore the PCM has been divided into 40 layers to model the temperature gradient through the PCM. In liquid regions of the PCM, flow is assumed to be laminar and heat transfer primarily occurs by conduction rather than

Parameter	Symbol	Value
Specific heat capacity of PCM, solid	c_{pcms}	2900 J kg^{-1} K^{-1}
Specific heat capacity of PCM, liquid	c_{pcml}	2100 J kg^{-1} K^{-1}
Latent heat of PCM	L	2.1×10^5 J kg^{-1}
Density of PCM, solid	ρ_{pcms}	860 kg m^{-3}
Density of PCM, liquid	ρ_{pcml}	780 kg m^{-3}
Thickness of PCM	z_{pcm}	0.05 m
Thermal conductivity of PCM, solid	k_{pcms}	0.24 W m^{-1} K^{-1}
Thermal conductivity of PCM, liquid	k_{pcml}	0.15 W m^{-1} K^{-1}
PCM layers	l	40
PCM melting temperature	T_{melt}	0–50°C in 1°C intervals
Heat transfer enhancement factor	p	2

Table 3.2: Properties of the phase change material used in this study. All phase change material properties are taken from Malvi *et al.* (2011).

convection, an assumption validated by other models (Hassan, 2010). Ideally convection should be included and the simulation performed in at least two dimensions (Huang *et al.*, 2004), however a 1D model has been shown to be adequate in reality (Ciulla *et al.*, 2012). For the study goal of determining changes on a global basis, a 2D model would be too computationally intense. The properties of the PCM are shown in table 3.2.

The heat content of a non-isothermal PCM can be modelled using the enthalpy method or the effective heat capacity method (Lamberg *et al.*, 2004). The enthalpy method describes the total heat content of the PCM as a monotonically increasing, continuous and invertible function of temperature. Based on paraffin wax PCM melting profiles in the literature (Lamberg *et al.*, 2004; Zukowski, 2007) the enthalpy function of the PCM can be described to a good approximation by a hyperbolic tangent model:

$$\begin{aligned} H = \frac{1}{2}\Big[& C_{\text{pcms}} T_{\text{pcm}} (1 - \tanh(s(T_{\text{pcm}} - T_{\text{melt}}))) \\ & + (Q_{\text{liq}} + C_{\text{pcml}}(T_{\text{pcm}} - T_{\text{melt}}))(1 + \tanh(s(T_{\text{pcm}} - T_{\text{melt}})))\Big] \end{aligned} \tag{3.7}$$

where s is a scale factor that describes the steepness of the phase change region of the enthalpy function as shown in section 3.2.3. $s \to \infty$ for an isothermal PCM. In eq. (3.7), the cumulative heat required to melt the PCM is given by

$$Q_{\text{liq}} = \frac{A z_{\text{pcm}}}{l} \left(\rho_{\text{pcms}} c_{\text{pcms}} T_{\text{melt}} + \rho_{\text{pcml}} L \right) \tag{3.8}$$

and the solid and liquid heat capacities C_{pcms} and C_{pcml} respectively of each layer are

$$C_{\text{pcm}} = A c_{\text{pcm}} \rho_{\text{pcm}} \frac{z_{\text{pcm}}}{l} \tag{3.9}$$

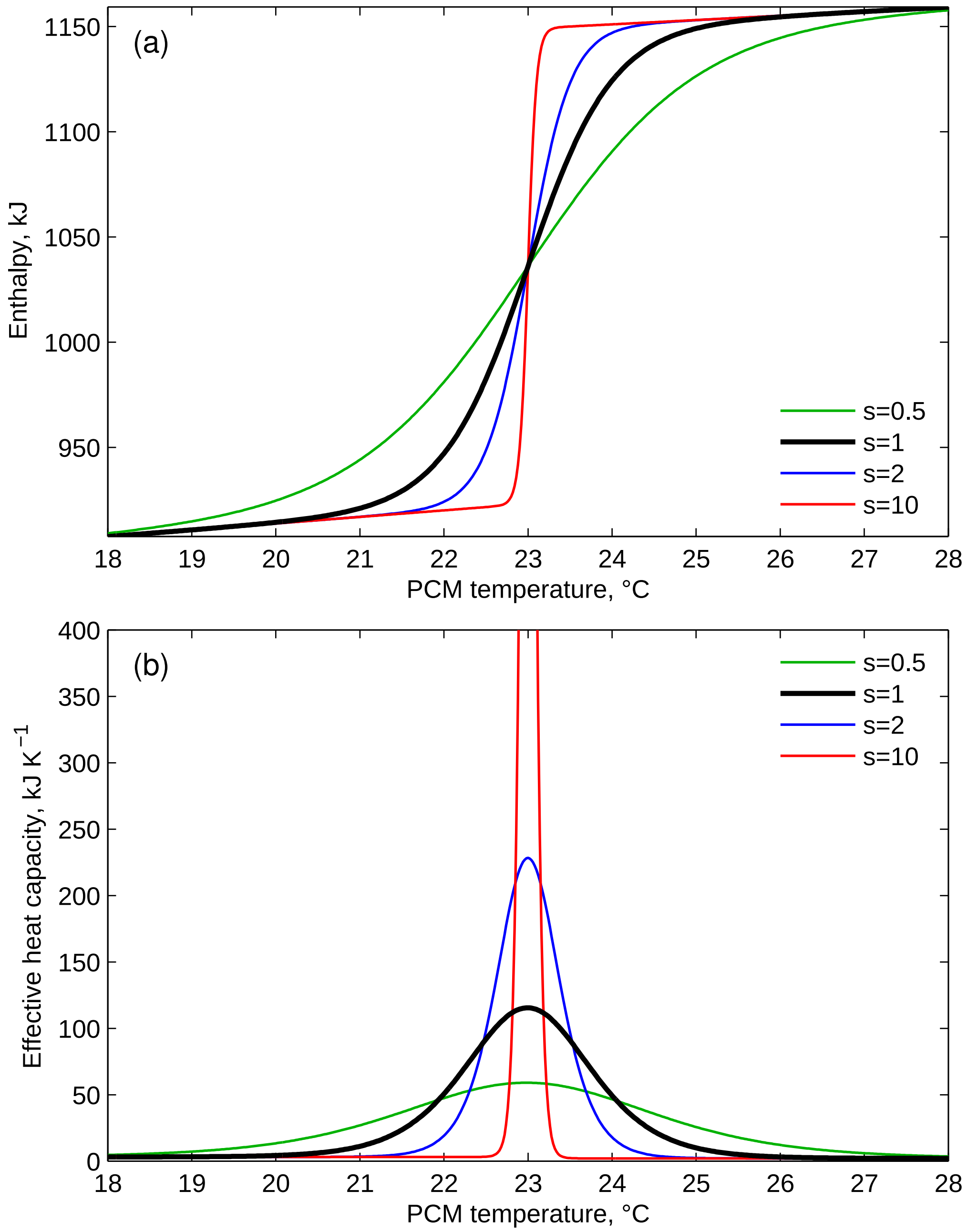

Figure 3.2: (a) The enthalpy function of the paraffin wax PCM used in this simulation. $s = 1$ is used in this model. The effect of varying s is shown on the enthalpy curve. The PCM melting temperature is 23°C. (b) Effective heat capacity function for the PCM for values of s used in section 3.2.3.

where the parameters for solid or liquid PCM from table 3.2 are used in eq. (3.9) as appropriate.

The effective heat capacity of the PCM layer is given by the derivative of enthalpy with respect to temperature (Bridgman, 1914) and after rearrangement becomes

$$\begin{aligned} \frac{\mathrm{d}H}{\mathrm{d}T} = \frac{1}{2}\Big[& C_{\mathrm{pcms}}(1-\tanh(s(T_{\mathrm{pcm}}-T_{\mathrm{melt}}))) \\ +s(Q_{\mathrm{liq}}-C_{\mathrm{pcms}}T_{\mathrm{melt}}+C_{\mathrm{pcml}}(T_{\mathrm{pcm}}-T_{\mathrm{melt}}))\,\mathrm{sech}^2(s(T_{\mathrm{pcm}}-T_{\mathrm{melt}})) & \\ +C_{\mathrm{pcml}}(1+\tanh(s(T_{\mathrm{pcm}}-T_{\mathrm{melt}})))\Big]. & \end{aligned} \tag{3.10}$$

The appearance of s defines the “sharpness” of the peak of the function (section 3.2.3) of effective heat capacity by temperature in the phase change region influenced by the sech^2 term (sech represents the hyperbolic secant such that $\mathrm{sech}\,x = 1/\cosh x$). As s gets larger, the phase change temperature range gets smaller so that the total area under the curve is preserved. Physically, the area under the “hump” of the curve represents the latent heat L. As $s \to \infty$, the effective heat capacity function tends towards a Dirac delta function.

The thermal conductance of each PCM layer $j = 1, \ldots, 40$ is given by the proportion of solid and liquid PCM in each layer which follows from the enthalpy function:

$$\kappa_{\mathrm{pcm}j} = \frac{\kappa_{\mathrm{pcml}} - \kappa_{\mathrm{pcms}}}{2}(1+\tanh(s(T_{\mathrm{pcm}j}-T_{\mathrm{melt}}))) + \kappa_{\mathrm{pcms}} \tag{3.11}$$

where the thermal conductance of solid (κ_{pcms}) and liquid (κ_{pcml}) PCM is

$$\kappa_{\mathrm{pcm}} = \frac{Apk_{\mathrm{pcm}}}{z_{\mathrm{pcm}}/l}. \tag{3.12}$$

3.3 Energy balance scheme

3.3.1 Meteorological data

Synoptic monthly means of the 2 m air temperature T_a, 10 m eastward and northward wind components (U, V) and surface solar radiation downwards G were taken from the ECMWF ERA-Interim reanalysis data. The full resolution model of $0.7^\circ \times 0.7^\circ$ contains too many datapoints for efficient computation so a lower resolution of 1.5° longitude × 1.5° latitude was used. The 12-month period spanning July 2012 to June 2013 was used as the meteorological year under consideration. Synoptic monthly means (averages over the same time of day for each month) were used rather than daily mean observations. This speeds up the computation by a factor of approximately 30.

Monthly mean synoptic data is available 8 times per day from 0000 UTC in 3-hour steps. The surface solar radiation downwards field gives the GHI totals in 3-hour steps for the half-days ending at 0000 UTC and 1200 UTC. To recover the mean irradiance for each

3-hour period, the difference between the irradiation values at the start and the end of each 3-hour time period was taken and this total divided by 10800 seconds. The mean irradiance values derived were deemed to be the irradiance values at the midpoint of each 3-hour period (i.e. at times 0130 UTC, 0430 UTC, and so on). The magnitude of the 10 m wind speed is $W = \sqrt{U^2 + V^2}$. From the 3-hour irradiance, temperature and wind speed data, hourly values of each variable were extracted using cubic spline interpolation.

3.3.2 Numerical model

The energy balance through the PV/PCM system is modelled as a system of 44 simultaneous differential equations. The change in temperature in each layer is governed by

$$\frac{\mathrm{d}T_{\mathrm{glass}}}{\mathrm{d}t} = \frac{1}{C_{\mathrm{glass}}}\left[q_{\mathrm{sw,f}} + q_{\mathrm{lw,f}} + q_{\mathrm{conv,f}} \ + \kappa_{\mathrm{glass}}(T_c - T_{\mathrm{glass}})\right] \tag{3.13}$$

$$\frac{\mathrm{d}T_c}{\mathrm{d}t} = \frac{1}{C_c}\left[\kappa_c(T_{\mathrm{alu1}} + T_{\mathrm{glass}} - 2T_c) \ + A\alpha_c\tau_c(1-\alpha_{\mathrm{glass}})G - P_{\mathrm{out}}\right] \tag{3.14}$$

$$\frac{\mathrm{d}T_{\mathrm{alu1}}}{\mathrm{d}t} = \frac{1}{C_{\mathrm{alu}}}\left[\kappa_{\mathrm{alu}}(T_{\mathrm{pcm1}} + T_c - 2T_{\mathrm{alu1}})\right] \tag{3.15}$$

$$\frac{\mathrm{d}T_{\mathrm{pcm1}}}{\mathrm{d}t} = \frac{1}{\mathrm{d}H/\mathrm{d}T_{\mathrm{pcm1}}}\left[\kappa_{\mathrm{pcm1}}(T_{\mathrm{pcm2}} + T_{\mathrm{alu1}} - 2T_{\mathrm{pcm1}})\right] \tag{3.16}$$

$$\frac{\mathrm{d}T_{\mathrm{pcm}j}}{\mathrm{d}t} = \frac{1}{\mathrm{d}H/\mathrm{d}T_{\mathrm{pcm}j}}\left[\kappa_{\mathrm{pcm}j}(T_{\mathrm{pcm}(j+1)} + T_{\mathrm{pcm}(j-1)} - 2T_{\mathrm{pcm}j})\right], \quad j = 2,\ldots,39 \tag{3.17}$$

$$\frac{\mathrm{d}T_{\mathrm{pcm40}}}{\mathrm{d}t} = \frac{1}{\mathrm{d}H/\mathrm{d}T_{\mathrm{pcm40}}}\left[\kappa_{\mathrm{pcm40}}(T_{\mathrm{alu2}} + T_{\mathrm{pcm39}} - 2T_{\mathrm{pcm40}})\right] \tag{3.18}$$

$$\frac{\mathrm{d}T_{\mathrm{alu2}}}{\mathrm{d}t} = \frac{1}{C_{\mathrm{alu}}}\left[\kappa_{\mathrm{alu}}(T_{\mathrm{pcm40}} - T_{\mathrm{alu2}}) + q_{\mathrm{lw,b}} + q_{\mathrm{conv,b}}\right] \tag{3.19}$$

where T_i is the temperature of each layer, alu1 and alu2 refer to the front and back aluminium sheets, and t is time.

The reference system differs from the PV/PCM system in that T_{alu1} in eq. (3.14) becomes T_{alu}, eqs. (3.15) to (3.18) are omitted and eq. (3.19) is modified to become

$$\frac{\mathrm{d}T_{\mathrm{alu}}}{\mathrm{d}t} = \frac{1}{C_{\mathrm{alu}}}\left[\kappa_{\mathrm{alu}}(T_c - T_{\mathrm{alu}}) + q_{\mathrm{lw,b}} + q_{\mathrm{conv,b}}\right]. \tag{3.20}$$

The change in nomenclature from alu2 to alu highlights the fact there is only one aluminium sheet in the reference system. The heat flows between the PV systems and the ambient are given by

$$
\begin{aligned}
q_{\mathrm{sw,f}} &= A\alpha_{\mathrm{glass}}G && (3.21)\\
q_{\mathrm{lw,f}} &= A\sigma(\varepsilon_{\mathrm{sky}}T_{\mathrm{sky}}^4 - \varepsilon_{\mathrm{glass}}T_{\mathrm{glass}}^4) && (3.22)\\
q_{\mathrm{conv,f}} &= Ah_a(T_a - T_{\mathrm{glass}}) && (3.23)\\
q_{\mathrm{lw,b}} &= A\sigma(\varepsilon_{\mathrm{ground}}T_{\mathrm{ground}}^4 - \varepsilon_{\mathrm{alu}}T_{\mathrm{alu(2)}}^4) && (3.24)\\
q_{\mathrm{conv,b}} &= Ah_a(T_a - T_{\mathrm{alu(2)}}) && (3.25)\\
P_{\mathrm{out}} &= A\eta I && (3.26)
\end{aligned}
$$

with G the GHI [W m^{-2}] and T_{a} the ambient temperature. In this study, the PV/PCM systems are assumed to be horizontally aligned. This would not usually be the case in reality as PV modules will often be aligned at an optimal tilt for the location as explored in chapter 5, or constrained by for example roof geometry. However, this does enable use of the 1D heat transfer simulation and reported results are likely to be on the conservative side. It is assumed that $T_{\mathrm{ground}} = T_{\mathrm{a}}$ (Notton *et al.*, 2005). The sky temperature is described by the relationship of Swinbank (1963):

$$T_{\mathrm{sky}} = 0.0552T_{\mathrm{a}}^{1.5}. \qquad (3.27)$$

For the windward (top) face of the PV panel, forced convection due to the wind will dominate free convection. The empirical heat transfer coefficient of Loveday & Taki (1996) is used:

$$h_{\mathrm{a}} = 8.91 + 2.00W \qquad (3.28)$$

which is valid for wind speeds W up to 15 m s^{-1}. The cell is assumed to be configured on an open mount and as such the coefficient of convective transfer is assumed to be the same on the reverse side of the panel. If a building-mounted PV system is considered, the module temperatures will be higher.

Efficiency is calculated from eq. (2.44). The temperature coefficient $c_1 = 0.0045$ K^{-1}, and the low-light coefficient $c_2 = 0.1$. The STC efficiency η_{ref} is taken to be 15.6%, typical for a commercial c-Si module (Fraunhofer ISE, 2015). Other parameters relevant to the PV cell energy balance scheme used in eqs. (3.13)–(2.44) are given in table 3.3.

The initial conditions for the temperature of each layer of the PV cell were taken from the NOCT relationship (eq. (2.45)) with $T_{\mathrm{NOCT}} = 45$°C. The model was run from local solar midnight in each location in order to give the model time to stabilise with no solar irradiance input, therefore except in polar summer the initial condition for cell temperature is that it is equal to air temperature.

Parameter	Symbol	Value
Area of PV panel	A	1 m^2
Absorptance of glass	α_{glass}	0.05
Absorptance of cell	α_c	0.9 (Notton *et al.*, 2005)
Transmissivity of glass	τ_{glass}	0.95 (Notton *et al.*, 2005)
Stefan-Boltzmann constant	σ	5.67×10^{-8} W m^{-2} K^{-4}
Emissivity of the sky	ε_{sky}	0.95 (Jones & Underwood, 2001)
Emissivity of glass	$\varepsilon_{\text{glass}}$	0.95
Emissivity of the ground	$\varepsilon_{\text{ground}}$	0.95 (Jones & Underwood, 2001)
Emissivity of back layer	ε_{alu}	0.02

Table 3.3: Parameters used within this study to simulate the energy balance through the PV cell.

3.3.3 Cell temperature under PV/PCM model

The temperatures of a solar cell from both a PV/PCM system and a reference system are shown for the grid cell containing Leeds for the month of June (fig. 3.3a). The addition of the PCM layer causes a delay in temperature rise compared to the reference cell before the PCM has commenced melting because of the additional thermal mass in the system which absorbs heat from the PV cell layer. When the PCM begins to reach the melting temperature, thermal energy is absorbed by the PCM as it starts to melt, which further slows down the rate of temperature increase in the PV cell. Peak temperature in the PV/PCM cell is reached later than peak temperature in the reference cell. The larger thermal mass of the PV/PCM cell results in it cooling more slowly than the reference cell after reaching peak temperature, and as it approaches the PCM melting temperature from the liquid phase thermal energy is returned from the PCM to the solar cell causing the cell to remain warmer than the reference cell. By the time of day that the PV/PCM cell is warmer than the reference, irradiance levels are low and the PV panel generates only a small fraction of its total daily electricity output. This is expected, in line with previous outdoor experiments (Huang *et al.*, 2006). The effect is displayed in fig. 3.3b, where it is shown that the gain in power from the PV/PCM cell compared to the reference cell during the middle of the day more than offsets the marginal negative contribution in the early morning and late afternoon when irradiance levels are much lower than at midday. Through the evening, the PV/PCM cell is significantly warmer than the reference cell as the PCM layer continues to dispose of its heat.

3.4 Modelling flowchart

The modelling flow diagram is shown in fig. 3.4.

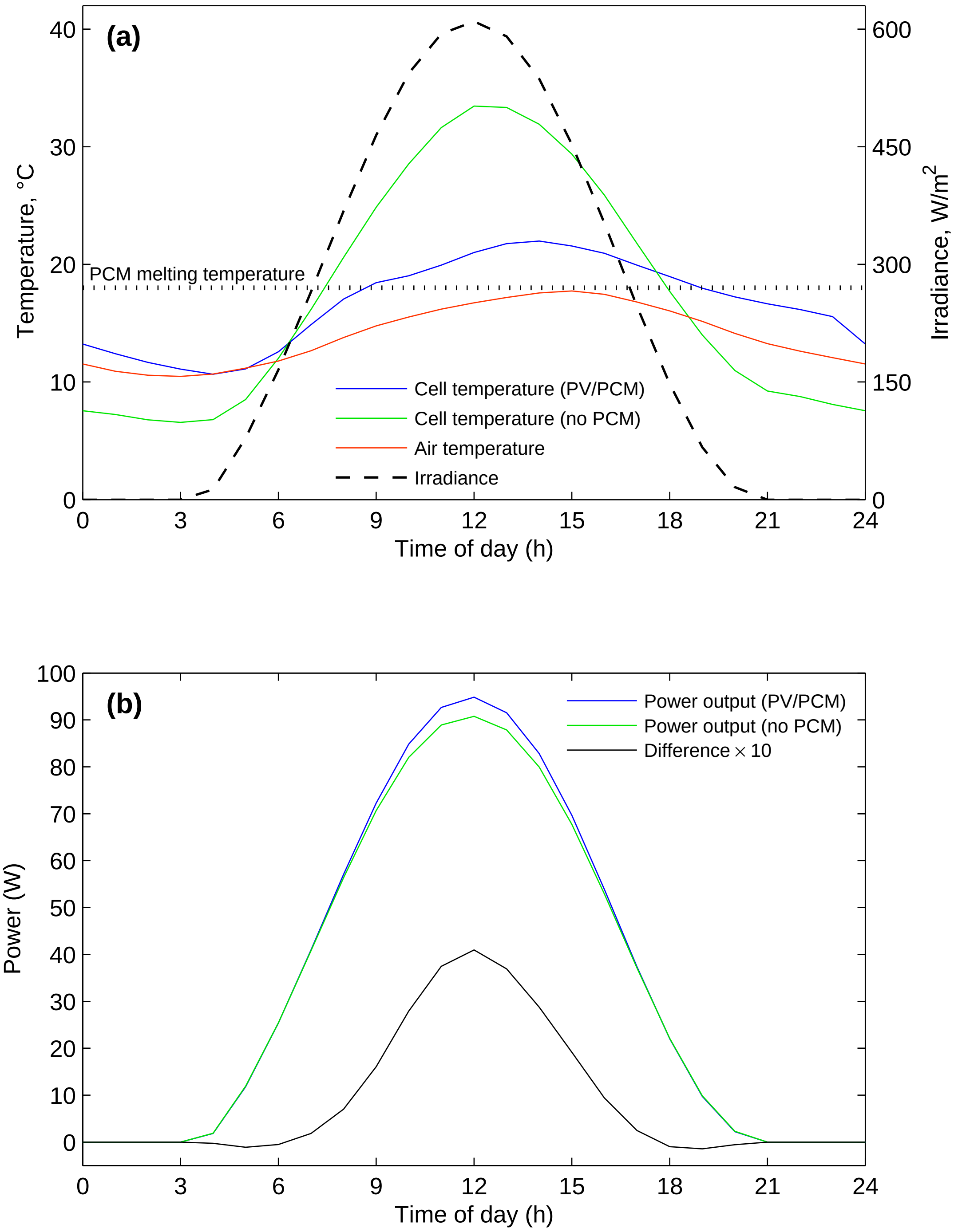

Figure 3.3: (a) Temperatures of PV/PCM and reference cells. PV cell temperature with a PCM (blue) and without a PCM (green) for the ECMWF grid cell containing Leeds (54°N, 1.5°W) in June. Also shown is air temperature (red) and horizontal solar irradiance (black dashes, right scale). The PCM melting temperature is 18°C. (b) Power output from PV/PCM cell and reference cell. Also shown is the power output improvement of PV/PCM cell multiplied by a factor of 10 (black curve).

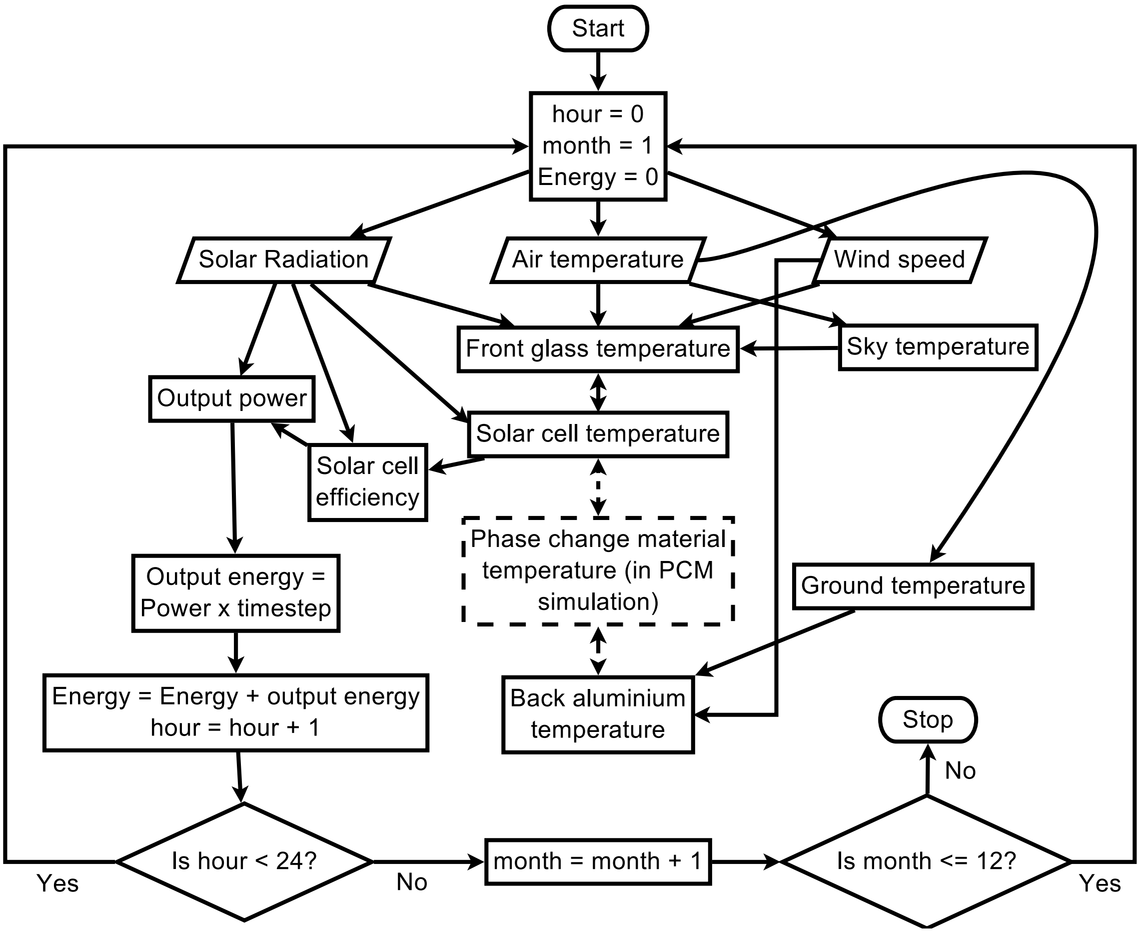

Figure 3.4: Flow diagram of modelling process

3.5 Results of global simulation

Energy output was calculated for all land points on the 1.5°× 1.5° ERA-Interim reanalysis grid for all land points excluding the Antarctic continent. The total annual energy output at each grid point, in kWh, is given by

$$E = \frac{365}{12000} \sum_{m=1}^{12} \sum_{h=0}^{23} I_{hm} \eta_{hm}. \tag{3.29}$$

Irradiance and solar cell efficiency are sampled hourly, and the sum runs over the hours of each typical day h and months of the year m. The factor of 365/12 is to scale the one day per month result to a full year and the additional factor of 1/1000 converts from Wh to kWh.

3.5.1 Annual increase in energy output

Figures 3.5a and 3.5b show the annual average irradiance and temperature from the ERA reanalysis data. The power output for each grid point was calculated both under the reference PV panel and the PV/PCM system for PCM melting temperatures varying between 0–50°C in 1°C intervals, and the PCM melting temperature that produced the largest gain in energy output at each grid point was found (fig. 3.5c). The general trend is for regions that experience the highest ambient temperatures to benefit from the higher PCM melting temperatures, with the optimal melting temperature in excess of 30°C for much of Africa, the Middle East, South Asia, Australia, and Latin America. There are several notable areas of high annual irradiation where low PCM melting temperatures are favoured such as the region northeast of the Himalayas and in the mountain ranges on the west coast of Latin America. Regions which are typically cool and do not receive high irradiation levels show a preference for lower PCM melting temperatures.

The largest relative improvements from PV/PCM systems are located in Africa, the Middle East, Central and Latin America, and the Indonesian archipelago (fig. 3.5d). An improvement in energy output of over 6% is seen on the western coast of Mexico and improvements of over 5% are seen in many regions. These highly suitable locations for PCM are all characterised by high ambient temperatures, except for on the west coast of Latin America. In all other parts of the world, although the relative improvement tends to be lower, there is still a positive increase in electrical energy output to be gained from using a PCM with the optimal melting temperature for the location.

The greatest absolute energy increase using a PCM is again to be found in tropical regions and is mostly coincident with the locations of relative improvement as shown in fig. 3.5e, with parts of the Sahara, Central America, Chile and the Arabian peninsula showing an annual electrical output increase of over 20 kWh m^{-2}.

3.5.2 Sensitivity of energy output increase to PCM melting temperature

Locations that are geographically varied and where large solar farms either currently exist or are planned to be built were investigated further to determine sensitivity to PCM melting temperature. These locations are displayed in table 3.4 and fig. 3.5f.

The relative and absolute improvements in energy output for the PV/PCM module compared to the reference is shown for the full range of PCM melting temperatures in fig. 3.6. At all locations, the improvement in solar PV performance is peaked around the optimal value, however, a PCM melting temperature that is slightly above or below the optimal temperature will still deliver most of the increase in performance available at the optimal value. It can be seen in fig. 3.6 that when a PCM melting temperature that is significantly different from the optimal is used, performance improvement does not decline further with any additional excursion from optimal melting temperature and is still positive.

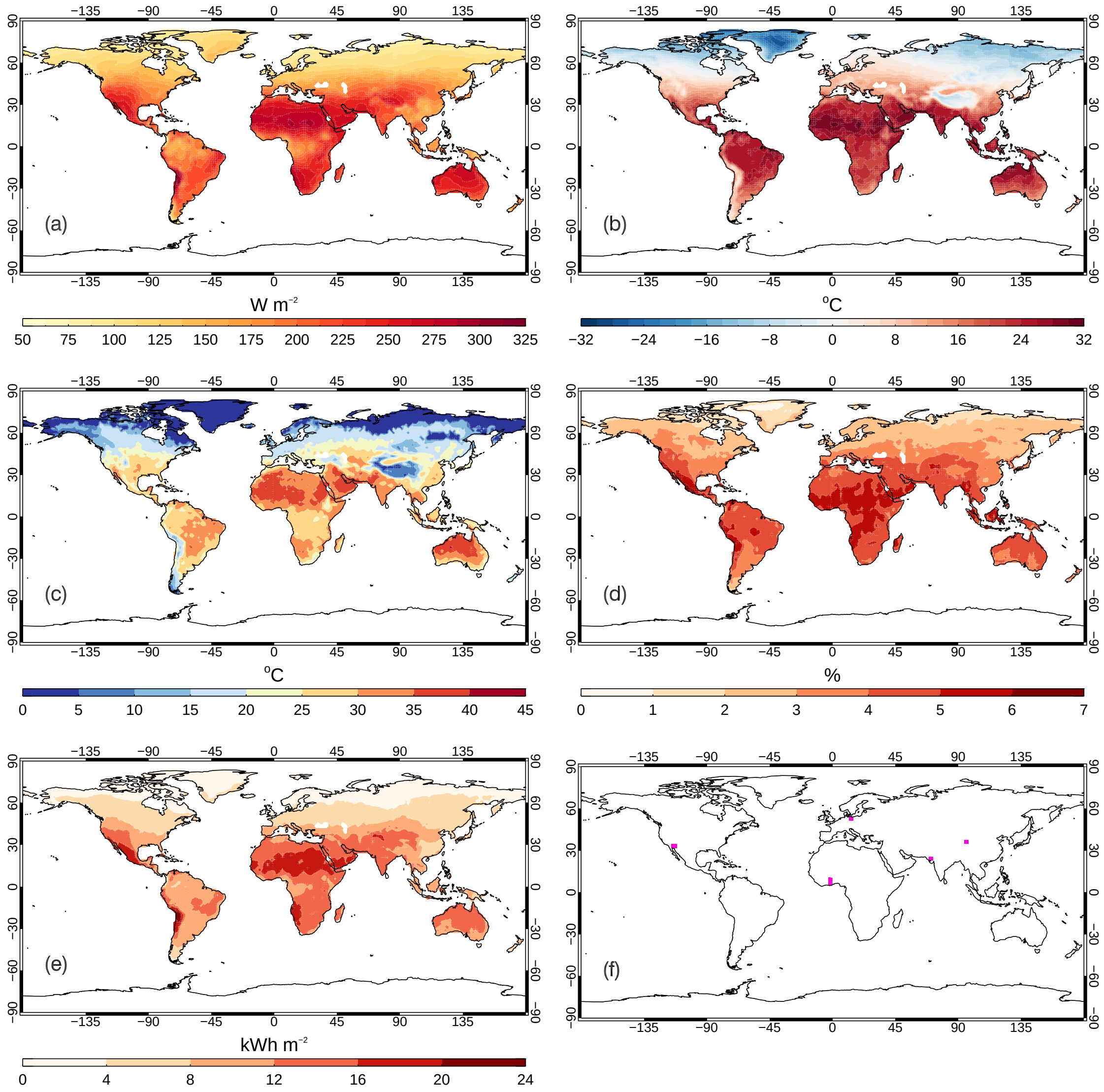

Figure 3.5: (a) Daily-averaged horizontal insolation for the 12 month period July 2012–June 2013 from the ERA-Interim dataset. (b) Average near-surface air temperature for the July 2012–June 2013 period from ERA-Interim dataset. (c) PCM melting temperature that leads to the greatest increase in solar PV energy output in the PV/PCM system. (d) Increase in electrical output from using the PV/PCM system over the PV reference system with the PCM melting temperature equal to the ideal value from fig. (c). (e) Total improvement in annual electrical output for a PV/PCM system over the PV reference with the PCM melting temperature equal to the ideal value in fig. (c). (f) Locations used in the sensitivity analysis (section 3.5.2).

3.5.3 Discussion of simulation results

Overall, areas experiencing high levels of solar irradiance appear to benefit most from PCM cooling. This follows from eq. (3.13) and eq. (3.14) in which a large solar irradiance input G drives an increase in PV front glass and cell temperatures so efforts to mitigate these temperature rises should lead to increased PV efficiency. The most beneficial PCM melting temperature depends more on the ambient temperature; a hot climate will require a high PCM melting temperature and a cool climate favours a low PCM melting temperature. For areas with comparable yearly irradiation, a cooler climate is still

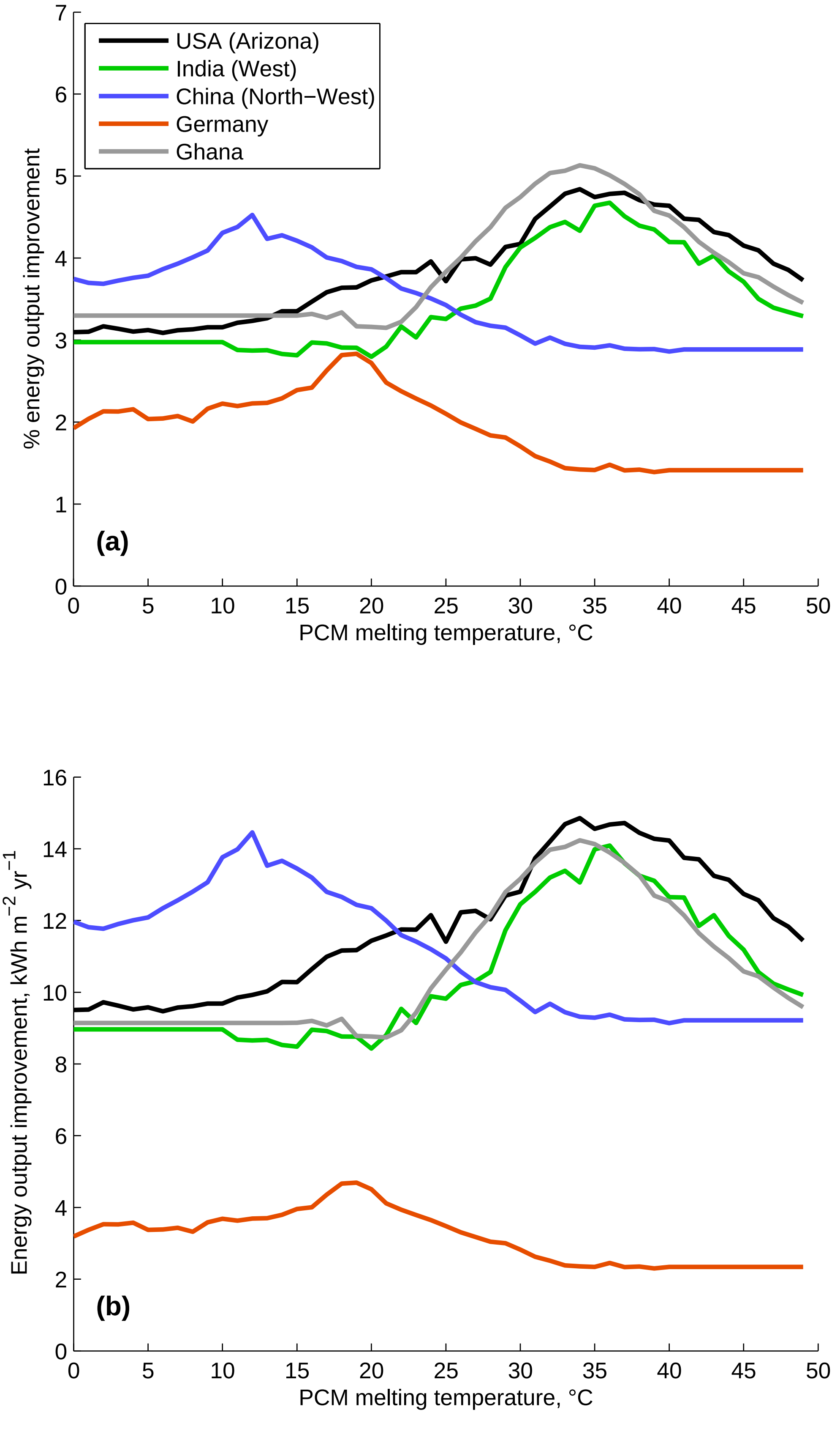

Figure 3.6: The improvement in (a) relative and (b) absolute PV output as a function of PCM melting temperature T_{melt}.

Name	Location	Size	Reference
Agua Caliente, USA	33.0°N, 113.5°W	250 MW	First Solar (2012)
Mesquite, USA	33.3°N, 112.9°W	150 MW	Energy Matters (2013)
Charanka, India	23.9°N, 71.2°E	214 MW	McMahon (2012)
Golmud, China	36.4°N, 95.3°E	200 MW	Cohen (2012)
Neuhardenberg, Germany	52.6°N, 14.2°E	145 MW	Lenardic (2011)
Nzema, Ghana	5–11°N, 0–3°W	155 MW	Rhead (2012)

Table 3.4: Characteristics of large solar farms investigated. The precise location of Nzema is not known so the latitude/longitude grid that covers the whole of Ghana has been investigated. The two arrays in the USA are close enough together to be grouped in the same grid cell to the resolution of the model. See also fig. 3.5f.

preferable with PCM as the PCM helps to keep cell temperature nearer to the ambient, and if the ambient temperature is lower the baseline efficiency will be higher.

The greatest improvements in PV/PCM cell performance are realised by choosing a PCM that fully melts over the course of the day and fully re-solidifies over the evening and before sunrise the next day, making use of the latent heat capacity of the phase change material. Following this, PCM melting temperatures that are too high or too low do not produce the required effect, however, the addition of the PCM as a thermal mass to the solar cell does slow down heating and cooling of the solar cell to the effect that the PV/PCM cell does not get as warm as the reference cell during peak solar hours. It is shown in the variation of T_{melt} in fig. 3.6 that using a PCM melting temperature that differs from the ideal temperature by a few degrees also results in a significant improvement in PV energy output performance where at least part of the latent heat capacity of the PCM is used.

It is difficult to validate these results with those in the literature as it does not appear that published results for a successfully operating PV/PCM system for a full year exist. In their simulations Malvi *et al.* (2011) find the ideal T_{melt} to be 28°C for a diurnal temperature range of 10–20°C, and 32°C for a diurnal temperature range of 20–30°C, both with a 12-hour day with irradiance varying sinusoidally and plane irradiance peaking at 1000 W m^{-2}. This is approximately the range of optimal T_{melt} seen in tropical and subtropical areas year-round from the results in fig. 3.5c, where this temperature range, length of day and irradiance level are broadly seen for much of the year.

The longest outdoor experiments for a comparable PV/PCM system to the one considered in this chapter were over the course of two weeks by Hassan *et al.* (2015) in Pakistan and Ireland. The PCM melting temperatures for the PCMs selected for this experiment were 22.5°C and 29.8°C. This is a little lower than optimal for Pakistan (30–40°C) and higher than optimal for Ireland (15–20°C, fig. 3.5c). However PCMs were selected for this experiment based on considerations other than melting temperature, in particular their performance in laboratory experiments compared to other PCMs at an ambient temperature of 20°C where they outperformed a paraffin wax PCM (Hassan *et al.*, 2010). When considering likely peak cell (65°C) and ambient (45°C) temperatures, Maiti *et al.* (2011) chose a PCM with melting temperature in the range of 56–58°C for a 1.75× concentrating PV system in India. While this is higher than the highest temperature shown to be of benefit for a flat-plate collector in this study, and above the optimal temperature for India shown to be around 35°C in this simulation (fig. 3.5c), the additional solar energy input from the concentrating system will increase cell temperatures beyond those expected at one sun.

In this global study one PCM is used for a full year of meteorological conditions and it is likely that there are many times throughout the year that the PCM is non-optimal. The variability of climate appears to have an influence on the effectiveness of PCM. In fig. 3.7, the monthly average irradiance and temperature is shown for each of the case study locations. Of these regions, Ghana experiences the smallest inter-seasonal variation in temperature and irradiance levels (fig. 3.7e) and shows the largest benefit in PCM-enhanced cooling (fig. 3.6a). The uniformity of year-round climate means that the annual optimal PCM melting temperature is closer to the monthly optimal for many months the year which may be why the *relative* increase in electricity output at optimal PCM melting temperature is slightly higher for Ghana than for Arizona. In Germany, where wintertime irradiance is very low but even summertime irradiance is lower than the other locations, the lowest relative PCM improvement is seen. PCMs may therefore be of limited benefit in areas of low solar irradiance but a PCM that is optimised for summer conditions should perform better than one optimised for the annual mean conditions in higher-latitude locations.

3.6 Economic assessment of PV/PCM

Hendricks & van Sark (2011) performed a cost assessment of PV/PCM systems for four different PCMs in two locations (Malaga, Spain and Utrecht, Netherlands). They considered only PCM material cost and did not include manufacturing costs or the costs of the PCM container. The costs were compared against the savings in electricity not purchased using consumer electricity prices. Hendricks & van Sark found that in the best case scenario of using a paraffin wax PCM with melting temperature of 42°C in Malaga, the payback period was 165 years. This far exceeds the expected lifespan of a PV module of 25 years. Hassan *et al.* (2014) argues that PV/PCM can become cost-effective for certain regions if materials can be purchased in bulk, in conjunction with learning rates that would lead to manufacturing costs reducing by a factor of 10. Their assessment was

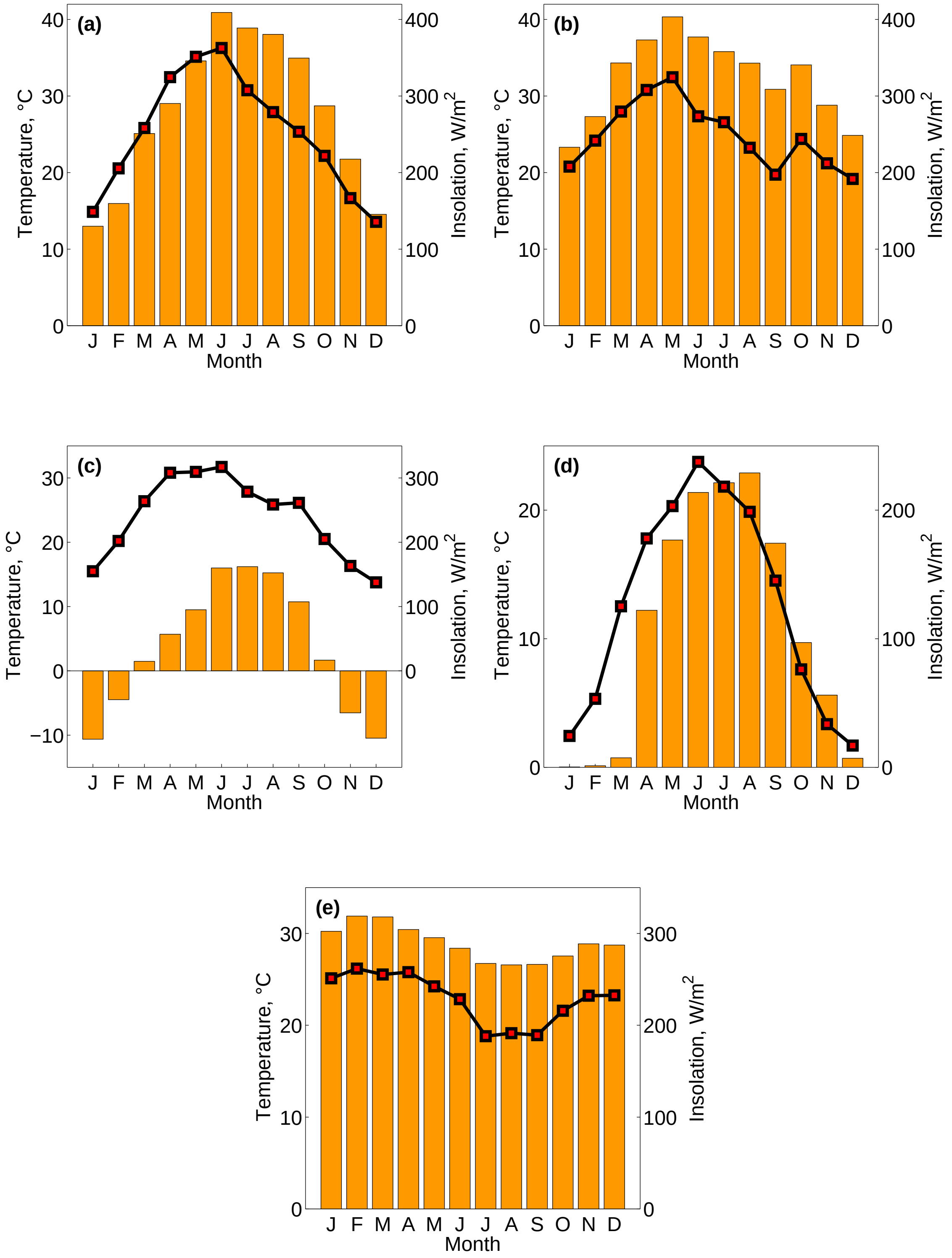

Figure 3.7: Climate data for the locations analysed in section 3.5.2: (a) Arizona; (b) India; (c) China; (d) Germany; (e) Ghana. Bars indicate temperature (left scale), lines indicate irradiance (right scale).

based on the cost of solar PV in €/kWp.

An illustrative cost assessment is performed to determine whether PV/PCM systems would currently be commercially viable based on the outputs from the global simulation. To implement 1 m^2 of PV/PCM at a depth of 0.05 m (total volume 0.05 m^3) would require 39 kg of PCM at its liquid density of 780 kg m^{-3}. To fabricate an aluminium container that is 1 m $\times$ 1 m $\times$ 0.05 m, a total surface area of 2.2 m^2 of aluminium is required (two faces of 1 m^2 and four sides of 0.05 m^2). The total mass of 5 mm thick aluminium required is therefore 2.2 m^2 $\times$ 0.005 m $\times$ 2700 kg m^{-3} = 29.7 kg. A greater volume may be required to provide overlap and ensure that the box is fully watertight. Aluminium costs are estimated based on the recent lower range of bulk sheet purchase prices from China of €0.60 kg^{-1}.

The majority of the costs arise from the PCMs rather than the aluminium. López-Navarro *et al.* (2014) used 165 kg of paraffin wax at a cost of €4.93 kg^{-1} from Rubitherm GmbH in Germany for a solar cooker, which would be enough for four solar modules in this present study. On the order of tons, it is probable that bulk prices are lower than this. Kenisarin & Makhamov (2007) report a unit price of €2.90–€3.50 kg^{-1} for Rubitherm products. This price has been used by Hendricks & van Sark (2011) in their evaluation. To compare to electricity prices, the 2007 figures from Kenisarin & Makhamov (2007) have been converted to 2013 prices by using compound German consumer price index (CPI) inflation figures for 2008–2013 of 9.0% (Triami Media BV, 2015) to give a cost range of €3.16–€3.82 kg^{-1}. The lower limit of €3.16 kg^{-1} has been used here to provide the best case scenario. System costs may be able to be lowered by using a smaller thickness of aluminium or a different PCM material. According to Hassan *et al.* (2014), bulk costs of salt hydrate PCMs could be as low as €1.90 kg^{-1}, around 60% of the price of paraffin waxes.

Adding the costs of the aluminium and the PCM, the attachment of the PCM box would cost €141.06 (table 3.5). These prices have not considered the costs of manufacturing the PCM boxes, which will include plant and machinery capital costs as well as workers wage costs, so this is considered a lower bound for PCM attachment. Assuming a 25 year lifespan, the price of electricity required to make a PV/PCM system cost-effective is shown in table 3.6. Retail electricity prices, which are also shown, would have to be at least this level or higher to make PV/PCM economically viable. This is not currently satisfied in any of the case-study locations.

An alternative measure of cost-effectiveness is the levelised cost of electricity (LCOE), which reflects the total lifetime costs divided by the total expected energy output over the lifetime of the power plant. The lifetime costs include the total of the initial setup

Commodity	Unit cost	Mass required	Total cost
PCM	€3.16 $\mathrm{kg^{-1}}$	39 $\mathrm{kg\ m^{-2}}$	€123.24 $\mathrm{m^{-2}}$
Aluminium	€0.60 $\mathrm{kg^{-1}}$	29.7 $\mathrm{kg\ m^{-2}}$	€17.82 $\mathrm{m^{-2}}$
Total			€141.06 $\mathrm{m^{-2}}$

Table 3.5: Example costs of materials required to include a 0.05 m layer of PCM with aluminium casing.

Location	kWh/yr additional PV output using optimal PCM (fig. 3.6b)	Cost of electricity to make PV/PCM worthwhile (2013) €¢ $\mathrm{kWh^{-1}}$	Retail cost of electricity (2013) €¢ $\mathrm{kWh^{-1}}$
US (Arizona)	14.85	38.0	8.3
India (Gujurat)	14.13	39.9	7.6
China (Qinghai)	14.45	39.0	2.9
Ghana	14.23	39.7	26.2
Germany	4.69	120.3	22.1

Table 3.6: Summary of electricity prices required to make PV/PCM cost-effective in each case-study region compared to indicative current costs. Data from years prior to 2013 have been adjusted to 2013 using country-specific CPI inflation figures from Triami Media BV (2015). References: US: U.S. Energy Information Administration (2014), India: Indian Express (The) (2012), China: Ma (2011), Germany: European Commission (2012a), Ghana: Electricity Company of Ghana Limited (2013).

costs, lifetime fuel and maintenance costs, and decommissioning costs, discounted over the lifetime of the installation (Branker *et al.*, 2011). Owing to variations and uncertainties in input variables, and choice of an appropriate discount rate (reflecting the time value of money or risk-free rate of return, an inherently uncertain parameter over the 25-year lifetime of a solar project), the LCOE can show a wide range of values. An analysis for solar PV shows a LCOE in the range of €0.08 $\mathrm{kWh^{-1}}$ to €0.12 $\mathrm{kWh^{-1}}$ for Germany (Kost *et al.*, 2013). For regions of high solar irradiance the estimate is in the range of €0.06 $\mathrm{kWh^{-1}}$ to €0.10 $\mathrm{kWh^{-1}}$. Therefore the central estimates of €0.10 $\mathrm{kWh^{-1}}$ for Germany and €0.08 $\mathrm{kWh^{-1}}$ for the other four case-study areas are used. As increases in output using PCM are less than 6% in all locations, an assumption that changes in energy output are approximately linear for LCOE estimates is assumed; as fixed costs of PCM materials have already been accounted for the benefits may be underestimated slightly.

Table 3.7 shows the additional levelised cost benefits of using PCM for the five case study regions. The lifetime cost benefits are less than €30 in each location, compared to the €141.06 that would be required to make PV/PCM worthwhile compared to using PV without a PCM.

Location	kWh/yr additional PV output using optimal PCM	× 25 year lifetime, kWh	LCOE, € kWh^{-1}	PCM cost benefit, €
US (Arizona)	14.85	371.25	0.08	29.70
India (Gujurat)	14.13	353.25	0.08	28.26
China (Qinghai)	14.45	361.25	0.08	28.90
Ghana	14.23	355.75	0.08	28.46
Germany	4.69	117.25	0.10	11.73

Table 3.7: Summary of levelised cost of electricity analysis in each case-study location. Costs are in 2013€.

3.7 Summary

In this chapter, a global simulation of a PV system with and without an attached phase change material (PCM) was presented. The PV energy output was determined using a numerical heat transfer model. This work extends previous studies by applying a PV/PCM model to a global scale, highlighting regions in which PV/PCM could provide a substantial increase in solar PV energy (up to 23 kWh per m^2 of installed capacity per year, or 6% increase in energy output in relative terms).

PV/PCM systems can curb the rapid rise in PV cell temperatures during the daytime and keep PV cell temperatures lower during the peak solar hours of the day, improving solar cell efficiency and electrical energy output. Heat is transferred from the PV cell to the PCM, which acts as a heat sink as it melts, both delaying temperature rise in the PV cell and keeping overall temperature rise lower than in a non-PCM cell. Heat is released back from the PCM layer to the solar cell through the evening and overnight.

The best results are seen where an ideal PCM melting temperature for the location in question is used and the PCM melts fully over the course of the day and re-solidifies in the evening before dawn of the next day. In this case the full latent heat content of the PCM is used and the PCM layer acts as thermal mass with a high effective heat capacity. PV/PCM systems provide the greatest improvements in absolute and relative terms in Africa, South Asia, Australia and Latin and Central America. These areas receive high solar irradiance and often experience high ambient temperatures year-round. Many of these are areas where solar energy could greatly aid development by providing an abundant, clean and reliable electricity source.

It has been demonstrated that single junction silicon PV/PCM systems are not currently cost-effective, but this may be possible for technologies such as concentrating PV, or by using lower cost or lower quantities of materials. Furthermore, tracking systems were not considered, which would increase irradiance incident on a PV panel and thus increase cell temperature. Based on this global overview, more detailed regional models could be explored to further isolate the conditions necessary for enhanced solar PV energy output using PCMs and the potential for cost-effective implementation. CPV may be one area where PCM cooling may be more cost-effective due to the greater need for cooling and smaller area of the cells.

In later chapters, the effect of climate change on PV efficiency is investigated. The rise in ambient temperatures under climate change will reduce PV efficiency. PCM cooling is one method that could be used under a future climate scenario in order to mitigate this effect.

Chapter 4

Solar energy transmission and cloud coverage

Chapter 3 showed that output power increases of up to 6% were possible globally using passive cooling of solar modules. The solar radiation data used to drive the model was available in three-hour timesteps on a $1.5^\circ \times 1.5^\circ$ global grid from the ECMWF dataset. In the UK, it is possible to improve the temporal and spatial resolution of solar energy prediction methods owing to a network of ground radiation stations that all report solar irradiation hourly.

This chapter describes the statistical distribution of irradiance received at the earth's surface as a function of cloud fraction, for the UK. The ultimate aim of this work is the generation of realistic cloud transmission data for usage in a stochastic weather generator, the details of which are in Bright *et al.* (2015). Contemporaneous measurements of solar irradiance and cloud fraction observations for 63 sites across the UK for four years are compared to a theoretical clear-sky algorithm to determine the transmission factor due to clouds. Such a weather generator, if coupled with observations of wind speed and temperature, could be used to generate a probabilistic model for the study in chapter 3.

Firstly, a review of previous studies on cloud transmission effects and probabilistic models is presented. The bulk of the chapter focuses on the clear-sky irradiance generation and statistical methods used, and the simplifications and application to a stochastic weather generator are described later in the chapter. It is shown that the distributions of cloud transmission do depend heavily on cloud fraction but are not independent of solar zenith angle.

4.1 Background and literature review

The most reliable way to determine the solar resource for a particular location is to set up long-term pyranometer observations. For many sites of interest, pyranometer records are not frequently obtained for a sufficiently long period prior to installation of a solar

Study	Derived quantity	Variables
Ångström (1924)	Daily clear-sky index	SD
Prescott (1940)	Monthly clearness index	SD
Wörner (1967)	Hourly clearness index	CF
Kasten & Czeplak (1980)	Hourly clear-sky index	CF, CT
Nielsen *et al.* (1981)	Hourly net and global radiation	CF
Brinsfield *et al.* (1984)	Daily global radiation	CF, OCF
Bristow & Campbell (1984)	Daily clearness index	DTR
Hargreaves *et al.* (1985)	Daily global radiation	DTR
de Jong & Stewart (1993)	Daily clearness index	DTR, PR
Supit & van Kappel (1998)	Daily clearness index	DTR, CF
Muneer *et al.* (1998)	Hourly beam and diffuse radiation	SD
Matszuko (2012)	10-minutely global radiation	CF, CT

Table 4.1: Relationships between meteorological variables and radiation. Key: SD = sunshine duration, CF = cloud fraction, CT = cloud type, OCF = opaque cloud fraction, DTR = diurnal temperature range, PR = precipitation. Clearness index, k_t, and clear-sky index, k_c, are defined in section 2.1.4. In this table, only correlations that predict transmission in all-sky (clouds inclusive) conditions are included; several clear-sky radiation models that are based on temperature, relative humidity and pressure exist (e.g. Muneer *et al.* (1998)).

energy system. A shorter-term period of pyranometer records may be sufficient to estimate the long-term climate if the inter-annual variability is not too great (Gueymard & Wilcox, 2011; Gil *et al.*, 2015). If this is not the case or no pyranometer records are available, other meteorological variables can be used as a proxy to estimate solar radiation. Meteorological records of temperature, pressure, cloud fraction, cloud type, rainfall and sunshine hours have been kept at many stations in many countries for decades, as they are often of greater interest to the meteorological community than solar radiation. In the past, relationships to solar radiation intensity to one or more of these variables have been discovered by several investigators (table 4.1).

Since clouds are one of the largest attenuating factors of solar radiation, cloud coverage can be a useful predictor of solar radiation. Typically cloud fraction is recorded at meteorological stations as an integer number of oktas, here denoted c_8, which is the number of eighths of the sky obscured by clouds (UK Met Office, 2010). An additional okta code 9 is used for situations where the sky is obscured by fog, haze or other meteorological phenomena, preventing the sky being observed. A further convention is to reserve okta 0 for completely cloudless sky and okta 8 for completely overcast sky, so the limits of okta 1 and okta 7 observations are extended to almost clear and almost overcast respectively (Jones, 1992) (table 4.2).

In table 4.1 there are five studies of interest, namely Wörner (1967), Kasten & Czeplak (1980), Nielsen *et al.* (1981), Brinsfield *et al.* (1984) and Matszuko (2012) which correlate cloud fraction to a radiation quantity. Supit & van Kappel (1998) extends the Wörner

okta c_8	cloud fraction f_c
0	precisely 0
1	just over 0 to 3/16
2	3/16 to 5/16
3	5/16 to 7/16
4	7/16 to 9/16
5	9/16 to 11/16
6	11/16 to 13/16
7	13/16 to just less than 1
8	precisely 1
9	sky obscured due to fog/haze/other meteorological phenomena

Table 4.2: Okta conventions for reporting cloud fraction

(1967) relationship to include diurnal temperature range and so is not a unique relationship for radiation as a function of cloud cover. These methods are briefly reviewed below.

4.1.1 Cloud fraction relationships

The relationship attributed to Wörner (1967)[1], as used by Supit & van Kappel (1998) and several other works, was derived from observations in Potsdam in Germany from 1957–59 and provides observations of clearness index by okta:

$$k_t = a_1 \sqrt{1 - c_8/8} + a_2. \tag{4.1}$$

The fitting constants a_1 and a_2 are the form of the equation used by Supit & van Kappel (1998).

Kasten & Czeplak (1980) found an empirical relationship between atmospheric transmission and cloud fraction using 10 years of data for Hamburg, Germany, for solar elevation angles above 5°:

$$k_c = 1 - a_1 (c_8/8)^{a_2} \tag{4.2}$$

where the cloudless-sky radiation [W m^{-2}] is modelled as

$$G_{\mathrm{cs}} = b_1 \sin\theta_e - b_2. \tag{4.3}$$

For Hamburg, $a_1 = 0.75$, $a_2 = 3.4$, $b_1 = 910$, $b_2 = 30$. This relationship was later found to be valid for 5 UK sites by Muneer & Gul (2000) where slightly better performance can be obtained by tuning coefficients for each site.

---

[1] The original article appeared in a journal from the German Democratic Republic and does not appear to be available.

Nielsen *et al.* (1981) developed a relationship for net (incoming minus outgoing) radiation from cloud fraction based on 5 years of observations in Denmark. A secondary correlation between global radiation and net radiation in the same paper can be used to derive global radiation from G cloud fraction:

$$G = \frac{a_0 + a_1 \cos\theta_z + a_3 \cos^3\theta_z - L}{a} \tag{4.4}$$

with a_j $(j = 0, 1, 3)$, a and L being okta-dependent constants.

The Brinsfield *et al.* (1984) method predicts solar radiation based on opaque cloud fraction in tenths, i.e. the fraction of the sky covered by clouds where the sky or higher cloud layers cannot be observed. Opaque cloud fraction is not often recorded and has to be estimated from observations of total cloud fraction. Matszuko (2012) tabulated observed 10-minutely insolation averages by cloud okta and solar elevation angle band for Krakow, Poland. From these observations, the clear-sky index can be calculated for each okta upon dividing by the okta 0 case.

In all of the reviewed papers on cloud fraction, there is a one-to-one relationship presented between cloud fraction and the radiation quantity of interest (k_t, k_c or G). Cloud fraction gives an idea of how likely it is that the sun is obscured by clouds, but does not provide any information as to how opaque the cloud is to solar radiation. The actual cloud transmission factor can take a wide variety of values. For example a sky could be overcast with thin cirrus clouds or thick nimbostratus clouds. In both cases, cloud fraction is 100% but the fraction of radiation reaching the ground can vary from 98–100% for cirrus to as low as 7% for nimbostratus (Matszuko, 2012). Although Brinsfield *et al.* (1984) considers opaque clouds, the various optical depths of both translucent and opaque clouds that are observed may still produce a distribution of results. For these reasons, the distributional spread of irradiance for a particular cloud coverage fraction can be more useful than its mean or median value.

4.1.2 Evolution of cloud fractions

The stochastic element of the model, detailed in Bright *et al.* (2015), is derived by creating a Markov chain of long-term cloud observations for a site of interest in the UK. A Markov chain is a discrete-time statistical process that defines the probability of the next state given the current state. In this work the state is cloud fraction in oktas and the discrete timestep is one hour. A Markov chain exhibits a memoryless property, in the sense that the following state does not depend on any of the previous states, only the current state. The transition matrix summarises the probability of changing from one state to the next.

		Future okta									
		0	1	2	3	4	5	6	7	8	9
Present okta	0	.7157	.0926	.0407	.0341	.0274	.0275	.0254	.0356	.0005	.0004
	1	.2744	.3330	.0954	.0631	.0480	.0504	.0597	.0747	.0006	.0008
	2	.1776	.1716	.1723	.1092	.0767	.0706	.0819	.1367	.0012	.0023
	3	.1367	.1202	.1317	.1376	.0926	.0991	.0980	.1678	.0143	.0020
	4	.1037	.0976	.0886	.1002	.1041	.1105	.1219	.2303	.0433	.0000
	5	.0658	.0780	.0755	.0785	.0889	.1260	.1498	.2680	.0683	.0012
	6	.0413	.0535	.0534	.0664	.0651	.0927	.1646	.3378	.1247	.0005
	7	.0140	.0236	.0233	.0256	.0272	.0405	.0684	.5026	.2741	.0007
	8	.0025	.0085	.0096	.0098	.0116	.0161	.0237	.1990	.7179	.0015
	9	.0247	.0152	.0114	.0000	.0017	.0000	.0105	.0799	.2232	.6334

Table 4.3: Transition matrix for cloud okta for the Church Fenton weather station, based on 12 years of consecutive hourly observations. From figure 2 in Bright *et al.* (2015); data produced by J. Bright.

The transition matrix for 12 years of observations from the Church Fenton MIDAS station, near Leeds, is shown in table 4.3. As expected from reality, hours of clear sky (okta 0) transition to hours of clear sky with high probability. The same is seen for overcast to overcast (okta 8) transitions. Meanwhile, transitions of clear to overcast and vice-versa are rare. Typically the highest probability for each state lies on or near the diagonal of the matrix, showing the tendency for persistence. The large amount of data collected allows for different Markov chains for each season, time of day (morning, afternoon and overnight), and by weather type (high pressure versus low pressure).

Ehnberg & Bollen (2005) used a Markov chain of cloud oktas based on observations from Gothenburg, Sweden, and coupled this with the Nielsen *et al.* (1981) relationship for global radiation as a function of okta and zenith angle (eq. (4.4)). Ngoko *et al.* (2014) uses a Markov chain model to select minutely values of the clearness index given the daily mean clearness index.

The idea is to extend the Ehnberg & Bollen (2005) Markov process to the distribution of cloud transmissions which will be described later in this chapter rather than the one-to-one relationship provided by Kasten & Czeplak (1980) or Nielsen *et al.* (1981).

4.1.3 Distributions of atmospheric transmission

It does not appear that the distributions of clear-sky index by cloud okta class have been investigated previously, and this will be the focus later in this chapter. However, statistical distributions of k_t, k_t' or k_c as a function of their longer-term mean values, $\overline{k_t}$, $\overline{k_t'}$ or $\overline{k_c}$, have received extensive attention in the literature, with the key studies summarised in table 4.4.

One reason to use $\overline{k_t}$ (or the normalised/clear-sky equivalent) as a distribution parameter is that it varies from month to month and day to day. Overcast months/days will have a low

Study	Random variable	Governing parameters	Location
Liu & Jordan (1960)	Daily clearness index	Monthly mean of daily clearness indices	4 sites in US
Bendt *et al.* (1981)	Daily clearness index	Monthly mean of daily clearness indices	90 sites in US
Olseth & Skartveit (1984)	Daily normalised clearness index	Monthly mean of daily normalised clearness indices	10 sites in northern Europe and Canada
Olseth & Skartveit (1987)	Hourly normalised clearness index	Monthly mean of hourly normalised clearness indices	3 sites in Norway and Canada
Graham *et al.* (1988)	Daily clearness index	Monthly mean of daily clearness indices	3 sites in Canada
Suehrcke & McCormick (1988)	Instantaneous, 1-min, 5-min, 20-min and hourly clearness index	One-year mean of instantaneous, 1-min, 5-min, 20-min and hourly clearness indices for different air mass bands	1 site in Australia
Graham & Hollands (1990)	Hourly clearness index	Monthly mean of daily clearness indices	3 sites in Canada
Jurado *et al.* (1995)	5-min, 10-min, 30-min and hourly clearness index	8-year mean of 5-min clearness indices for different air mass and time of day bands	1 site in Spain
Tovar *et al.* (1998)	1-min clearness index	Air mass	1 site in Spain
Hollands & Suehrcke (2013)	Instantaneous clear-sky index	Long-term mean of instantaneous clear-sky index	1 site in Australia

Table 4.4: Studies of distributions of solar transmission in the literature

$\overline{k_t}$ and clear months/days will have a high $\overline{k_t}$, but both are expected to show little variation in hourly or daily individual observations around these mean values. On the other hand, days or months with an intermediate $\overline{k_t}$ are more likely to show more variation in their individual k_t measurements, as there will be a combination of clear and cloudy hours or days.

A further advantage of using the clear-sky or clearness index rather than actual irradiance values is that it more readily correlates to other meteorological variables such as in the well-known Ångström-Prescott relationship between solar radiation and sunshine fraction s_f (cf. table 4.1):

$$k_t = a_0 + a_1 s_f \tag{4.5}$$

where a_0 and a_1 are locally and seasonally dependent constants (Almorox *et al.*, 2005). The original Ångström version of eq. (4.5) uses k_c in place of k_t and accordingly different values of a_0 and a_1.

The benefits of using the clear-sky index compared to the clearness index, namely the independence of air mass and solar zenith angle, have been outlined in section 2.1.4 for cloudless hours. Although k_t takes the projection of the sun's rays onto a horizontal surface at the top of the atmosphere into account, it does not account for the increased atmospheric path length that sunlight must travel through the atmosphere at low elevation angles (cf. eq. (2.19)). The study by Hollands & Suehrcke (2013) is particularly interesting, as it the only one that uses k_c (although both Olseth & Skartveit (1984, 1987) use k_t' where the normalisation is based on the lowest and highest observed clearness indices at each elevation angle). Hollands & Suehrcke (2013) uses a three-state model with truncated normal distribution curves to describe overcast sky, clear sky, and partially cloudy sky states and the contribution that each makes to the overall distribution of k_c. Figure 4.1, which is adapted from Hollands & Suehrcke (2013), shows the contribution of the three sky states to the instantaneous clear-sky index.

Unlike the papers in table 4.4, this chapter by contrast takes cloud okta c_8 as the governing parameter and generates distributions of k_c based on c_8. Since none of the studies use data from the UK, this is an additional extension to UK climates that has not been performed previously. By using k_c, and given good estimates of the atmospheric concentrations of aerosols, water vapour and ozone, the atmospheric transmission factor due to clouds alone can be investigated. In theory, the observed k_c value should be independent of airmass and atmospheric turbidity. Therefore, if cloud transmission distributions exhibit similar characteristics for regions in which the clear-sky transmission varies, then the clear-sky index approach can be used generally and is not limited to the region in which the observations were made.

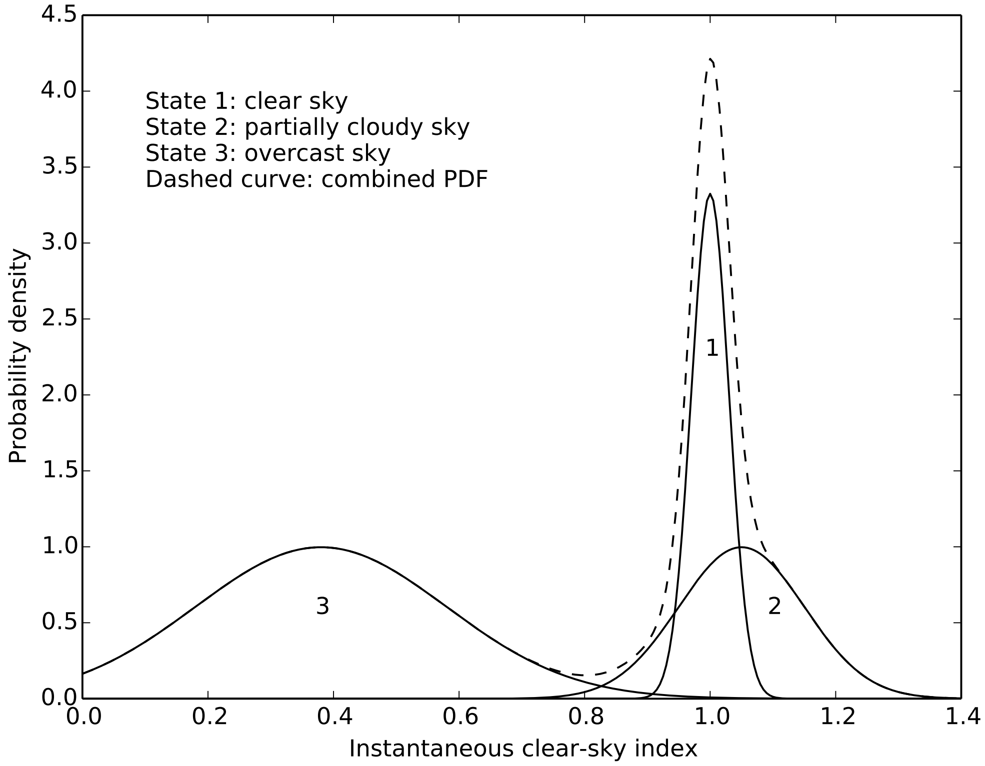

Figure 4.1: Instantaneous clear-sky index as a superposition of the distributions for (1) clear skies, (2) partially cloudy skies and (3) overcast skies. Figure adapted from Hollands & Suehrcke (2013).

4.2 Generating a clear-sky index database for the UK

The aim is to produce a distribution for clear-sky index for each cloud fraction class, so the starting point is to obtain all UK Met Office monitoring stations that record both cloud fraction and hourly GHI G concurrently.

4.2.1 Cloud observations

Cloud fraction observations can either be made by a human observer or a cloud-base recording laser (WMO, 2014). These methods can produce quite different results, with exact agreements only 39% of the time and agreements within 2 okta occurring 88% of the time for a case study in the Netherlands (Wauben *et al.*, 2006). For hourly weather data, a human observer would typically make a subjective judgement of the cloud-obscured proportion of the entire visible sky dome once per hour, while a cloud base recording laser consists of a zenith-pointing device that records the average time in the preceding hour that the laser beam was intercepted by clouds. The irradiation data collected by the Met Office is a sum over each hour, so there can be a difference between the dominant conditions of the previous hour and the cloud amount recorded at the end of the hour (Muneer & Gul, 2000). The cloud-base recording laser method assumes that the clouds overpassing the zenith during the hour are representative of the entire sky conditions, which are not always the case. Thin cirrus is sometimes not detected by the laser and fog can be mistaken for low-level overcast conditions. Additionally, because the solar zenith angle in the UK is always at least 27° but usually the sun is much lower, the clouds (or lack of) overpassing in the zenith direction may not be representative of those obscuring the sun or dominating the rest of the sky.

At stations that measure multi-level cloud coverage, the cloud-base laser recorder records the fractional coverage and cloud height of each layer. However, it is implied from Met Office guidance that observations of total cloud amount are only made when there is a human observer present at the weather station (UK Met Office, 2010). This occurs whether or not there is a cloud-base laser instrument at the weather station. It is therefore reasonable to assume that Met Office records of cloud fraction are assessed by a human observer taking into account the full sky dome.

A total of 64 stations with a wide geographical spread throughout the UK provided hourly observations of total cloud amount in oktas (c_8) and G for the years 2010–2013 inclusive. One station only produced two valid hours over the four years of observation, and has therefore been discounted. The 63 remaining stations are shown in fig. 4.2. QC checks for data are included in a MIDAS collection and data that was flagged as suspect by the MIDAS QC system was rejected; duplicates were also removed. To the remaining data, records were only kept if the measured irradiation total for the hour was greater than 0 kJ m^{-2} and the solar elevation angle for at least part of the hour was above 0°. A total of 1,121,334 hourly observations were retained.

4.2.2 Clear-sky irradiation

The problem of calculating atmospheric transmission in cloudless skies lends itself well to a radiative transfer approach. The clear-sky horizontal irradiation G_{cs} for each hour was simulated with the two-stream version of DISORT in libRadtran with a pseudo-spherical correction as described in section 2.2.6. A radiative transfer simulation is run for each daylight hour at the latitude, longitude and altitude of each MIDAS station in fig. 4.2 for the 2010–2013 period, for hours where both okta and irradiation measurements exist in the record and passed the Met Office applied QC checks.

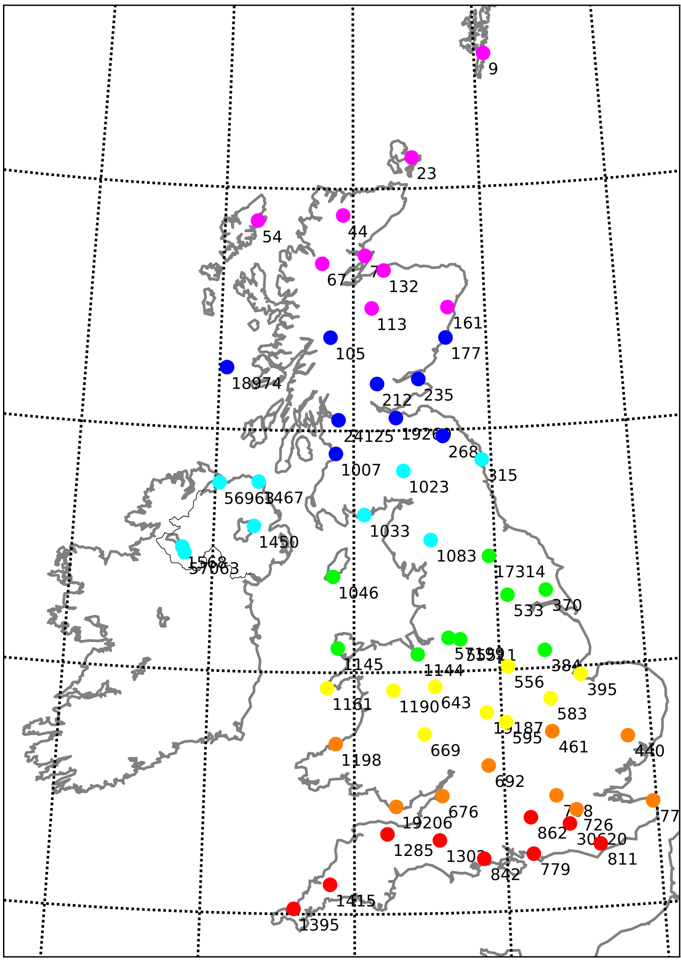

Figure 4.2: MIDAS stations that provide quality-controlled hourly irradiation and cloud fraction observations for 2010–2013. Station numbers refer to MIDAS station IDs; colour-coding is for investigation of geographic trends. The lines of longitude and latitude mark the boundaries of each GLOMAP aerosol climatology grid cell.

Atmosphere

libRadtran contains the set of six standard AFGL atmospheres (Anderson *et al.*, 1986) which are tropical, mid-latitude summer and winter, sub-Arctic summer and winter, and US standard. In the radiative transfer simulations, the background atmosphere for mixed gases concentration is provided by the mid-latitude summer atmosphere for April–September and mid-latitude winter for October–March. Absorption by CO_2 is not significant in the shortwave and previous studies have shown that changing the concentration has negligible effects for solar radiation (Oumbe *et al.*, 2008; Mueller *et al.*, 2009), so this concentration has not been changed from the original 1986 value. Rayleigh scattering depends slightly on atmospheric pressure, so the baseline profiles are modified by including monthly mean pressure and temperature profiles from each month from 2010–13 from the ECMWF reanalysis (section 2.3.2) on a spatial grid of $1.5 \times 1.5°$. Ozone is a strong absorber in the ultraviolet range and water vapour has absorption bands located throughout the near infrared, so the monthly average specific humidity (for water vapour content) and ozone mass mixing ratio from ECMWF are also provided.

Aerosol

The GLOMAP climatology is used for aerosols (section 2.3.4). This divides the MIDAS stations into 11 regions based on GLOMAP grid cell (fig. 4.2). As only the first moment of the aerosol phase function $\chi_1 = g$ is provided by GLOMAP, and $\chi_0 \equiv 1$ by definition, using more than two streams in the radiative transfer calculation is unnecessary. Tests performed between the 2-stream and 6-stream versions of DISORT (assuming a Henyey-Greenstein phase function for the higher phase function scattering moments in the 6-stream version such that $g^j = \chi_j$) for a number of locations in the UK using the GLOMAP data show differences of less than 1% for $\theta_z < 70^\circ$ and less than 4% for $\theta_z < 89.9^\circ$, typically within the ranges of cosine response error of high-quality pyranometers (Vignola *et al.*, 2012, Chapter 5).

Surface

Due to the lack of surface albedo measurements in the MIDAS data, the surface albedo has been taken from the IGBP library (section 2.3.5). This may underestimate the albedo from snow-covered surfaces in winter. Simulations with the two-stream solver in libRadtran show that a perfectly reflecting surface (albedo 1) predicts about 13% higher downwards radiation than a perfectly absorbing surface (albedo 0) for all solar zenith angles under cloudless sky. Real surfaces are not purely absorbing and snow-covered surfaces are not purely reflective so the actual differences are likely to be smaller than this for clear skies.

Solar position

To match the clear-sky simulation to observation as accurately as possible, a high-resolution algorithm for solar zenith angle is required. Met Office data recording conventions state that the observation recorded for each UTC hour (SYNOP climate message) is actually taken 10 minutes before the hour (UK Met Office, 2015a). For solar irradiation (HCM climate message), the time period of data collection runs from 70 minutes to 10 minutes before the observation time stamp. libRadtran provides the Blanco-Muriel *et al.* (2001) algorithm for calculating solar zenith angle, which provides long-term accuracy for solar zenith within 0.1°. The hourly average cosine of the zenith angle is calculated centred at 40 minutes prior to each hour of each day at each MIDAS station. This is calculated internally in libRadtran as an average of minutely samples using the Blanco-Muriel *et al.* (2001) algorithm. If the sun rises or sets during the hour, the zenith angle

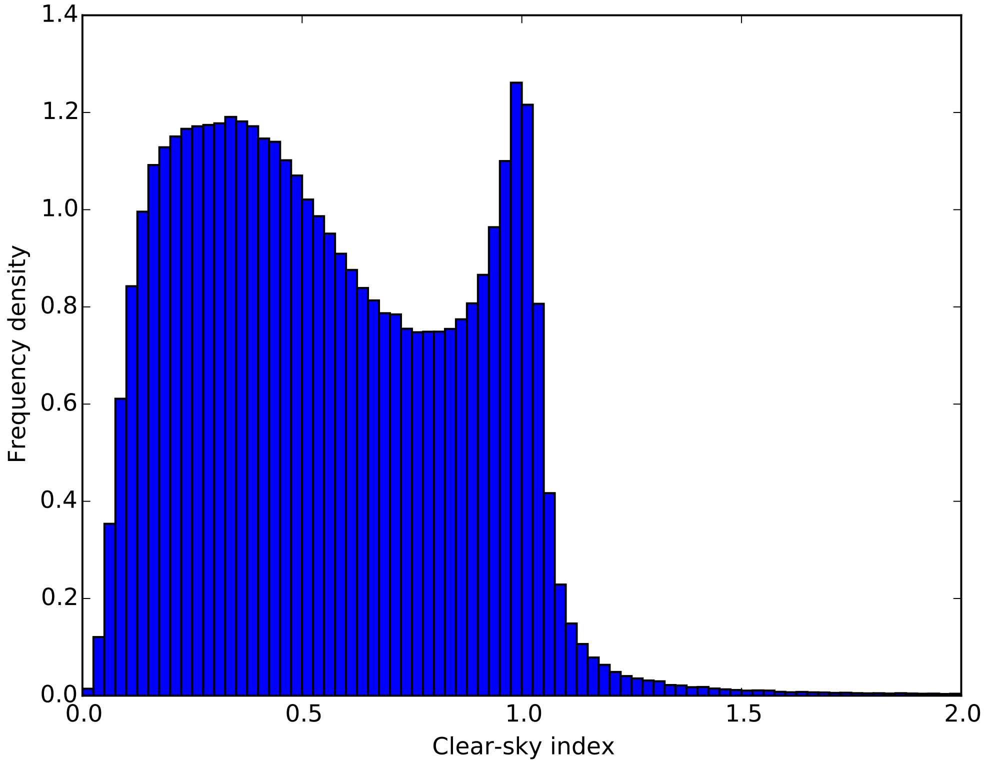

Figure 4.3: Histogram of all hourly k_c values from 63 UK weather stations, 2010–2013

is calculated over the daytime ($\theta_z < 90°$) portion of the hour, the calculation of which is also handled by libRadtran.

4.3 Distributions of clear sky index

4.3.1 All clear sky indices

Before isolating the values of clear-sky index for each okta, insight can be gained from the overall distribution of clear-sky index k_c, which is shown in fig. 4.3. The clear-sky index is calculated by dividing the observed value of the solar irradiation data from the MIDAS dataset by the theoretical clear-sky value as calculated by the radiative transfer procedure described in section 4.2.2 (cf. eq. (2.15)).

Clear-sky index

The overall distribution is clearly bimodal with contributions from clear hours near $k_c = 1$ and overcast hours near $k_c = 0.25$, but a lower number of values for intermediate clear-sky indices. Bimodal behaviour for hourly k_t' values has been observed in Norway and Canada (Olseth & Skartveit, 1987) with the monthly mean of hourly k_t' defining the shape of the distribution. The clear sky mode at $k_c = 1$ shows that the radiative transfer simulation provides a good estimate of irradiation in cloudless skies.

The three-state model as described by Hollands & Suehrcke (2013) for instantaneous clear-sky index (fig. 4.1) is partly observed in the hourly clear-sky indices for the UK. Unfortunately Hollands & Suehrcke (2013) do not provide hourly aggregated distributions of k_c in their paper, as it is likely that averaging out of an hour of instantaneous k_c values will cause more values to fall into the intermediate case between the cloudy and clear modes. In Hollands & Suehrcke (2013), whose study location was Australia, much of the weight of the overall distribution of instantaneous k_c lies in the clear-sky spike, whereas for the UK hourly values the overcast mode is more prevalent (fig. 4.3). This is more likely to be due to the differences between the climates rather than the aggregation time of solar radiation observations.

There are a significant number of values from hours where $k_c > 1$ indicating more solar radiation than would be expected under cloudless conditions for a number of hours. For instantaneous values of k_c this is expected from the cloud enhancement effect, whereby diffuse reflections from cloud sides and strong forward scattering from thin cloud layers can make the surface irradiance exceed the clear-sky value for short periods, and is indeed noted in Hollands & Suehrcke (2013). For hourly data, it is expected that the averaging time would make these fluctuations cancel out. Sources of these high k_c hours merit further investigation.

Clearness and normalised clearness index

In fig. 4.4, the same hourly solar radiation observations are binned by k_t and k_t' (using the Perez *et al.* (1990a) rescaling for clearness index, eq. (2.14)). The effect of this is to change the denominator from the theoretical clear-sky radiation in eq. (2.15) to the extraterrestrial radiation (eq. (2.13)) or a rescaling of this (eq. (2.14)). Neither the relationships for k_t or k_t' depend on a radiative transfer simulation so if there are errors in the clear-sky radiation values this should become apparent with a lower number of extreme observations for k_t and k_t'. When observations are grouped by clearness index (fig. 4.4a), the binomial character of the distribution is hard to discern as the clear-sky spike has been smoothed out by the airmass dependence of k_t. The distribution of k_t' (fig. 4.4b) preserves the shape of the clear-sky index distribution with the entire distribution shifted to the left such that the clear-sky spike is centred around 0.8. It can be observed that k_t' and k_c exhibit approximately the same level of airmass independence due to their similar distribution shapes. There are also fewer occurrences of very low transmittance under k_t', indicating that most instances of low clearness index in fig. 4.4a are airmass related.

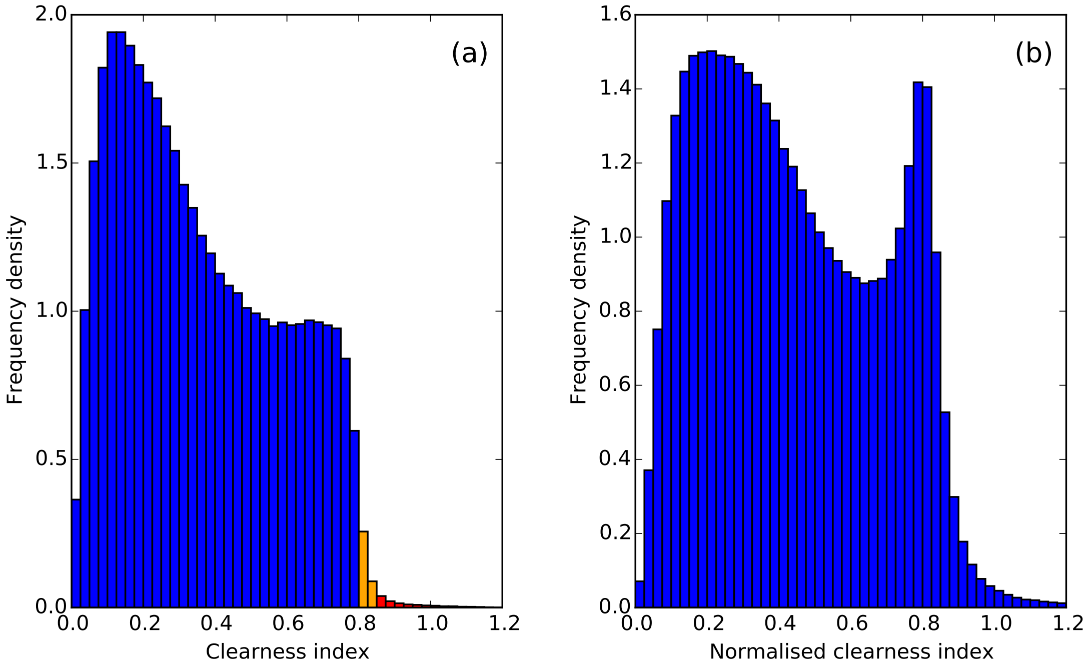

Figure 4.4: Histograms of (a) all hourly k_t observations and (b) all hourly k_t' observations from 63 UK weather stations. In (a), the "rare but possible" and "erroneous" observations have been highlighted yellow and red respectively.

There are very few observations where $k_t > 1$ and none where $k_t > 1.15$. It is not possible to determine whether these points are outliers due to instrumental uncertainty from the MIDAS irradiation values, inaccuracies in the calculated zenith angle, or if they actually occurred. Vignola *et al.* (2012, Appendix A) suggests that while minutely clearness indices can exceed 1 due to cloud enhancement effects, hourly-averaged k_t exceeding 0.85 is never observed. In fig. 4.4a a very rapid drop in k_t values above 0.8 is seen. Only 2% of hourly observations recorded by Erbs *et al.* (1982) for five sites in the US exceeded 0.8. For elevation angles above 10°, there were no hourly observations of k_t exceeding 0.85 for seven sites in the contiguous US (NREL, 1993). While elevation angles lower than 10° were not included, the larger air mass at these elevations make non-erroneous occurrences of high k_t values more unlikely, an observation noted by Perez *et al.* (1990a) when plotting k_t against elevation angle θ_e. Calculations in NREL (1993) using the Bird & Hulstrom (1981) clear-sky model, which is based on a radiative transfer code, places an upper limit of about $k_t = 0.9$ for air mass 1 in an atmosphere containing Rayleigh scattering alone, conditions which are never observed at sea-level. The Linke turbidity method gives a maximum k_t at AM 1 and $T_L = 1$ of 0.915 (fig. 2.4d), reducing to about 0.9 at the UK maximum zenith of 27°.

Based on these previous studies and the results obtained, it is possible to introduce an additional QC check to the MIDAS data by requiring that clearness index be below a certain value. While this may reject good data at low elevation angles because small errors in hourly elevation angle blow up when dividing by the extraterrestrial irradiation, on the whole setting a maximum k_t value should prevent erroneously high observations of k_c. It is decided to class observations of $k_t > 0.85$ as erroneous. Observations of $k_t > 0.8$ are deemed to be physically possible, but rare. From the next section onwards, when conducting analyses all datapoints where $k_t > 0.85$ have been excluded. Applying this criterion only rejects 0.34% of observations and is not expected to skew the results significantly by excluding a large number of good datapoints.

4.3.2 Distribution by solar elevation angle

If the high extremes of k_c are occurring at low solar elevation angles, it can be concluded that the clear-sky index is not entirely airmass independent. In fig. 4.5, the clear-sky index histograms are grouped into bins of elevation angle from 0–10°, 10–20° and so on up to the top group of 50–63°. These histograms reveal different characteristics of the clear-sky index distribution in each elevation angle bin. The $\theta_e \leq 10°$ bin is unimodal showing the greatest accumulation of k_c values around 0.2–0.4. The spread of values is the largest for any solar elevation class, and this group is also responsible for a large majority of the extremely high, $k_c > 1.2$, observations. For the $10 < \theta_e \leq 20°$ bin, the bimodal shape of the distribution starts to become apparent. Low k_c values are still more common, and there is a lower frequency of extremely high observations. As elevation angle increases, the $k_c \approx 1$ "spike" of the distribution becomes sharper and higher than the low k_c "hump", which starts to flatten out and become more uniform, and instances of $k_c > 1.2$ virtually disappear. The height of the spike could be an indication of generally fairer weather conditions at higher solar elevation angles, or could be a result in the reduction of the variance in k_c values in genuinely clear hours that cause the spike in the histograms to contract towards $k_c = 1$.

The histograms of k_t' by elevation angle group (not shown) are very similar to those of k_c up to a scaling factor, so it is unlikely that the calculated clear-sky values from the radiative transfer simulations contain serious errors.

There are several reasons why a large spread, including some very large, k_c values can occur for $\theta_e \leq 10°$. At low sun under a scattered cloud deck, reflections from the undersides of clouds can enhance diffuse irradiance, or clouds near the horizon in the solar direction can forward-scatter sunlight. The effect of snow in winter and how this enhances GHI has been described above. None of these effects are sources of error and represent real-world phenomena; they must therefore be included in the distributions.

Extreme high values of k_c that have not been filtered out by the $k_t > 0.85$ criterion could

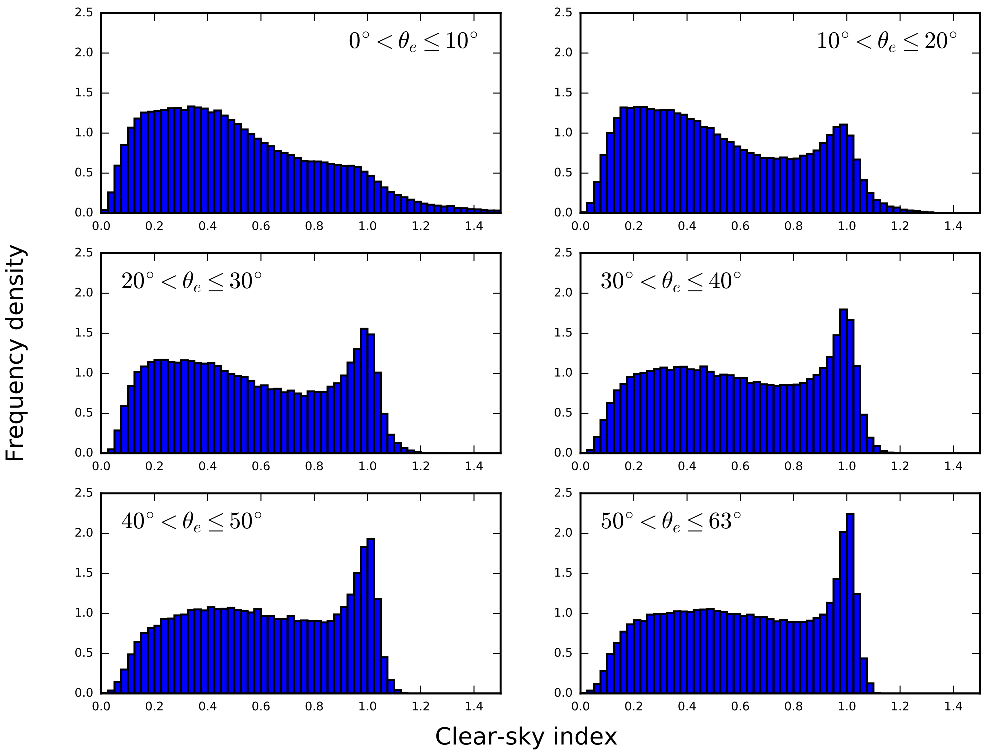

Figure 4.5: Histograms of observation of clear-sky index by solar elevation angle

be due to errors either in measurement or calculation. Irradiance reported by pyranometers becomes less reliable at low solar elevations due to cosine response errors (Vignola *et al.*, 2012, chapter 5). When generating k_c or k_t' values, the hourly average zenith calculations may not correspond with the exact solar position of the times the solar radiation observations were made, or the hourly cosine-weighted mean zenith angle still may not be an adequate representative of all conditions during the hours of sunrise and sunset. Furthermore, UK MIDAS practice of recording measurements at 10 minutes before the hour may not have been observed at all stations, or errors in the clock time at the MIDAS site may be present[2]. Large differences between $\cos\theta_z$ at the start and end of the hour can account for this. Although the pseudo-spherical correction for the curvature of the earth's atmosphere is made in the radiative transfer code, all instances where $\theta_z > 90^\circ$ are set to zero in the hourly averaging of zenith angle. In reality a small amount of diffuse irradiance at dusk and dawn is present and would contribute to the total received by a pyranometer. On the other hand, the absence of a $k_c \approx 1$ peak at low solar elevations can be due to instances of otherwise clear sky receiving a low k_c value if the sun is obscured by the horizon or trees in addition to the higher extreme values explained above.

---

[2] The datasets were originally analysed without the 10-minute offset where it was observed that the distribution spread was even greater.

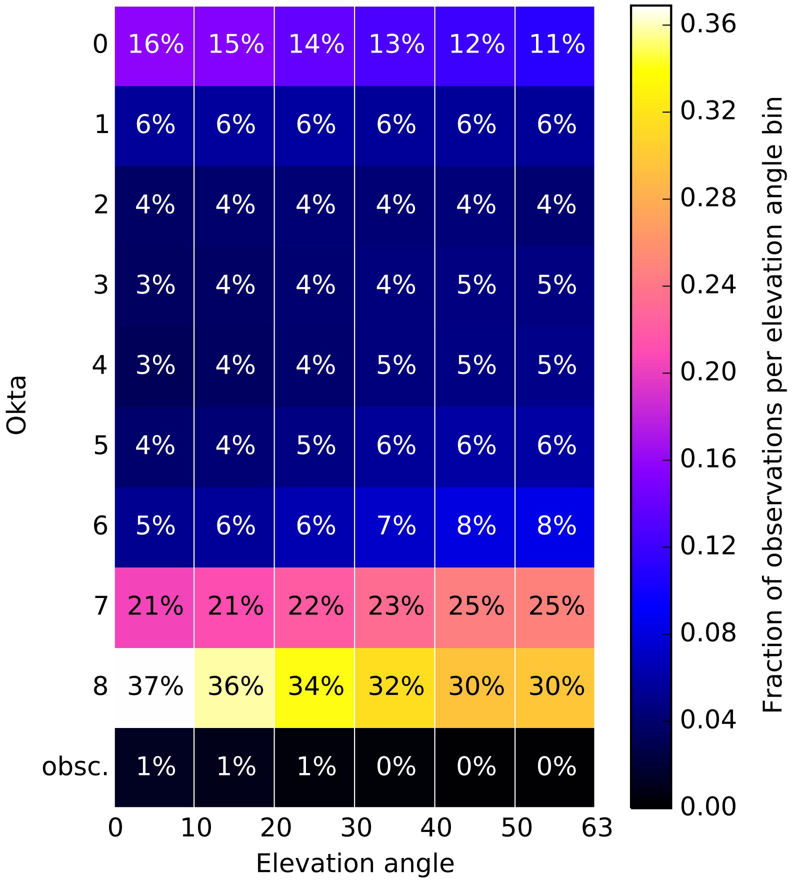

Figure 4.6: Joint histogram of okta frequency count for each elevation angle bin. Percentages and shading colour relates to the fraction of each elevation angle class (column) assigned to each cloud okta class. Columns may not sum to 100% due to rounding.

4.3.3 Distribution of cloud fraction by solar elevation angle

The other possibility is that the different distribution shapes in fig. 4.5 are not in fact erroneous at all and are caused by different cloudiness habits for each elevation angle group. For example, near sunrise and sunset, cloudy conditions could be dominant explaining the shape of this distribution when $\theta_e \leq 10^\circ$, whereas midday conditions in summer ($\theta_e > 50^\circ$) could be more associated with clear skies. To investigate this, a joint histogram of elevation by okta is shown in fig. 4.6. For all elevation angle groups, oktas 0, 7 and 8 are much more commonly observed than intermediate values. This helps to explain the bimodal distributions seen at each elevation angle bin except the lowest; the spike is generated by okta 0 hours, and the hump is generated by okta 7 and 8 hours. These “U-shaped” distributions of cloud okta, with most common observations near the high and low extremes, have been commented on by several authors (Henderson-Sellers *et al.*, 1981; Olseth & Skartveit, 1984; Jones, 1992). The distribution of cloud okta occurrence is often modelled using a beta probability density function (PDF) which can accommodate this bimodal shape (Falls, 1974).

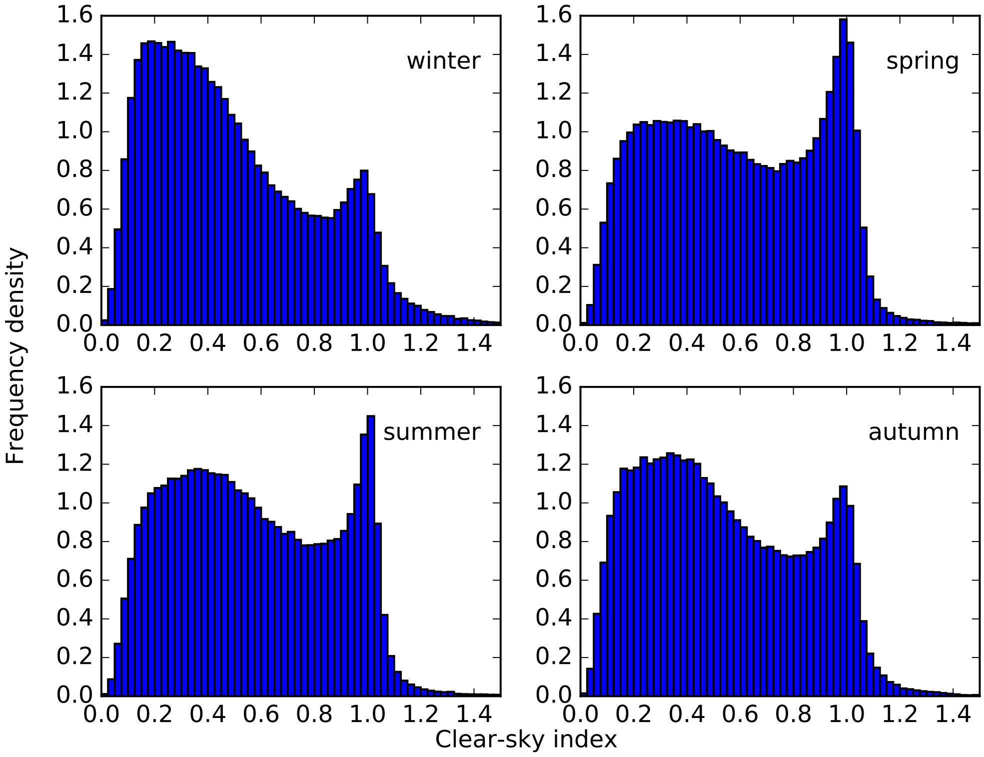

Figure 4.7: Distribution of clear-sky index by season

The frequency of okta 8 observations for $\theta_e \leq 10°$ is greater than for higher solar elevations, but so too is the frequency of okta 0 observations, which is surprising given the lack of $k_c = 1$ spike. The higher number of okta 8 observations for $\theta_e \leq 10°$ is offset by the lower number of okta 6 and 7 observations. For all six solar elevation classes, the sum of okta 6–8 counts is 62% or 63%. It cannot be assumed that the low solar elevation hours are typically more cloudy than the high solar elevation hours. The differences in the k_c histograms must be due to other factors.

4.3.4 Distribution by season

As low elevation angles have a wider spread of k_c, the next step is to determine whether there is any difference in clear-sky index by season. The seasons are defined in their usual sense: winter=December–February, spring=March–May, summer=June–August and autumn=September–November. The results are shown in fig. 4.7.

It is interesting to note that the clear-sky spike is more prominent in spring and summer. Spring and summer are clearer than autumn, which in turn is clearer than winter. The higher clear-sky spikes for spring and summer may be due to the highest elevation angles in these seasons. Therefore each season is sub-divided by elevation angle class in fig. 4.8. The seasonal differences here are fairly clear to see. For $\theta_e \leq 10°$, while there is no

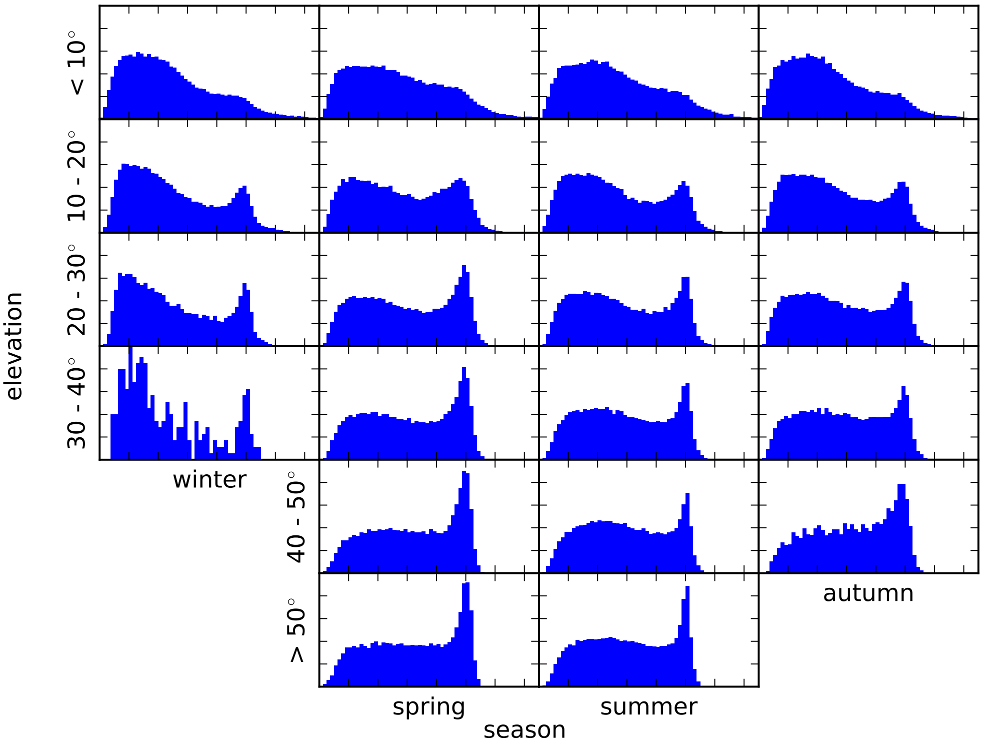

Figure 4.8: Distributions of clear-sky index for each elevation angle class and season. The x-axis runs from 0 to 1.5 with tick intervals of 0.2.

clear-sky spike for the spring distribution, the density difference between low and high k_c values is lower than for winter. For the 10–20° and 20–30° classes, the relative densities of the spike and hump are weighted towards more clear observations in spring, followed by summer, autumn and finally winter. Since only 4 years of data is used, it cannot be assumed that this represents a climatology for the UK. There are an insufficient number of observations to determine whether winter is less clear at $\theta_e > 30°$, but the spring → summer → autumn hierarchy continues.

It is likely therefore that the seasonal differences are caused by differences in cloudiness levels and not just elevation angle. The proportion of okta observations split out by season is shown in fig. 4.9. The two most interesting differences are that the proportion of okta 8 hours in winter is greater than at all other times of year, and the proportion of okta 0 hours in spring is clearly larger than the other seasons. Distributions in figs. 4.7 and 4.8 reflect this.

4.3.5 Distribution by MIDAS weather station

Owing to the influence of weather systems from the Atlantic and the rain-shielding effect of hills and mountains such as the Pennines, the western side of the British Isles typically

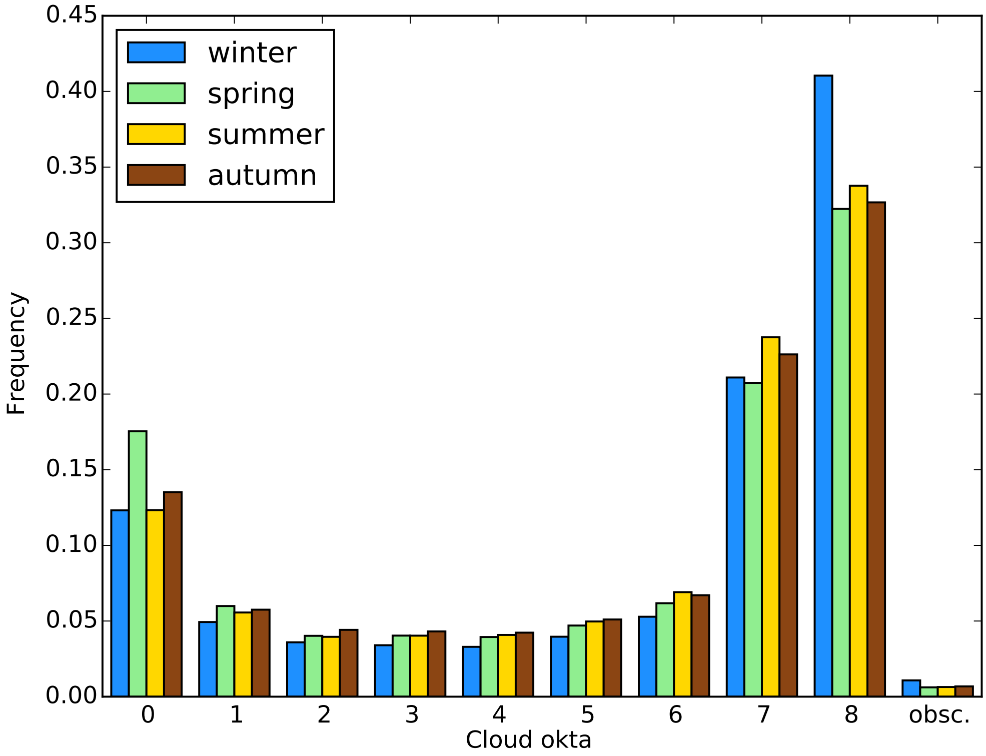

Figure 4.9: Cloud fraction occurrence each season

experiences more rainfall than the eastern side (UK Met Office, 2015b). To investigate whether this pattern is prevalent in cloud transmission, the k_c distribution from each of the 63 "valid" weather stations in fig. 4.2 is investigated individually.

The 63 stations are grouped into 7 regions by sorting the station latitudes in order from south to north. In fig. 4.10, the distribution of k_c for each weather station is shown. The subplot location in fig. 4.10 approximates the station's geographic location relative to the others, with each latitude band progressing from west to east. The colour scheme is the same as in fig. 4.2 and the station ID codes have been added for ease of cross-reference.

Most individual stations exhibit the bimodal characteristic of clear-sky index that is a feature of the aggregated distribution in fig. 4.3. Some individual stations, typically located in Scotland and Northern Ireland, have a low or non-existent clear-sky spike showing a tendency for cloudiness. From south to north, there is perhaps a slight trend for a decrease in overall cloud transmission by comparing the frequency densities of the low k_c humps, but this varies from station to station. There does not appear to be an overall trend in the west to east direction. It should be borne in mind that deficiencies in pyranometer quality and other localised affects may affect the k_c values produced from individual stations.

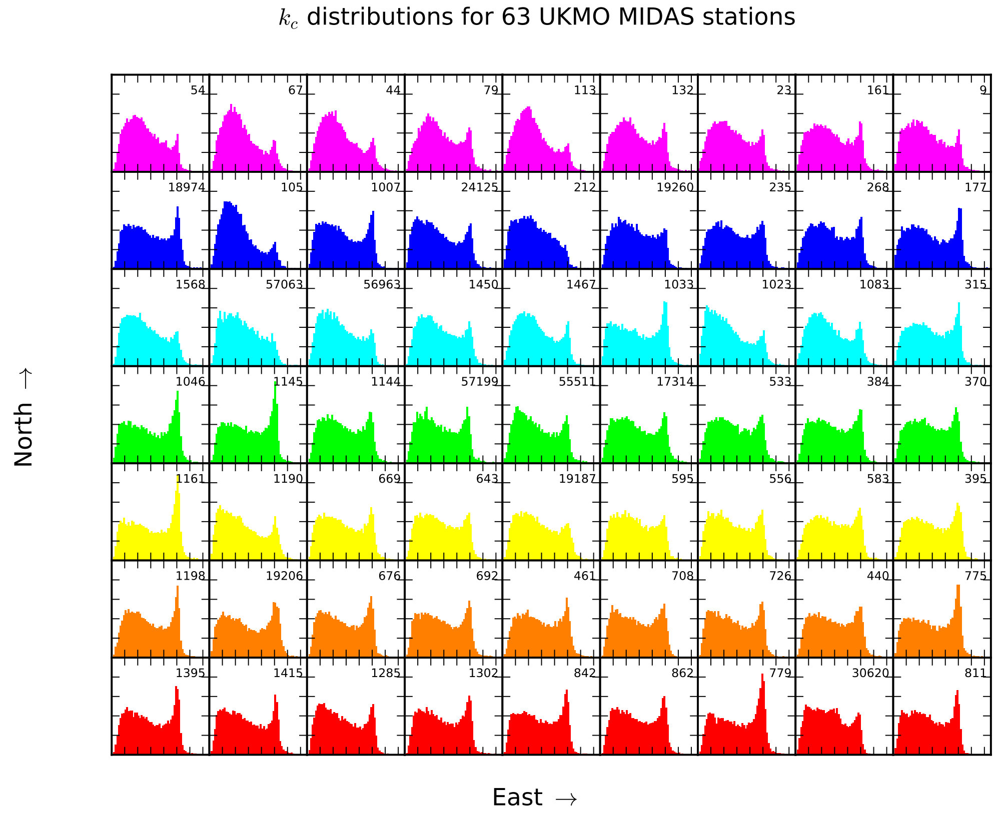

Figure 4.10: Histograms of k_c for each individual MIDAS station. Station ID numbers are in the top-right of each histogram. For station locations, refer to fig. 4.2.

4.3.6 Distribution by okta

The observations of k_c were grouped by okta class as shown in fig. 4.11.

Each okta class shows a unimodal distribution which changes from left-skewed at the lower oktas, through to approximately symmetric at oktas 5–6, to right-skewed at oktas 7–8 and obscured sky. As could be expected the $k_c \approx 1$ mode from the overall distribution in fig. 4.3 is supplied from okta 0 and okta 1 classes with contributions from oktas 2 and 3. The low mode of the overall k_c distribution results from oktas 7 and 8. Oktas 4–6 have intermediate modal values, but do not contribute as much to the overall distributions as they are observed less often (fig. 4.6), thus giving the overall distribution its bimodal shape.

What may be less expected is the large weight of the left tail for oktas 0 and 1, where derived clear-sky indices are much less than 1 for no or very few recorded clouds. For oktas 6 and 7, there are a significant number of observations where the irradiation received exceeds the theoretical clear-sky amount. This phenomenon is reduced but not entirely absent for okta 8.

The large spread of values for each distribution shows the inadequacy of using a one-

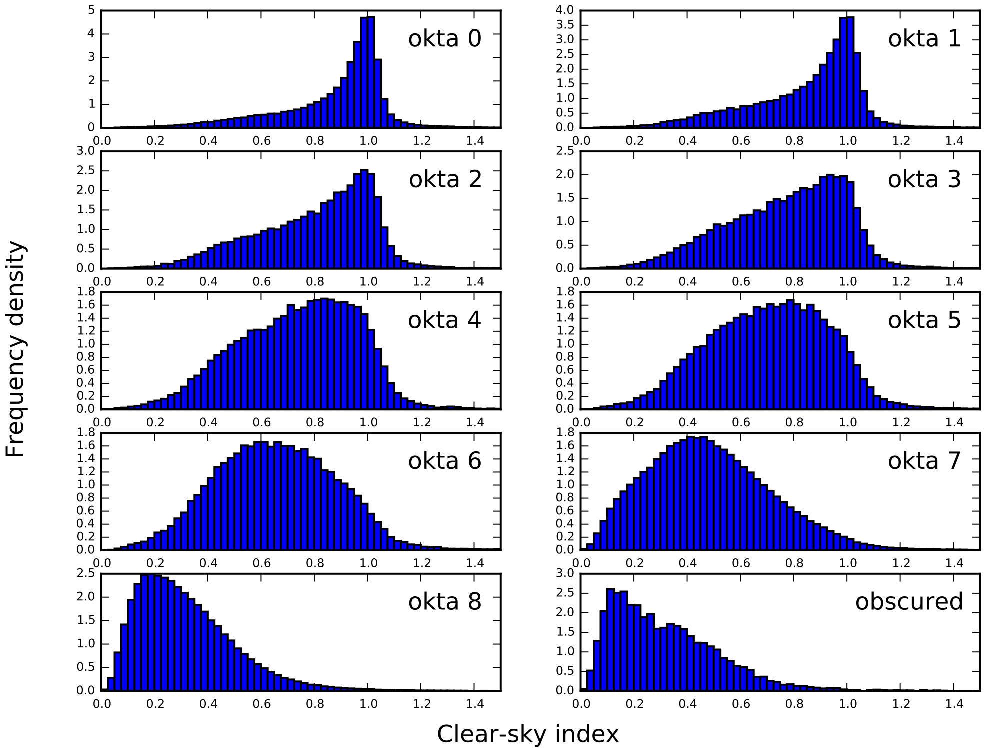

Figure 4.11: Histograms of the k_c value at each cloud okta class

to-one correspondence between cloud fraction and k_c. To illustrate this further, the Kasten-Czeplak relationship (eq. (4.2)) for two individual sites both in the Scottish Islands (Stornoway, station ID 54 and Lerwick, station ID 9) with similar annual k_c distributions is shown in fig. 4.12. The spread of k_c values derived for each okta is also shown as a boxplot. Instead of using eq. (4.3) for the clear-sky irradiance the theoretical value from radiative transfer computations are used and following Kasten & Czeplak (1980) hours where the calculated hourly mean elevation angle is less than 5° have not been included. A small modification is made to eq. (4.2) by multiplying it by a numerical prefactor as the mean clear-sky index for okta 0 is less than 1. Unlike in Kasten & Czeplak (1980) datapoints are not limited to hours in which okta is constant between the start and end of the hour, but analysis has shown that this makes little difference to the results.

For Lerwick, the site-specific Kasten-Czeplak coefficients do not differ much from those at Hamburg (exponent 3.4, attenuation factor 0.75), but for Stornoway the fit is drastically different and is almost inverse linear with cloud okta. The Stornoway case is interesting as Muneer & Gul (2000) found that the Kasten-Czeplak coefficients were a good fit for data from 1992. Nonetheless, using the value suggested by the Kasten-Czeplak curve fit neglects much of the plausible range of k_c that is seen at each okta. The curves were fitted using least-squares regression in Python. For lower oktas at Lerwick it can be seen that

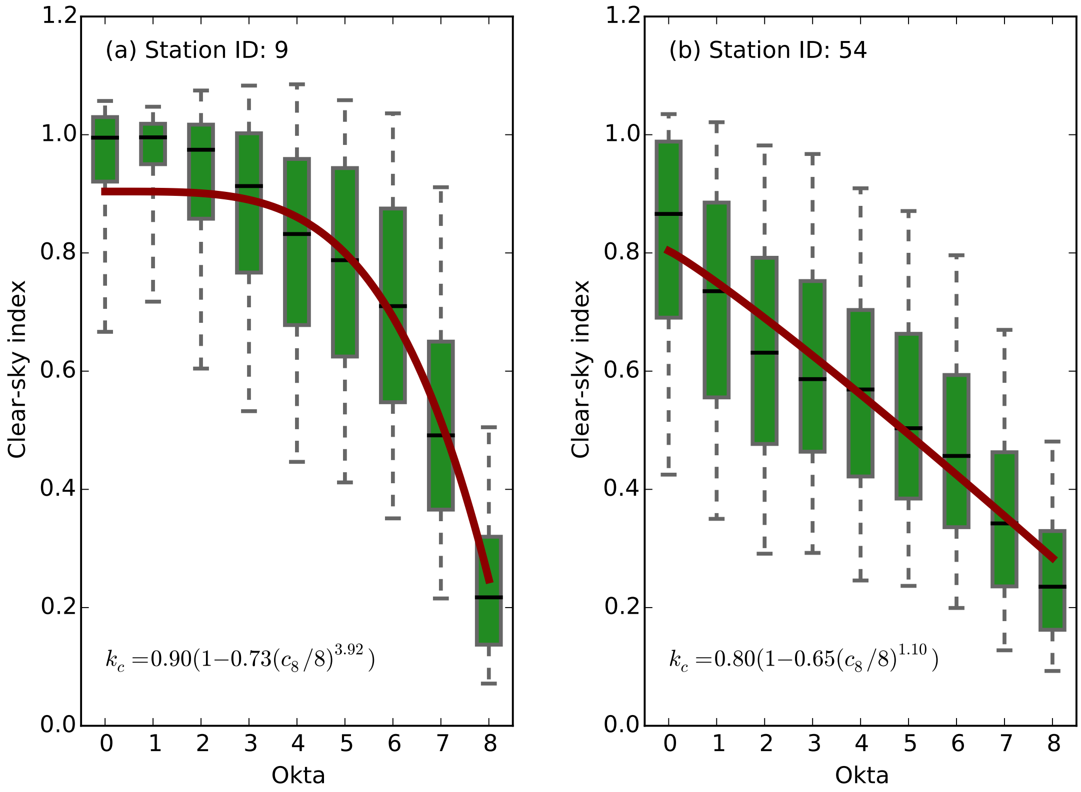

Figure 4.12: Kasten-Czeplak relationships, thick red curve, for (a) Lerwick (station ID 9) and (b) Stornoway (station ID 54). The boxplots show the median (black line), 25–75 percentile range (green box) and 5–95 percentile range (whiskers) for each okta class.

the mean fit lies a long way below the median value of k_c, showing the influence of the heavy left tail of the lower oktas on the mean. At Stornoway, less than 25% of okta 0 observations exceed $k_c = 1$, so there is a possibility at this site that the assumptions used in the clear-sky model are incorrect. However, the cloud transmissions of other oktas relative to okta 0 will remain the same and the exponent of 1.10 should not change under a different clear-sky model.

4.3.7 Joint distribution by okta and elevation angle class

To investigate the spread of the distributions further, particularly in relation to the heavy left tail for okta 0, the distributions at each okta class were subdivided by elevation angle group (fig. 4.13). It can be seen that except for okta 8, the distribution of derived k_c is qualitatively different for the $\theta_e \leq 10°$ group than for other elevation angles. For the cloudless/almost cloudless situations of oktas 0–1, the distributions for $\theta_e \leq 10°$ show a higher proportion of low k_c values than for higher elevation angle classes. For oktas 2–7, the distributions move from right-skewed at $\theta_e \leq 10°$ to left-skewed or approximately symmetric at higher elevation angle classes. Only the overcast okta 8 distributions show much similarity between elevation angle classes, and even in this case the shape of the tail

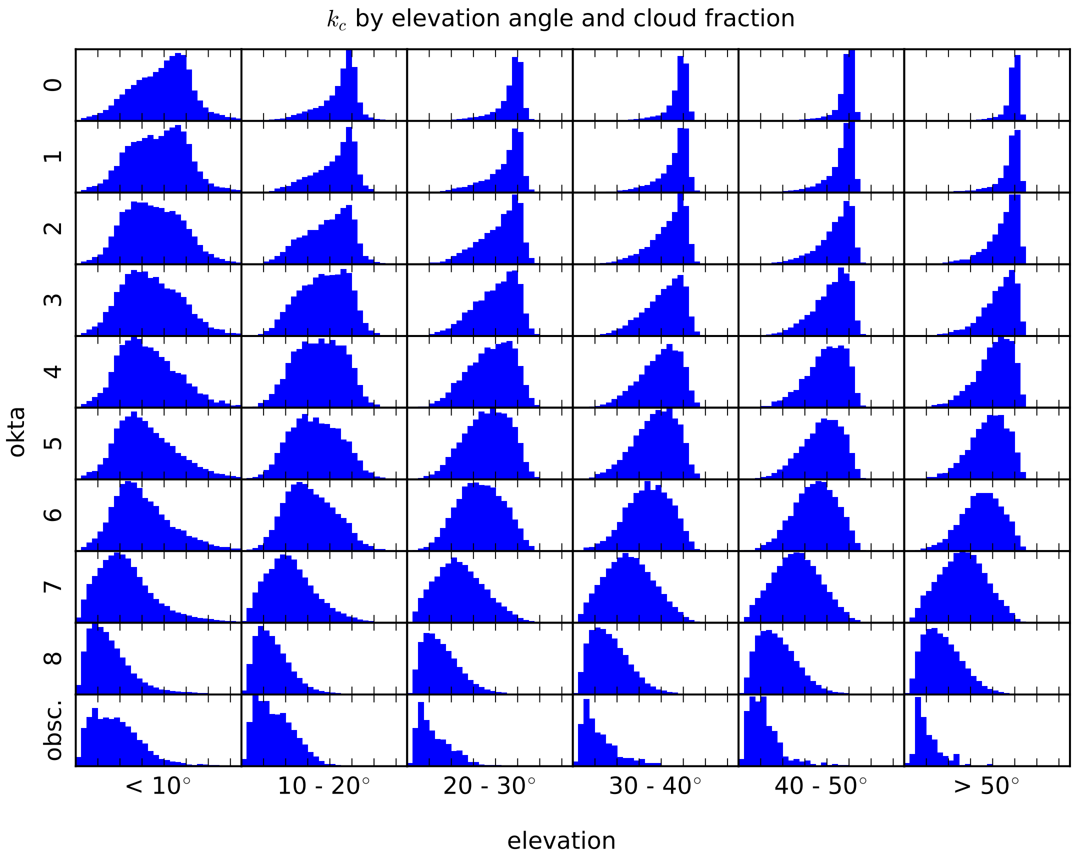

Figure 4.13: Matrix of histograms of k_c values for each okta class and solar elevation angle band. The x-axis range runs from 0 to 1.5 with ticks in intervals of 0.2. y-axis scales have not been standardised to more easily discern distribution shapes.

on the right-hand side admits higher values in the lower elevation angle groups.

One explanation for the differences in distribution shape by elevation angle class for oktas 1–7 are the relative probabilities of the solar beam being obscured by cloud. At low solar elevations, the chances of the solar beam being obstructed are greater, as there is both a greater path length through the cloud for each sunbeam to travel and a greater projected area for each cloud to obscure (fig. 4.14). A related effect was noticed by Muneer & Gul (2000) who found that the relationship between sunshine fraction and okta was dependent on solar elevation and was not linear. The effect of cloud projection with all else being equal would lead to lower k_c values for lower elevations which reflects what is seen at oktas 1–7. Low k_c values at okta 0 for $\theta_e \leq 10°$ could be effects from horizon obstruction, ground reflection, small errors in zenith angle for sunrise/sunset hours, or other differences as described in section 4.3.2.

Another reason is that as cloud okta is measured at the end of the hour and irradiation is reported as an hourly sum, there will likely be a number of hours in which clouds could affect a preceding hour's irradiation total but have dispersed by the end of the hour. This hour will still be recorded as okta 0, but will not have been cloudless for the entire preceding hour. For okta greater than 0, a similar effect of cloud dispersion, or the opposite

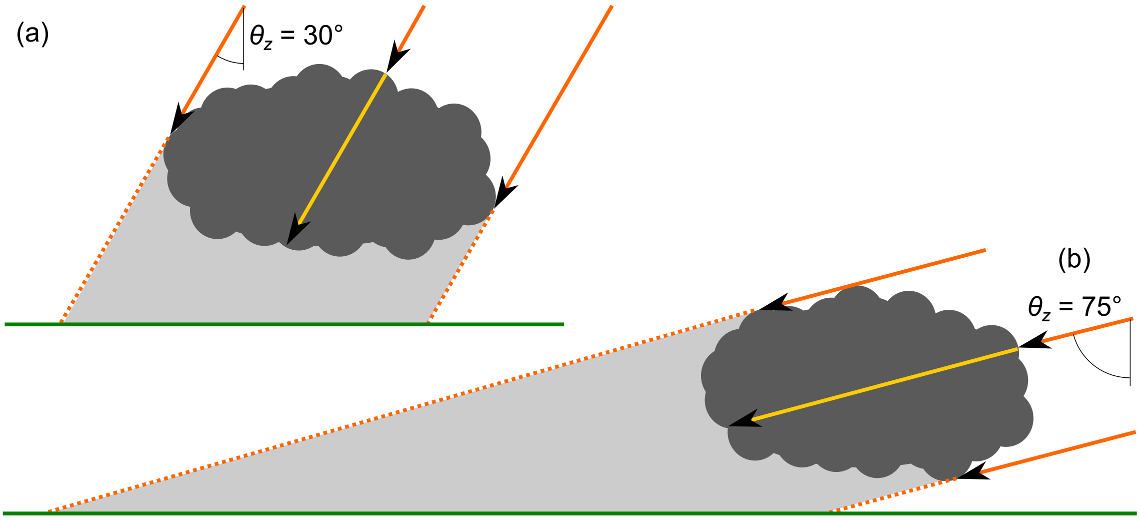

Figure 4.14: Schematic of cloud shading for the same (fictional) cloud for solar zenith angle of (a) 30° and (b) 75°. Both the shaded area (light grey) and the maximum path length of the solar beam (yellow arrow) increases at high solar zenith angles.

effect of cloud accumulation where predominantly clear hours increase in cloudiness towards the end of the hour and receive a high okta class, can be the cause of low and high instances of k_c relative to that okta class mean, respectively. Previous studies on clear-sky transmission have limited irradiation observations to hours in which okta does not change from the start of the hour to the end of the hour (Kasten & Czeplak, 1980) or used a weighted average of the current, preceding and next hour's cloud fraction (Muneer & Gul, 2000). This condition has not been imposed in this work as the goal is to relate irradiation measurements and cloud fraction from the same hourly observation and such low and high measurements should be expected occasionally.

4.4 Fitting statistical models

It is seen in fig. 4.13 that the distribution characteristics are different between low and high solar elevation angles for each okta. In the first instance it can be seen there is a clear divide between solar elevation angles of greater than and less than 20°. Initially therefore, distribution fits have been considered for $\theta_e > 20°$ only. A summary of the first four moments of the distributions by okta are given in table 4.5. As reflected by the distribution shapes, the mean clear-sky index decreases as okta increases. The standard deviation has its lowest value for clear skies, increases steadily to its largest value at okta 7, and decreases again for okta 8 and obscured skies. Overcast skies have a higher standard deviation than clear skies because of the variety of cloud optical thicknesses that can occur. Intermediate oktas have higher standard deviations still, as both cloud optical thickness and the "on–off" process of clouds and cloud breaks passing the solar beam path, combined with cloud enhancement and cloud reflection, can produce a wide range

	Mean	St. dev.	Skewness	Kurtosis
okta 0	0.9423	0.1212	−2.391	7.308
okta 1	0.9038	0.1532	−1.641	2.797
okta 2	0.8566	0.1724	−1.092	0.9020
okta 3	0.8226	0.1788	−0.8215	0.2811
okta 4	0.7809	0.1887	−0.6206	−0.04745
okta 5	0.7441	0.1921	−0.4675	−0.2066
okta 6	0.6833	0.1974	−0.2328	−0.3998
okta 7	0.5111	0.2160	0.2045	−0.5071
okta 8	0.3362	0.1745	0.8230	0.5962
obscured	0.2442	0.1543	1.2700	1.602

Table 4.5: Statistics of the distributions of clear-sky index by okta class

of hourly-averaged transmission values.

The skewness describes how non-symmetric a distribution is, and the values of skewness represent the observed shapes of the distributions moving from left-skew through symmetric to right-skew. Finally, the (excess) kurtosis is a measure of how much of a probability distribution weight is in the distribution tails, with a high kurtosis indicating heavy tails. The normal distribution is defined to have a kurtosis of 0 such that negative kurtosis is sub-normal. The low oktas 0 and 1 contain large amounts of their distributions in the heavy left tails, whereas the intermediate oktas are closer to normal, and oktas 8 and 9 revert to positive kurtosis, a consequence of the right tails of these distributions.

4.4.1 General fit per okta

The highly negatively-skewed oktas 0–4 provide a particular challenge as positively-skewed distributions tend to appear more commonly in natural processes (McLaughlin, 2014). There are no simple probability distributions that fit all oktas well. The beta distribution could be a candidate, but would require defining a maximum and minimum allowable k_c to map on to the domain of [0,1]. Therefore, the two cases were considered separately: oktas of 4 or less, and oktas of 5 or more plus obscured sky. At the crudest level these boundaries could be considered “mostly clear” and “mostly cloudy” respectively.

Oktas 0–4: the skew-t distribution

After investigating over 80 distributions in Scientific Python (SciPy, Jones *et al.*, 2015), there were no candidate distributions that provided a good fit to the okta 0 and 1 histograms owing to the large negative skew and large kurtosis. A complicated, 4-parameter distribution, the skew-t (Azzalini & Capitanio, 2003), provides a reasonably good fit to

Parameter	μ	σ	α	ν
okta 0	1.038	0.07559	−3.361	2.042
okta 1	1.052	0.1357	−5.548	2.762
okta 2	1.061	0.2424	−7.357	10.68
okta 3	1.051	0.29	−6.364	1.059×10^6
okta 4	1.022	0.3063	−4.601	4.683×10^6

Table 4.6: Skew-*t* coefficients for clear-sky index distributions, for oktas 0–4 and solar elevation angle above 20°.

the mostly clear cases. The skew-*t* distribution is not provided in Scientific Python and was coded separately by the author.

The skew-*t* distribution has been used to model stock market returns (Bauwens & Laurent, 2005), biomedical records from athletes (Azzalini & Capitanio, 2003), fibre-glass strength (Jones & Faddy, 2003) and crab claw length (Choudhary *et al.*, 2014) amongst other datasets. There are several related skew-*t* distributions that are defined slightly differently (Aas & Haff, 2006). The definition used in this chapter is that of Azzalini & Capitanio (2003). The PDF of this skew-*t* distribution is given by

$$f(x) = \frac{1}{\sigma} t_\nu \left(\frac{x-\mu}{\sigma} \right) 2T_{\nu+1} \left(\alpha \frac{x-\mu}{\sigma} \sqrt{\frac{\nu+1}{x^2+\nu}} \right) \tag{4.6}$$

where $t_\nu(\cdot)$ represents the PDF of the standard Student-*t* distribution with ν degrees of freedom and $T_\nu(\cdot)$ is the cumulative distribution function (CDF) of the Student-*t* distribution (see for example Zelen & Severo (1964)).

The skew-*t* distribution takes the four parameters μ, σ, α, ν. μ and σ define the location and scale of the distribution. Unlike the normal distribution μ and σ do not correspond to the mean and standard deviation of the skew-*t* distribution in the general case. α is a skewness parameter, where a positive (negative) value of α indicates right (left) skew of the distribution. $\nu > 0$ is the degrees of freedom, which has some analogy to the standard *t* distribution. Low values of ν indicate fat tails. The skew-*t* distribution is related to the skew-normal distribution, which is the limiting case as $\nu \to \infty$ as in the non-skewed versions of these distributions. The skew-normal distribution was also investigated on the okta histograms, but was unable to account for the fat tails present in oktas 0 and 1. The parameter fits for the skew-*t* distribution in fig. 4.15 are given in table 4.6.

One unsatisfactory aspect of the skew-*t* distribution is that it does not easily relate to some physical representation of cloud thickness or cloud fraction. Additionally with four parameters, it is more likely to fit real data than statistical models with fewer parameters and it should not be surprising that it performs fairly well.

Parameter	a	d	p
okta 5	0.9629	3.425	8.61
okta 6	0.866	3.264	5.688
okta 7	0.6633	2.263	3.157
okta 8	0.1301	3.288	1.118
obscured	0.0009736	5.636	0.4616

Table 4.7: Generalised gamma coefficients for clear-sky index distributions, for oktas 5–9 and solar elevation angle above 20°.

Oktas 5–9: the generalised gamma distribution

The generalised gamma is a superset of several common distributions used in mathematics and engineering, and includes the gamma, exponential, Weibull, chi-squared, normal and lognormal distributions as special or limiting cases. The PDF is given by (Stacy, 1962)

$$f(x) = \frac{p/a^d x^{d-1} \exp(-(x/a)^p)}{\Gamma(d/p)} \tag{4.7}$$

where a, d and p are parameters and $\Gamma(\cdot)$ is the gamma function that generalises factorials to all real numbers. The generalised gamma distribution fits to oktas 5–9 are shown in table 4.7.

The method of maximum likelihood estimation in Python was used to fit the skew-t and generalised gamma PDFs to each okta distribution. The plots are shown in fig. 4.15 for $\theta_e > 20°$; the fits are less good when lower solar elevations are included.

Visually, the fits are fair to good for most oktas. The physical interpretation of these distributions can be considered as follows. For low oktas, the skew-t distribution sets the peak around a value close to 1, representing predominantly clear skies, with a heavy left tail to account for varying levels of cloudiness. For the high oktas, the starting point is an assumption of a varying level of cloud obscurity (given by k_c near zero and much of the distribution contained in the low-k_c hump) which tails off exponentially to high k_c values to take into account the small number of hours where there is extensive cloud breaks or the cloud is very light.

It would be beneficial to analyse the goodness of fit in the tails of the distribution with a probability plot. However as the CDF of the skew-t distribution cannot be represented analytically, it has to be approximated numerically. To generate the probability plot the CDF would need to be evaluated numerically each time, and with over 300,000 datapoints contained in the okta 0–4 classes, this appears to be beyond the computational resources available.

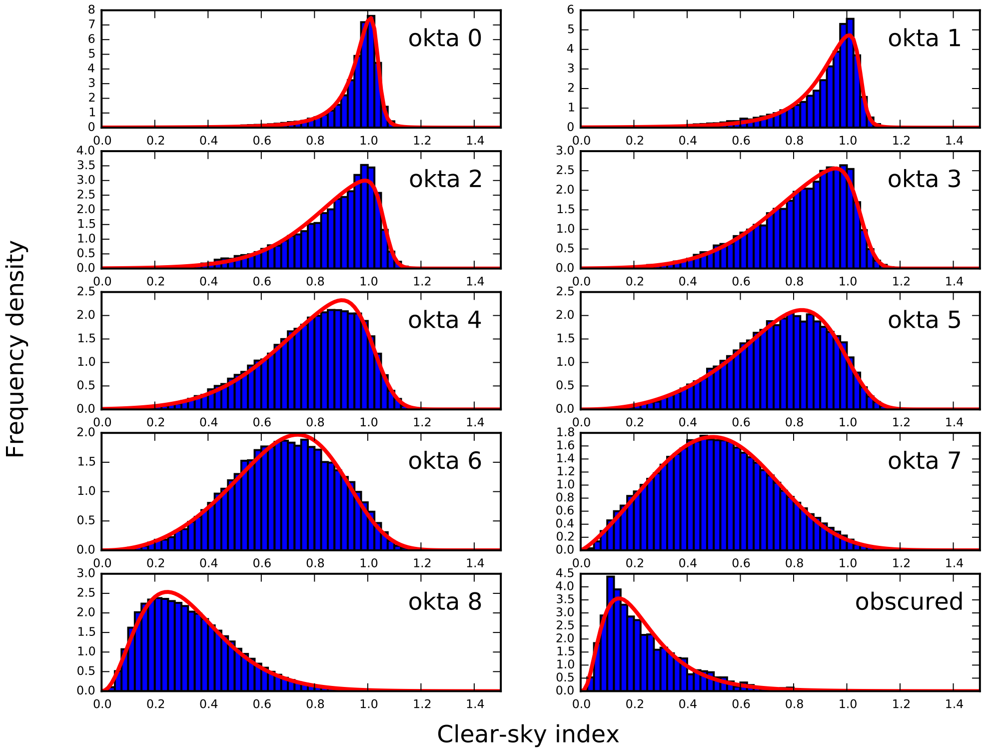

Figure 4.15: Skew-t (okta 0–4) and generalised gamma (okta 5–8 & obscured) fits to histograms of k_c for $\theta_e \geq 20°$.

4.4.2 Application to weather generator

As described earlier, the purpose of generating a dataset of cloud transmissivities for the UK is for a stochastic weather generator. The weather generator model produces a minutely irradiance time series. Fluctuations in demand, as well as changes in resource availability due to cloud shading, occur on the order of minutes (Cao & Sirén, 2014). While some dedicated solar radiation stations such as BSRN and National Renewable Energy Laboratory (NREL) do report irradiance minutely, the network of high-quality radiation stations doing so is sparse. Therefore, a method to downscale hourly statistics to minutely data is required.

The weather generator uses a minutely sun-obscured model, meaning that for every model minute the sun is deemed to either be obscured by cloud, or not obscured. There are therefore two distributions: one for clear-sky minutes, and one for cloudy minutes. A Markov chain generates the base cloudiness for the hour in oktas. This determines the number of minutes that are obscured by cloud. Then, the clear-sky index for each minute is modelled depending on whether the sun is obscured for the minute and cloud fraction for the hour.

The weather generator is coded in Matlab, and as such has a smaller range of available probability distributions than Python. The skew-t is unsuitable for generation of the large arrays of random variables needed for the weather generator because its CDF does not admit a closed form. The CDF of the generalised gamma distribution can be represented analytically but is not native to Matlab, so simpler distributions for cloudy skies were sought. In fig. 4.16 a normal curve has been fit to the okta 0 distribution and a number of distributions related to the generalised gamma have been fit to oktas 6, 7 and 8. The reasoning behind this is explained below.

4.4.3 Clear sky minutes

As shown in fig. 4.11, the distribution for okta 0 shows more left-skew than would be expected. The left tail gradually narrows as elevation angle increases (fig. 4.13). As previously described the left tail may be due to clouds that are present and obscure the sun partially during the hour of irradiation measurement but disperse by the end of the hour, or due to local turbidity effects such as mist, haze or pollution. Where pyranometers are not ventilated, it is possible that on clear mornings ice and dew can settle on the pyranometer dome, preventing all of the sunlight reaching the thermopile. It may also be due to horizon obstruction or ground reflection at low elevation angles, or error in pyranometer response. There is also a possibility that high-level cirrus clouds that were present have been unseen by the observer at the MIDAS station. Notwithstanding all of these provisions, it should be expected that for "genuinely" clear, cloudless hours under normal turbidity conditions, the clear-sky index will be centred around unity. This is indeed observed from the spike in each k_c distribution above 10° elevation. The spike centred around $k_c = 1$ indicates that the GLOMAP aerosol climatology coupled with ECMWF water vapour and ozone assumptions implemented in the clear-sky simulation are sound for the long-term mean, except at possibly a few stations where local climatology effects dominate such as Stornoway. It can therefore be assumed that the actual clear-sky irradiance can be drawn from a probability distribution centred on $k_c = 1$, where the fluctuation describes the actual water vapour, aerosol and ozone conditions away from the climatological average for that month.

Because clear-sky irradiance should only depend on the extraterrestrial irradiance, zenith angle, and atmospheric turbidity, where the latter can be assumed approximately constant over the hour, there should be no reason not to use the hourly values to model minutely clear-sky irradiance. To remove some of the influence of variations caused by low k_c values at low elevations, only hours where $\theta_e > 40^\circ$ have been kept. A visual fit to the spike of the distribution gives a normal probability curve with mean 1.0 and standard deviation 0.033. The normal curve in fig. 4.16 has been scaled by 85%. In the Hollands & Suehrcke (2013) model of instantaneous k_c, the clear-sky component is modelled with a normal distribution curve centred on $k_c = 1$.

In Bright *et al.* (2015), a normal distribution with mean of 0.99 and standard deviation 0.08 is used. This distribution was derived by considering hours where the solar elevation angle is greater than 10° and only included data from the 2012 calendar year. With a large standard deviation, large fluctuations away from $k_c = 1$ occur often, so a smaller standard deviation is more realistic.

4.4.4 Sun-obscured minutes

Overcast hours

Genuinely overcast hours will have an obscured sun for the whole hour and minute-by-minute clear sky index generally does not exhibit much variation (Skartveit & Olseth, 1992). It is therefore appropriate to select a baseline k_c value from the okta 8 distribution.

The reasonable fit of the generalised gamma distribution also suggests that one of its sub-distributions or limiting cases may be appropriate. Rozwadowska (2004) found that cloud liquid water content and cloud optical depth for marine stratocumulus clouds follows a lognormal distribution for optical depth for okta 8. This suggests a good starting point for investigation of cloud transmission. It is well known that not all clouds over the UK are stratocumulus, and the presence of scattering means that a distribution that holds for optical depth may not hold for transmission.

It is found in reality that the lognormal distribution is not the best fit to the data. The gamma distribution provides a fair fit and is difficult to discern from the generalised gamma, therefore it has been selected for the okta 8 distribution.

Partially cloudy hours

Partially cloudy hours present a more challenging situation as both cloud transmissivity and cloud fraction affect hourly irradiation. It could be expected that the cloud types and cloud transmissivity associated with partially cloudy situations are different to overcast clouds. Fair weather cumulus will differ to poor weather nimbostratus.

An additional distinction is made to separate okta 7 from oktas less than 7. This is because okta 7 makes up over 20% of observations alone and accounts for situations where the sky is almost, but not completely, overcast. Cloudy periods from lower oktas are assumed to follow the okta 6 hourly k_c distribution. Okta 6 was chosen as it represents a mostly cloudy state, so much of the hourly k_c distribution will relate to moments when the sun is obscured and it will not be affected by too many clear sky gaps. It is expected that cloud transmission that will be qualitatively different from oktas 7 and 8.

Hourly okta	k_c distribution for cloudy minutes	PDF
0	N/A	
1–6	$\text{Normal}(\mu = 0.6784, \sigma = 0.2046)$	$\exp(-(x-\mu)^2/2\sigma^2)/\sigma\sqrt{2\pi}$
7	$\text{Weibull}(d = 2.4061, a = 0.5577)$	As eq. (4.7) with $p = d$
8 or 9	$\text{Gamma}(d = 3.5624, a = 0.0867)$	As eq. (4.7) with $p = 1$

Table 4.8: Baseline clear-sky indices used for cloudy minutes

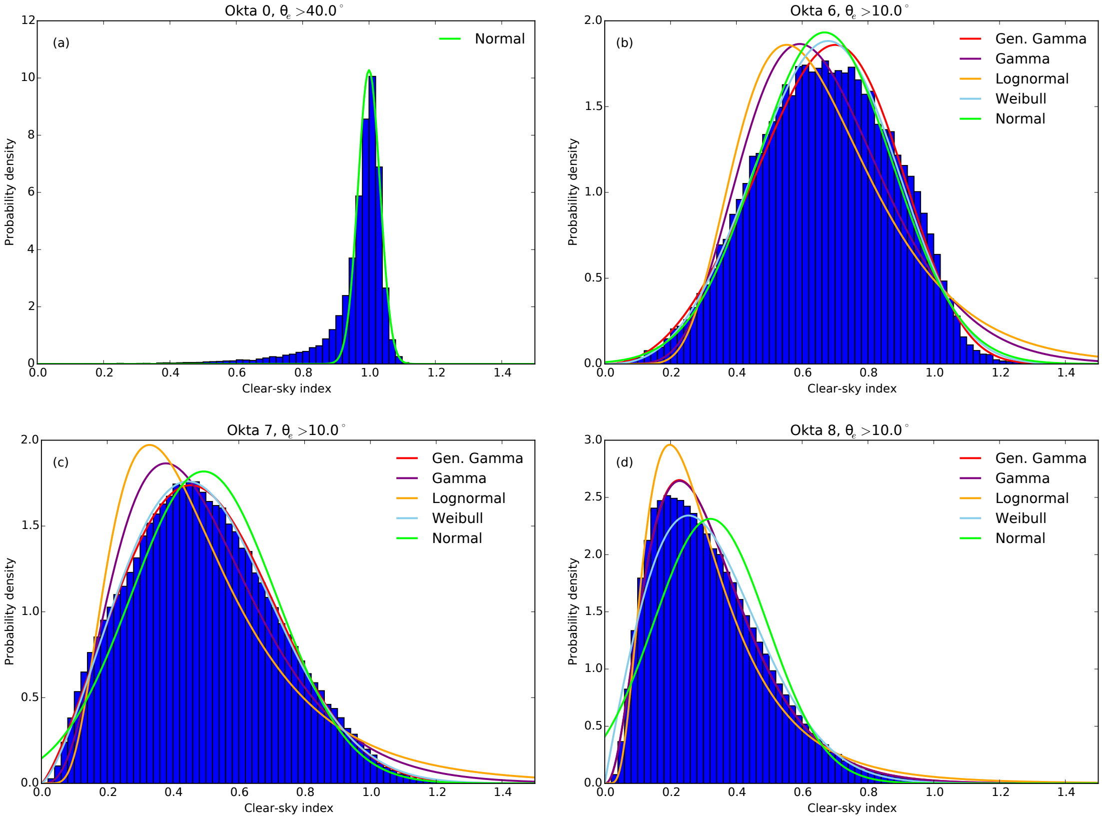

Figure 4.16: Simpler distribution fits to (a) okta 0 (clear-sky), (b) okta 6 (partially cloudy), (c) okta 7 (near overcast) and (d) okta 8 (overcast) situations

The okta 7 distribution follows a Weibull curve very well and is assumed to be appropriate for this state. The okta 6 distribution can be modelled adequately with a normal or a Weibull distribution. The normal distribution was chosen on the basis of a simpler mathematical representation.

The distribution parameters derived from the histograms and shown in table 4.8 are similar to, but different from, those in Bright *et al.* (2015). In this chapter, four years of data were used, whereas to generate the distribution fits in Bright *et al.* (2015) only 2012 was used. Additionally in the Bright *et al.* (2015) distributions, the upper k_t limit of 0.85 was not imposed, and the 10-minute to the hour convention for observations was not applied.

4.4.5 Minutely variation

Left in this form, the clear and cloudy minutes from each hour will exist in a binary fluctuation between the cloudy and clear k_c values. Such a two-state clear-cloudy model can be a useful simplification but does not represent observed conditions. There will also be discrete jumps in baseline k_c values between hours for both clear and cloudy minutes. To solve this issue, the baseline k_c value for cloudiness varies linearly from one hour to the next, and for clear-sky minutes, only one value is selected that applies to all clear-sky minutes on the same day. Then, statistical Gaussian noise is added to the baseline clear or cloudy k_c minute by selecting multipliers from a normal distribution with mean 1 and standard deviation equal to

$$\sigma = 0.01 + 0.003c_8 \tag{4.8}$$

for cloudy minutes and

$$\sigma = 0.001 + 0.0015c_8 \tag{4.9}$$

for clear minutes, where c_8 is the baseline hourly okta.

Two more adjustments are made: if the minutely k_c selected from the distribution as amended by the stochastic variation is less than 0.01, it is set to 0.01. Radiative transfer simulations over the full range of zenith angles have shown this corresponds to a plane-parallel cloud with optical depth of over 500. The second adjustment prevents very high values of k_c from occurring in the open-ended distributions by setting the maximum clear-sky index to be

$$k_{c,\max} = 27.21\exp(-114\cos\theta_z) + 1.665\exp(-4.494\cos\theta_z) + 1.08 \tag{4.10}$$

This formula was derived by fitting a least-squares curve to the highest values of k_c observed for each 1° elevation angle bin.

4.4.6 Direct/diffuse splitting and tilted irradiance

The clear-sky index is useful in that it provides a relationship to the transmission of the direct beam (Behrendt *et al.*, 2013). If k_c lies between $19/69 \approx 0.275$ and 1, an empirical relationship is

$$G_B = G_{B,\mathrm{cs}}(k_c - 0.38(1 - k_c))^{2.5} \tag{4.11}$$

where $G_{B,\mathrm{cs}}$ is the theoretical beam clear-sky value that can be calculated easily using libRadtran. In the weather generator the HELIOSAT method (Hammer *et al.*, 2003), which is based on monthly average Linke turbidity from global maps produced by Remund *et al.* (2003), is used to calculate $G_{B,\mathrm{cs}}$ as it does not require an external call to libRadtran from the weather generator in Matlab and the HELIOSAT method is fast and flexible. For lower k_c values, it can be assumed that the sun is fully obscured and $G_B = 0$, whereas for $k_c > 1$ the beam is enhanced proportionally such that $G_B = G_{B,\text{cs}} k_c$. The diffuse irradiance is calculated as expected such that $G_D = G - G_B \cos\theta_z$.

If the irradiance on a tilted plane is required, then this can be calculated with a direct-diffuse transposition model such as the Klucher method; this is discussed extensively in chapter 5.

4.5 Summary

A distributional approach for transmission of solar energy through clouds is undertaken in this chapter, where the distributions are conditioned on solar elevation angle and cloud fraction class (okta). This is an advancement on previous studies on the effect of cloud transmission of solar radiation, which use a one-to-one relationship between cloud transmission and cloud fraction.

. The hourly cloud transmission for the UK is shown to be bimodal, which supports observations from a number of other countries. It is shown that even when efforts are made to normalise the air mass effect of atmospheric transmission by using a clear-sky index instead of the more usual clearness index, there is still an elevation angle dependence which may be due to increased path length transmission through clouds. This affects the shape of the distributions for solar elevation angles less than 20°.

It is difficult to fit common statistical distributions to the histograms of clear-sky index by okta, because cloud transmission is dependent on solar elevation angle. The skew-*t* distribution for oktas 0–4 and generalised gamma distribution for oktas 5–8 and the obscured sky provide a reasonably good fit for elevation angles above 20°. This is at least in part due to these distributions being multi-parameter models. Reasonable simple fits for okta 6 (normal), okta 7 (Weibull) and okta 8 (gamma) have been determined to use as the baseline cloud transmissions in a stochastic weather generator. The distribution of okta 0 was modelled as a normal distribution around $k_c = 1$ following physical arguments and the work of Hollands & Suehrcke (2013). A Gaussian multiplier is used to downscale the generated hourly values of k_c to minutely values. The model is shown to validate well against real one-minute data from the Camborne BSRN station. Full details are provided in Bright *et al.* (2015).

One weakness of the weather generator method is that it is unable to model the very significant cloud enhancement effects that occur on the order of seconds to minutes. Cloud enhancement typically occurs in broken cloud fields where the sun reflects from the sides of clouds alongside the solar beam being transmitted, and causes GHI to exceed the clear-sky value (i.e. k_c significantly greater than 1); in some cases cloud enhancement can exceed the extraterrestrial irradiance ($k_t > 1$). These effects are sufficiently prolonged to be noticed in one-minute data. A natural extension to the weather generator is to include the effects of cloud enhancement, and to downscale the model to shorter timescales, for example one second. Work in this area is currently ongoing.

Chapter 5

Plane irradiance using an integrated radiance method

In chapter 4, a radiative transfer procedure for estimating transmission in clear skies was found to be reasonably accurate for solar zenith angles less than 80°, as shown by the height of the clear-sky spikes in the cloud distributions. It was shown that the UK experiences frequent cloud cover year-round as indicated by the bimodal shape of the seasonal histograms. It would be useful to include clouds in computational estimates of surface solar radiation rather than including them as a probabilistic adjustment at a later stage as was performed in the previous chapter. While the UK benefits from a dense and historical network of high-quality meteorological measurement stations, this is not true for several other parts of the world.

In this chapter, cloud properties are included within the radiative transfer simulation to simulate the all-sky[1] radiation. The cloud (and other atmospheric) properties are derived from satellite observations. The method is demonstrated for assessment of horizontal irradiance. By using a high number of streams in the radiative transfer code, the ground-level radiance distribution can be obtained, which can then be numerically integrated to obtain the tilted irradiance at an arbitrary panel orientation. The tilted irradiance is of importance because solar PV panel alignments are rarely flat.

A physically-derived procedure for calculating tilted irradiance is described, which is referred to as the Integrated Radiance (IntRad) method. The ground-level radiance field is calculated from radiative transfer and this is integrated over the 2π steradian hemisphere of view where the base of the hemisphere is in the plane of tilt. By using satellite data as the inputs, good agreement with horizontal irradiation observations with the BSRN dataset is observed. Five MIDAS sites are also included to show this method's suitability to UK conditions. The tilted irradiation cannot be validated against BSRN data, however, one site of high-quality tilted irradiation data from NREL at Boulder, Colorado, USA, is used for validation. For BSRN sites, comparisons against popular tilted radiation mod-

---

[1] any sky condition, not limited to clear or overcast conditions

els in the literature are shown. For European and African BSRN sites included in the validation a further comparison is made against the popular Photovoltaic Geographical Information System (PVGIS) online tool.

As all of the input data are standard variables in climate models or reanalysis datasets, this method can be used to predict tilted irradiance in future climate experiments.

5.1 Background and literature review

The orientation of a plane solar collector such as a PV panel can be varied in the tilt and azimuth directions in order to maximise the incident irradiance. As placing pyranometers in several different plane orientations at one site is not typically performed and not a desirable allocation of resources for most solar energy installers, good models to predict the tilted irradiance are necessary. There are two concepts fundamental to the method described. Firstly, the radiative transfer concept is extended to include cloud optical properties as described in the introduction. Secondly, tilted irradiance is derived from a numerical integration of the surface diffuse radiance field that is generated by the radiative transfer calculation. The section below provides background on including clouds in solar energy radiative transfer modelling and existing tilted irradiance models in the literature are introduced.

5.1.1 Treatment of clouds in solar energy radiative transfer modelling

Radiative transfer principles are frequently used to model clear-sky solar irradiance, for example in the SPCTRAL2 (Bird & Riordan, 1986), SMARTS (Gueymard, 1995) and SOLIS (Mueller *et al.*, 2004) models. The SMARTS code is especially pertinent as it provides the solar spectrum used for the ASTM-G173 AM1.5 standard (section 2.5).

Clouds can be introduced as an adjustment to the clear-sky values. For example in chapter 4, clear-sky radiative transfer values were adjusted by applying a cloud transmission factor that was taken from a distribution of long-term observations and depended on the cloud fraction. Cloud albedo values reported from satellites can be correlated to cloud transmission (Cano *et al.*, 1986) or the ground-level spectrum tuned based diffuse and global irradiance (Nann & Emery, 1992). In other studies cloud effects are included directly within the radiative transfer code. Lohmann *et al.* (2006) used cloud data from the ISCCP with the two-stream DISORT radiative transfer code within libRadtran to estimate surface DNI and GHI. Deneke *et al.* (2008) used cloud retrievals from the Meteosat satellite family in combination with 16-stream DISORT to estimate solar irradiance in the Netherlands. They showed a mean bias difference (MBD) and RMSD of -3.0% and 4.2% for monthly insolation. Mueller *et al.* (2009) used a lookup table approach for clouds with transmissions pre-calculated with radiative transfer and values interpolated from the lookup table. They used a cloud effective radius of 10 μm for water droplets using the Hu & Stamnes (1993) parameterisation of the phase function and did not consider ice clouds. While this may be sufficient for GHI, this approach is less accurate when calculating the radiances required for the tilted irradiance as in the current study.

One of the most difficult aspects of using radiative transfer concepts to include clouds is that the direct and diffuse transmission depends strongly on cloud microphysical properties, which is why neglecting ice clouds and setting a fixed effective radius size for water clouds may be an oversimplification for calculating radiances and hence tilted irradiance. Current satellite products often include the required cloud microphysical and optical properties, namely cloud phase (water or ice), cloud optical depth, and cloud droplet effective radius, to allow radiative transfer simulations including clouds to be performed.

There are several motivations for inclusion of clouds inside the radiative transfer calculation for generating radiance fields. The first is for the development of solar energy models that can be applied to a wide variety of historical, current and future datasets, for example the ECMWF reanalysis or CMIP5 climate models considered in this thesis, as well as satellite observations. Another is the spectral effects of cloud attenuation are better captured with radiative transfer simulation, which is important for PV as shown in chapter 6.

In this chapter, the optimal tilt angle of a fixed-angle solar collector is considered. In the absence of horizon obstruction, shading, or radically different morning and afternoon weather conditions, the equatorial direction (i.e. facing south in the northern hemisphere) provides the best azimuthal alignment. A south-facing panel is primarily considered to reduce the size of the search space for optimisation, although non-south alignments can be considered as shown in section 5.5.4. The solar panel tilt angle is varied in steps of 1° to find the irradiance at each angle and the irradiance calculated at these tilts summed over a year of operation to determine the optimal orientation.

5.1.2 Review of tilt models

The tilted irradiance G_T can be considered physically as the sum of direct, diffuse and reflected components of sunlight such that (Gueymard, 2009)

$$G_T = G_B \cos\theta_i + G_D R_D + \rho (G_B \cos\theta_z + G_D) R_R \tag{5.1}$$

where G_B is the DNI arriving on the tilted plane at incidence angle θ_i, G_D is the diffuse irradiance on a horizontal plane, R_D is the diffuse transposition factor, ρ is the surface albedo and R_R is the reflected transposition factor. The transposition factors indicate the proportion of diffuse and reflected irradiance received by a tilted plane.

The following paragraphs introduce some commonly-used tilt models, and methods that have been used to optimise tilt angle.

Latitude-based

A "rule of thumb" for annual optimal tilt is that is should be equal to latitude on the basis that this minimises the incidence angle between the solar beam and the normal to the panel surface at solar noon. Effectively, this sets $\cos\theta_i$ as close as possible to 1, and assumes that the diffuse and reflected components in eq. (5.1) are either small or that the diffuse irradiance mostly arises from the same direction as the solar beam.

Several authors have proposed a modification to this simple form of the general formula such that the optimal tilt β_{opt} is

$$\beta_{\text{opt}} = Al + B \tag{5.2}$$

where l is latitude, A is in the range of 0.9–1.0 and B is between -15 and $+30$, in degrees. These formulae were derived for solar water and space heating (Armstrong & Hurley, 2010b; Yadav & Chandel, 2013, and references therein). Given the range of latitude-tilt relationships spans at least 45°, it is clear that even this rule of thumb is location dependent and these relationships are not suitable for general usage.

Additionally, for areas of the world with significant cloud cover, the equal-to-latitude assumption does not hold true due to the frequent obscuring of the sun by clouds. Armstrong & Hurley (2010b) showed that for Dublin, Ireland, at a latitude of 53°, the yearly optimal tilt was 33° using a clearness-index based correlation for the diffuse radiation amount and the Perez *et al.* (1990b) diffuse irradiance model which is introduced later in this section. This is outside of the range of the latitude-tilt relationships in eq. (5.2). It also suggests that the diffuse radiation under cloud cover is significant, and not distributed in the same manner as the direct beam.

Isotropic models

One simple way to handle the diffuse radiation is to consider it to be isotropic, meaning that it is the same intensity from every direction. Owing to geometrical considerations, the diffuse transposition factor in eq. (5.1) is $R_D = (1+\cos\beta)/2$ where β is the tilt measured from horizontal. This is the Liu & Jordan (1962) model. The Badescu (2002) isotropic model was proposed to properly account for the azimuthal (from the perspective of the solar collector) contribution to the isotropic sky diffuse radiation. Badescu (2002) therefore suggests $R_D = (3+\cos 2\beta)/4$. Despite its higher geometrical precision, the Badescu model is seldom preferred to the Liu-Jordan model in the solar energy literature even today, possibly due to the simplicity and long history of use for the former.

If the reflected irradiance is also assumed to be isotropic, the reflected transposition factor is $R_R = (1-\cos\beta)/2$ for the Liu-Jordan model and $R_R = (1-\cos 2\beta)/4$ for the Badescu model. R_D and R_R are simply the fractions of the sky and ground that are in view of the tilted plane in 2 dimensions and 3 dimensions for the Liu-Jordan and Badescu models respectively.

Further modifications have been made to the geometric argument to take account the observed reality that in the northern hemisphere, southern skies appear brighter. Thus Koronakis (1986) suggests $R_D = (2+\cos\beta)/3$. As this is applicable only for a south-facing plane based on sky brightness in this direction it is not strictly an isotropic model but has been classified as such (e.g. in Gracia-Amillo & Huld (2013); Yadav & Chandel (2013)). A better term would be “one-parameter”.

Anisotropic models

The benefit of both latitude-tilt relationships and isotropic/one-parameter models are their simplicity. However, both are incapable of reproducing the wide range of diffuse radiation situations found other than those where very clear skies prevail year-round (where latitude-tilt is appropriate) or in heavily overcast situations (where isotropic diffuse irradiance is a good approximation).

Therefore more sophisticated models were developed for R_D, to account for the directional dependence of sky radiance. Temps & Coulson (1977) placed 49 pyranometers at tilts in steps of 15° in zenith and 30° in azimuth (only one direction was considered assuming symmetry) to create an irradiance map for clear sky conditions. It is found there are three components of sky diffuse radiation: the circumsolar, which emanates from near the direction of the sun and is a consequence of forward scattering due to aerosols; the horizonal, describing an apparent increase in brightness towards the horizon; and the isotropic. Klucher (1979) extended the Temps & Coulson model by including a modulating factor $F = 1-(G_D/(G_B\cos\theta_z + G_D))^2$ to account for cloudy skies:

$$R_D = \left(\frac{1+\cos\beta}{2}\right)\left(1+F\sin^3\frac{\beta}{2}\right)\left(1+F\cos^2\theta_i\sin^3\theta_z\right). \tag{5.3}$$

The first term in eq. (5.3) is the Liu-Jordan isotropic model, the second term is the additional horizonal component, and the third term is the circumsolar contribution. If cloudiness is high, $F \approx 0$ and the sky radiation is approximately isotropic being dominated by the first term of eq. (5.3). For clear skies F approaches 1 and the anisotropic Temps-Coulson model is recovered. A slightly different anisotropic model that differentiates between clear and cloudy cases and arises from the same arguments was introduced by Reindl *et al.* (1990).

The main advantages of the Klucher model are that R_D is relatively easily calculated, is analytic, relates to physical reality, and is easy to grasp. Other anisotropic tilted irradiance models (Skartveit & Olseth, 1986; Gueymard, 1987; Perez *et al.*, 1990b; Muneer, 1990) use increasingly complex, empirically-derived equations with numerical coefficients but have high popularity due to their generally good representation of tilted irradiance (Gueymard, 2009; Gracia-Amillo & Huld, 2013). The Muneer (1990) model is of particular interest, as it is the tilt model used in PVGIS that is compared later in this chapter. The complexity in Muneer's model arises in using different relationships for shaded/overcast and sunlit surfaces with a correction for low solar elevation angles. The expressions for each case are more complex than that shown in eq. (5.3).

Performance of tilted irradiance models

A comparison between ten tilt models at the NREL site at Golden, Colorado, USA, found that most anisotropic models did not predict irradiance with a satisfactorily low error for tilted planes compared to the bounds of instrumental error from pyranometers (Gueymard, 2009). In fact, the relatively simple Klucher (1979) model performed at least as well as several of the more complex models. An intercomparison of 15 models in Denmark, France and Spain showed that isotropic models were deficient and that no one anisotropic model generally performed better than the others consistently when considering different cloud conditions, tilt angles and azimuth angles (Gracia-Amillo & Huld, 2013). Therefore, the continued development of tilt models that can adequately model all atmosphere, cloud, zenith and panel orientation conditions is desirable.

Optimising tilt

To find the optimal tilt, models can be run for a range of likely candidate tilt angles to determine the β_{opt} which maximises G_T. This is the approach taken with the IntRad method to find optimal tilt (the so-called iteration method). Another approach is to not be concerned with the tilted irradiance available at an arbitrary angle if the goal is only to seek the optimal tilt angle for a given location or conditions.

Barker & Christensen (2001) introduced a dependence on local average clearness index to determine how close to latitude the optimal tilt angle β_{opt} would be with the following

Study	Optimisation method	Diffuse irradiance	Location & latitude	β_{opt}
Chang (2009)	Artificial neural network	Not included	Taiwan, 25°	23.25°
Chang (2010)	Particle swarm optimisation	Isotropic	Taiwan, 25°	18.16°
Armstrong & Hurley (2010b)	Iteration	Perez	Ireland, 53°	33°
Talebizadeh *et al.* (2011)	Genetic algorithm	Isotropic	Iran, 32.5°	29.05°

Table 5.1: A selection of optimisation methods for optimal tilt angle of a solar collector

relationship:

$$\beta_{\text{opt}} = \pm[(0.379 + k_{t,\text{year}})l - 20.6(1 - k_{t,\text{summer}}/k_{t,\text{winter}})] \tag{5.4}$$

with l representing latitude and $k_{t,j}$ representing clearness index where for j winter = {November, December, January} and summer = {May, June, July} (vice versa in the southern hemisphere). The ± symbol denotes positivity in the northern hemisphere and negativity in the southern hemisphere if southern hemisphere latitudes are defined as negative. Clearness index is derived from the irradiation totals over the time period of interest and is described in section 2.1.4. The formula was derived using the Perez *et al.* (1990b) diffuse irradiance model.

Several novel optimisation techniques, inspired by biological and physical processes, have been developed in recent years. These methods, including artificial neural networks, genetic algorithm and particle swarm optimisation, have been applied to optimising tilt angle in various parts of the world (table 5.1).

As the differences between the studies by Chang (2009, 2010) (table 5.1) show, the result obtained from optimisation methods depends on the diffuse radiation assumption used (or whether it is included at all). Therefore, describing the diffuse radiation distribution accurately is essential.

5.2 Determining tilted irradiance from radiances

If the diffuse radiance distribution is known, it is not necessary to use a tilt model based on an empirical relationship for R_D in eq. (5.1). The irradiance on a tilted plane angled at tilt β and azimuth γ is a combination of the downwards and upwards radiance fields such that the bounds of the integration is over the hemisphere with base in the plane of the solar collector (Gueymard, 1987):

$$G_D R_D = \int_0^{2\pi} \int_0^{\theta_m} I(\theta, \phi) \cos\theta_d \sin\theta \, \mathrm{d}\theta \, \mathrm{d}\phi \tag{5.5}$$

where the angle between the normal of the tilted plane and the radiance direction of interest is given by

$$\cos\theta_d = \cos\beta \cos\theta + \sin\beta \sin\theta \cos(\phi - \gamma) \tag{5.6}$$

and the bound of the integration θ_m is in the plane of the solar collector such that

$$\theta_m = \frac{\pi}{2} - \tan^{-1}(\cos(\phi - \gamma) \tan\beta). \tag{5.7}$$

θ is the polar angle and ϕ is the azimuthal angle.

McArthur & Hay (1981) used radiance distributions obtained from fish-eye photographs. This consisted of dividing the photographic image into 2629 discrete regions, measuring the brightness for each region, and assigning a radiance value I [W m^{-2} sr^{-1}] to each region as a function of the image brightness. The pixel values of the images were calibrated to an in-situ actinometer which provided the radiance values. Equation (5.5) is approximated numerically by summing each radiance element over small solid angles $\Delta\theta\Delta\phi$ such that

$$G_D R_D \approx \sum_j \sum_k I(\theta_j, \phi_k) W \Delta\theta_j \Delta\phi_k \tag{5.8}$$

where

$$W = \max(0, \cos\theta_{dj} \sin\theta_j) \tag{5.9}$$

to ensure only the radiances in the field of view of the solar collector are counted. $\cos\theta_{di}$ is as given in eq. (5.6) with (θ, ϕ) replaced with (θ_j, ϕ_k). The McArthur & Hay (1981) method obtained agreement to ±10% for horizontal diffuse irradiance and ±5% for tilted irradiance on a south-facing plane (30° , 60° and 90° tilt), in a variety of sky conditions.

Gueymard (1987) started from the basis of calculating the weighted average of the clear and overcast radiance fields before performing the integration and applying coefficient fits to the result to generate the anisotropic tilt model referenced in the previous section. Cloud opacity was used as the weighting factor between clear and overcast radiance distributions. According to Gueymard, cloud opacity is an observation recorded at some airports. If it is not available it can be estimated from total cloud amount, hours of sunshine or diffuse-to-global irradiance ratio, G_D/G. The Gueymard coefficient series is fairly complex, being a third-order polynomial in $\cos\theta_i$ added to a sine series in panel tilt angle, the coefficients of which are themselves third-order polynomials in solar elevation angle.

Brunger & Hooper (1993) derived an empirical model for the sky radiance distribution taken from radiometer measurements of the sky. The relationship was a function calculated from tabulated observations of clearness index and diffuse-to-global ratio. As with the Perez equation for diffuse irradiance, the Brunger coefficients are from a discrete lookup table. The complexity of the Gueymard formula and the discrete lookup table approach of the Brunger formula show that it is difficult to ascribe an algebraic relationship between sky radiance and diffuse tilted irradiance, especially one from a physical basis.

Using digital photographs available today, it is possible that the McArthur & Hay (1981) method could be used to provide more accurate estimates of tilted irradiance by assigning pixel brightness values from a fish-eye camera directly to radiances. This could be performed instantly, without the need to digitise photographic negatives. In practice, sky radiance can be measured with instruments such as the EKO MS-321LR Sky Scanner[2].

In the IntRad method described in this chapter, the diffuse radiance field is calculated using the DISORT radiative transfer code as part of the libRadtran package (section 2.2.6). The radiative transfer equation is solved numerically with 16 streams, the minimum recommended for calculating radiances (Mayer *et al.*, 2012). The diffuse radiance field I is calculated at a resolution of 3° in the polar direction and 10° in the azimuthal direction. In DISORT, a pseudo-spherical correction has been implemented to improve accuracy at low solar elevations (Dahlback & Stamnes, 1991).

The downwelling radiances account for the anisotropy of the sky whereas the upwelling radiances from the ground are assumed to be isotropic and are equal to

$$I(\theta_j, \phi_k) = \frac{1}{\pi}\rho(G_B \cos\theta_z + G_D), \qquad \theta_j > 90^\circ. \tag{5.10}$$

At non-zero tilts, the field of view will include some upwelling radiances from the ground and exclude any sky radiances emanating from directions behind the solar collector. The relative weight of each radiance bin to the tilted irradiance total is governed by W in eq. (5.9).

The numerical approximation in eq. (5.8) is performed for the diffuse irradiance only. The DNI is simpler to calculate. From the Beer-Lambert law (eq. (2.19)) the DNI is

$$G_B = G_0 \exp(-m_a \tau) \tag{5.11}$$

τ is the overall sum of the optical depths of all extinction phenomena in the atmosphere, e.g. mixed gases, ozone, water vapour, aerosols and cloud droplets. For a tilted plane, the

---

[2] `http://eko-eu.com/products/solar-radiation-and-photonic-sensors/sky-scanner/ms-321lr-sky-scanner`

direct incidence irradiance is

$$G_{BT} = G_B \cos \theta_i \tag{5.12}$$

where the incidence angle θ_i follows a similar form to eq. (5.6):

$$\cos \theta_i = \cos \beta \cos \theta_z + \sin \beta \sin \theta_z \cos(\phi_a - \gamma). \tag{5.13}$$

Here, θ_z is the solar zenith angle and ϕ_a is the solar azimuth angle. In order to greatly speed up computations, the correlated-*k* method (section 2.2.7) is used to calculate broadband radiance for the 61×36 radiance directions at the 3° zenith × 10° azimuth resolution.

The radiative transfer method bears an advantage over anisotropic tilt models in that no assumption of the size and shape of the circumsolar region is made. When making ground irradiance measurements, DNI is not usually discernible from diffuse irradiance that has been scattered into the region of the solar disc or diffuse radiation emanating from the solar region that has been caused by strongly forward scattering aerosol or thin cloud. This can cause issues in calculating the direct and diffuse contributions as a decision has to be made on the angular size of the circumsolar region (Blanc *et al.*, 2014). Often a half-angle of 2.5° is used with all irradiance inside this region treated as direct, which is the World Meteorological Organization (WMO) definition of DNI for pyranometer measurements. However, the actual size of the circumsolar region depends on the present sky conditions and can be greatly enhanced in conditions of high aerosol and thin cloud. In the IntRad model, all radiation that has been scattered at least once is correctly treated as diffuse regardless of the scattering direction with the directional distribution handled by the radiance method.

5.3 Inputs into the model

To generate the radiance field, inputs of the atmospheric state, location altitude, clouds, aerosols and surface albedo are required. Although any climate, satellite or reanalysis dataset that provides all of the necessary inputs can be used, the MODIS instrument data on the Aqua and Terra satellites are used for all parameters except aerosols for which a climatological run from a dedicated aerosol model (GLOMAP) is used.

MODIS Level 3, 8-day mean data for ozone, water vapour, and cloud parameters (MOD08E3 and MYD08E3 data series, both Collection 5.1) were used. Surface albedo was obtained from the combined Terra and Aqua 16-day running mean albedo product MCD43C3, which is updated every 8 days. The resolution of the atmosphere and cloud data is 1° × 1° and the albedo data is 0.05° × 0.05°. 8-day time resolution is used as a trade-off between capturing fluctuations in weather conditions and computational efficiency. Daily and monthly timesteps are also available for the Level 3 MODIS data.

5.3.1 Atmosphere

Well-mixed gases in the atmosphere are a source of Rayleigh scattering which is dependent on wavelength. Shorter wavelengths are scattered more strongly, approximately proportional to the fourth power of wavelength.

The location and time of year dictates which of the particular AFGL atmospheres were selected in the calculation, however as discussed in chapter 4 the impact of well-mixed GHGs on the final result is negligible. Ozone and water vapour are included, so the total atmospheric column depths of ozone and water vapour are taken from the MODIS data.

5.3.2 Clouds

Clouds are both the largest attenuating factor in the transmission of solar radiation and the source of the largest uncertainty for many regions of the world, the principal exceptions being in areas of high aerosol optical depth and infrequent clouds such as deserts. Both liquid and ice water clouds exhibit complex scattering properties. As discussed in section 2.2.3 the optical properties of clouds are determined by cloud droplet effective radius r_{eff}, cloud water content and cloud geometric height. From these factors the radiative properties (single scattering albedo ω, phase function $P(\cos\Theta)$ where Θ is the scattering angle, and optical depth τ_c) can be determined. How the cloud microphysical properties are converted to radiative properties depends on the parameterisation used.

Owing to the large uncertainties in modelling clouds in time and space, it was decided to use a simplified approach with two atmospheric columns, one clear and the other overcast. The resulting radiance distribution is weighted between the two situations based on cloud fraction f_c. To define the cloudy column, the cloud liquid water content C_l, cloud ice water content C_i (both g m^{-3}), cloud fraction, cloud height h_c, $r_{\mathrm{eff},l}$ and $r_{\mathrm{eff},i}$ (effective radius for liquid and ice) are used. $r_{\mathrm{eff},l}$ and $r_{\mathrm{eff},i}$ may be, and usually are, different. Occasionally no MODIS cloud droplet effective radius can be determined. Where this occurs, a size of 10 µm is used for liquid droplets and 30 µm for ice crystals, following the convention used in ISCCP.

Where both liquid and ice clouds are present, they are aggregated into the same column to create one mixed-phase cloud. The MODIS data provides cloud water paths p_l and p_i whereas libRadtran requires inputs of C_l and C_i. The satellite retrieval of liquid and ice water path is an average of clear and cloudy observations, so to get the water path for cloudy pixels only, p_l and p_i are divided by cloud fraction f_c. To convert cloud water paths to cloud water content, it needs to be divided by cloud geometric height h_c (eq. (2.29)). For single scattering albedos $\omega \rightarrow 1$, which is the case for the majority of solar wavelengths (Hu & Stamnes, 1993), the fraction of transmitted to incident irradiance is approximately independent of the cloud geometric height. This has previously been demonstrated in radiative transfer calculations (Rozwadowska, 2004; Oumbe *et al.*, 2008). For mathematical convenience and consistency with other investigations (e.g. Lohmann *et al.* (2006)) the somewhat arbitrary h_c of 1 km has been chosen. The exception is where the cloud top height h_t derived from the satellite data is determined to be less than 1 km in which case it extends down to the surface. Currently h_t is only reported for Aqua, so cloud top pressure p_t, which is available from both satellites, was converted to height for both Terra and Aqua data using the pressure-altitude relation:

$$p_t/p_0 = \exp(-h_t/h_0) \tag{5.14}$$

with $p_0 = 1013$ hPa and $h_0 \approx 8.5$ km being the atmospheric scale height. Where no cloud top pressure is available in the retrievals, a level of 700 hPa, corresponding to a height of about 3 km, has been assumed. The most important reason to include cloud top height is to determine whether the clouds retrieved for a $1^\circ \times 1^\circ$ grid cell are determined to be below the site of interest in mountainous areas.

MODIS provides a third cloud state, “undetermined”, which is returned when the cloud retrieval algorithm detects clouds in a pixel but fails to identify their phase. For the undetermined cloud water path in a $1^\circ \times 1^\circ$, half is assumed to be liquid and half to be ice. The specific assumptions used for modelling liquid and ice clouds are detailed below.

Liquid clouds

As cloud droplets can be modelled very well as spheres and are typically several times larger than the wavelength of light in the solar spectrum, for calculating radiances it is recommended to use the full Mie scattering parameterisation for liquid cloud droplets (Mayer *et al.*, 2012). The Mie parameterisation provides ω and the moments of $P(\cos\Theta)$ as a function of wavelength. This is available as an extension to the core libRadtran package in the form of pre-calculated lookup tables generated using the Wiscombe (1980) Mie scattering code. Effective radius $r_{\mathrm{eff},l}$ is provided by the MODIS data, and this corresponds to a gamma distribution of droplet radii for the Mie calculations.

Ice clouds

The cloud retrieval algorithm for Collection 5.1 in MODIS uses a mixture of particle habits depending on the maximum diameter D_{max} of the ice crystals: 50% solid columns, 15% 3D bullet rosettes and 35% hexagonal plates for particles where $60 < D_{\mathrm{max}} < 1000$ μm, and 45% solid columns, 45% hollow columns and 10% aggregates for particles where $1000 < D_{\mathrm{max}} < 2000$ μm (Baum *et al.*, 2005; Menzel *et al.*, 2010; Minnis *et al.*, 2011). A definition of 100% solid columns has been used in IntRad due to the difficulties of mixing habit types and the fact that solid columns make up the largest part of the mixture in the range of $60 < D_{\mathrm{max}} < 2000$ μm corresponding to $r_{\mathrm{eff},i}$ of approximately 20–120 μm. This encompasses the majority of ice cloud effective radius retrievals. Out of the single-habit assumptions, solid columns provide the best estimates of ice water content and $r_{\mathrm{eff},i}$ (Baum *et al.*, 2005). The ice scattering has been represented by a double Henyey-Greenstein (DHG) phase function using the Key *et al.* (2002) model. The DHG is a convenient simplification of the real phase function that is suitable for modelling radiances due to its ability to somewhat account for the forward and backward scattering peaks better than the simpler single Henyey-Greenstein (HG) phase function (Mayer *et al.*, 2012). The DHG phase function is smooth and does not include effects such as the 22° and 46° halo scattering peaks present in pristine hexagonal columns and plates. The roughened hexagonal column phase function has a less strong forward scattering component than pristine hexagonal columns and does not exhibit a halo effect, therefore is represented better by the DHG phase function. The assumption of roughened hexagonal columns provides the lowest RMSD in optical depth for MODIS retrievals (Xie *et al.*, 2012) adding justification for the smooth DHG phase function approximation.

5.3.3 Aerosols

A monthly aerosol climatology is provided by the GLOMAP model (section 2.3.4). MODIS data for aerosol has not been used as aerosol properties are not always available over land, particularly in desert regions which are important for solar energy and aerosols are prevalent.

5.3.4 Albedo

The surface albedo is the proportion of downwards irradiance that is reflected by the earth's surface. In reality, surface albedo is a function of wavelength and solar zenith angle as direct and diffuse irradiance components have different reflectance properties. Albedo is important in the tilted irradiance calculation as it defines the amount of reflected irradiance available from the ground that is available to a solar collector. Even at zero tilts, a higher surface albedo can increase downwards irradiance due to multiple reflections between surface and atmosphere, particularly if clouds are present (Gueymard, 2009).

The black-sky and white-sky albedos are calculated from the bi-directional reflectance distribution function which describes the reflected radiance as a function of incident and reflected directions. Black-sky albedo is the albedo assuming all direct irradiance and no diffuse irradiance and is a function of solar zenith angle, whereas white sky albedo assumes a purely diffuse isotropic source and is independent of solar geometry. White sky albedo has been used in the IntRad simulation as its solar zenith independence makes it easier to use. Deneke *et al.* (2008) has shown that this does not introduce significant error in a variety of conditions. Surface albedo is spatially and temporally variable, even throughout the course of the same day (Gueymard, 2009), with the surface properties within a few metres of the solar collector of greatest importance.

Sometimes it is possible that there are no albedo values retrieved during a 16-day period for some parts of the world. This could happen where consistent cloudy conditions prevent observations of the surface being made. In these cases where no albedo measurement exists for a $0.05^\circ \times 0.05^\circ$ cell, the mean value from the 21×21 cells surrounding the grid square ($1.05^\circ \times 1.05^\circ$) is used. In very rare cases where no 1.05° mean exists, the spectral albedo is taken from the global $\frac{1}{6}^\circ \times \frac{1}{6}^\circ$ map of different surface types in the IGBP land cover dataset (section 2.3.5).

5.4 Modelling flowchart

The modelling flow diagram is shown in fig. 5.1.

5.5 Application of the model

5.5.1 Evaluating performance

The two measures used to evaluate models are the mean bias difference MBD and root-mean-square difference RMSD. The MBD is a measure of bias that describes how far, on average, the models agree, whereas the RMSD measures the spread between model estimates. Both are normalised by the mean of the data and expressed as a percentage. Therefore

$$\mathrm{MBD} = \frac{1}{N\bar{o}} \sum_{j=1}^{N} (e_j - o_j) \tag{5.15}$$

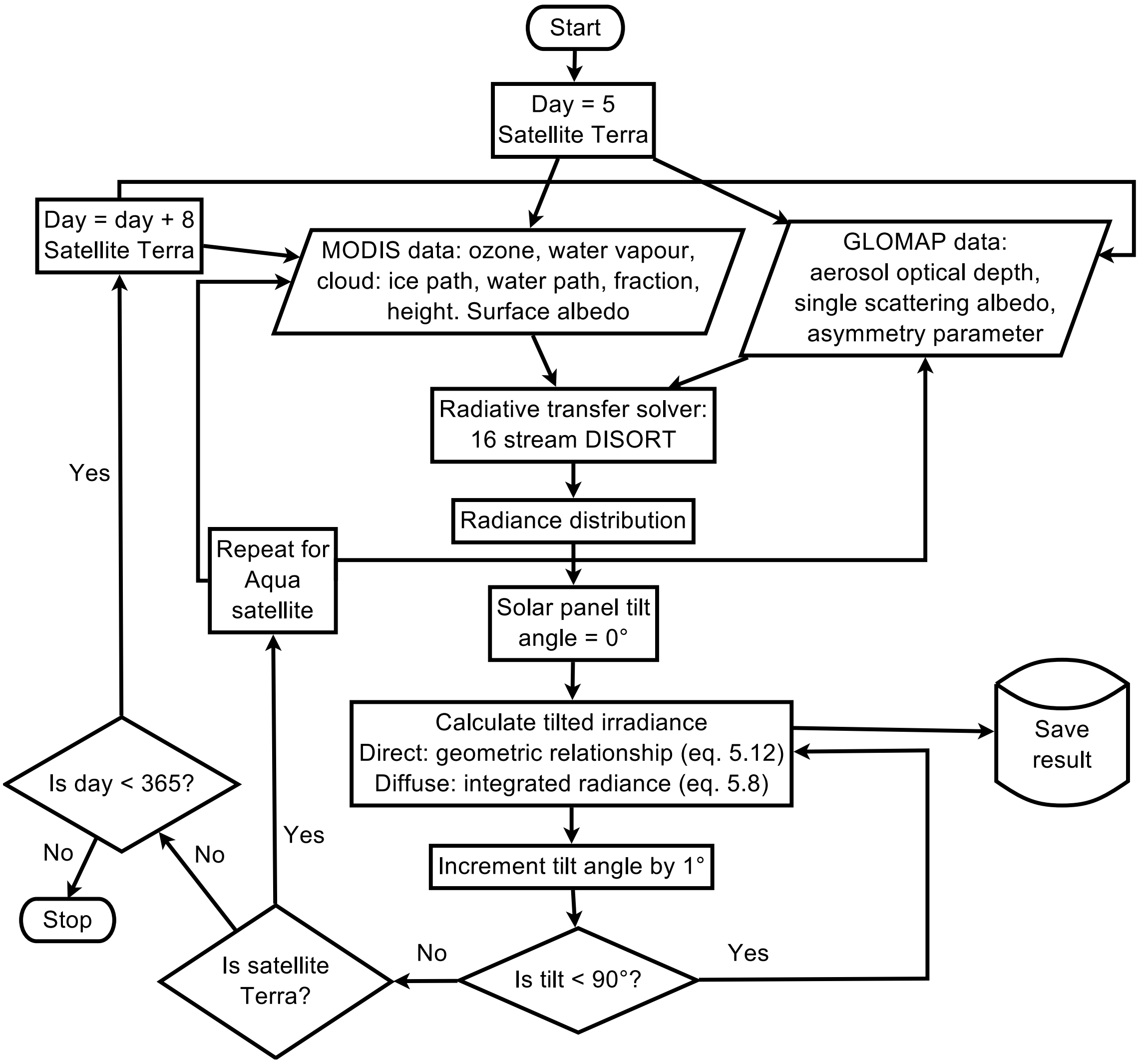

Figure 5.1: Flow diagram of modelling process

and

$$\mathrm{RMSD} = \frac{1}{\bar{o}}\sqrt{\frac{\sum_{j=1}^{N}(e_j - o_j)^2}{N}} \tag{5.16}$$

where e_j are the estimates provided by the model, o_j are the observed values or otherwise estimates provided by a reference model, and $\bar{o}$ is the mean of the observations.

One year of atmosphere, cloud and albedo data from 2013 was input into the radiative transfer calculation, and the solar zenith and azimuth were calculated at the centre of each hour for the middle day in each 8 day period. The diffuse radiance field L and direct horizontal insolation $G_B \cos\theta_z$ for each hour are the outputs from libRadtran. Plane irradiance for a particular tilt and azimuth is obtained by applications of eqs. (5.8) and (5.12) and summing the results.

5.5.2 Radiance distributions

Figure 5.2 shows the diffuse radiance distributions for clear sky, overcast sky and all sky, for the hour of 12:30pm for the 8-day period centred on 6 June 2013 for the Church Fenton weather station near Leeds (MIDAS station ID 533 in chapter 4). The clear-sky case includes mixed gas, water vapour, ozone and aerosol attenuation. The anisotropy of clear-sky diffuse radiation due to the circumsolar region, and to a lesser extent the bright section near the horizon, can be seen from fig. 5.2a. If an overcast sky is assumed (fig. 5.2b), it can be seen that the radiance distribution is much different, with a maximum intensity between the solar position and zenith which becomes apparently uniformly less intense away from this maximum towards the horizon. Figure 5.2c shows the all-sky weighted radiance distribution taking into account the cloud fraction, which for this hour was 56.4%. The circumsolar peak is still apparent, but the horizon brightening contribution is hard to discern and the remaining sky radiance is more isotropically distributed than in the clear-sky case.

5.5.3 Tilted irradiance map

The radiance distributions for the same location were integrated over all polar and azimuthal alignments using eq. (5.8), and the direct beam included, to provide a tilted irradiance map (fig. 5.3). Figure 5.3a shows that when there are no clouds, the ideal panel alignment is more or less normal to the solar beam. There is a fairly wide tolerance around the optimal position as a result of the cosine of incidence angle being approximately 1 for small incidence angles. As shown in fig. 5.2a, the majority of the diffuse radiation is from the circumsolar region, with both contributes to the beam alignment being optimal and the wide tolerance in optimal tilt. Figure 5.3b shows that in an overcast sky, the ideal panel alignment is horizontal and independent of the solar direction even though the corresponding radiance distribution is slightly off-zenith. In this example the optical depth of the cloud layer is 8.8, which is thick enough to obscure the solar beam (Oumbe *et al.*, 2008) with the resulting diffuse irradiance approximately isotropically distributed. Figure 5.3c shows the all-sky tilted irradiance map with the cloud fraction of 56.4%. The optimal tilt of the solar collector is centred around the solar position as in the clear-sky case, but with corresponding lower irradiance values.

5.5.4 Yearly tilted irradiation

Radiance distributions were obtained for each hour of the middle day (day 5) for each 8 day period, and integrated using eq. (5.8) to produce tilted irradiance. The direct beam contribution was included. Hourly irradiance outputs were then multiplied by the number

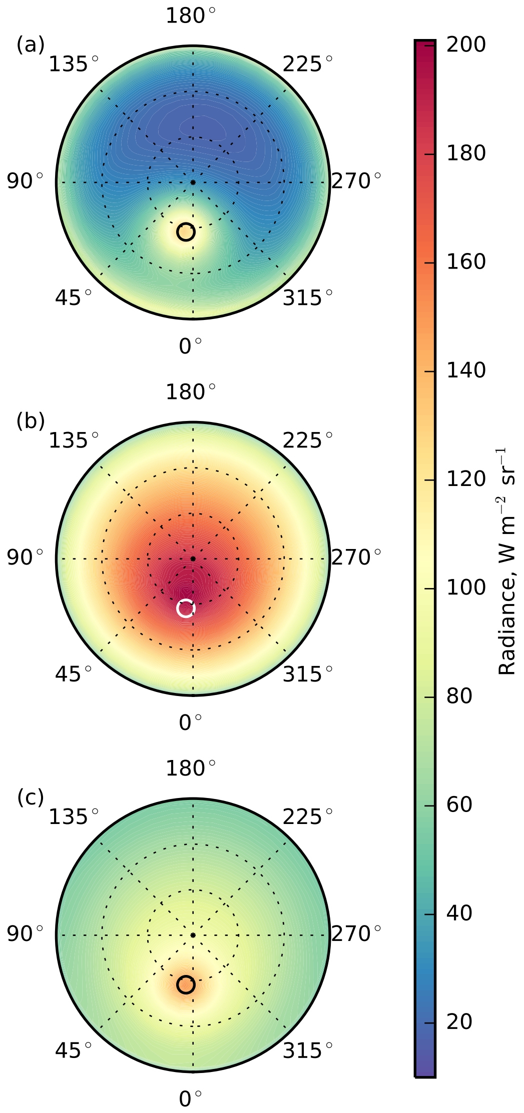

Figure 5.2: Radiance distributions (looking upwards) for the Church Fenton weather station for 12:30pm on 6 June. Distance from the centre represents polar angle and angular coordinate represents azimuth angle. (a) clear sky radiance distribution, (b) overcast radiance distribution (water cloud optical depth of 8.8), (c) all-sky distribution based on clear sky and cloudy sky distributions with cloud fraction equal to 56.4%. Solar position is represented by the circle at zenith 32.9°, azimuth 8.2° .

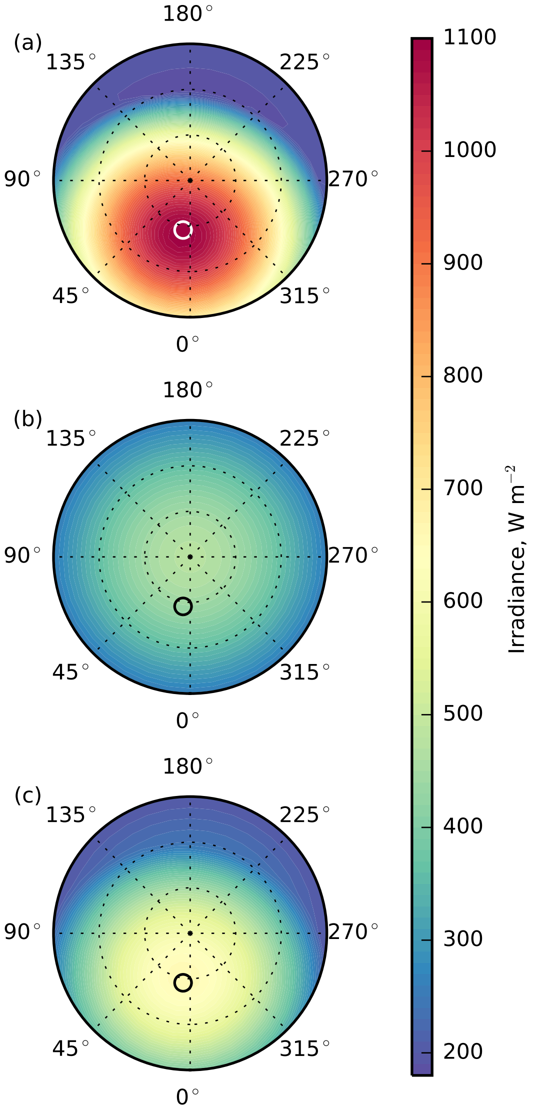

Figure 5.3: Tilted irradiance maps for the Church Fenton weather station for 12:30pm on 6 June. Distance from the centre represents tilt angle with centre representing a horizontal alignment and the edge of the circle represents a vertical alignment. Angular coordinate represents azimuthal alignment. (a) clear sky, (b) overcast sky (water cloud optical depth of 8.8), (c) all-sky, weighted combination of clear and overcast cases, with cloud fraction equal to 56.4%. Solar position is represented by the circle at zenith 32.9°, azimuth 8.2°.

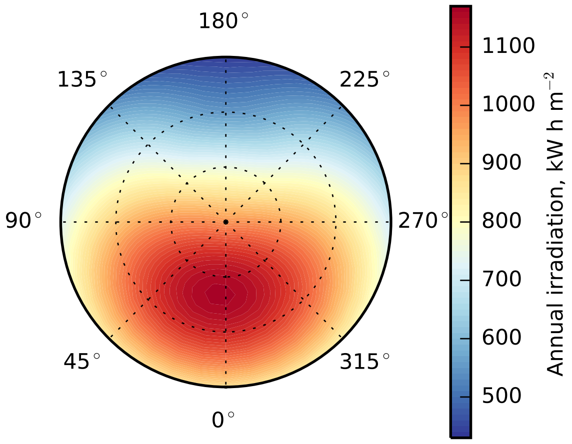

Figure 5.4: Plane irradiation map for Church Fenton (latitude 53.8°N, longitude 1.2°W, altitude 8 m) for the year of 2013

of days in each period (8, except for the last period of the year which is 5 or 6) and summed to generate the yearly irradiation. For Church Fenton weather station, the yearly irradiation map is shown in fig. 5.4.

The optimal tilt for this location calculated using the IntRad method is 40° from the horizontal and azimuth 6° west of south. The slight west-facing optimal azimuth highlights that the afternoon conditions may be clearer than the morning based on the difference in cloud retrievals between the Aqua and Terra satellites, although the difference in yearly output between 6° and 0° is very small and at 0° azimuth the optimal tilt is still 40°.

At this location $l = 53.8°$, and for 2013 the annual, summer, and winter clearness indices are $k_{\mathrm{t,year}} = 0.424$, $k_{\mathrm{t,MJJ}} = 0.458$ and $k_{\mathrm{t,NDJ}} = 0.332$. These low mean clearness indices are indicative of frequently cloudy conditions. The Barker-Christensen optimal tilt estimated in eq. (5.4) predicts $\beta_{\mathrm{opt}} = 38°$ for Church Fenton, close to the 40° calculated with the IntRad method. Both models suggest the optimal tilt is more horizontal than latitude in this location, similar to the result observed by Armstrong & Hurley (2010b) for Ireland.

5.5.5 Treatment of broken cloud fields

As described in section 5.3.2, the model uses a linear combination of clear and overcast radiance distributions weighted by the cloud fraction. In reality, clouds exhibit both vertical and horizontal heterogeneity, and the 1D approximation is a simplification of the 3D picture (Marshak & Davis, 2005). The diffuse reflections from the sides of clouds, along with cloud shadowing, will impact the ground-level radiance field. It is important to determine whether the lack of including 3D effects is a serious shortcoming of the model.

Therefore the radiance distributions are compared to those generated by the UniSky simulator software available from `http://www.unisky.sav.sk` (Kocifaj, 2012; Kocifaj & Fečko, 2014; Kocifaj, 2015). The UniSky simulator can model 3D clouds either as a regular grid, or as randomly orientated. Random clouds can be grouped into a preferred sky sector, simulating the effects of a morning or evening weather front. For random cloud fields, a random seed is specified on input, allowing reproducibility of random simulations.

To keep the simulations consistent, as the two models take different parameters, a simple case is considered. The solar zenith angle is set to 30° and azimuth to 0°, cloud fractions of 20% and 80% with base at 3 km, geometric height 1 km and optical depth 10, and a single monochromatic calculation at 550 nm wavelength is performed. A generic aerosol with a Henyey-Greenstein phase function ($g = 0.7$), optical depth $\tau_a = 0.2$ and single scattering albedo $\omega = 0.9$ is prescribed and surface albedo is set to zero. Both models use the nadir-view cloud fraction, which is the proportion of horizontal area covered by clouds to the total area, as viewed from a nadir-viewing instrument such as a satellite.

An additional parameter used in UniSky is the cloud reflectance. This is not supplied explicitly IntRad but can be calculated. As cloud reflectance is dependent on optical depth, a plane-parallel cloud with $r_{\text{eff}} = 10$ µm, optical depth 10, base 3 km and vertical extent 1 km, with full Mie phase function, was modelled in libRadtran. Reflectance was found to be 40.7% at 550 nm, based on the ratio of upwelling to downwelling irradiance at the top of atmosphere with molecular scattering and absorption suppressed. Clouds are modelled as spheres in UniSky; the default value of 0.5 km radius is used.

100 runs of the random cloud field in UniSky were generated with the parameters described above, with the random seed ranging sequentially from 1 to 100. Two examples of these diffuse radiance fields for sun unobscured and sun obscured are shown in fig 5.5. The 100 random runs could simulate a short period of time in which solar zenith angle and weather conditions remain relatively constant overlaid with a wind-driven broken cloud field. As UniSky does not include the DNI as an output (M. Kocifaj, personal communication), this was determined from eq. (5.11) with the total optical depth the sum of each component:

$$\tau = \tau_c + \tau_a + \tau_R \tag{5.17}$$

where $\tau_a = 0.2$, $\tau_R = 0.00879(\lambda/1000)^{-4.09}$ is the Rayleigh scattering optical depth at 550 nm of 0.1014 calculated as in Kocifaj (2012) and τ_c is equal to 10 if the pixel is obscured by cloud and 0 otherwise.

Each of the 100 radiance fields produced by UniSky for both the 20% and 80% cloud fraction, along with the calculated beam component, was numerically integrated using a south-facing plane with tilt angle running from 0 to 90°. For the libRadtran run, radiance

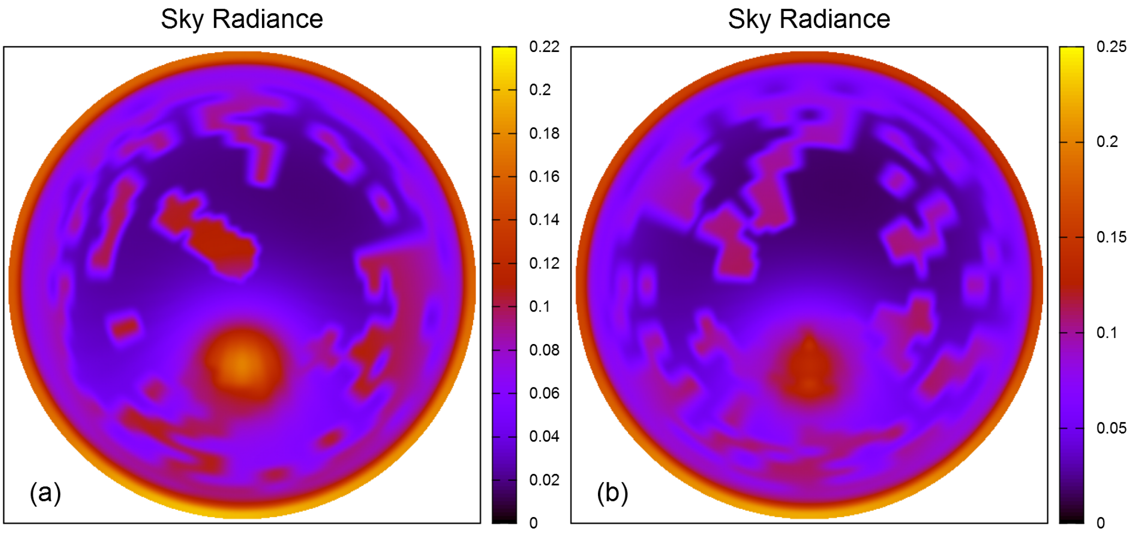

Figure 5.5: UniSky radiance distributions for two broken cloud regimes ($c_f = 0.2$) where (a) the sun is not obscured and (b) the sun is obscured. Units are radiance normalised to the extraterrestrial DNI [sr^{-1}].

fields with cloud optical depth of 10 and cloud fractions of 20% and 80% were calculated and the numerical integration applied. The mean value from the 100 UniSky runs is compared to the libRadtran output and the results for tilt angle ranging from 0 to 90° facing south are shown in fig. 5.6.

For the 0.2 cloud fraction, in both the libRadtran and the mean of the UniSky runs, the irradiance for this situation is maximised when the tilt angle is 29°. The effect of cloud obscurity can clearly be seen in the bimodal character of the UniSky runs characterised by the clustering of the thin grey lines in fig. 5.6a. When a cloud lies in front of the sun, the irradiance at optimal tilt is around 0.2 of its extraterrestrial values whereas it is close to 0.9 in the unobscured case. The majority of this effect is due to the difference in direct beam transmission between the two modes. The libRadtran method predicts a slightly higher irradiance at all tilt angles under this method compared to UniSky.

As cloud fraction increases, the plane-parallel approximation becomes more appropriate. As the UniSky simulator does not include multiple scattering within cloud layers (M. Kocifaj, personal communication), only the gaps between clouds contribute substantially to downwelling radiances. At a cloud fraction of 0.8, in fig. 5.6b, it can be seen that these gaps do not occur often, and the long-term averaged irradiance is estimated to be very low - about 0.1 of the extraterrestrial at optimal tilt. Furthermore, despite the high cloud attenuation, optimal tilt is shown to be 29° with the average of the UniSky simulations and 16° with the IntRad method. It is recommended (Kocifaj, 2015) to approximate a high cloud fraction with an aerosol layer that represents forward scattering by cloud water droplets in UniSky. For broken clouds under low cloud fraction, the good correspondence between the two models for long-term insolation shows that the 3D reality can adequately simplified into the 1D weighted clear/overcast simulation. For high cloud fractions, the

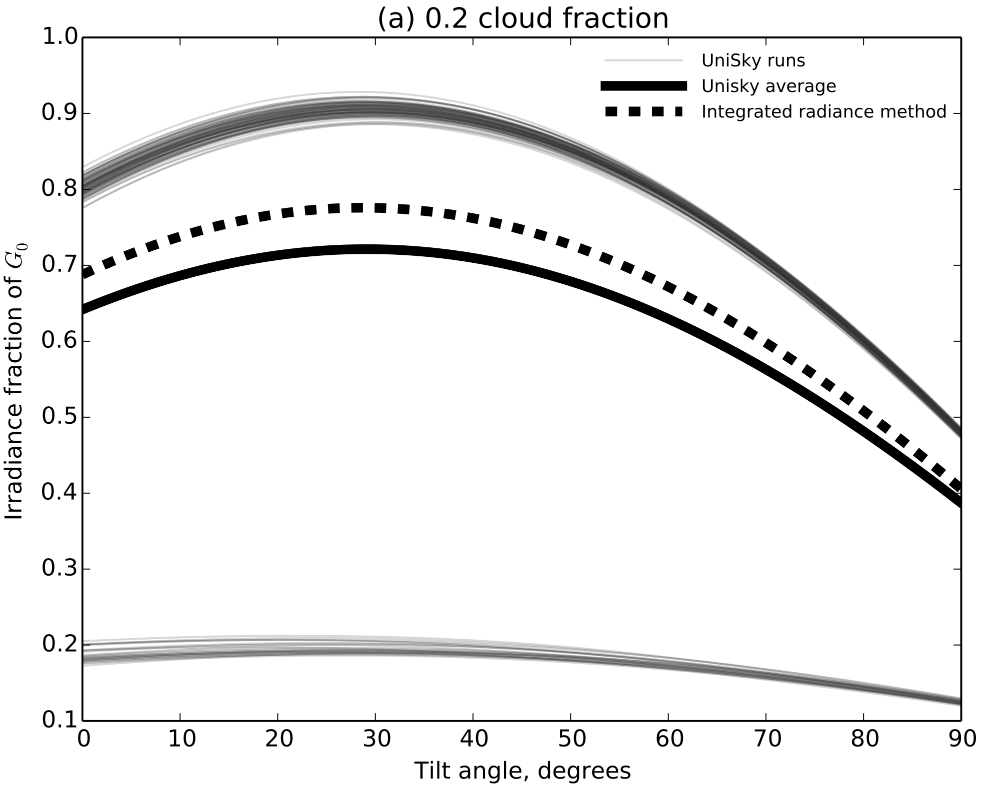

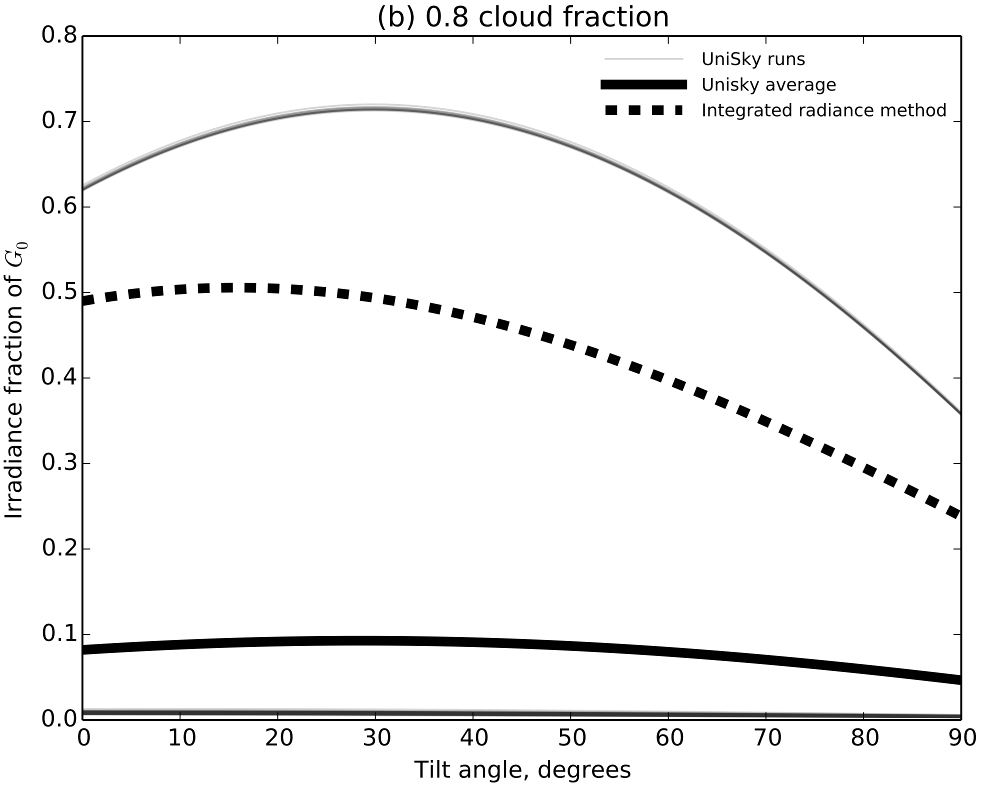

Figure 5.6: Plane irradiance as a function of panel tilt for 100 runs of the UniSky simulator with random cloud geometry, the UniSky average, and the 1D weighted average radiances from libRadtran, for $\theta_z = 30^\circ$ and (a)$f_c = 0.2$; (b) $f_c = 0.8$.

Source ID	Code	Station name	Lat.	Lon.	Alt. (m)
1395	Cam	Camborne	50.218°N	5.327°W	87
719	Wis	Wisley	51.310°N	0.475°W	38
533	ChF	Church Fenton	53.836°N	1.197°W	8
918	Dun	Dunstaffnage	56.451°N	5.439°W	3
9	Ler	Lerwick	60.140°N	1.183°W	82

Table 5.2: List of MIDAS stations used in the validation and comparison.

sky is approximately homogeneous and the 1D approximation is valid.

5.6 Model performance

5.6.1 Validation against horizontal irradiation measurements

Yearly irradiation predicted from IntRad using MODIS data is validated against horizontal irradiation measurements from high-quality MIDAS and BSRN pyranometer data, and is shown in fig. 5.7. MIDAS is used for UK locations and BSRN used for non-UK locations. Camborne (Cam) and Lerwick (Ler) are MIDAS stations that also supply data to BSRN. At the time of writing the BSRN data were not available so the MIDAS data have been used.

Five MIDAS sites were selected on the basis of wide geographical coverage within the UK and a minimal amount of missing or bad data for 2013. Where missing hours do occur in the MIDAS data, the data has been filled by using the mean irradiation from the corresponding hour in the same month. The selected MIDAS sites are shown in table 5.2.

The MBD between the annual irradiation derived from IntRad and the pyranometer data is $+0.56\%$ and the RMSD is $+6.69\%$. Of the sites where the IntRad method deviates from the measured values by more than 10%, two (Izaña and Sonnblick) are at mountaintop sites at altitudes 2373 m and 3109 m respectively. In these areas, the 1° resolution of the MODIS atmosphere data may not be large enough to capture all of the micro-climatic effects in mountainous regions. As discussed by Gueymard & Wilcox (2011), the spatial variation in irradiance measurements is highest in coastal and mountainous areas. Clouds are particularly difficult to attribute as sometimes the site location may be above the mean cloud height for the 8 day period whereas in reality the station is not cloud-free for the entire 8 days. Furthermore if the cloud deck is below the station altitude, the albedo from the point of view of the pyranometer changes, and backscattering effects between the cloud layer and the atmosphere above the station can enhance the downwards radiation. It is unlikely that the MODIS albedo product includes these effects as it is calculated from clear sky scenes, and this could be a source of error.

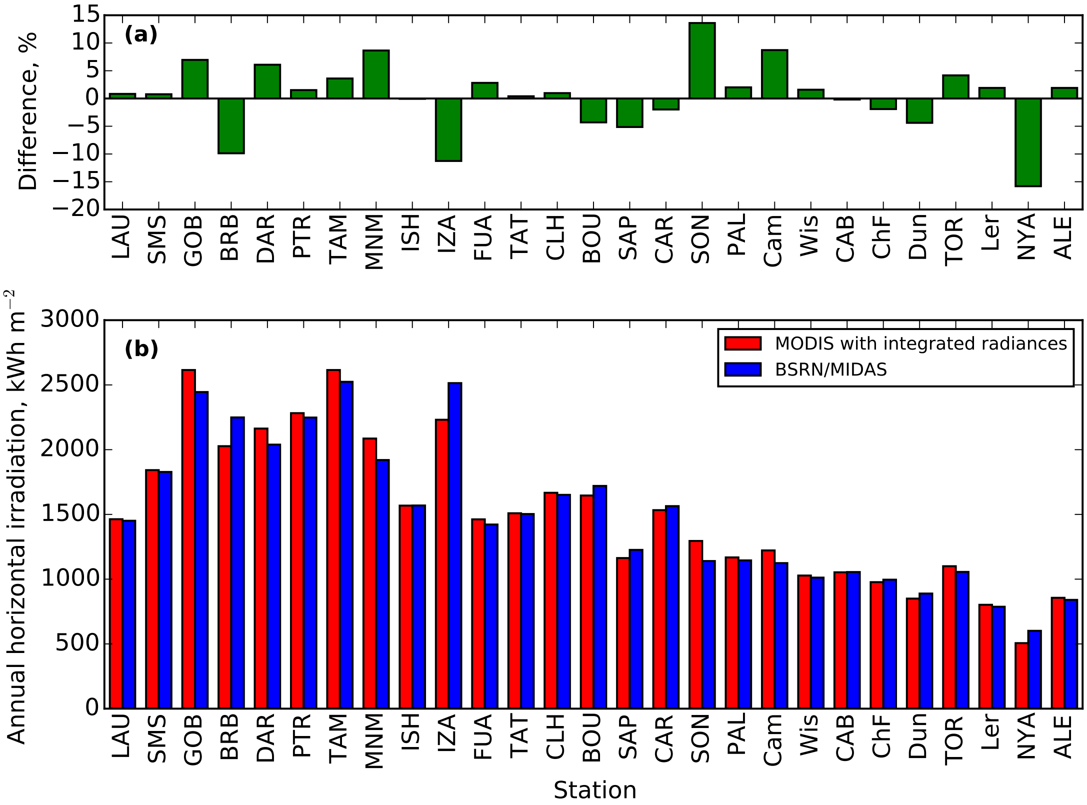

Figure 5.7: Validation of integrated radiance method using MODIS data against pyranometer measurements. (a) Differences between IntRad method and BSRN/MIDAS irradiation, and (b) the absolute values of IntRad and BSRN/MIDAS irradiation. For station names and locations, refer to tables 2.4 and 5.2.

The other location with a greater than 10% relative error, Ny-Ålesund, is at very high latitude (78.9°N), where satellite retrievals from MODIS become less reliable. In addition, in such a high-latitude site, solar declination can vary widely over the course of an 8-day period in spring and autumn and as such the solar geometry used in IntRad may not be representative. Interestingly, the other high latitude location, Alert in the far north of Canada (82.5°N), shows a better good agreement with the model. This could be due to a higher annual irradiation than Ny-Ålesund indicative of clearer conditions, as the annual horizontal irradiation at Alert is similar to that at Dunstaffnage at 56.4°N. Brasilia, the fourth poorest site for agreement with a 9.9% underestimation, suffers from a large amount of incomplete data in the 2013 BSRN dataset which may result in a large error in the "observation" value for this site. Brasilia passes the QC test because all 96 15-minute bins are present for each month as required by the Roesch *et al.* (2011) QC procedure (section 2.3.1), but for some months there are as little as 7 days of data present.

5.6.2 Validation and comparison of tilted irradiation

It is difficult to validate the tilted irradiation model on a global basis because there are few comparable high-quality long term measurements of tilted irradiance available worldwide.

Tilt	Integrated radiance model (kWh m^{-2} yr^{-1})	Eppley PSP measurements (kWh m^{-2} yr^{-1})	Difference
Horizontal	1760.0	1684.2	+4.5%
40°S	2120.4	2010.0	+5.5%
90°S	1479.3	1402.9	+5.4%
90°E	1085.4	1138.6	−4.7%
90°W	976.7	922.2	+5.9%
90°N	420.5	479.3	−12.3%

Table 5.3: Validation of tilted irradiation from the integrated radiance model against ground measurements from NREL.

One site provides data that can be used for validation.

Validation against tilted irradiation measurements form NREL

The NREL Solar Radiation Research Laboratory (SRRL) (Andreas & Stoffel, 1981) produces horizontal and tilted irradiation datasets which are available from their website at `http://www.nrel.gov/midc/srrl_bms/`. Tilted irradiation is measured at 40°S and at 90°S, W, E and N, using Eppley PSP pyranometers. Horizontal radiation is measured with a number of different pyranometer models. For consistency, the ventilated, corrected Eppley PSP horizontal irradiation measurement is used. The NREL site is located in Golden, Colorado, at 39.74°N, 105.18°W at an altitude of 1829 m.

The validation against the NREL station measurements is shown in table 5.3. The horizontal irradiation estimate from the integrated radiance model is 4.5% higher than the NREL measurement using the Eppley PSP. For the 40° and 90° south-facing tilts, the relative error is slightly higher but does not grow appreciably. The model captures some of the diurnal variation in weather conditions at this site, as seen by the differences between east- and west-facing tilt estimates, however underestimates the magnitude of the diurnal variation with an overestimate for the west-facing pyranometer and an underestimate for the east-facing pyranometer. This may be due to the timing of the satellite overpasses, approximately 90 minutes before and after local solar noon on average, whereas east- and west-facing wall irradiances will be at their maximum earlier and later in the day, respectively. The north-facing estimate is considerably less good than for the other orientations, however, it is not likely that serious consideration would be given to tilting panels poleward given the low overall yield estimate.

Comparison with tilted irradiation estimates from PVGIS

The optimal tilt angle predicted by the integrated radiance model, and the irradiance predicted at this optimal tilt, are compared with results from the online PVGIS solar resource

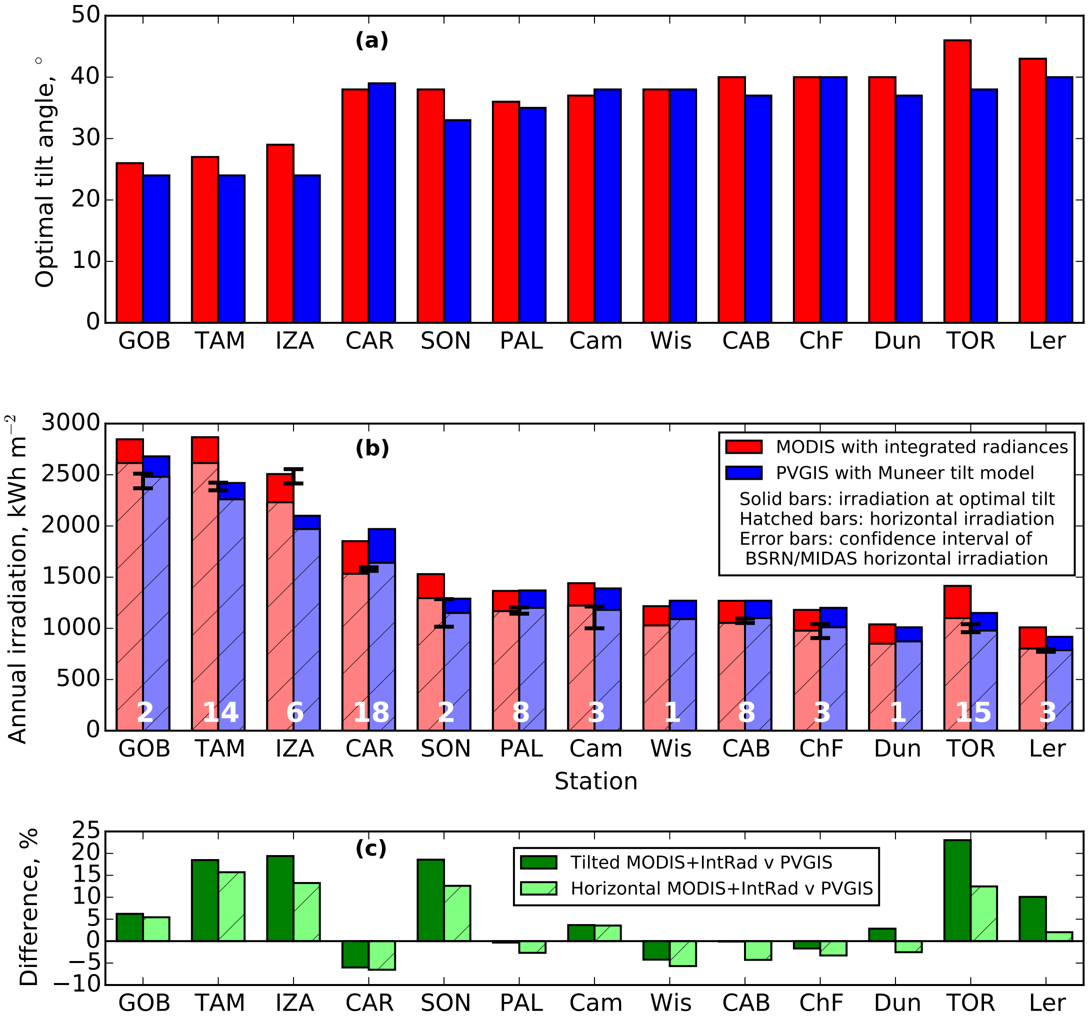

Figure 5.8: Comparison of integrated radiance method using MODIS data against results from PVGIS for optimal tilt angle and yearly irradiation at optimal tilt. (a) optimal tilt angles between the two models, (b) irradiation at optimal tilt (solid bars) and GHI (pale hatched bars), and (c) the differences between the two models for irradiation at optimal tilt (solid bars) and for GHI (pale hatched bars). For station names and locations refer to tables 2.4 and 5.2. In (b), the estimate of long-term mean yearly irradiation is depicted with error bars, and the number of years of irradiation data used in the estimate of long-term mean is shown as a white number near the bottom of the bars.

estimation tool in fig. 5.8 (European Commission, 2012b). PVGIS is a validated model that derives solar irradiance from the Meteosat satellite cloud product and calculates tilted irradiance using the Muneer model (Muneer, 1990). Additionally the PVGIS model reports GHI with a MBD of within ±5% for all but 4 BSRN and other surface irradiance measurement sites out of 23 (Huld *et al.*, 2012) whereas the Muneer (1990) tilt model gives a MBD of +5.3% and RMSD of 9.6% for vertical, south-facing planes, with considerably lower errors for 45° and 60° south-facing planes for the EU Joint Research Centre (JRC) test site at Ispra, Italy. 13 of the 27 validation sites used in section 5.6.1 fall within the spatial boundaries of PVGIS.

The comparisons do not correspond to the same time period as the PVGIS database uses data from the CM-SAF satellite products, namely Meteosat First Generation (MFG, 1998–2005) and Meteosat Second Generation (MSG, 2006–2011), and it is not stated which particular BSRN station years are used to validate these datasets (Huld *et al.*, 2012). The validation against BSRN and MIDAS ground stations uses 2013 data. The comparison with PVGIS is not a validation of the IntRad model for this reason, but a sense-check against a widely-used tilted irradiance database. Where possible, an estimate of the long-term mean irradiation at each site has been provided.

Figure 5.8a shows that in the majority of locations the predicted annual optimal tilt angle is steeper than in PVGIS, ranging from -1° at Carpentras and Camborne to $+8^\circ$ at Toravere. Part of the differences may be due to, on average, higher horizontal irradiation values predicted from IntRad compared to PVGIS (fig. 5.8b), suggesting that IntRad predicts a lower cloud fraction or greater cloud transmission than PVGIS does in general. The effect of this is large at the three low latitude sites of Gobabeb, Tamanrasset and Izaña where in each case IntRad predicts an optimal tilt slightly steeper than the latitude location, showing the influence of the direct beam and circumsolar diffuse components of solar radiation.

Figure 5.8b compares both the irradiation at optimal tilt and the horizontal irradiation between IntRad and PVGIS. To introduce some sense of how the annual horizontal irradiation varies at each of the BSRN and MIDAS sites, the confidence interval for long-term mean annual irradiation has been estimated at each site. This was performed by using all available full years of data from BSRN, whereas for MIDAS sites years as far back as 2010 were considered. The range of estimates for long term means are shown as error bars.

The 95% confidence range is $\bar{x} \pm T_{n-1}^{-1}(0.975)\sqrt{\frac{s_x^2}{n}}$ where $\bar{x}$ is the mean yearly irradiation of n years of measurement, s_x^2 is the sample variance of these n years and $T_{n-1}^{-1}(\cdot)$ is the inverse CDF of the Student-t distribution with $n-1$ degrees of freedom. It is evaluated at 0.975 to return the positive value of the number of standard errors $\left(\sqrt{\frac{s_x^2}{n}}\right)$ from the mean for a two-tailed test. The number of years used to estimate the long-term mean is shown as a number for each station in fig. 5.8b.

For Izaña it is interesting to note that IntRad under-predicts horizontal irradiation for the 2013 calendar year quite substantially compared to the BSRN pyranometer data as shown in fig. 5.7, however the PVGIS estimate is even lower. Although the two methods are not validated against the same time period as previously mentioned, the range of likely long-term means for Izaña estimated from 6 years of observations at this site (2009–2014) is substantially higher than both the PVGIS and IntRad estimates. Therefore it can be inferred that both models find evaluating the irradiation at this site, which is both on a mountain and an island, difficult. At Toravere, it is possible that the large differences in optimal tilt between the models result from the horizontal irradiation differences. IntRad shows only a slight overestimation compared to BSRN (fig. 5.7), but the 2013 irradiation estimate from IntRad is above the long-term mean estimated range. The PVGIS estimate is within this range, towards the lower end. The combination of 2013 being a sunnier than average year alongside IntRad slightly overpredicting and PVGIS being towards the lower end of long-term estimation is likely to account for much of the differences in optimal tilt and annual irradiation at optimal tilt.

Figure 5.8c shows that in every location there is a more positive difference in the irradiation at optimal tilt than the GHI between IntRad and PVGIS. This effect is seen even at Carpentras and Camborne where optimal tilt estimated by IntRad is more horizontal that in PVGIS, indicating a difference between the Muneer tilt model used in PVGIS and the integrated radiance method. This is supported by the Dunstaffnage site where PVGIS predicts a higher annual GHI total but lower irradiation at optimal tilt.

5.6.3 Comparison with isotropic and Klucher tilt models

One of the drawbacks at present to the IntRad model is the computational time needed to produce a year of data for each site. In fig. 5.9, the IntRad model is compared to the Klucher model introduced in eq. (5.3) and the Liu-Jordan isotropic diffuse model. In Gueymard (2009), the Klucher model was validated against minutely pyranometer data from the NREL site at 40°S and 90°S tilts, where for all-sky conditions the MBD was -1.4% and 0.3% respectively. These differences are much smaller than the 5.5% and 5.4% shown by the IntRad model for the same site (table 5.3), however this should be expected owing to the fact that minutely pyranometer data was used in Gueymard (2009) and the input data from IntRad are from 8-day averages of twice-daily measurements.

The Klucher and isotropic irradiation values are taken from the direct and diffuse horizontal irradiance outputs provided by libRadtran, so they will be slightly different to the values measured by a pyranometer that would typically include the 2.5° region around the sun as DNI. For most locations, the Klucher and IntRad models do not differ greatly in either total irradiation or calculated optimal tilt angle. The principle exceptions to this are at the high-latitude Ny-Ålesund station and the mountaintop Sonnblick station. At Ny-Ålesund, the isotropic model is a good approximation which is likely due to the high frequency of overcast conditions at this site (compare to Alert, at higher latitude, but much greater yearly irradiation, as previously discussed). At Sonnblick, it is not known why the IntRad tilted irradiation profile is close to the isotropic and not the Klucher, but as the weather station is located at a mountaintop, this could have an effect.

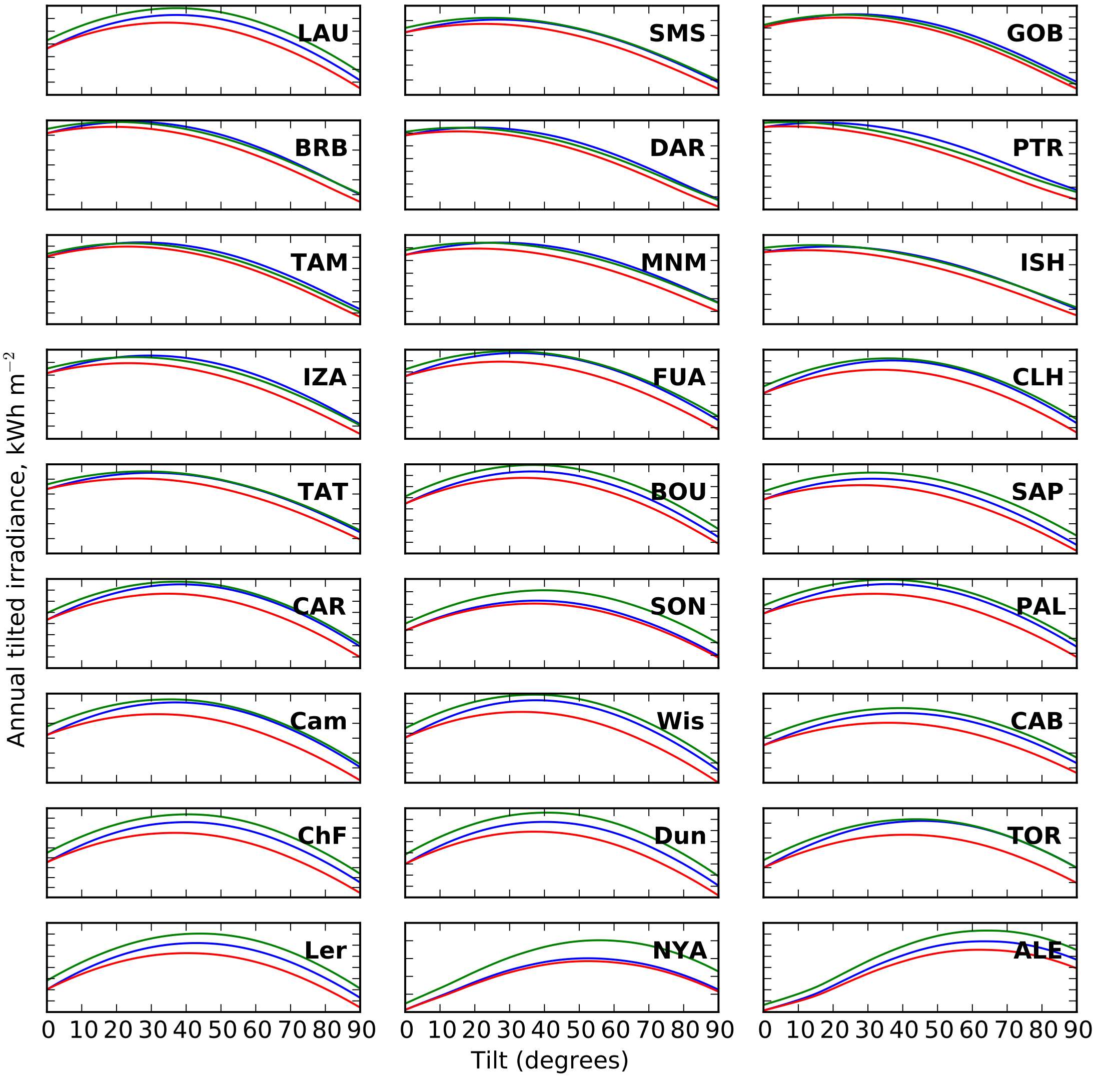

Figure 5.9: Comparison of the IntRad (blue), Klucher (green) and isotropic (red) tilt models for the 27 BSRN and MIDAS sites used in the validation ordered from south to north.

5.7 Applications, improvements and limitations

The integrated radiance method is possible to evaluate globally as the satellite retrieval data from MODIS has global coverage. The method is applicable to any dataset in which aerosol parameters, ozone, water vapour, cloud liquid water path, cloud ice water path and cloud fraction are available. The necessary inputs to the model also exist in meteorological reanalysis and climate models. The aerosol parameters are available in MODIS but often suffer from large gaps in data, so in the IntRad model they are obtained from the GLOMAP global aerosol model. Aerosol reanalysis datasets such as MACC (`http://apps.ecmwf.int/datasets/data/macc-reanalysis`), which assimilates observations and forecasts into a consistent gridded dataset in a similar way to ECMWF, can be used. Thus, the integrated radiance model can be used for determining a realistic optimal tilt for an arbitrary climatic condition, and solar energy resource calculated on this basis.

It should be mentioned that MODIS satellite retrievals are not always available or are of low quality. The limit of MODIS orbital tracks are at 82° N/S, and for latitudes greater than 77° N/S the satellite tracks overlap. Successive retrievals may not be independent and observational nadir angles may be higher towards the poles as the satellites do not overpass above/below 82° N/S (Hubanks *et al.*, 2008). On the other hand, these regions are currently unimportant for solar energy generation.

In many regions, clouds are the largest input uncertainty because the radiative properties of aerosols, water vapour and ozone are less significant when the entire solar spectrum is considered. The direct and diffuse radiation fields are spectrally dependent (Forster & Shine, 1995) and although a spectral calculation is performed and then integrated over all solar wavelengths to obtain broadband irradiance, the spectrally-dependent irradiance was not considered. When applied to assessing the energy output of PV technologies, spectral considerations will be shown to be important in the next chapter. This could affect the optimal PV tilt angle.

It is possible to improve the spatial and temporal resolution of the results obtained. MODIS Level 3 8-day mean data has been used in this model for atmosphere and albedo. Level 3 data is available daily, the use of which may improve accuracy at the expense of an 8-fold increase in computational time. Greater accuracy may be obtained by using the Level 2 satellite swath data, which has a nadir resolution of 1 km and will usually overpass a location at least once per day, although there are small gaps in the satellite overpass tracks near the equator that are not covered every day by the Level 2 or Level 3 daily data. Geostationary satellites such as Meteosat, which are used in the PVGIS procedure, can provide a higher spatiotemporal resolution than MODIS and may help to improve the diurnal performance of the model.

It is shown however that for locations at low and moderate altitude and latitude, sufficient agreement for horizontal and equator-facing tilts for yearly irradiation is obtained with the 8-day data. To use higher resolution data will require many more radiative transfer simulations per location per year, and will need the use of pre-calculated lookup tables or a multi-variable regression fit to allow swifter calculation of the radiance fields. It is currently infeasible in terms of computational time to run a yearly simulation using the IntRad method for each grid cell of a global grid which would prevent it being used in its current form for optimising tilt angle in climate studies, as would be intended for use in chapters 6 and 7 of this thesis. By systematically varying input variables, for example cloud fraction, cloud water path, surface albedo, water vapour, ozone content and solar zenith angle over a range of feasible values, the radiance values at each 10°×

3° bin can be interpolated from lookup table values given a suitable interpolation system. As the input parameter space is multi-dimensional, this may still require a prohibitive number of radiative transfer calculations to build a lookup table. An alternative idea may be to derive a multi-variable regression of tilted irradiance from the direct, diffuse and reflected horizontal irradiance and solar zenith and relative solar azimuth angles from the calculations already performed in this chapter, and then to compare these horizontal irradiance results from the 16-stream radiative transfer computation from DISORT to a much faster solver such as TWOSTR or RODENTS (section 2.2.6). Then, tilted radiation and optimal tilt could be derived for any situation using the horizontal irradiance outputs from the faster solver and the derived regression relationships. Both of these are areas for future investigation.

The Klucher model, in most locations, agrees well with the IntRad model presented in this chapter. It may be questioned why a complex method for calculating tilted irradiance is required when a simple geometric formula that only relies on DNI and diffuse horizontal irradiance (DHI) performs sufficiently well in a variety of cases. One application is when horizon shading becomes an issue, and the radiance distribution can be modified to take into account shading. The IntRad model has been applied in this context for urban areas by Gooding *et al.* (2015), whereas it is less easy to apply a shading correction to the Klucher model (or any other tilt model which assumes an unobstructed horizon).

5.8 Summary

In this chapter, IntRad, a computational method to calculate the all-sky irradiance on a plane of arbitrary alignment, which is globally applicable, is presented. There are two steps to the method described: the first step takes in satellite observations of the atmospheric state, including cloud fraction and cloud water content, and runs the DISORT radiative transfer code to produce both the direct radiation and the angular distribution of the diffuse radiation. The second step integrates the diffuse radiance distribution over a hemisphere with base in the plane of the angled solar collector to provide the tilted radiation estimate. The inclusion of clouds inside the first step is an advancement on other radiative transfer methods for solar energy modelling, which tend to use radiative transfer models for the clear-sky, horizontal radiation, and add in clouds as an adjustment to the clear-sky values. The integration of radiance values in the second step is, in the limit of angular bin size tending to zero, a physically exact method of determining diffuse radiation on a plane of arbitrary tilt and orientation, and an improvement on empirical tilt models that are currently used in the literature. Errors are introduced by (1) differences in the satellite values of the atmospheric state compared to the real conditions, including the 1D representation of clouds in the model compared to 3D clouds in reality; (2) parameterisations and discrete layering of the atmosphere used in the radiative transfer code compared to the real atmosphere and real transfer of radiation; (3) the discrete sum of the $10^\circ \times 3^\circ$ angular bins used compared to the real-world situation of a continuous variation in radiance with sky position.

The horizontal irradiation predicted by the IntRad model is compared to contemporaneous pyranometer data from MIDAS and BSRN and agrees to within ±10% for all but 3 sites out of 27. The MBD between the IntRad method and BSRN/MIDAS across all sites is +0.56% and RMSD is 6.69% for horizontal irradiance. When validated against the NREL tilted irradiance dataset the IntRad model predicts the annual irradiation within ±6% for all orientations except 90°N. The magnitude of error for tilted irradiance on 40° and 90° south-facing planes is similar to that for horizontal irradiance. The Klucher model provides a better estimate of the annual irradiation at the NREL site than IntRad in Gueymard (2009), however minutely direct and diffuse radiation data from pyranometers located at the NREL site was used to derive the tilted radiation from the Klucher model compared to one morning and one afternoon observation averaged over an 8-day period for a $1^\circ \times 1^\circ$ grid square, so the results are likely to be improved owing to the higher time resolution of input data. The diurnal variation in prevailing weather conditions is partially captured by analysis of the difference between east- and west-facing estimates of annual irradiation compared to pyranometer measurements at the NREL site, although underestimated. Due to a lack of high-quality tilted irradiance measurement stations, it is not possible to validate against tilted irradiance measurements globally, but the validated PVGIS model is used as a comparison. The main differences between the model and the Muneer (1990) tilt model used in PVGIS are the steeper optimal tilt angles and more positive relative differences between tilted irradiation and horizontal irradiation. In mid-latitude and low-to-moderate altitude sites, where PVGIS has been validated, the models produce similar results. In order to draw more robust conclusions about the optimal tilt angle from the model, a larger network of tilted irradiance measurements would be required. However, the limited model comparisons and validations show that the model produces sensible results and could be applied where ground measurements of tilted irradiance are not available.

The optimal tilt angle at a particular location is dependent on the meteorological conditions and cannot be related to a single parameter. A radiative transfer simulation is run to produce a ground-level radiance field, which is numerically integrated over the tilt angle of interest. The required inputs of cloud liquid water path, cloud ice water path, cloud fraction, temperature, ozone, water vapour and surface albedo are standard variables from satellite observations, meteorological reanalysis or climate model data. Any scheme that provides the aerosol phase function, optical depth and single scattering albedo can be used for aerosols.

Chapter 6

Future climate effects on spectral transmission of irradiance

In chapter 5, a method to calculate horizontal and tilted irradiance from radiative transfer methods was described. The radiative transfer procedure includes clouds and is not just limited to clear sky. It was shown that the method compares well to horizontal irradiation measurements from the MIDAS and BSRN networks.

This chapter extends the work described so far in two ways. First, it considers the spectral irradiance instead of the broadband irradiance. This is more applicable to PV with the differing spectral responses of semiconductors to light of different wavelengths. Secondly, it introduces a future climate scenario, whereas all of the work performed up until this point consider the present or recent past. It is shown in this chapter that changes in c-Si solar PV output could be more than ±20% different to present, in some locations. Some materials fare better or worse than c-Si due to spectral and temperature coefficient effects, and in general the higher the bandgap energy of a PV cell, the better it performs in a future climate compared to present.

Following a review of previous studies on the effect of climate change on solar energy and ways of assessing spectral impacts, the climate variables and solar cell model used to calculate solar energy output is introduced. The effect of each climate variable (clouds, water vapour, aerosols and temperature) on different PV semiconductor materials is investigated. The global changes expected under one run of the HadGEM2-ES climate model under RCP8.5 compared to the recent past, for a variety of semiconductor materials, is presented. Finally the appropriateness of using the HadGEM2-ES climate model as a representative of the population of climate models for this study is discussed.

6.1 Background and literature review

It is well-established that substitution of fossil-fuel energy generation with renewable technologies such as PV is one of a number of strategies to mitigate the effects of climate change. Somewhat less investigated is how changes to the climate itself affects the availability of renewable resources. Wind, solar, hydroelectric and wave power are all dependent to a greater or lesser extent on weather and climate (Harrison & Wallace, 2005; Seljom *et al.*, 2011). If a transient time period is considered it could be argued that biomass resources are also dependent on how the climate evolves over the next few decades and the suitability of feedstocks to adapt and thrive in conditions that may be very different to present.

6.1.1 How climate change affects solar energy

There is a small but growing body of literature that investigates how climate change could affect solar energy (table 6.1). The previous studies can be divided into two groups: those that analyse the changes in global output using global climate models (GCMs)[1], and those that analyse domains ranging from country to continent scale in regional climate models (RCMs), at higher spatial resolutions than GCMs.

Global climate models

Crook *et al.* (2011) assessed the global potential for PV and CSP from changes in solar insolation, cloud cover and temperature predicted from the UK Met Office HadGEM1 and HadCM3 climate models under the SRES A1B narrative. They showed that solar PV resource is expected to increase in Europe, the Eastern US and northwestern parts of Latin America and decrease almost everywhere else. The observed changes in PV output range from around -18% in the Himalayas to $+8\%$ in Eastern Europe. Wild *et al.* (2015) undertook a similar exercise using all 39 available models from CMIP5 over the time period of 2006–2049 using the reference period of 2006–2015. They analysed the annual percentage difference in solar PV energy output across the world, finding an expected median increase of up to 1% per decade in southeast China, Japan, and Europe under the RCP8.5 scenario. Decreases of between 1–2% per decade are expected in the boreal regions of North America and Russia with smaller decreases in the western US, northwestern China, and India. The sign of the changes by region predicted by Wild *et al.* (2015) are mostly coincident with the Crook *et al.* (2011) study. The use of 39 models allows determination of statistical significance, and some regions of low-to-moderate future changes in PV seen in Crook *et al.* (2011) for HadGEM1 were not found to be significant in the ensemble of 39 models in Wild *et al.* (2015). If the rates of change in solar power output from the Wild

---

[1] Originally the acronym GCM stood for General Circulation Model which represented the dynamics of the atmosphere and ocean. As models have become more sophisticated over the years, further components such as atmospheric chemistry, the carbon cycle and sea-ice have been included. Strictly speaking this superset of climate models are called Earth System models, but Global Climate Models can be used as a catch-all term to represent both types of model.

Study	Region	Output	Climate model	Scenario	Future	Baseline
Crook *et al.* (2011)	Global	PV, CSP	HadGEM1, HadCM3	SRES A1B	2080–2100	1985–2005
Wild *et al.* (2015)	Global	PV	All 39 models used in CMIP5	RCP8.5	2006–2049	1985–2005
Pan *et al.* (2004)	US	Solar radiation	RegCM2 forced from HadCM2	1% per year CO_2	2040–2049	1990–1999
Pašičko *et al.* (2012)	Croatia	PV	RegCM forced from ECHAM5	SRES A2	2011–2040, 2041–2070	1961–1990
Burnett *et al.* (2014)	UK	Solar radiation	UKCP09	SRES B1, A1B, A1FI	2040–2069, 2070–2079	1961–1990
Gaetani *et al.* (2014)	Europe, Middle East, Africa	PV	ECHAM5-HAM	SRES B2 with IIASA aerosol scenarios	2030	2000
Panagea *et al.* (2014)	Greece	PV	ENSEMBLES	SRES A1B	2011–2050, 2061–2100	1950–2000, 1985–2005

Table 6.1: Summary of previous studies of climate change effects on solar energy

et al. (2015) study for statistically significant regions are maintained and extrapolated to the timescale of the Crook *et al.* (2011) study (about 95 years), the overall results between the two studies are of comparable magnitude.

Regional climate models

Pan *et al.* (2004) assessed changes under the 1% per year CO_2 increase experiment for solar radiation in the US. 1% per year CO_2 is often used as a climate model diagnostic rather than a representation of a likely climate outcome, although it can nevertheless provide some useful information about a model's response. For example, no aerosols are included, which are an important attenuator for clear-sky radiation. The 1% CO_2 is a relative, compound year-on-year increase such that a doubling of CO_2 occurs in 70 years ($1.01^{70} \approx 2$). The RegCM2 RCM, which has a spatial resolution of 52 km, was used with boundary conditions provided by an earlier, coarser-resolution Met Office GCM, HadCM2. Over a 50-year time period, the change in solar radiation over the contiguous US was estimated to decrease in most places, by up to 20% in the west, with small increases in the southeast. For the south and east US this trend is confirmed by Wild *et al.* (2015) for CMIP5 models due to a reduction in cloud fraction in these areas although the negative result predicted for the rest of the US is less significant. A reduction in radiation expected in the western US could be due to the HadCM2 model used to force the RCM: Crook *et al.* (2011) shows a large reduction in insolation for the western US for HadGEM1 (another Met Office GCM), with similar results reported for HadCM3.

Pašičko *et al.* (2012) details a variety of climate-related factors that can affect the change in PV power output, namely temperature, precipitation, GHI, snow cover, extreme weather and wind. Using the SRES A2 scenario coupled to a regional climate model, and outputs of temperature and total cloud fraction, they use a temperature-efficiency relationship (e.g. eq. (2.44)) and assume that GHI increases in proportion to the amount that cloud fraction reduces. When combined with other factors, Pašičko *et al.* concludes that solar energy in Croatia will remain broadly the same as present, but do not quantify any of the factors except for the separate effects of changes in GHI (+2%) and temperature (−4%).

Gaetani *et al.* (2014) assessed three aerosol emission scenarios from the ECHAM5-HAM climate model under the SRES B2 climate change simulation, showing that the changes in PV energy output for 2030 compared to 2000 depend strongly on the aerosol assumption used. The lowest aerosol scenario of maximum feasible reduction leads to decreases in PV output of over 5% in the central belt of Africa, Saudi Arabia and western Russia but an increase of more than 5% in western Europe. Under the higher aerosol level of constant year 2000 levels, the magnitude of the changes is lower except for central and eastern Europe which experience PV output declines of 5% or more. Although running a GCM, output was only provided for spatial regions covered by the PVGIS online software tool (Huld *et al.*, 2012) (Europe, the Middle East and Africa) as PV panel tilt angle was optimised according to the PVGIS method. The Muneer tilt model, which is used in the PVGIS method, requires inputs of diffuse irradiance. Diffuse irradiance was considered by the authors, but as ECHAM5-HAM does not provide the diffuse-to-global ratio, the diffuse irradiance has to be estimated from monthly climatologies.

Burnett *et al.* (2014) used the UK Met Office UKCP09 5 km × 5 km probabilistic model to assess future broadband solar irradiance for the United Kingdom. UKCP09 is driven by one of three emissions scenarios termed "high", "medium" and "low", which correspond respectively to SRES A1FI, A1B and B1. The probabilistic model gives the 10%, 50% and 90% values from the distribution of future solar irradiance changes. The baseline data was taken from radiation observations from 18 MIDAS stations. Burnett *et al.* show that future solar resource is expected to increase over the majority of the UK for both the 2050s and 2080s future time horizon. The changes range from a 6.8% increase in the south-east of England to a 0.3% decrease in the north of Scotland for the 2080s, medium emission scenario at the 50% point of the distribution.

Panagea *et al.* (2014) used five European RCMs from the ENSEMBLES project at a spatial resolution of $0.25^\circ \times 0.25^\circ$ to predict changes in PV output in Greece. Over the period 2061–2100 the mean predicted changes vary from -2% in the east of the country to $+3\%$ in the west compared to baseline PV output calculated from 1950–2000 temperature and 1985–2005 irradiance observations. However, the uncertainty spread between the five models is large, up to 12%, and the models do not always agree on the sign of the change for each region.

6.1.2 An extension to spectral irradiance

The most important factors for solar PV energy are solar irradiance and solar cell temperature. It was shown in chapter 5 that irradiance is dependent on the transmission of the atmosphere and is influenced by clouds, aerosols, water vapour, ozone and mixed gases. Cell temperature is affected by irradiance and ambient temperature as shown in eq. (2.45). All of the previous studies into climate change effects on PV energy output consider broadband irradiance. Alongside the global (total) irradiance and its direct and diffuse components, there is the possibility that climate change will affect the spectral distribution of irradiance, through changes in water vapour, clouds and aerosols. As PV cells are made from semiconductor materials which exhibit differing responses at different wavelengths, the future solar resource will be spectrally dependent.

Zdanowicz *et al.* (2005) considered optimising the semiconductor bandgap for different values of air mass. These considerations can be extended by also optimising for climate.

There are several ways to assess the quality of the solar spectrum and its suitability for different semiconductor materials, which are reviewed briefly in the remainder of this section.

Average photon energy

One measure of the spectral distribution of irradiance is the average photon energy (APE) (Betts, 2004) which is defined as:

$$E_{\mathrm{APE}} = \frac{\int_a^b G_\lambda(\lambda)\,\mathrm{d}\lambda}{q\int_a^b N(\lambda)\,\mathrm{d}\lambda} \tag{6.1}$$

where a and b are the upper and lower limits of the wavelength integration, G_λ is the spectral irradiance, q is the elementary charge (1 eV by definition) and N is the number of photons of a particular wavelength arriving.

The higher the value of APE, measured in eV, the more "blue-shifted" and energetic the spectrum is. Behrendt *et al.* (2013) used a radiative transfer simulation to investigate the changes in APE to varying atmospheric components. Increases in cloud optical depth and precipitable water vapour increase APE, increasing aerosol optical depth (for a rural aerosol) decreases APE, and an increase in air mass and solar zenith angle due to greater Rayleigh scattering path length decrease APE slightly.

The APE measure benefits from the simplicity of characterising the spectral properties with a single number in units of eV. On the downside, APE does not provide a method to reproduce the actual shape of the solar spectrum (an extreme example is provided in Minemoto *et al.* (2009)) and secondly, the APE value depends on the upper and lower wavelength limits a and b over which the solar spectral irradiance is integrated. For example, the full solar spectrum as received on the earth's surface contains photons ranging from about 290–4000 nm, and most measurement devices do not measure the whole spectrum. If APE is reported on a much narrower range such as the 350–1050 nm range used by Minemoto *et al.* (2009), important spectral information at higher wavelengths, which is useful for lower bandgap semiconductors, is absent.

Useful fraction

The useful fraction (UF) (Gottschalg *et al.*, 2003) considers the portion of the solar spectrum that can be converted by a semiconductor to the total broadband spectrum:

$$f_{\mathrm{UF}} = \frac{\int_{\lambda_{\min}}^{\lambda_{\max}} G_\lambda(\lambda)\,\mathrm{d}\lambda}{\int_{290}^{4000} G_\lambda(\lambda)\,\mathrm{d}\lambda} \tag{6.2}$$

The limits of the integral in the denominator are in nm. For each semiconductor material, the lowest and highest photon wavelengths that can be converted into current by the semiconductor are represented by $\lambda_{\min}$ and $\lambda_{\max}$. Betts (2004) showed that there is a very good correlation between UF and APE, and that the correlation is material-dependent. The higher the bandgap of the material in energy terms, the lower the useful fraction.

Spectral mismatch factor

The APE and UF can be useful metrics to characterise the spectrum. However, they do not convey any information about how well a semiconductor converts photons of a particular wavelength.

An alternative measure is the spectral mismatch factor (SMM) (Nofuentes *et al.*, 2014) which compares the ratio of short-circuit current delivered by a particular semiconductor material under the incident spectrum G_λ to the short-circuit current that would be delivered under the ASTM-G173 AM1.5 spectrum $G_{\lambda,\mathrm{STC}}$. Formally,

$$f_{\mathrm{SMM}} = \frac{\int_a^b G_{\lambda,\mathrm{STC}}(\lambda)\,\mathrm{d}\lambda \int_a^b G_\lambda(\lambda) S(\lambda)\,\mathrm{d}\lambda}{\int_a^b G_\lambda(\lambda)\,\mathrm{d}\lambda \int_a^b G_{\lambda,\mathrm{STC}}(\lambda) S(\lambda)\,\mathrm{d}\lambda}. \tag{6.3}$$

$S(\lambda)$ is the wavelength-dependent spectral response of the solar cell, which is defined in section 6.3. In summary, if $f_{\mathrm{SMM}} > 1$, there is an effective gain in power output under the incident spectrum compared to the AM1.5 STC and an effective loss if $f_{\mathrm{SMM}} < 1$. SMM takes into account both the spectrum and the semiconductor material dependence.

Dirnberger *et al.* (2015) showed the SMM increased with increasing semiconductor bandgap when taking $3\frac{1}{2}$ years of spectral irradiance and PV module output measurements in Germany. They showed that the gain in output energy for a particular spectrum compared to the ASTM-G173 AM1.5 spectrum does not always correspond in a one-to-one fashion to APE which can return the same value for different spectrum shapes.

For the study presented in this chapter, the definition of the SMM is altered to compare the differences in solar PV output between two climate scenarios instead of the differences between a measured spectrum and the AM1.5 STC spectrum. The solar spectrum can vary depending on the constituent atmospheric state, which is different between past and future climate runs. The SMM defined to compare past and future climate is referred to as the spectral climate change factor (SCC) and is defined such that

$$f_{\mathrm{SCC}} = \frac{\int_a^b G_{\lambda,\mathrm{past}}(\lambda)\,\mathrm{d}\lambda \int_a^b G_{\lambda,\mathrm{future}}(\lambda) S_{\mathrm{future}}(\lambda)\,\mathrm{d}\lambda}{\int_a^b G_{\lambda,\mathrm{future}}(\lambda)\,\mathrm{d}\lambda \int_a^b G_{\lambda,\mathrm{past}}(\lambda) S_{\mathrm{past}}(\lambda)\,\mathrm{d}\lambda}. \tag{6.4}$$

Furthermore, the spectral response of semiconductors is dependent on the temperature of the semiconductor, which is in turn a function of irradiance and ambient temperature. These changes are built-in to SCC by allowing $S(\lambda)$ to vary with semiconductor temperature. The role that climate plays in past and future spectral irradiances and spectral responses is described in section 6.3.

The detailed balance limit (Shockley & Queisser, 1961) suggests that the ideal bandgap is in the range of about 1.0–1.7 eV for single junction solar cells, and is a tradeoff between utilising the greatest possible part of the solar spectrum (lowest energy bandgap) versus the increased output power per absorbed photon (highest energy bandgap). The focus is on five popular PV semiconductor materials with bandgaps in this region (c-Si, GaAs, $CuInSe_2$, $CuGaSe_2$ and CdTe), plus InGaP and Ge which are outside this range but often used in high efficiency triple-junction concentrating PV cells (Yamaguchi *et al.*, 2008). The global PV output for the solar spectrum over the 2080–2100 timeframe is evaluated compared to PV output for the 1985–2005 solar spectrum using c-Si as a baseline and comparing other materials relative to c-Si.

6.2 Climate variables

In this chapter the solar PV resource in both the RCP historical (for 1985–2005) and RCP8.5 (for 2080–2100) simulations of the UK Met Office HadGEM2-ES climate model is investigated.

The variables of interest (table 6.2, top) are extracted from run 5 of the historical and run 4 of the RCP8.5 experiments of the HadGEM2-ES model. Each run (ensemble member) of a climate model is initialised from a different point in the past of a model control run (Jones *et al.*, 2011) which provide the initial conditions for each realisation. Internal variability inside the model control run, and sensitivity to even small perturbations in the initial conditions, ensure that each realisation is sufficiently independent.

The bottom section of table 6.2 details the variables that have been extracted from runs 1–4 of the historical and RCP8.5 experiments, which are used for optimising tilt angle and evaluation of climate model spread.

Variable	CMIP5 name	Name
Aerosol optical depth at 550 nm	od550aer	τ_{a550}
Aerosol optical depth at 870 nm	od870aer	τ_{a870}
Total cloud fraction	clt	f_c
Cloud condensed (liquid plus ice) water path	clwvi	p
Cloud ice water path	clivi	p_i
Cloud-top effective droplet radius	reffclwtop	$r_{\mathrm{eff},l}$
Precipitable water vapour	prw	w
Daily Maximum Near-Surface Air Temperature	tasmax	$T_{\max}$
Daily Minimum Near-Surface Air Temperature	tasmin	$T_{\min}$
Surface downwelling shortwave radiation	rsds	$G\cos\theta_z$
Top-of-atmosphere downwelling shortwave radiation	rsdt	$G_0\cos\theta_z$

Table 6.2: Variables from HadGEM2-ES used in spectral irradiance simulations.

The Delta-Eddington two-stream radiative transfer model RODENTS (section 2.2.6) is run using the variables provided by the climate model. RODENTS is used instead of the TWOSTR solver because of the occasional errors found in the latter when using optically thick clouds at high zenith angle. The tradeoff is that RODENTS does not include a pseudospherical correction so contributions from hours with low solar elevations may be underestimated, however, since relative changes are of interest and the 360-day nature of the HadGEM2-ES model means that the solar geometry is the same in the past and future runs, this should not affect the results. A two-stream solver must be used to keep the computational times reasonable (on the order of one day for the whole world for each climate run). In chapter 4, TWOSTR was a better choice as the pseudospherical correction was important and clouds were not included in the radiative transfer calculations.

The AFGL US standard atmosphere is specified to determine the molecular scattering and absorption for mixed gases and ozone. While ozone absorption is important in the UV part of the spectrum, the spectral response function $S(\lambda)$ of solar cells is low in the UV region. Additionally, CMIP5 does not provide ozone concentration as a model output for HadGEM2-ES. Therefore no change in the baseline ozone level has been assumed.

Adjustments to the baseline clear-sky atmosphere are made by varying the precipitable water vapour column w [mm] and aerosol optical depths (AOD) at 550 nm and 870 nm, τ_{a550} and τ_{a870}. The rural aerosol model of Shettle (1989) is used which accounts for the single-scattering albedo and phase function parameters by wavelength. While an aerosol model that prescribes single-scattering albedo and phase function would be desirable in order to fully characterise aerosol properties, it is not provided by the list of output variables from CMIP5. Clearly it would not be possible to investigate changes in aerosols if a climatology such as GLOMAP is used in this study.

When two optical depths at different wavelengths are known, the aerosol optical depth $\tau_{a\lambda}$ at wavelength λ can be modelled according to the Ångström relationship (Ångström, 1929):

$$\frac{\tau_{a\lambda}}{\tau_{a550}} = \left(\frac{\lambda}{550}\right)^{-\alpha} \tag{6.5}$$

$$\alpha = -\frac{\log(\tau_{a870}/\tau_{a550})}{\log(870/550)}. \tag{6.6}$$

This allows the aerosol optical depth to be determined across all wavelengths of the solar spectrum which is necessary for spectral irradiance calculations.

Clouds are introduced by considering the total cloud liquid water path and cloud ice path [kg m^{-2}] from HadGEM2-ES. The ice and liquid water paths are converted to 1 km thick plane-parallel clouds with bases of 1 km above the ground. The total cloud liquid water path p_l is the difference of the total water path and ice water path, i.e. $p_l = p - p_i$. Cloud water paths are reported over the entire grid cell. So to determine the cloud water path of the cloudy column these numbers are divided by the cloud fraction f_c. By assuming a 1000 m cloud geometric height, the cloud water paths in kg m^{-2} correspond to cloud water content in g m^{-3} for input into libRadtran.

As in chapter 5, a two-column approximation is then used to weight the contributions from the clear and cloudy portions of the grid square in the radiative transfer calculation. For liquid clouds, the top-of-cloud effective droplet radius is a CMIP5 output and has been included to compare between the future and past scenarios; there is no indication of ice cloud crystal size provided, so the ice effective radius of 30 µm is used (Rossow *et al.*, 1996). The optical depth, phase function and single scattering albedo as a function of wavelength is determined by the parameterisations of Hu & Stamnes (1993) for liquid clouds and Fu (1996) for ice clouds. Optical properties at wavelengths other than 600 nm are determined by the Hu & Stamnes and Fu relationships.

The radiative transfer calculation is run for each daytime hour of the afternoon, starting at 12:30pm local solar time, at each grid square. The results are extended to the morning assuming symmetry as only monthly average climate variables are available. The solar declination on the 16th day of each month is used. From these assumptions the solar zenith angle is easily calculated from eqs. (2.2) to (2.4). Daytime is defined as any moment where the solar zenith angle is less than 90°.

For global simulations, the correlated-*k* method is used to calculate spectral transmission (section 2.2.7). For investigating the sensitivity to PV output with spectrum changes, the REPTRAN parameterisation at a resolution of 5 points cm^{-1} is used (Gasteiger *et al.*, 2014). The REPTRAN method approximates a line-by-line calculation. In the global simulation, the spectral direct and diffuse spectral irradiance fluxes $G_B(\lambda)$ and $G_D(\lambda)$ [W m^{-2} nm^{-1}] are calculated from the radiative transfer model for each land grid point and month in the time periods considered.

The PV cell temperature is a function of ambient temperature and influences the PV cell efficiency (eq. (2.44)). To calculate the monthly average daytime temperature T_a the approach of Crook *et al.* (2011) is used where temperature is assumed to vary sinusoidally over the course of the day with a maximum at midday and a minimum at midnight. Without any further information as to how diurnal temperatures evolve at different times of the day, at different parts of the world and in past and future climates, it is not clear that a more complicated assumption is warranted. The evolution of temperature can be described by

$$T_a = \frac{T_{\max} + T_{\min}}{2} + \frac{T_{\max} - T_{\min}}{2} \cos(h) \tag{6.7}$$

where h is the hour angle (0° at midday and 180° at midnight). In the global simulations, the first calculation performed at 12:30pm corresponds to $h = 7.5°$ with successive hours increasing by 15°.

In fig. 6.1, the difference between the historical 1985–2005 and RCP8.5 2080–2100 runs of HadGEM2-ES are shown for f_c, τ_c, $r_{\mathrm{eff},l}$, w, τ_{a550}, τ_{a870}, $G \cos\theta_z$ and average daytime temperature $T_{\mathrm{day}} = (3T_{\max} + T_{\min})/4$. Cloud fraction (fig. 6.1a) shows a tendency to increase at both poles but decreases at most mid-latitude and tropical regions. Cloud optical depth (fig. 6.1b) increases by the most extreme amount in the far northern latitudes and coastal Antarctica and is positive over most of Asia and northern Europe. Decreases in cloud optical depth are seen in the Mediterranean area, southern Africa, Australia, the eastern US and the northeastern region of South America among other places. Positive changes in cloud liquid droplet effective radius are seen in Europe, northeastern US and the Far East (fig. 6.1c). Water vapour shows the greatest increases in tropical regions (fig. 6.1d) but is positive everywhere. Aerosol optical depth increases strongly over western central Africa, eastern Africa, the Himalayan region and Australia whereas it decreases strongly in eastern China (fig. 6.1e and f). One consequence of a reduced aerosol loading is larger cloud droplets, and there is a rough correspondence between reduction in aerosols and increase in $r_{\mathrm{eff},l}$. The changes in τ_{a550} are larger than changes in τ_{a870}, so that absorption by aerosols is stronger in the visible range than in the infrared. Global broadband insolation is shown for comparison in fig. 6.1g, where as it may be expected the increases in solar radiation correspond with the regions in which cloud fraction and aerosol optical depth is reduced and vice versa. Daytime land temperatures are shown to increase globally by at least 4°C, with the greatest rises occurring in the northern polar regions (fig. 6.1h).

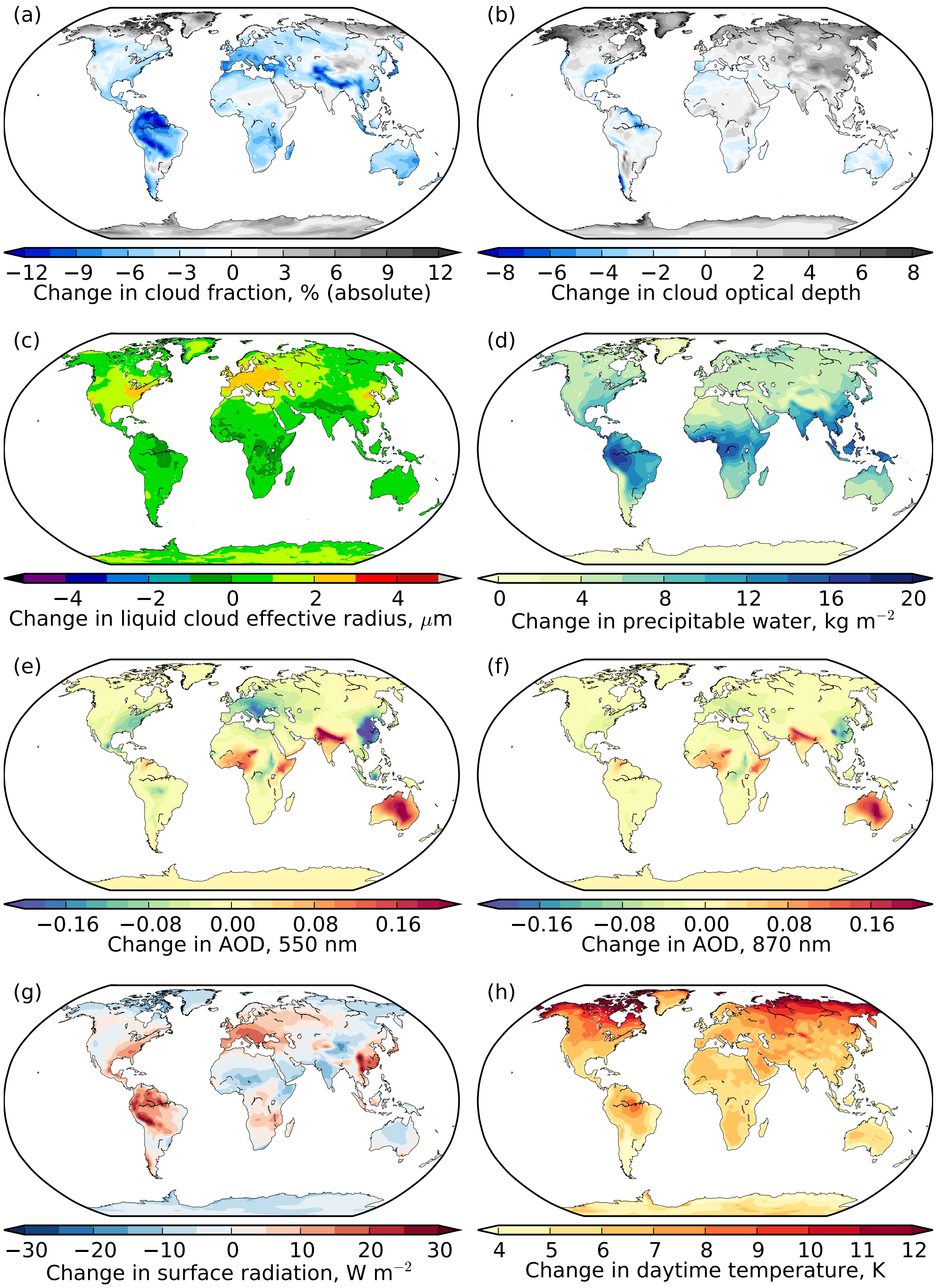

Figure 6.1: Changes in (a) cloud fraction, (b) cloud optical depth, (c) cloud droplet effective radius, (d) precipitable water vapour, aerosol optical depth at (e) 550 nm and (f) 870 nm, (g) solar insolation and (h) daytime temperature under RCP8.5, 1985–2005 to 2080–2100.

The effects of these changes are investigated on the solar cells of interest later on. Firstly it is necessary to determine how these climate variables cause spectrum changes, and prior to this, the effect of spectral irradiance on solar cell power output.

6.3 Solar cell model

When photons interact with a PV cell, electrons are excited from the valence band of the semiconductor into the conduction band. If an electric field is present within the device, electrons flow towards one side of the cell with the positive charge (the absence of an electron, or “hole”) moving the other way, generating a current. The ease of which electron-hole pairs are generated depends on the semiconductor bandgap.

6.3.1 Cell current and semiconductor bandgap

The climate variables described in section 6.2 form the inputs to the PV cell scheme (fig. 6.2). In this simulation a cell that can be modelled as an ideal diode, without losses for series and shunt resistances, and the minimum possible dark saturation current, has been assumed. The result is that the theoretical cells are close to the detailed balance limit efficiency for a single-junction cell under one sun. While this limit can never be reached in practice, it is likely that technology will continue to improve and the solar cells of 2080 will be more efficient than those available today.

The current density J and voltage V in the solar cell is modelled using the one-diode characteristic equation (Markvart & Castañer, 2005),

$$J = J_{\mathrm{ph}} - J_0 \left(\exp\left(\frac{qV}{nkT_c} \right) - 1 \right) \tag{6.8}$$

where k is the Boltzmann constant equal to 8.61×10^{-5} eV K^{-1}, q is the elementary charge, n is the diode ideality factor, T_c is the cell temperature, J_0 is the reverse saturation current density, and J_{ph} is the photocurrent density. In the ideal diode model, $n = 1$. For modelling more realistic solar cells a non-ideal diode with $n > 1$ or the two-diode model may be used. In the ideal case $J_{\mathrm{ph}} \approx J_{\mathrm{sc}}$ where J_{sc} is the short circuit current density (Markvart & Castañer, 2005) and they are taken to be interchangeable in this chapter.

J_0 is a material-dependent quantity, the choice of which has a large impact on the rates of change of open circuit voltage and fill factor with temperature (Singh & Ravindra, 2012). A number of relationships exist in the literature based on experimental fits of open circuit voltage values (Nell & Barnett, 1987) although they have only been calculated for c-Si and GaAs cells. Loferski (1956) calculated values of J_0 for c-Si, InP, GaAs and CdTe based on diffusion lengths. The parameters used to derive Loferski’s values are not applicable

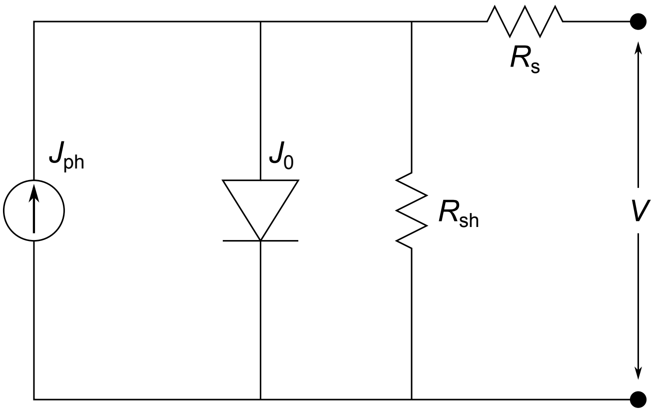

Figure 6.2: One diode schematic of solar cell. In the ideal case assumed in this chapter, the parasitic resistances are ignored so that the series resistance $R_s = 0$ and the shunt resistance $R_{sh} = \infty$.

to present day solar cells due to improvements in technical expertise. To overcome these difficulties, generalise to other materials, and to avoid choosing one particular empirical relationship over another, an ideal case is assumed where J_0 is minimised according to the detailed balance limit and the only degrees of freedom in the equation are the bandgap E_g, which accounts for the choice of semiconductor material, and cell temperature. The relevant expression is (Baruch *et al.*, 1995)

$$J_0 = \frac{q}{k}\frac{15\sigma}{\pi^4}T_c^3 \int_{E_g/kT_c}^{\infty} \frac{t^2}{e^t - 1}\,\mathrm{d}t. \tag{6.9}$$

Here, $\sigma = 5.67 \times 10^{-8}$ W m^{-2} K^{-4} is the Stefan-Boltzmann constant. The integral in eq. (6.9) is evaluated numerically.

J_{sc} depends on the cell illumination and semiconductor bandgap. The bandgap is related to temperature by the Varshni relationship (Varshni, 1967):

$$E_g(T_c) = E_g(0) - \frac{aT_c^2}{T_c + b} \tag{6.10}$$

where $E_g(0)$ is the bandgap at 0 K, and $E_g(0)$, a and b are material-dependent constants. The relevant parameters for the materials investigated in this chapter are given in table 6.3. Only photons that have higher energy (lower wavelength) than the bandgap can be converted into an electron-hole pair and contribute to the electric current. The corresponding maximum wavelength of photon conversion [nm] is given by $\lambda_g = 1240/E_g$ for E_g in eV (Singh & Ravindra, 2012).

The bandgap wavelength λ_g determines the upper limit of the external quantum efficiency (EQE) curve, $Q(\lambda)$. EQE is defined as the proportion of incident photons that are converted to charge carriers at each wavelength. State-of-the-art solar cells have EQEs that approach unity in the critical wavelength bands (Green *et al.*, 2014). A square EQE re-

Material	$E_g(0)$ [eV]	a [10^{-4} eV K^{-1}]	b [K]
Ge (Varshni, 1967)	0.7412	4.561	210
$CuInSe_2$ (Rincón *et al.*, 1983)	0.988	1.36	210
Si (mono c-Si) (Varshni, 1967)	1.1557	7.021	1108
CdTe (Allahverdi & Yükselici, 2008)	1.502	3.24	160
GaAs (Varshni, 1967)	1.5216	8.871	572
$CuGaSe_2$ (Meeder *et al.*, 2003)	1.7258	2.9	244
InGaP (Ishitani *et al.*, 1994)	1.985	7.661	544

Table 6.3: Varshni parameters for the PV materials investigated in this study. Parameters for InGaP obtained from least-squares curve-fitting from data provided in Ishitani *et al.* (1994).

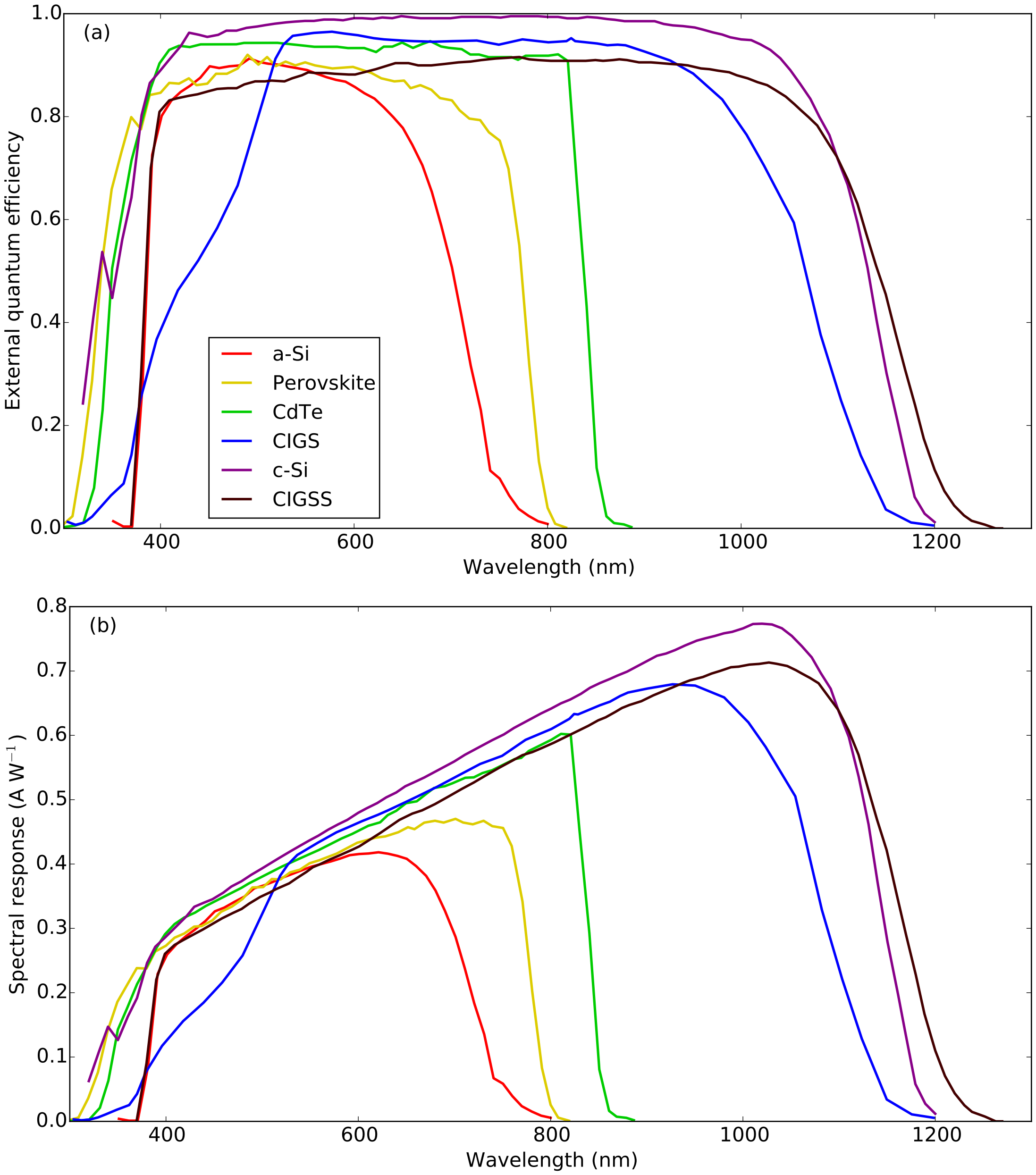

Figure 6.3: (a) External quantum efficiency and (b) spectral response curves from six current world-leading solar cells. Source: (Green *et al.*, 2014, and references therein).

sponse is assumed such that $Q(\lambda) = 0.95$ for $\lambda \leq \lambda_g$ and $Q(\lambda) = 0$ for $\lambda > \lambda_g$. In reality $Q(\lambda)$ is not uniform across wavelengths as the factors which reduce EQE such as surface reflection, electron-hole recombination, and minority carrier diffusion, are functions of wavelength. The real EQE curves for six world-leading solar cells of different material are shown in fig. 6.3a, which include perovskite, amorphous silicon (a-Si) and CuInGaSeS (CIGSS) cells not considered in this chapter. The shape of real EQE curves are also dependent on temperature, but EQE tends to only be reported for one set of ambient conditions, usually STC. Assuming a square EQE curve and allowing the upper limit of $Q(\lambda)$ to vary with temperature allows change in ambient temperature to be included in the overall effects.

The EQE is related to the spectral response of a solar cell [A W^{-1}] (Betts, 2004)

$$S(\lambda) = Q(\lambda)\frac{q}{hc}\lambda \tag{6.11}$$

where h is the Planck constant and c is the speed of light. For a constant $Q(\lambda)$ the linear dependence on λ means that longer wavelength photons with energy just above E_g contribute the most to the spectral response. This can be seen for the six real-world solar cells from the spectral response plots in fig. 6.3b. From $S(\lambda)$ the short circuit current density J_{sc} is calculated:

$$J_{\mathrm{sc}} = \int_0^{\lambda_g} G_T(\lambda)S(\lambda)\ \mathrm{d}\lambda \tag{6.12}$$

where $G_T(\lambda)$ is the spectral irradiance [W m^{-2} nm^{-1}]. For consistency with the relationship introduced earlier in eq. (6.2), the lower limit of the integration can be set to 290 nm, the shortest wavelength found to be transmitted by the atmosphere in the radiative transfer simulations.

6.3.2 Open circuit voltage

The open circuit voltage V_{oc} is calculated by setting the current density to zero in eq. (6.8) and rearranging, such that

$$V_{\mathrm{oc}} = \frac{nkT_c}{q}\log\left(\frac{J_{\mathrm{sc}}}{J_0}+1\right). \tag{6.13}$$

6.3.3 Output power

The output power density of a cell is $P = JV$ where J and V are given by eq. (6.8). As the voltage applied across the cell increases, the resulting current decreases. The point $(V_{\mathrm{mp}}, J_{\mathrm{mp}})$ corresponding to the maximum power can be found by taking $d(JV)/dV = 0$

and rearranging to obtain

$$V_{\mathrm{mp}} = V_{\mathrm{oc}} - \frac{nkT_c}{q} \log\left(1 + \frac{V_{\mathrm{mp}} q}{nkT_c}\right). \tag{6.14}$$

Equation (6.14) is implicit in V_{mp} and is solved using the Newton-Raphson numerical method. J_{mp} is found by substituting V_{mp} for V in eq. (6.8).

6.3.4 Cell temperature

It can be seen that eqs. (6.8) to (6.10) and (6.12) to (6.14) all depend directly or indirectly on cell temperature T_c. An increase in T_c narrows the bandgap according to eq. (6.10), which leads to an increase in λ_g. This allows more photons to be converted and increases J_{sc}. Conversely J_0 increases which leads to a reduction in V_{oc}. In most cases the reduction in V_{oc} outweighs the increase in J_{sc} and consequently output power decreases with increasing cell temperature. Cell temperature is a property of the energy balance of the solar cell, which includes the shortwave radiative input. A semi-empirical correlation for T_c derived by Skoplaki *et al.* (2008), using Loveday & Taki's expression for convective cooling, is

$$T_c = T_a + \frac{0.32}{8.91 + 2.00W} G_T \tag{6.15}$$

where T_a is ambient temperature, W is wind speed and G_T is the plane broadband irradiance [W m^{-2}], i.e. $G_T(\lambda)$ integrated over all wavelengths. W in this chapter is taken to be 1.0 m s^{-1} in both past and future simulations.

6.3.5 Plane irradiance

In order to calculate $G_T(\lambda)$, an assumption needs to be made about the solar module alignment. Climate models and radiative transfer calculations provide values of horizontal irradiance. As seen in chapter 5, a horizontal alignment for a solar panel is rarely optimal, particularly outside of tropical regions. A tilt angle equal to latitude fares better in general, but it still sub-optimal in areas with significant cloud. The ideal case would be to use the method developed in chapter 5 to calculate tilted irradiance and optimal tilt, but in the current non-optimised version of the tilt model, computing the optimal tilt for every point of a GCM is computationally too slow. Therefore, the Barker & Christensen (2001) optimal tilt model is used where the clearness indices are calculated from the shortwave downwelling radiation variables (rsds and rsdt, table 6.2) contained in the climate models. These are considered to be equivalent to the GHI and extraterrestrial horizontal irradiance respectively, and the clearness index is simply the ratio of the two values.

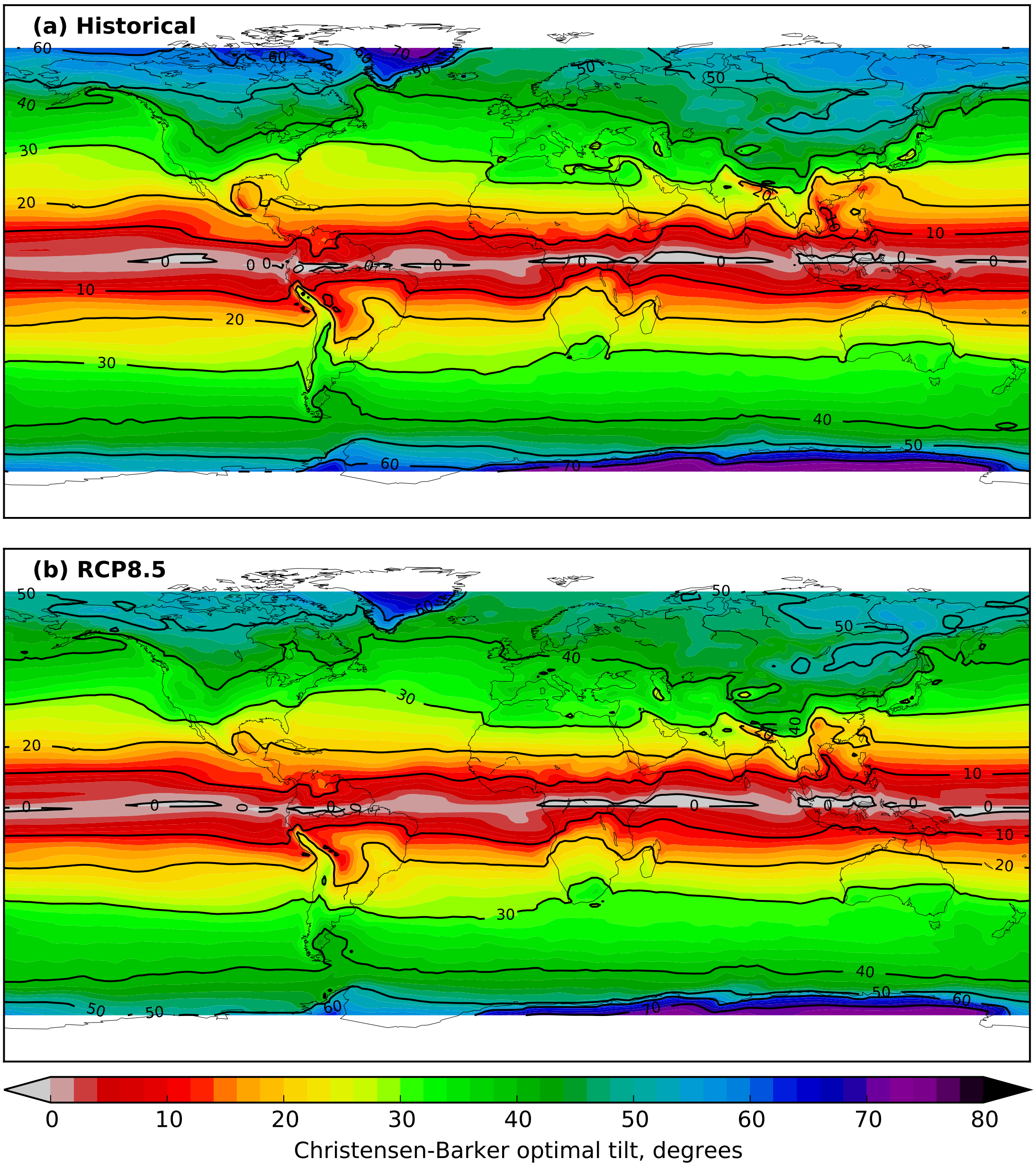

Figure 6.4: The global, equator-facing optimal tilt angle calculated from the Christensen-Barker method, using HadGEM2-ES climate model data as inputs, for (a) historical and (b) RCP8.5 simulations.

Figure 6.4 shows the optimal equator-facing tilt using the Christensen-Barker method for both the historical and RCP8.5 simulations. The clearness index is undefined for the winter hemisphere polewards of 75° in eq. (5.4) as extraterrestrial irradiance is zero. For these latitudes, the panel tilt angle is assumed to be equal to latitude.

Due to its geometrical simplicity and relatively good agreement with the IntRad method of chapter 5, the Klucher diffuse irradiance model (eq. (5.3)) is used to calculate G_T with optimal tilt angle from fig. 6.4. Exceptional accuracy in the tilted irradiance model is not justified by uncertainty in the input variables. The application of a two-stream solution (RODENTS) to the radiative transfer equation, which is itself an approximation,

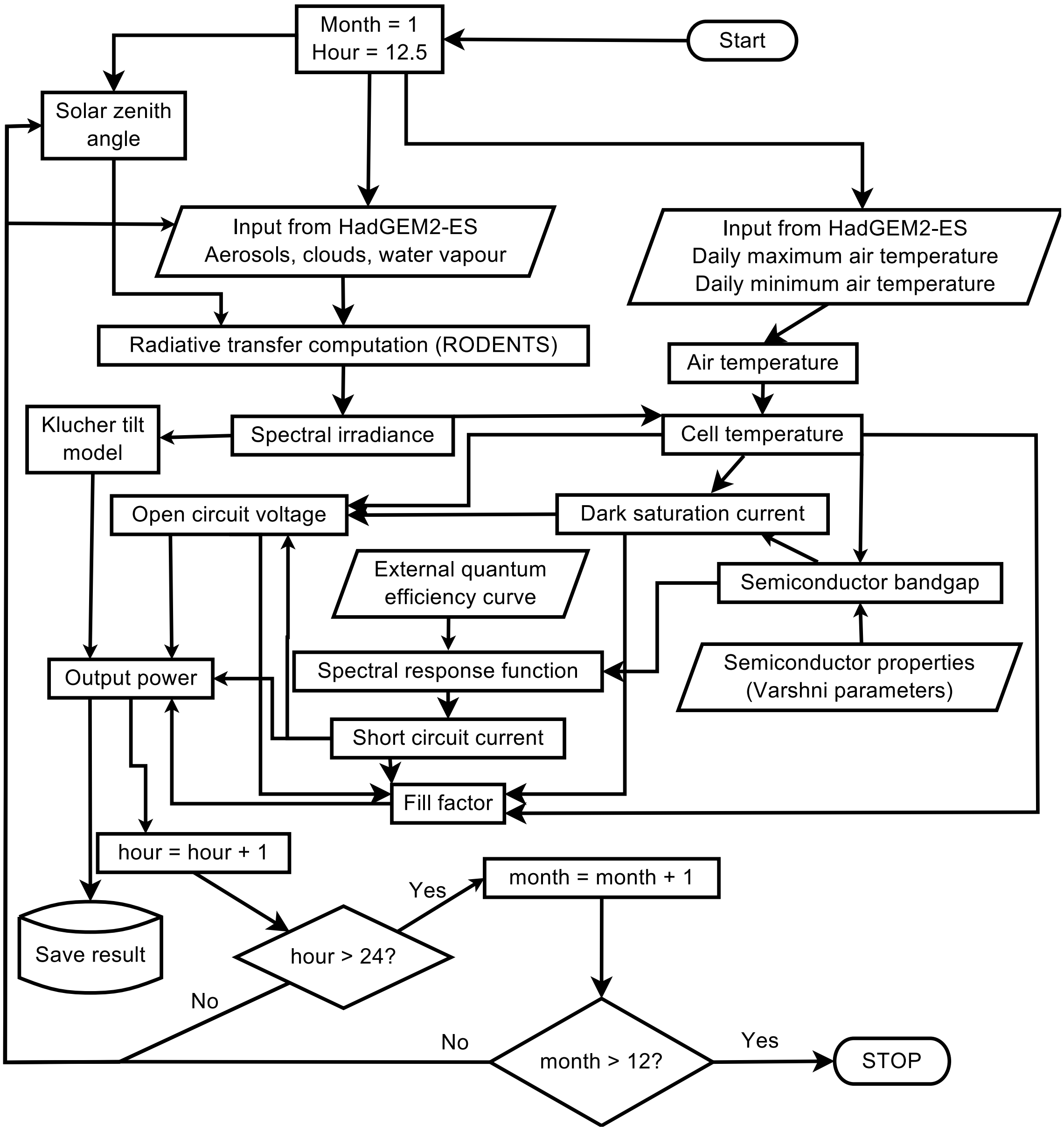

Figure 6.5: Flow diagram of modelling process

also makes IntRad unusable for this investigation. At least 16 streams are required to calculate radiances with libRadtran. Location-specific effects such as horizon shading and surface albedo will affect the tilted irradiance in practice. On the GCM grid-cell level, horizon shading cannot be generalised. In this simulation the surface albedo from the IGBP dataset is used. While land-use changes are both a driver and consequence of climate change, they are not the focus of this investigation.

6.4 Modelling flowchart

The modelling flow diagram is shown in fig. 6.5.

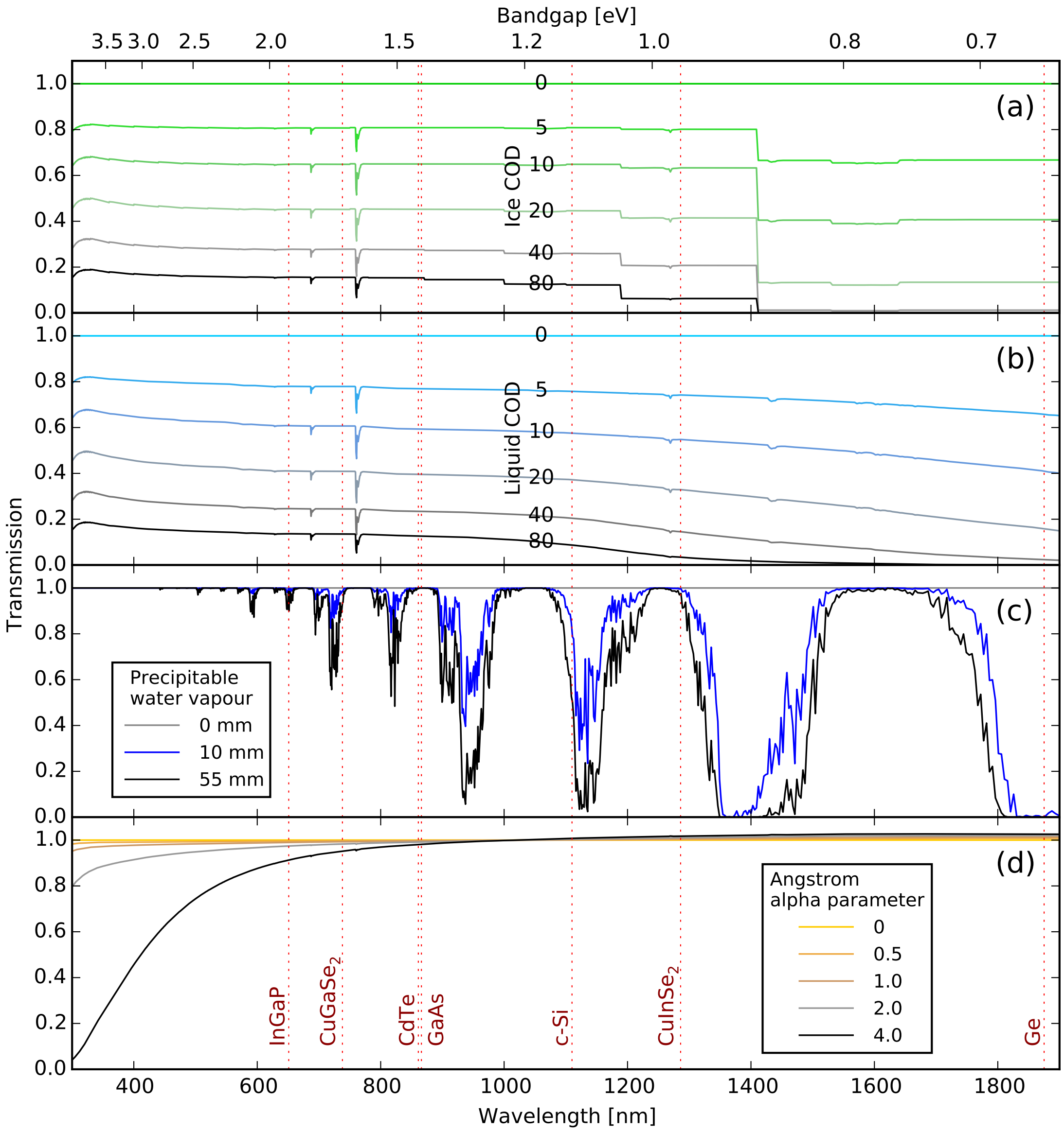

Figure 6.6: The effect of an increase in (a) ice cloud optical depth (COD), (b) liquid water cloud optical depth, (c) precipitable water vapour and (d) Ångström α exponent on the spectral transmission of solar radiation. The y-axis is relative absorption compared to a clean, clear, dry atmosphere with only Rayleigh scattering present except for in (d) where a background aerosol is also specified and $\tau_{a1000} = 0.1$. Also shown is the bandgap of the semiconductor materials investigated at 25°C. Solar zenith angle is 0° with a zero surface albedo. Because optical depth is a function of wavelength, the conversion between cloud water path and optical depth is taken at 600 nm using eqs. (2.31) and (2.36).

6.5 Sensitivity of PV materials to climatic variables

In fig. 6.6, the effect on relative spectral transmission of increasing p_i, p_w, w and aerosol optical depth is shown, and in fig. 6.7 these effects along with cell temperature T_c are investigated on each semiconductor material.

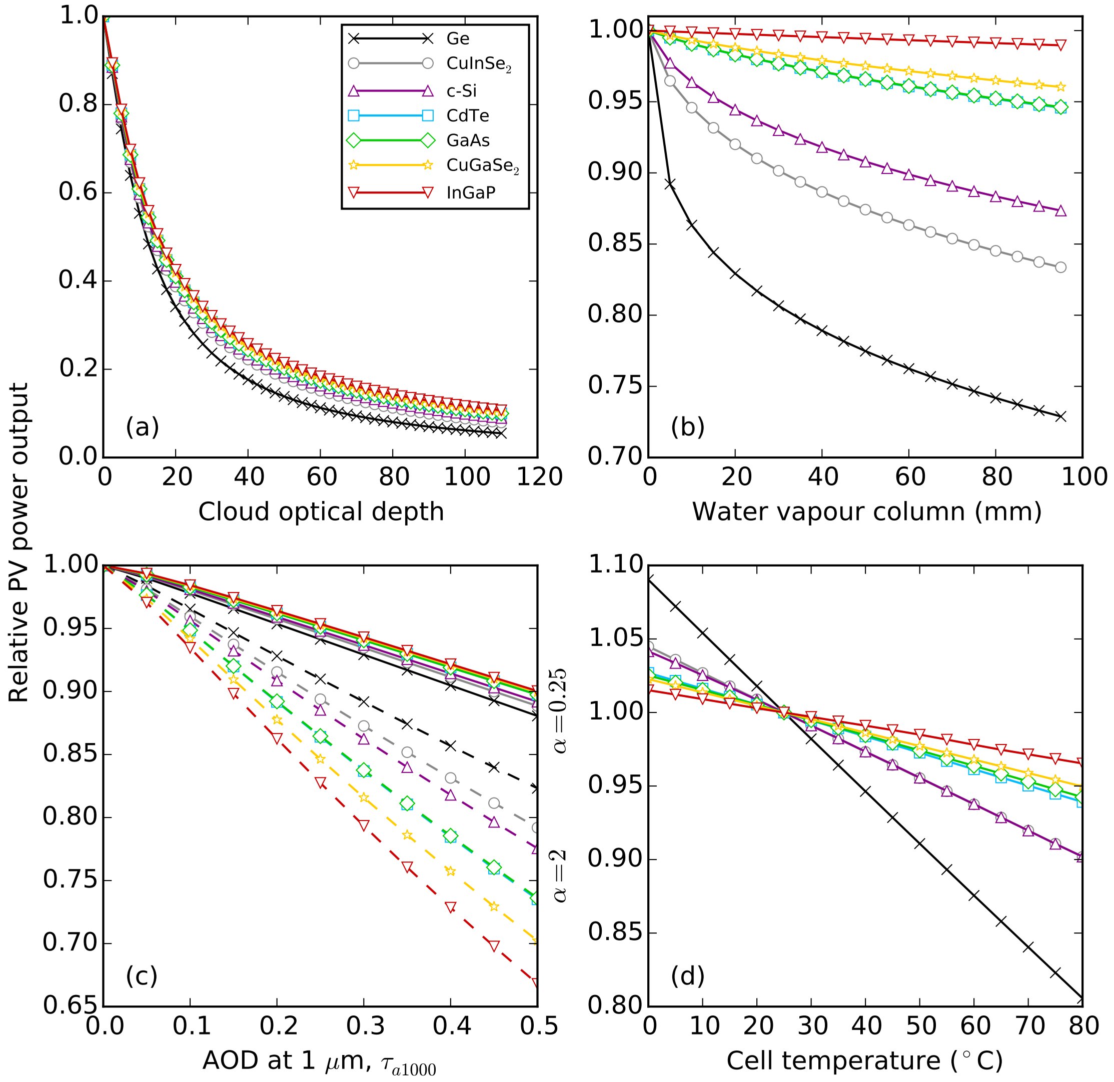

Figure 6.7: The relative power output for each PV material with increasing (a) cloud optical depth, (b) water vapour, (c) aerosol optical depth at 1 µm for Ångström exponent $\alpha = 0.25$ (solid) and $\alpha = 2$ (dashed) compared to a dry, clean, cloudless atmosphere. (d) Relative power output by cell temperature compared to standard testing conditions.

6.5.1 Clouds

It can be seen that the effects of ice clouds and water clouds (fig. 6.6a and b) are broadly similar. Liquid water and ice cloud droplets are fairly non-selective in the UV and visible region, with a slight tendency for shorter wavelengths to be transmitted more. This effect increases at higher cloud optical depths. In the infrared region, cloud droplets attenuate solar radiation more efficiently. As clouds are more opaque to longer wavelengths, the spectrum is blue-shifted and high-bandgap PV cells will perform comparatively better under increasing cloud cover. The notches seen around 680 and 760 nm relate to oxygen absorption and the large jumps seen in the ice cloud extinction are due to discontinuities in the Fu (1996) ice cloud parameterisation.

The spectrally-dependent effect of clouds is dominated by broadband extinction (fig. 6.7a) and any relative gains by material choice are minor compared to the total cloud attenuation. Nevertheless the relative difference in power output between high and low bandgap materials for the same cloud optical depth is not small. In cloudy regions of the world this could be important. Liquid and ice clouds produce very similar results when convoluted with solar cell spectral response curves. Figure 6.7a is not shown for ice.

6.5.2 Precipitable water vapour

Water vapour exhibits distinct absorption bands in the visible and near-infrared part of the spectrum (fig. 6.6c). The majority of the water vapour absorption occurs in the near infrared and red end of the visible part, centred at 1900, 1400, 1140 and 940 nm with smaller bands around 820 and 710 nm and overtones further into the visible range. This means that increases in water vapour results in a blue shift in the spectrum. The absorption is non-linear with water vapour column depth. Figure 6.6c shows that there is a large increase in absorption between 0 mm and 10 mm but a smaller increase between 10 mm and 55 mm.

As spectral response of solar cells increases with wavelength, water vapour is a critical absorber for cells with bandgaps in the infrared region. Photons with energy just below the bandgap (wavelengths slightly shorter than λ_g) contribute the most to the output power due to the wavelength dependence in the integral in eq. (6.12). A high-bandgap semiconductor such as InGaP is less affected by increases in water vapour as $H_2O(g)$ is not efficiently absorbing for photons with a greater energy than 2.0 eV. For cell materials within the one junction ideal bandgap range (1.0–1.7 eV), $CuGaSe_2$ exhibits a fairly modest decline in output power for an increase in water vapour. The bandgaps of both $CuGaSe_2$ and InGaP avoid the large water vapour absorption bands in the near-infrared part of the spectrum. At the other end of the range, c-Si and $CuInSe_2$ perform less well as many of the wavelengths which contribute most to the overall spectral response of these cells are in the near-infrared and are absorbed strongly. Ge is heavily affected by water vapour even at a low level of water vapour in the atmosphere.

6.5.3 Aerosols

Absorption by aerosols is modelled by applying a standard background rural aerosol from Shettle (1989), which is a default option in libRadtran, and modifying the optical depth by using the Ångström formulae (eqs. (6.5) and (6.6)). The analysis shows that the Ångström exponent $\alpha > 0$ everywhere in both the past and future climate model runs so that aerosols attenuate shorter wavelengths more strongly. When α is small, the absorption by aerosols is approximately equal across wavelengths, whereas for high α there is much stronger absorption at short wavelengths compared to long. A high value of α reddens the spectrum and favours low-bandgap materials. In polluted conditions, i.e. as τ_a increases, these effects become quite pronounced (fig. 6.7c, dashed lines where $\alpha = 2$). τ_{a1000}, the AOD at 1 μm, is chosen as the x-axis as this corresponds to the Ångström β parameter. It should be noted that for the monthly climate data, values of $\tau_{a1000} > 0.2$ are rare, however values of τ_{a1000} exceeding 4 exist. For a low value of α, there is little difference in relative cell performance with increasing aerosol optical depth and cell power output is a near linear function of τ_{a1000} (fig. 6.7c, solid lines where $\alpha = 0.25$).

6.5.4 Temperature

Increasing cell temperature has a negative effect on cell efficiency and output power for most PV cells in normal operating conditions. The 25°C cell temperature and 1000 W m^{-2} irradiance at AM1.5 prescribed by STC are not often found in reality as to achieve this would require a high irradiance combined with a very low ambient temperature (Betts, 2004; Gottschalg *et al.*, 2013). According to eq. (6.15), an ambient temperature of -4.3°C would be required to achieve a cell temperature of 25°C at 1000 W m^{-2} irradiance.

In fig. 6.7d the relative power output of each cell compared to $T_c = 25$°C is shown. For constant irradiance and with a slight change of notation from eq. (2.44), the power output of a solar cell can be approximated as a linear function of its temperature so that

$$\frac{P}{P_{25}} = 1 - \Theta(T_c - 25). \tag{6.16}$$

and P_{25} is its power output at 25°C.

For the semiconductors investigated, the temperature coefficient Θ varies from 0.0006 K^{-1} for InGaP to 0.0017 K^{-1} for c-Si over the range of T_c from 25–80°C, noting that the power decline with temperature is approximately linear in this range. In general, it is found that the temperature coefficient is lower for higher bandgap cells, giving these materials a future climate advantage. The temperature coefficients derived by the one-diode, detailed balance method in this chapter are lower than the typical real-world values of 0.0045 K^{-1} for c-Si, 0.0035 K^{-1} for CuInSe$_2$ and 0.0025 K^{-1} for CdTe (Zondag, 2008), and lower than those calculated by Singh & Ravindra (2012) using a similar one-diode method by 30–60% for the cells common to both studies (c-Si, GaAs, CdTe and CdS). Singh & Ravindra used an empirical relationship for J_0 based on real-world data rather than the idealised case which likely accounts for these differences. Experiments by Singh *et al.* (2008) showed that the temperature coefficient is lower for higher efficiency cells of the same material. This is evidenced in part by today's world-leading 25.6% efficient c-Si cell having a temperature coefficient of 0.0025 K^{-1} (Green *et al.*, 2014), much lower than the typical c-Si cell and closer to the calculated ideal value of 0.0017 K^{-1}.

6.6 Global changes in PV energy output

The annual energy outputs are calculated by summing up the power outputs calculated at each hour within each month, multiplied by the number of days in the month.

6.6.1 Baseline changes for c-Si

c-Si is the best understood and most widely utilised PV cell material comprising over 80% of worldwide production (Razykov *et al.*, 2011). Crystalline silicon provides the best optimisation between efficiency and cost combined with low toxicity. c-Si is therefore used as a baseline both to analyse the sensitivity of energy output to each climate variable, and to compare the overall results from other semiconductors.

The global simulation shows that the projected change in c-Si PV energy output using the spectral climate change factor is not homogeneous across the world (fig. 6.8). PV energy output increases of over 10%, and in some areas over 20%, are expected in Europe, eastern China, and parts of South America. The biggest decreases in c-Si energy output occurs in the boreal regions, Greenland, and Antarctica, where significant deployment of solar PV is unlikely. In more important regions, a negative change in PV output above 5% can be expected in parts of equatorial Africa, India and northwest China.

6.6.2 Attribution of climate variables

The contributing factors to the total PV output change were investigated by modifying clouds, water vapour, aerosol and ambient temperature one at a time to the 2080–2100 value and holding the others constant at the 1985–2005 value. In all cases, the panel tilt angle was fixed at the optimal value for historical conditions. In fig. 6.9a, clouds (cloud fraction, cloud optical depth and liquid cloud effective radius) was modified while the other variables were held constant. Clouds account for much of the total changes in c-Si energy output seen, especially in areas where a total increase in c-Si PV output is projected for the future. By comparison with fig. 6.1a, it can be seen that cloudiness is expected to increase in Antarctica and the high northern latitudes and accounts for much of the reduction in c-Si PV output predicted for these areas. Figure 6.9b shows that changes due to water vapour are largely detrimental to c-Si energy output. For much of the mid- and low-latitude areas, the decrease in energy output is less than 2%, but can be more than

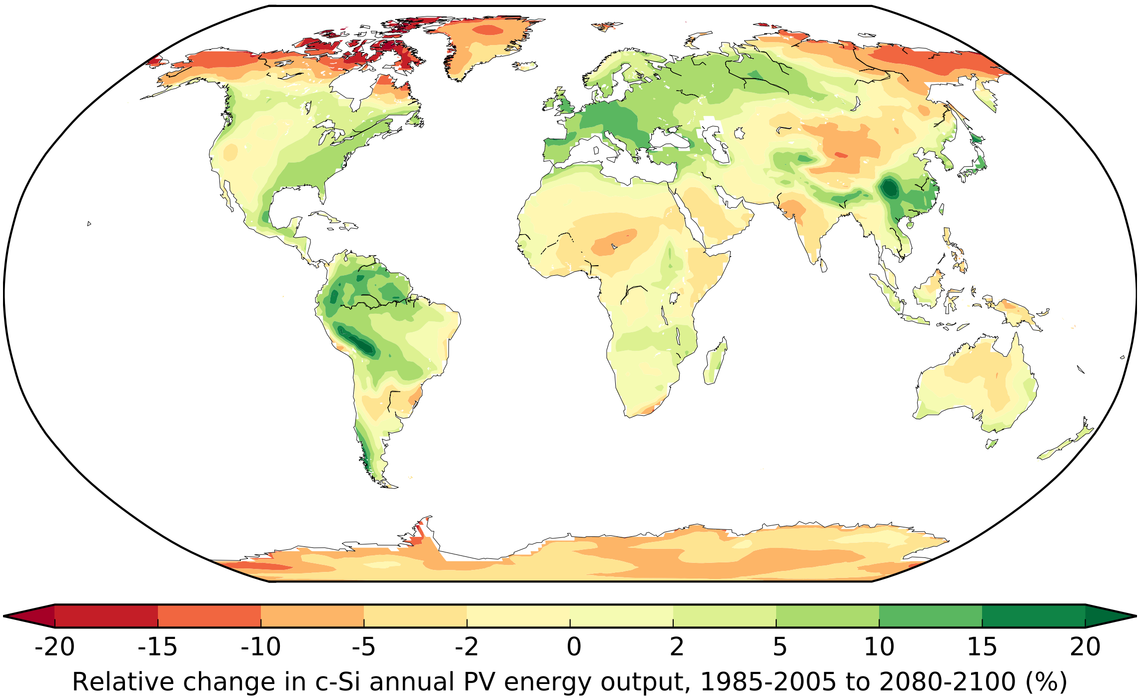

Figure 6.8: Relative change in PV energy output for c-Si solar cells under the RCP8.5 scenario in the HadGEM2-ES model for 2080–2100 compared to 1985–2005.

this in high latitudes. This is consistent with a study which only considered clear-sky spectral effects of water vapour and used the real-world EQE curve for c-Si from fig. 6.3 (Smith *et al.*, 2015). One area in eastern Africa actually sees a small increase in energy output when comparing future to present effects of H_2O. Figure 6.9c shows the changes due to aerosols. For Australia, central Africa and western India, the increase in aerosols lead to a large overall decrease in energy output which outweighs cloud effects in these regions. Changes in aerosols lead to positive changes in c-Si energy output in Europe, eastern China and the eastern US, suggestive of a reduction in anthropogenic pollution in these regions. Clean air policies in Europe and Asia may contribute to the reduction in atmospheric aerosol over the 2080–2100 time period, particularly for example in China. This is noted by the increase in cloud droplet effective radius from fig. 6.1c. A reduction in solar transmission due to aerosol effects is seen over Australia, the Himalayas and western Africa, which could be due to a drying in these regions and is unlikely to be due to anthropogenic emissions. The changes in output energy due to changes in expected solar cell temperature calculated from the changes in ambient temperature alone are not large (fig. 6.9d). This is likely due to the low temperature coefficients calculated from the one-diode detailed balance model; at $0.0017\ \mathrm{K}^{-1}$, daytime temperatures would need to rise at least 12°C to exceed a 2% energy output decline.

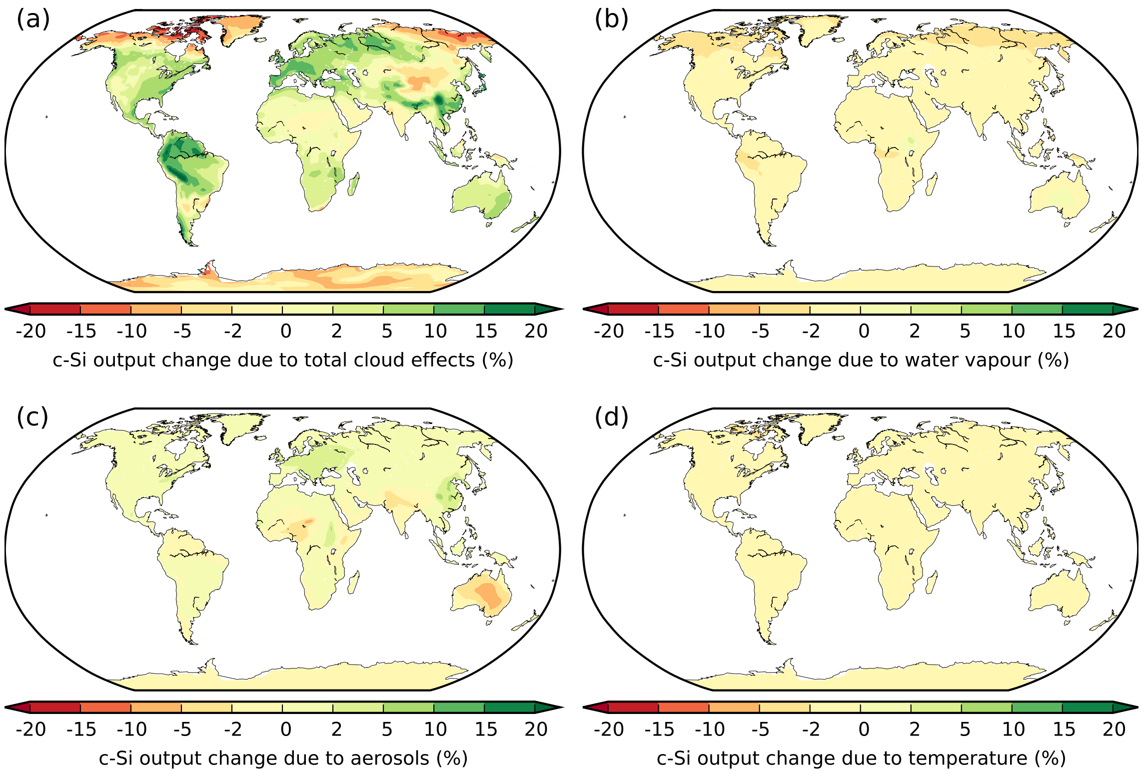

Figure 6.9: Components of the change in c-Si PV output with the stated variable set to the 2080–2100 values and other variables held constant at 1985–2005 values. (a) clouds; (b) water vapour; (c) aerosols; (d) daytime temperature.

6.6.3 Differences for other semiconductors relative to c-Si

The change in energy output for each semiconductor material in the 2080–2100 timeframe compared to 1985–2005 compared to the change for c-Si is also analysed (fig. 6.10). This can be thought of as finding δ such that

$$\delta = \frac{f_{\mathrm{SCC}} - f_{\mathrm{SCC,Si}}}{f_{\mathrm{SCC,\,Si}}} \tag{6.17}$$

where f_{SCC} and $f_{\mathrm{SCC,Si}}$ are the spectral climate change factors calculated for the material in question and c-Si respectively.

As expected, semiconductors with a greater sensitivity to increases in water vapour and cloud optical depth, Ge and $\mathrm{CuInSe_2}$, show a more negative change in energy output than for c-Si (fig. 6.10a,b). These are the semiconductors with lower bandgaps than c-Si. Conversely, the semiconductor materials with higher energy bandgaps than c-Si are more robust to a change in climate than c-Si is (fig. 6.10c–f). The greatest differences are where the effects of a change in temperature and cloud optical depth are highest, and are over 7% for some areas of northern Russia and Canada for InGaP (fig. 6.10f). These locations are not ideal for siting solar PV plants, but the changes are positive in sign for these semiconductors globally. Some differences in the changes by technology

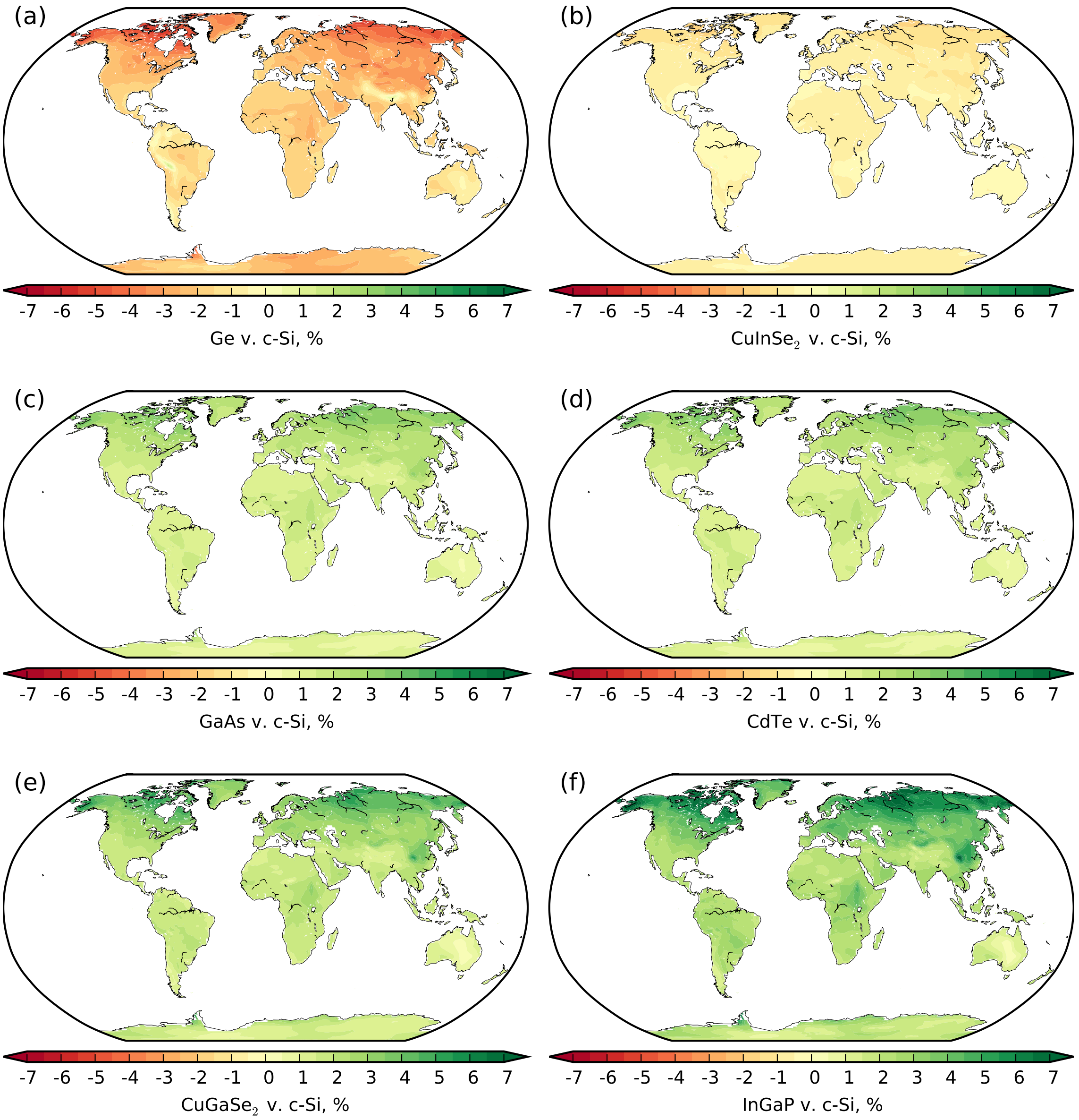

Figure 6.10: Normalised differences (δ in eq. (6.17)) in PV output between each semiconductor and c-Si for changes from 2080–2100 compared to 1985–2005.

can be seen in areas of high aerosol increase (Australia, Himalayas and central Africa) where the changes are less negative for Ge and $CuInSe_2$ and less positive for the other semiconductors. Assuming a large enough Ångström α parameter, this would be expected according to fig. 6.7(c).

6.7 Comparison of HadGEM2-ES with other climate models

As shown in fig. 6.9, clouds are the most important factor for global c-Si energy output changes. Cloud extinction affects all solar wavelengths, and although cloud optical depth creates a slight spectral effect it is dominated by overall reduction in atmospheric

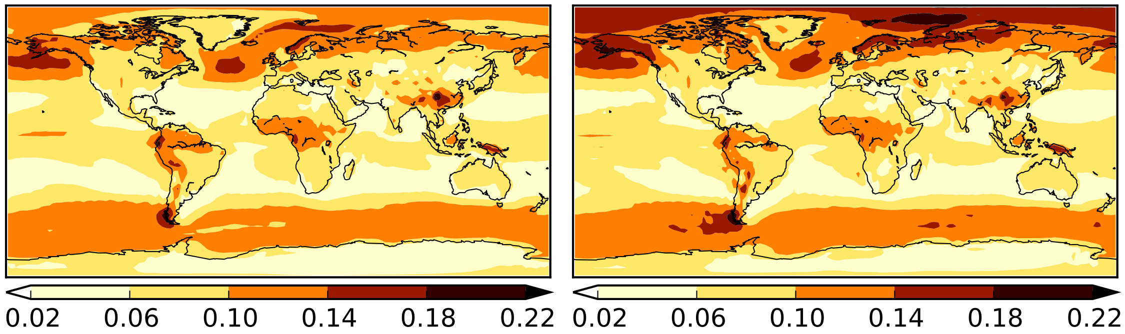

(a) 1985-2005 CMIP5 rsds CV (b) 2080-2100 CMIP5 rsds CV

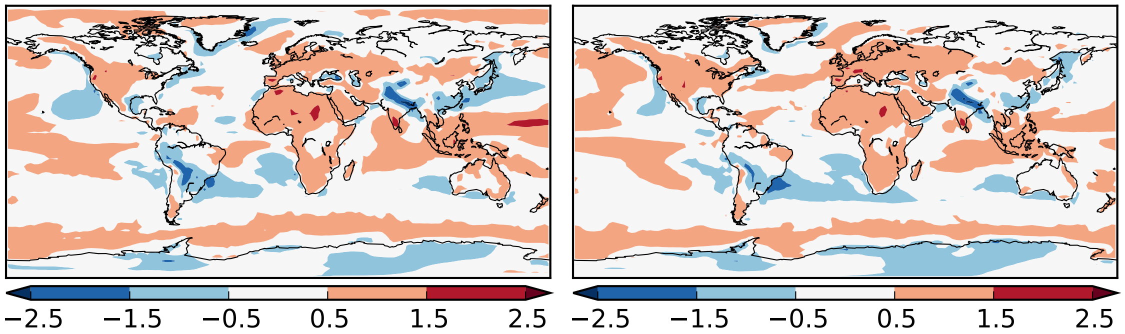

(c) 1985-2005 HadGEM2-ES run5 rsds s.d. (d) 2080-2100 HadGEM2-ES run4 rsds s.d.

Figure 6.11: (a) coefficient of variation in rsds of 39 CMIP5 models for 1985–2005 in the CMIP5 historical experiment; (b) same as (a), for 2080–2100 under RCP8.5; (c) number of standard deviations from the CMIP5 mean for rsds in run 4 of the HadGEM2-ES model used in this study under the CMIP5 historical experiment for 1985–2005; (d) same as (c), for 1985–2005 under RCP8.5.

transmittance. The second greatest effect is due to aerosols, which exhibit some spectral dependence. Clouds are one of the greatest uncertainties inside climate models due to how different models treat sub-grid scale processes and cloud microphysical properties (Boucher *et al.*, 2013).

As the HadGEM2-ES model is one of 39 climate models submitted to CMIP5 by different modelling centres worldwide, an analysis of all 39 model ensembles used in the CMIP5 historical and RCP8.5 scenarios has been undertaken. The analysis has been undertaken using the shortwave downwelling solar irradiance (rsds) variable. To determine where the chosen realisations of HadGEM2-ES, run 5 of the historical and run 4 of RCP8.5, sit within the population of all models, the number of standard deviations from the CMIP5 multi-model mean has also been analysed. The coefficient of variation (CV), defined as the ratio of the standard deviation of the irradiance over all models to the mean of the irradiance of all models, is used to assess the level of difference between models. A low CV represents a low level of spread between models.

Figure 6.11a and fig. 6.11b show the coefficient of variation for 1985–2005 and 2080–2100 respectively. Each "sample" is one year of solar irradiation for each of the 39 models, so the CV is measuring inter-year variation as well as inter-model variation. In most low- and mid-latitude areas the CV is similar, or slightly higher, in the future ensemble compared to the past. As such, climate models tend to show a similar or slightly greater (but not much greater) spread of values for solar radiation for the most important parts of the world for PV. Over boreal land areas and the Arctic ocean the future CMIP5 ensembles show a greater model spread than the historical ones, which is indicative of the myriad climate feedbacks and predicted faster rate of warming in these regions. Figure 6.11c and d show the position of HadGEM2-ES run 5 historical and run 4 RCP8.5 within the total model population in terms of number of CMIP5 standard deviations from the CMIP5 mean. The standard deviation from the multi-model mean is approximately the same in both the past and future experiments, which allows the use of these particular model runs as a consistent representative of the population of climate models. Over Europe, the Middle East, Africa and North America, HadGEM2-ES shows a tendency to predict a higher surface irradiance than the CMIP5 mean by between 0.5 and 1.5 standard deviations. There are some areas where HadGEM2-ES shows a lower irradiance than the multi-model ensemble mean, for example the Himalayas and parts of South America. It is likely that the results shown in this chapter would differ upon using a different climate model, but if the climate model predicted less or more radiation by the same amount in each region compared to the CMIP5 mean in past and future, such as HadGEM2-ES appears to, the sign of the changes by region should be the same using a different model.

6.8 Summary

A handful of previous studies (table 6.1) have compared the changes in PV energy output expected in a future climate. However, they rely on broadband irradiance only and do not take into account interaction of the solar spectrum with the spectral response of a PV semiconductor, and only one study has considered a tilted PV collector, whereas all others use the values of horizontal radiation to determine the changes to PV output in a future climate. In this chapter these two contributions are made to the existing literature.

The changes in solar PV energy output with respect to the RCP8.5 climate change scenario are shown to be mostly dependent on broadband attenuation from changes in cloud patterns. The changes in PV output are heterogeneous across the world, ranging from a decrease of more than 10% in some parts of Africa and Australia (and the less important regions of Antarctica and far north of North America and Russia) to increases of over 10% in Europe, the eastern US, South America and China. Although the absorption and scattering due to clouds is a function of wavelength, the changes in spectral transmission through clouds is dominated by the broadband effects of changes in cloud fraction and cloud optical depth. A selection of a particular semiconductor material on the basis of its spectral properties is not an important consideration in parts of the world where clouds are, and will remain, frequent. In a few locations such as western Africa and Australia the increases in aerosol optical depth are more important than changes in cloudiness.

Comparing the results in this chapter to previous work, the outcomes are more optimistic than the global changes shown in c-Si PV output by Crook *et al.* (2011) over a similar future time frame. The RCP8.5 climate simulation used in this study is more extreme than the A1B scenario investigated in Crook *et al.*. Some differences should be expected between the studies in light of the updated climate model, different radiative forcing scenario, and inclusion of spectral effects. Another reason for the more optimistic outlook in this work is that the theoretically-derived temperature coefficients are lower than the real-world values assumed in Crook *et al.*. Nevertheless, the areas where strongly positive and strongly negative changes in PV energy output broadly agree between the two studies. The strongly positive changes in Europe and eastern China, and negative changes in central Africa, India, Canada, Russia and Antarctica shown in this chapter are also present in Wild *et al.* (2015). The overall positive change in South America and negative change in Australia in this analysis was found not to be statistically significant for the population of 39 CMIP5 GCMs across the CMIP5 ensemble in Wild *et al.* (2015) for the timeframe of 2006–2049. As this study considers a timeframe further into the future, it is possible that a statistically significant trend would emerge for these regions in RCP8.5 by 2080–2100.

Differences in energy output between semiconductor technologies can be seen. This can be explained by the difference in spectral responses of solar cells. Increases in clouds and water vapour tend to shift the spectrum towards to the blue, and increases in aerosols tend to shift the spectrum towards the red, except where the Ångström α exponent is low. Increases in ambient temperature also negatively affect PV energy output, the extent of which is dependent on the temperature coefficient of the semiconductor. Within the Shockley-Queisser detailed balance limit ideal range of 1.0–1.7 eV for a single-junction solar cell, materials with a bandgap towards the higher end of this range such as $CuGaSe_2$ are slightly more robust to increases in clouds, water vapour, aerosols (for low α) and temperature than materials towards the lower end of this range such as $CuInSe_2$. As such, high bandgap materials may show a marginal performance advantage, up to 10% and even greater in the northern Boreal regions, for $CuGaSe_2$ compared to c-Si over low bandgap materials in the future. High-efficiency concentrating PV cells such as the InGaP/InGaAs/Ge triple-junction present an interesting case, as the top InGaP layer is expected to see a gain in energy output in the future whereas the bottom Ge layer is expected to suffer a energy output loss relative to c-Si. The middle InGaAs layer exhibits a bandgap similar to CdTe and GaAs and will show a slight improvement compared to c-Si. As multi-junction cells are required to be current-matched, changes in solar spectral properties may present an additional challenge for optimisation of energy output from concentrating PV.

Chapter 7

Impacts of stratospheric sulphate geoengineering

In chapter 6, the effects of a future climate scenario on fixed-angle solar PV panels were investigated. Spectral transmission through the atmosphere and the spectral response of different PV materials was taken into account. It was demonstrated that the climate change effects, including changes due to the solar spectrum, could account for power output changes exceeding ±10% in many parts of the world and ±20% in localised regions, for c-Si under the RCP8.5 forcing scenario with a 2080–2100 future time horizon. A small spectral effect was seen with high bandgap semiconductors performing better.

The climate change scenarios laid out in the CMIP5 RCP scenarios prescribe radiative forcing levels based on a group of socioeconomic narratives. While geoengineering is discussed in AR5, the "headline" RCP scenarios do not consider it, however a smaller geoengineering model intercomparison study, GeoMIP, has been created to assess the differences between models (Kravitz *et al.*, 2011). Geoengineering, artificially manipulating the earth's climate, has been suggested as a way to reverse or lessen the impact of anthropogenic climate change (Budyko, 1976; Crutzen, 2006) and has received greater attention in recent years (Boucher *et al.*, 2013). As solar energy changes under baseline RCP scenarios have had little attention so far, it is unlikely that a detailed global study on solar power changes under geoengineering climate scenarios have been considered at all. This chapter introduces such an investigation for PV, and the work of the previous chapter is extended to include two-axis tracking PV and CSP alongside fixed-angle, optimally oriented PV panels.

Firstly an introduction to geoengineering using stratospheric sulphate aerosols is presented. The climate model and variables of interest are then described, following which the geoengineering experiment is introduced. The following sections report the results, where it is shown that large and significant changes for tracking PV and CSP can be expected in energy output when geoengineering is implemented. A method of calculating where changes are statistically significant is defined. The final section summarises.

7.1 Background and literature review

Given the slow progress of policy action on climate change up until the present, geoengineering can be considered a technological climate change mitigation strategy (Lenton & Vaughan, 2009). It could potentially be deployed if future policy progress continued to be inadequate or as a last-ditch attempt to stop runaway climate change if all other short-term fixes are insufficient. Geoengineering concepts fall into two main categories: solar radiation management (SRM) and CO_2 removal. In terms of the earth's energy budget, SRM either reduces the input or increases the reflection of shortwave radiation to/from the earth-atmosphere system, and CO_2 removal increases the longwave output from the earth. Both methods are designed to reduce the radiative forcing and lead to a global cooling effect.

Stratospheric sulphate injection (SSI) is one SRM geoengineering method proposed to reduce planetary warming (Boucher *et al.*, 2013) by increasing the earth's planetary albedo and reflecting a greater proportion of solar radiation back into space. The concept of SSI is to mimic the production of reflective volcanic sulphate aerosols. The 1991 eruption of Mt. Pinatubo ejected 20 Tg SO_2 into the stratosphere (Bluth *et al.*, 1992), causing a globally averaged cooling effect of about 0.5°C (Lacis & Mishchenko, 1995). Unlike well-mixed greenhouse gases, stratospheric sulphate aerosols have a lifetime ranging from days to a few years (Rasch *et al.*, 2008) and are not evenly distributed spatially. Due to this short lifetime, the SSI programme must be continuous to be effective.

Other SRM methods include marine cloud brightening, space sunshades, and increasing the surface albedo (Lenton & Vaughan, 2009). There will be solar power consequences for all of these methods. Notwithstanding the cost and practical realities of such a task, placement of solar mirror at the L1 sun-earth Lagrange point will most likely produce negative solar energy effects due to the reduction of incoming radiation at the top of the atmosphere. Surface albedo enhancement on the other hand will probably increase solar energy yield both directly from ground reflection and indirectly through atmospheric backscattering. The effects of marine cloud brightening may be positive, negative or neutral and probably not spatially homogeneous, depending on changes in atmospheric dynamics.

Sulphate particles scatter radiation and increase the diffuse component at the expense of direct and total radiation. It is expected that both PV and CSP potential would decline in the case of a climate geoengineered with SSI (Robock *et al.*, 2009; Oppenheimer *et al.*, 2014), but the effect on CSP would be greater as CSP can only use direct radiation. In the year following the Mt. Pinatubo eruption, on-peak CSP capacity at the large SEGS array in California was reduced by about 20% (Murphy, 2009). A secondary effect of sulphate injection that directly affects the radiation budget would be an increase in cloud condensation nuclei and reduction in size of cloud droplets (Ramanathan *et al.*, 2001) which would affect cloud radiative properties in both the shortwave (important in this study) and longwave (important in climate projections). Other side effects of SSI could include ozone depletion (Tilmes *et al.*, 2008), disruption to Asian and African monsoons (Robock *et al.*, 2008), and changes in precipitation patterns more generally. Because SSI does not reverse the increasing concentrations of atmospheric CO_2, the ocean will continue to absorb some of the atmospheric excess which results in acidification. This can be damaging for marine ecosystems and the human systems that are reliant on them. There may be other undesirable side effects that will only become known upon deployment of an SSI programme. Finally, ethical and practical concerns of geoengineering exist, such as whether humans have the right to deliberately alter the climate further in preference to targeting the source of the problem (greenhouse gas emissions), and whether such a programme is financially, politically and technically viable.

7.2 Climate runs

The Met Office Hadley Centre coupled atmosphere-ocean model, with full carbon cycle modelling and extended stratosphere, HadGEM2-CCS, (Martin *et al.*, 2011; Hardiman *et al.*, 2012) is used to simulate historical warming from 1860 to 2005 and future warming to 2099 based on the RCP 4.5 emissions scenario. The most important atmospheric process included is the oxidation of SO_2 gas to the H_2SO_4 sulphuric acid aerosol condensate (Bellouin *et al.*, 2007). The extended stratosphere in HadGEM2-CCS can better represent stratospheric-tropospheric interactions than the low-top equivalent HadGEM2-CC model, the former extending to a vertical limit of 84 km on 60 model levels and the latter to 39 km on 37 vertical levels. Important processes for sulphate aerosols including gravitational sedimentation are better resolved.

The SSI geoengineering simulation simulates the injection of SO_2 into the tropical stratosphere from 2020 onwards at an altitude of 16 km to 25 km over the equator and at a rate of 10 Tg SO_2 per year on top of the RCP4.5 scenario. RCP4.5 was selected as the main RCP for analysis in GeoMIP (Kravitz *et al.*, 2011). For both the RCP4.5 and SSI simulations, the timeframe of 2040–2059 is used for the analysis. Photovoltaics and CSP have generally assumed lifetimes of 25–30 years (Köberle *et al.*, 2015) so for systems developed in 2015 the analysis period for geoengineering will overlap with the system's lifetime. After 20 years of injection starting in 2020, the geoengineering has reached its full effect. To compare the future geoengineered (SSI) and non-geoengineered (RCP4.5) against the recent past, the historical simulation output for 1985–2005 is also analysed. For the RCP4.5 and SSI simulations, three ensemble members were produced, and one member for the

Variable	CMIP5 name	Name
Surface downwelling shortwave radiation	rsds	G
Surface diffuse downwelling shortwave radiation	rsdsdiff	G_D
Near-surface air temperature	tas	T_a

Table 7.1: Variables from HadGEM2-CCS used in the SSI, RCP4.5 and historical simulations.

historical simulation is available. The climate model simulations were produced by Scott Osprey (Oxford University) and Lawrence Jackson (University of Leeds) with the analysis performed by the author. Unlike in chapter 6, only the broadband solar radiation is considered in this investigation (table 7.1), as spectral radiation was not available on the 3-hour timescale.

3-hourly values of total and diffuse shortwave downwelling radiation and near-surface air temperature (G, G_D and T_a respectively) are extracted for 2040–2059 from each ensemble member in the SSI and RCP4.5 simulations and for 1986–2005 from the historical simulation table 7.1. The DNI G_B is simply recovered as

$$G_B = \frac{G - G_D}{\overline{\cos\theta_z}} \tag{7.1}$$

where $\overline{\cos\theta_z}$ is the mean cosine of the zenith angle for daytimes in the corresponding 3-hour period. This is determined by taking 6-minutely samples of $\cos\theta_z$ and finding

$$\overline{\cos\theta_z} = \frac{1}{N} \sum_{\cos\theta_z > 0} \cos\theta_{z,j} \tag{7.2}$$

where N is the number of samples in the 3-hour period in which $\cos\theta_z > 0$ and j runs from 1 to N. The effective azimuth angle is taken from the central time in the 3-hour period. The reason why $\overline{\cos\theta_z}$ is used is because solar zenith angle varies enough over the course of the three hour period to make the midpoint time zenith unrepresentative in some cases.

Figure 7.1 shows the differences (SSI minus RCP4.5, SSI minus historical and RCP4.5 minus historical) between the ensemble means for T_a, G and G_B. Regions where the differences between simulations are not significant at the 5% level have been shaded; the method of calculating uncertainty is described in section 7.5. SSI cools the Earth compared to RCP4.5 with greater cooling over land, which is also significant for the majority of the world (fig. 7.1a). Differences between the SSI and historical runs are smaller, and in general the SSI program does not fully reverse the underlying temperature rise from RCP4.5 (fig. 7.1b). In RCP4.5 near-surface air temperature is warmer than in the historical simulation as expected, with greater warming in the Arctic and over

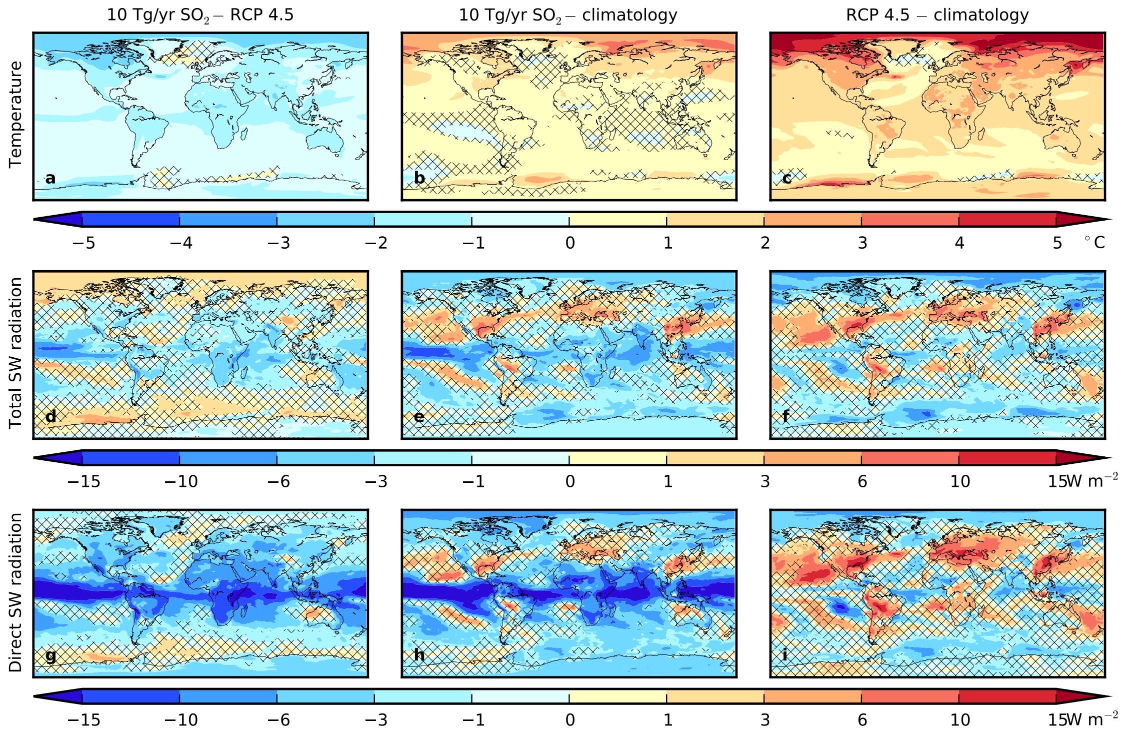

Figure 7.1: Changes in surface air temperature change (top row), downwelling surface shortwave radiation (middle row) and downwelling surface direct shortwave radiation (bottom row) for SSI minus RCP4.5 (left column), SSI minus historical (middle column) and RCP4.5 minus historical (right column). Shaded areas are where differences between 20-year means are not significant at the 5% level.

land (fig. 7.1c). This change is significant in most regions. Changes in total radiation are significant in fewer places than for changes in temperature (fig. 7.1d–f). The largest changes are seen under the influence of SSI for direct radiation in fig. 7.1g–h. Global average differences in direct radiation transmission are 5.54 W m^{-2} between SSI and RCP4.5. The largest surface shortwave changes occur in the tropics for SSI because, although the sulphate aerosol is spread across the globe, the aerosol is more concentrated near the equator where it is injected. There are large changes in direct radiation present in the baseline RCP4.5 climate change scenario compared to the historical (fig. 7.1i).

Figure 7.2 shows the globally averaged temperatures in the three models. The global mean changes in temperature are area-weighted, i.e. the contribution of a grid cell to the global average is proportional to the cosine of its latitude. It is seen that the rates of warming of around 0.3°C/decade are similar between all three scenarios. In RCP4.5 the trendline is almost a linear continuation of the historical trendline, and the global mean temperature is 1.45°C above that in the historical simulation. SSI is successful in reducing global average temperatures below the RCP4.5 simulation by a global average of 0.94°C, but the background warming trend is still present. The reduction of global temperatures in the early 1990s due to the Mt. Pinatubo eruption are reproduced in the historical simulation, although are not as great as the 0.5°C suggested by Lacis & Mishchenko (1995).

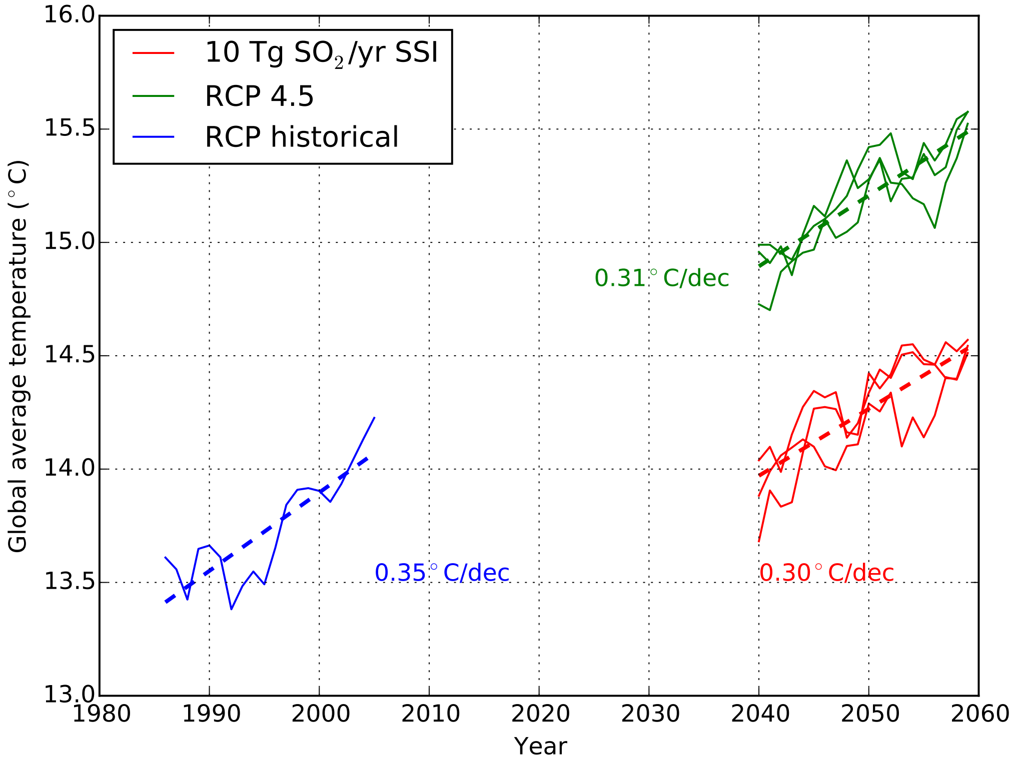

Figure 7.2: Global average temperature trends for the SSI, RCP4.5 and historical simulations with average warming rates per decade. The three runs of the SSI and RCP4.5 simulations are shown separately.

Figure 7.3 shows the area-weighted trends for total radiation, direct radiation and diffuse radiation. The historical trend for radiation is complicated by the Mt. Pinatubo eruption. The influence of this can be seen as a decline in total and direct shortwave radiation and an increase in the diffuse component between the years of 1991–1994. In the absence of the Mt. Pinatubo eruption the trend is possibly for a small global brightening due to a decrease in air pollution (Wild, 2009). The future radiation datasets show very clear differences between RCP4.5 and SSI. The difference between the peak of Mt. Pinatubo influence in 1992 and a “normal” year in the 1990s is approximately the same as the difference between the RCP4.5 and SSI simulations.

7.3 Application to solar power output

Three solar power systems are considered: a fixed-angle PV array, a two-axis tracking PV array, and a one-axis tracking CSP parabolic trough. As c-Si is currently the dominant PV cell material, it is considered for this study, although as spectral effects are not included any differences in technology will be due to temperature and low-irradiance coefficients in eq. (2.44), and this relationship is used to assess changes. Therefore, the temperature effect on efficiency in this simulation (0.0045 K^{-1}) will be more important

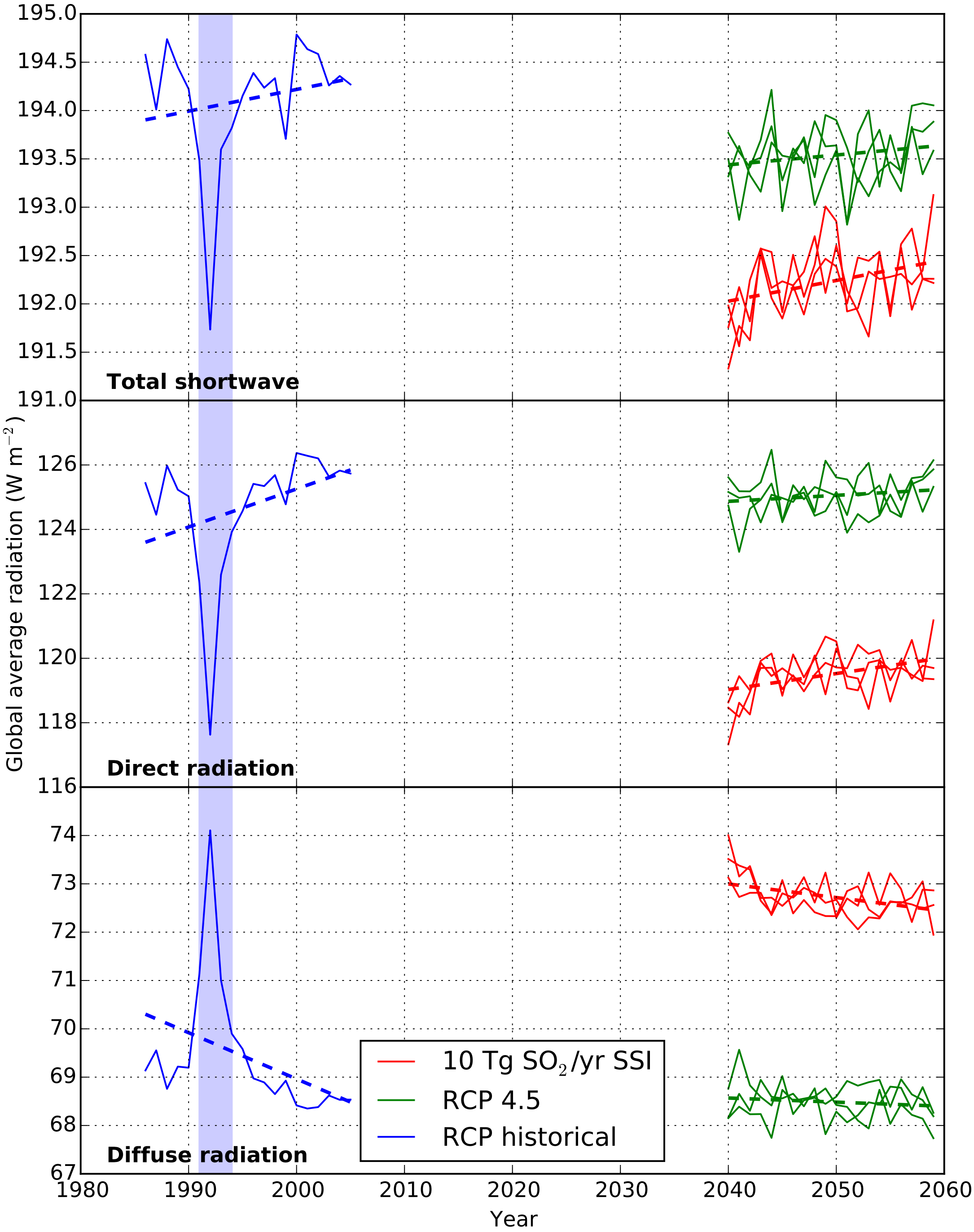

Figure 7.3: Global average radiation trends for the SSI, RCP4.5 and historical simulations. The three runs of the SSI and RCP4.5 simulations are shown separately. The influence of the 1991 Mt. Pinatubo eruption is shaded.

than in chapter 6 (0.0017 K^{-1}). The cell temperature is calculated as in eq. (6.15) with a wind speed of 1 m s^{-2}. Fixed-angle PV panels are the most common configuration for domestic-scale installations and utility plants. The fixed-angle PV experiment optimises equator-facing tilt using the Barker-Christensen method using eq. (5.4) for latitudes below 75° and equal to latitude above 75°, and the optimisation is performed separately for the historical, RCP4.5 and SSI climate scenarios. Analogously to chapter 6, the top-of-atmosphere radiation (rsdt) for the historical and future time periods were obtained from the CMIP5 portal to calculate the summer, winter and annual clearness indices required for the Barker-Christensen tilt method.

In both the fixed and two-axis tracking PV experiments, the surface albedo is set to 0 to remove effects of ground reflection, and the Klucher diffuse irradiance model (eq. (5.3)) is applied. The only difference therefore between the two experiments is the influence of the incidence angle $\cos\theta_i$ which is always equal to 1 for daytime periods in the tracking PV case and a function of solar position (eq. (5.13)) in the fixed PV case.

The principle of CSP is to focus direct sunlight onto an absorber using mirrors, creating a temperature differential with the surroundings that can do useful work. There are several different methods that can be used to achieve this, including linear Fresnel reflectors, parabolic dishes, heliostats, and parabolic troughs (Kalogirou, 2004). As parabolic trough CSP collectors have been extensively deployed and tested (Köberle *et al.*, 2015), a parabolic trough collector with a one-axis east-west tracking system such as the type seen in the SEGS array in the Mojave Desert in California (Kearney, 1989) is used in this analysis. In a parabolic trough collector, direct sunlight is focused onto an absorber tube containing heat transfer fluid, usually oil, using concave mirrors. The fluid circulates through the power plant and is used to raise steam to drive turbine generator sets. As CSP requires direct sunlight, collectors track the sun to align the focused sunlight to the absorber tube.

For a variety of CSP technologies, the efficiency to a good approximation has been found to be (Kalogirou, 2004)

$$\eta_{\mathrm{CSP}} = k_0 - \frac{k_1(T_i - T_a)}{G_B \cos\theta_i} \tag{7.3}$$

for some empirical choices of k_0 and k_1. Experiments at Sandia National Laboratories for the IST parabolic trough give $k_0 = 0.762$ and $k_1 = 0.2125$ (Dudley, 1995; Kalogirou, 2004). The efficiency of a CSP collector depends on the working fluid inlet temperature and the condenser temperature, which are the largest unknowns. The fluid inlet temperature is taken to be held fixed at 115°C following Crook *et al.* (2011), so that an increase in ambient temperature improves CSP efficiency by requiring less heat from the surroundings to heat up the working fluid. The incidence angle in eq. (7.3) for a one-axis E-W

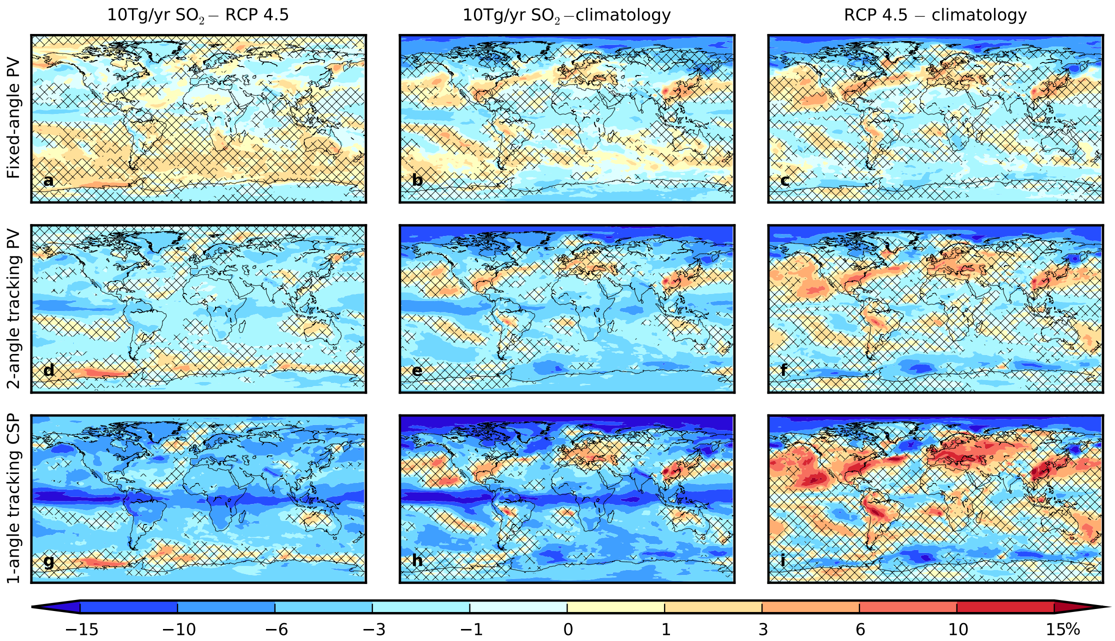

Figure 7.4: Percentage changes in power output yield for fixed-angle PV (top row), two-angle tracking PV (middle row) and two-angle tracking CSP (bottom row). Differences between SSI and RCP4.5 (left column), SSI and historical (middle column) and RCP4.5 and historical (right column). Shaded areas are where differences between 20-year means are not significant at the 5% level

parabolic trough is not the same as the incidence angle for a two-axis flat plate collector like PV, and is given by (Kalogirou, 2004)

$$\cos\theta_i = \cos l \cos h + \cos\delta \sin^2 h \tag{7.4}$$

where l is latitude and h and δ are the hour angle and declination as defined in section 2.

Figure 7.4 shows the differences in energy output between each simulation ensemble mean for each considered technology. Regions where changes are not significant at the 5% level have again been shaded. The overall differences for fixed-angle PV between SSI and RCP4.5 are small and tend to be within ±3% (fig. 7.4a). Compared to the historical simulation, in both the SSI and RCP4.5 simulations decreases in energy output of a few percent occur in the important solar energy generating regions of Africa, the Middle East, India and the Western US for fixed PV (fig. 7.4b,c). Geoengineering tends to slightly amplify the negative effects already present in RCP4.5. For 2-axis tracking PV, the changes due to SSI over land are mostly negative compared to RCP4.5 (fig. 7.4d). The reduction in direct radiation under SSI accounts for these differences as tracking PV systems are more sensitive to changes in direct irradiance. SSI lessens some of the increase in tracking PV output over Europe, the Eastern US and East Asia that is seen in RCP4.5 compared to the historical simulation (fig. 7.4e,f).

Differences between historical and future solar energy output are larger for CSP than for PV. In the SSI simulation energy output decreases by more than 10% compared to RCP4.5

for many regions, particularly in a band across the equator where sulphate particles are more concentrated (fig. 7.4g). Typically, CSP plants are most cost-effective in the arid regions between the equator and 40° in both hemispheres (Köberle *et al.*, 2015) due to the high DNI contribution. Here too, the impacts of SSI compared to the RCP4.5 simulation can be seen for CSP energy output. RCP4.5 shows significant positive changes to CSP energy output in Europe, the Far East, eastern US and in Latin America, in some cases by more than 15%, compared to the historical simulation (fig. 7.4i). These increases are made smaller in magnitude and less significant by SSI (fig. 7.4h). The areas of greatest change in CSP output under RCP4.5 and SSI correspond with the areas of greatest change in direct downwelling surface shortwave radiation.

7.4 Modelling flowchart

The modelling flow diagram is shown in fig. 7.5.

7.5 Significance analysis

The significance analysis is performed by using an independent sample Student t-test to determine whether the differences observed between each simulation are significant at the 5% level. The t-test is valid if the yearly means within each simulation satisfy a normal distribution and the inter-simulation variances are constant. Therefore, these assumptions were first checked before using the tests.

A normal probability plot for the 3 runs of the 20 sample years of the SSI simulation for the grid square which contains Leeds is shown in fig. 7.6. This plots the observed annual mean temperatures on the y-axis against a theoretical normal fit on the x-axis. If the data were perfectly normally distributed, they would lie on the diagonal line. For this dataset, the assumption of a normal distribution is not too inaccurate. To perform this analysis globally, the D'Agostino-Pearson test (D'Agostino, 1971; D'Agostino & Pearson, 1973) can be performed. This provides a probability (p-value) that the data do not satisfy a normal distribution. This does not imply that the data *are* normally distributed in reality, merely that they are "sufficiently" normal for further tests relying on the normal assumption to be performed. A criterion of $p > 0.05$ is often applied to make this decision but such a choice is subjective. For the example presented in fig. 7.6, $p = 0.574$, and there is no evidence to suggest the data are not normally distributed. The data has not been detrended as the year-on-year global trends shown for temperature and radiation in figs. 7.2 and 7.3 are often overwhelmed by the inter-annual variability at the grid cell level (in other words, the signal-to-noise ratio is small).

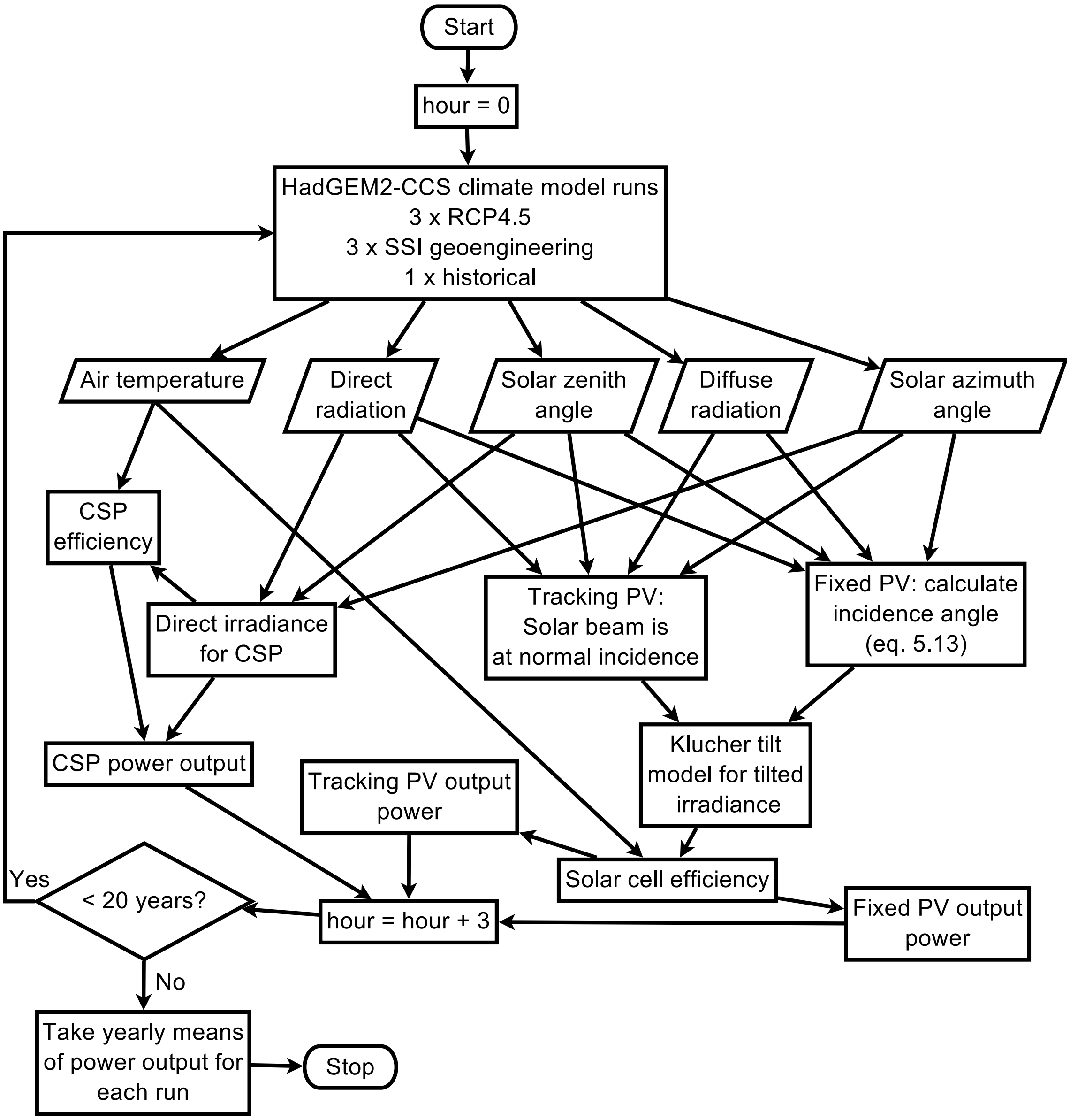

Figure 7.5: Flow diagram of modelling process

For each test, there are 60 sample years for the SSI and RCP4.5 simulations (20 yearly observations × 3 ensemble members) and 20 sample years for the historical simulation. The plots of p-values falling into the categories of $p < 0.01$, $p < 0.02$, $p < 0.05$ and $p < 0.10$ for T_a, G and G_B, and the power outputs for each technology are shown in fig. 7.7. For white areas where $p > 0.10$, which occurs over most land areas, there is no evidence to suggest that the data cannot be assumed to be normally distributed.

The assumption of equal variances can be tested with the Bartlett test (Snedecor & Cochran, 1989) assuming the data is sufficiently normally distributed, which is broadly true for the datasets considered as shown in fig. 7.7. Again, the test returns a p-value that can be used to make a subjective assessment of equality of variances. Figure 7.8 shows that the assumption of equal variances is valid for most land points as $p > 0.10$. As the Bartlett test is sensitive to non-normality, many of the regions where the test shows

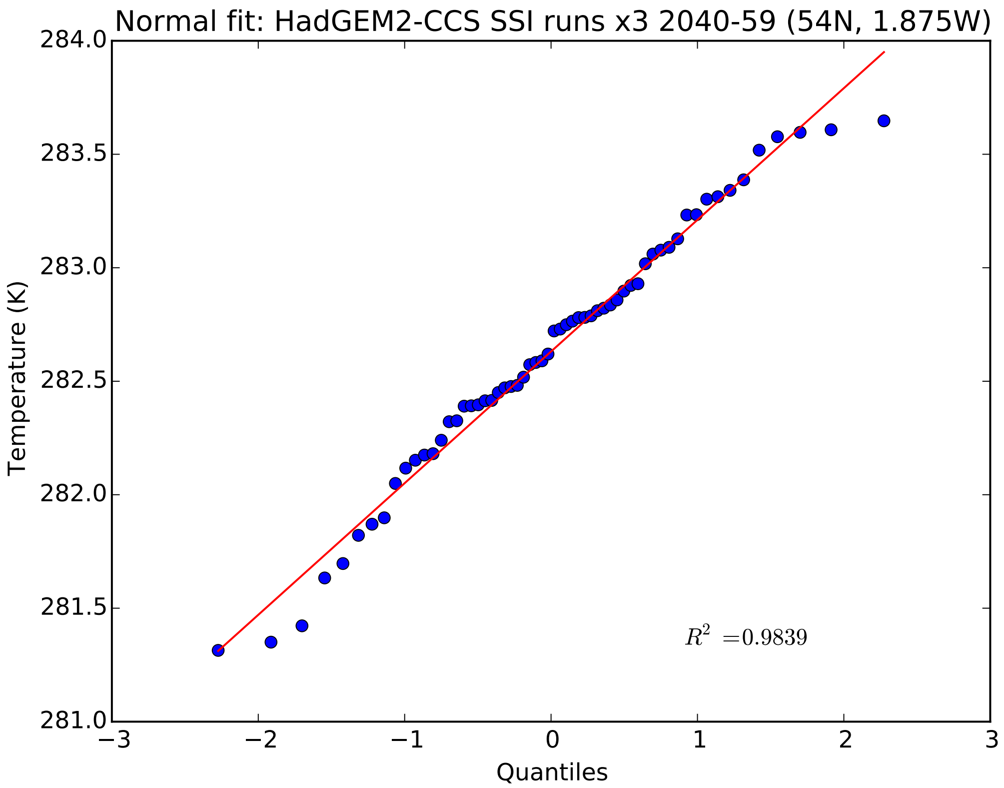

Figure 7.6: Normal probability plot for the SSI simulations for the GCM grid cell containing Leeds

evidence of non-equal variances coincide with those that reject the normal assumption.

As the majority of grid cells did not fail the assumptions for normality or equal variances, an independent-sample t-test can be used to determine uncertainty. The independent sample t-test determines whether the means of two ensembles are different. Like the D'Agostino-Pearson and Bartlett tests, it returns a p-value. A low p-value indicates that there is evidence to suggest the means are different. Shaded areas in figs. 7.1 and 7.4 are where $p > 0.05$, suggesting in these regions the means between the variables in question are not (statistically) significantly different. The unshaded areas are the ones where statistical significance is observed; as expected, they tend to coincide with the largest absolute changes.

7.6 Summary

In this chapter, the assessment of solar energy changes in a future climate, that was first considered in chapter 6, is extended to cover a future scenario in which geoengineering is used to deliberately used to manage global temperature rises. Global effects of stratospheric sulphate geoengineering have been assessed for PV and CSP energy outputs.

The climate model simulation of geoengineering with stratospheric sulphate injection

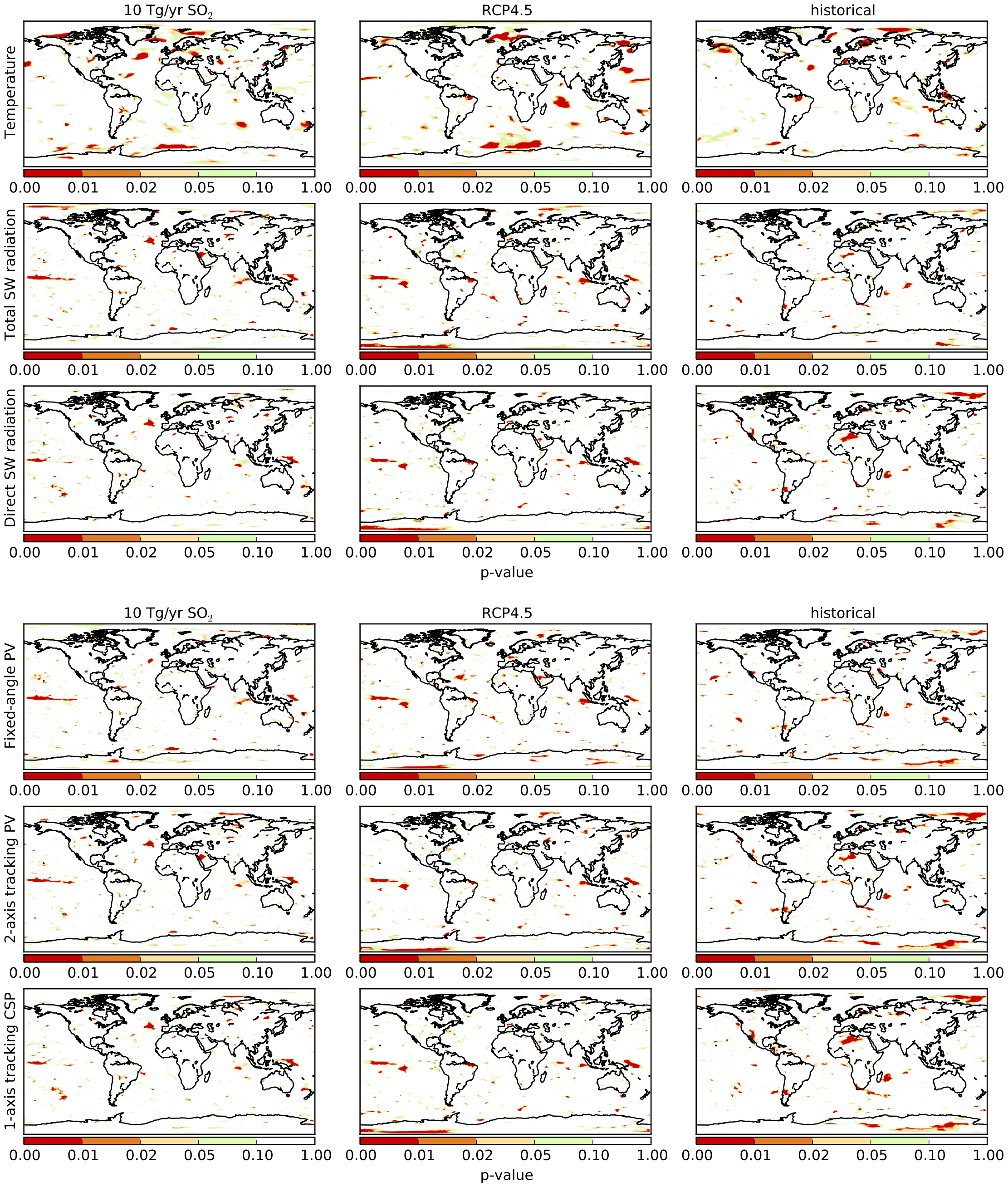

Figure 7.7: *p*-values of the D'Agostino-Pearson tests for normality for the temperature, total radiation and direct radiation (top figure) and fixed-angle PV, two-axis tracking PV and 1-axis tracking CSP (bottom figure) for the SSI, RCP4.5 and historical simulations

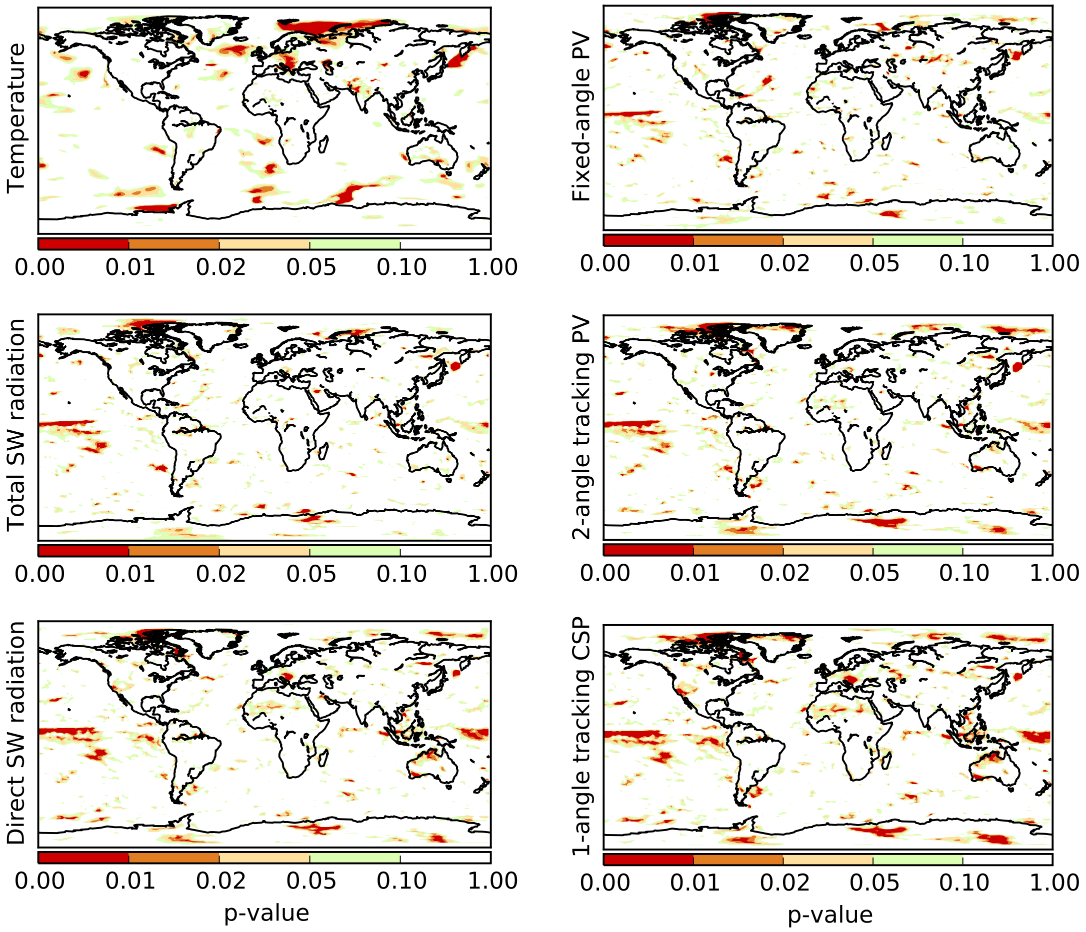

Figure 7.8: p-values of the Bartlett tests for equal variances between the SSI, RCP4.5 and historical simulations for the temperature, total radiation and direct radiation (left figure) and fixed-angle PV, two-axis tracking PV and 1-axis tracking CSP (right figure)

shows a significant impact on CSP energy output worldwide with declines in the range of over 10% for some land areas compared to a baseline climate change simulation without SSI (RCP4.5). The changes are spatially variable, with a large decrease in power output expected across the equatorial band under the SSI runs, but are negative almost everywhere. This is to be expected due to the attenuation of direct radiation. The effect of SSI on PV is less, due to the ability of PV to utilise diffuse radiation which increases under SSI. If geoengineering were to be seriously considered, the knock-on effect of likely reduction in solar power should be built in to future forecasts.

The results presented in this chapter are from one climate model with sulphate injection at particular latitude and altitude. Firstly, different GCMs may show different dispersion effects and climate responses. Secondly, under different sulphate injection regimes, it is likely that the regional changes will be different to the equatorial injection modelled in this study (Jones *et al.*, 2010). Sulphate injection can be planned to achieve specific climate goals, for example the restoration of Arctic sea ice by distributing SO_2 at high latitudes (Jackson *et al.*, 2015). With this in mind, this work shows that there is a significant negative difference in solar power output for CSP for the 2040–2059 timeframe between a climate geoengineered with SSI and the RCP4.5 moderate radiative forcing scenario. These differences are statistically significant for the important solar energy generating regions of Africa, the Middle East, India, western USA and the northern half of Latin America. The differences for tracking PV are less negative and are significant in fewer regions, whereas for fixed PV the differences are small. The positive changes between the RCP4.5 simulation and the 1986–2005 climatology are significant where they are greatest in magnitude. Whilst local topographical and microclimatic effects, along with human, economic and environmental considerations, will always dominate decisions on siting solar PV and CSP arrays, climate models provide an informative picture of the future changes to solar energy output that could be expected.

The changes in CSP output are broadly in line with what is observed by Murphy (2009) in the years following the Mount Pinatubo eruption. Under a climate permanently forced by a stratospheric aerosol loading similar to about half of that seen in the Mount Pinatubo eruption, CSP output is reduced (compared to RCP4.5) over most land areas in the range of 3–10% compared to the 20% suggested by Murphy.

Comparing the baseline climate change scenario of RCP4.5 to the historical over the 2040–2059 (fig. 7.4c and f) with the changes seen under RCP8.5 for 2080–2100 assessed in chapter 6, it can be seen that the direction of change largely agrees between the two studies. This should be expected as the climate models used are from the same model family. Given the higher radiative forcing and longer timeframe for the chapter 6 study, the magnitude of the changes in the RCP8.5 simulation are generally greater.

Chapter 8

Conclusions and further work

In this thesis, the global changes in solar energy in future climate scenarios are investigated and models developed that can provide resource assessments given a variety of input data. The main findings are summarised, applications of the research are discussed, and limitations and extensions to future work suggested.

8.1 Research summary, applications, and key findings

This results in this thesis can broadly be divided into solar resource estimation in present and recent past climates (chapters 3–5) and resource estimation in future climates (chapters 6 and 7). Here, the impact and novelty of each of the chapters 3–7 is discussed.

8.1.1 Phase change materials

Chapter 3 shows the significant effect of module operating temperature on PV energy output. Using phase change materials to mitigate the rise in temperature throughout the course of the day, it is shown that gains in PV power output of up to 6% are possible. Areas where PV/PCM is predicted to be most beneficial are largely coincident with regions that experience high annual insolation, typically between 30°N and 30°S, and the optimal melting temperature of the PCM is influenced by the mean annual temperature. While several modelling and experimental studies have considered PV/PCM, no previous analyses have explored this globally using diurnally- and seasonally-varying weather conditions.

While it is shown that under the current levelised cost of electricity for solar energy and PCM material prices such a strategy would not be cost effective in general, there may be benefits to using PCM-enhanced cooling for technologies where material costs and cooling demands are higher than for flat-plate crystalline silicon solar modules. One suggestion would be using PCM as a heat sink in concentrating multijunction solar cells.

Furthermore, PCM-cooling may be one way to mitigate any losses in PV performance output due to temperature changes in future climates.

8.1.2 Cloud transmission statistics

Chapter 4 describes the statistics of solar transmission through clouds, compared to that of a clear sky. This variable is denoted the clear-sky index. The analysis was performed for cloud fractions ranging from clear sky to fully overcast for 63 sites in the UK, encompassing over one million data hours. This extends previous work that either provided a one-to-one relationship between cloud fraction and solar transmission (e.g. Kasten & Czeplak (1980)) or the statistical distributions of clearness or clear-sky index by its long-term means (e.g. Graham & Hollands (1990)). Additionally, it provides an estimate of solar radiation at sites where hourly cloud fraction is known but solar radiation characteristics are not.

A theoretical model, based on radiative transfer, was used to determine clear-sky irradiance. For high solar elevation angles, the clear-sky model performs well compared to observations from the UK Met Office MIDAS network of ground irradiance measurements for okta 0 (cloudless) skies. Although the modal value of clear-sky index is close to one, there is a heavy left-tail to observations of clear sky irradiance which could be due to unrecorded cloudiness or high atmospheric turbidity. At lower solar elevation angles, the spread of clear-sky index values becomes greater.

The distributions of clear-sky index by cloud fraction show a progression from left-skewed at okta 1 (one-eighth cloud coverage), to approximately symmetric at okta 6–7, to right-skewed at okta 8. While the shape of the distributions are elevation-angle dependent, good fits are obtained for all datapoints with solar elevation angle above 20° using a skew-*t* distribution for oktas 0–4 and a generalised gamma distribution for oktas 5–8 and the fog-/haze-obscured sky state. As these distributions are complex, simpler distributions to represent the clear-sky transmission and transmission through clouds for partially cloudy, mostly cloudy and overcast skies are suggested for fast computations. These simpler statistics of clear-sky index form the basis of a stochastic 1-minute irradiance generator in Bright *et al.* (2015) that uses an observationally-derived Markov chain model to determine the next hour's cloud fraction based on the current hour. This 1-minute model can be used in demand modelling and grid applications.

8.1.3 Integrated radiance method for plane irradiance

In chapter 5, the use of radiative transfer modelling is extended to cloudy skies. A model is introduced that uses satellite-derived inputs of cloud, atmosphere and surface albedo to generate a surface radiance field. The surface radiances are integrated numerically to calculate irradiation on a tilted plane. The method is referred to as IntRad.

While including clouds within radiative transfer models is a well-founded problem (indeed, is used by all climate models), including clouds is seldom used to model irradiances for solar energy purposes. On the other hand, clear-sky radiation is frequently used in solar energy applications (e.g. SPCTRAL2 (Bird & Riordan, 1986), SMARTS2 (Gueymard, 1995) and SPECMAGIC (Mueller *et al.*, 2012)). There appears to be no good reason why clouds are not included in radiative transfer models for large-scale solar irradiance modelling, as clouds are often included as a broadband adjustment after the clear-sky calculation (e.g. Cano *et al.* (1986); Mueller *et al.* (2004, 2012)), so it is unlikely to be less accurate than including clouds within the radiation calculation. The assumption is tested by comparing horizontal irradiation totals from the model to those measured by the high-quality network of pyranometers worldwide from the BSRN network, as well as a selection of MIDAS sites that were used in chapter 4; overall agreement is shown to be good, although some sites differed by more than 15%, principally those at high altitude or latitude.

The inclusion of clouds inside the radiative transfer calculation is both different to other methods, and necessary for calculation of the ground-level diffuse radiance field for tilted irradiance. The tilt method presented is different to "classical" tilt models in the literature, which tend to use combinations of the direct normal irradiance and diffuse horizontal irradiance. IntRad does not calculate the tilted irradiance as a function of the DNI and DHI but directly from the radiative transfer calculation. One advantage of this method is that it can be used to predict solar energy resource in areas where horizon shading is significant, by modifying the horizon radiances to take into account the shading. Such a method has been used by Gooding *et al.* (2015), with encouraging early results, with proposed extension to city-scale solar energy resource modelling.

8.1.4 Solar energy resource in a future climate

Chapter 6 extends the radiative transfer modelling of solar radiation further by considering spectrally-resolved irradiance, and how the solar spectrum affects PV semiconductors with differing bandgaps. This is one further advantage of including clouds within radiative transfer models, as the solar transmission through clouds is spectrally dependent. This chapter also introduces a future climate scenario for the first time. Previously, the effect of climate change on solar energy resource has been investigated regionally or globally in a handful of studies (e.g. Crook *et al.* (2011); Wild *et al.* (2015)), where the broadband solar radiation is taken as the main variable of interest. Here, two advancements are made. Firstly, the spectral breakdown of solar radiation is considered. As PV materials are semiconductors with a spectral response function, different incident solar wavelengths contribute to the output power with different weights. Secondly, as climate and radiative transfer models provide totals of horizontal irradiance, a tilt model is applied to the calculated irradiance based on the optimal tilt calculated using the Barker & Christensen (2001) method. This will better represent real-world conditions, in which solar panel tilts are optimised to maximise incident radiation and are seldom aligned horizontally.

Using the spectral transmission of solar radiation, the future climate changes for RCP8.5, a high radiative forcing scenario, are shown to exceed 5% in Europe and western Russia, the east coast of the US, eastern China, Japan, and much of Latin America over the timeframe of 2080–2100 compared to 1985–2005. Decreases of 5% or more can be seen in the northern and southern polar regions, central Africa, western India and north-west China. These changes are mostly due to clouds and are replicated whichever semiconductor material is used, implying that the spectral effect is small. However, relative differences compared to c-Si are observed, with higher semiconductor bandgaps showing more positive changes than c-Si between present and future climates, and vice versa for lower bandgap materials.

These forecasts can help to drive solar energy siting decisions. While the changes seen are not significant enough for previously low-resource areas such as western Europe to overtake high-resource areas like India, as investment decisions are made based on an expected rate of return, and, as argued by Gueymard (2009) and Pašičko *et al.* (2012), a difference of a few percent in expected energy output can make the difference between whether a project is financially viable or not.

8.1.5 Applications of geoengineering

In chapter 7, the future climate scenarios are extended to consider geoengineering with stratospheric sulphate aerosols. All future climate change studies on solar energy to date have considered scenarios where no large-scale deliberate attempts to offset global temperature changes have been considered. Geoengineering is one extreme method that has been proposed to reduce surface temperatures in the absence of an effective global climate policy or adverse climate changes becoming apparent. Under a geoengineering scenario, attenuation of direct sunlight by the aerosol layer is detrimental for concentrating solar power (CSP) in many of the regions where it is currently most appropriate and cost-effective, compared to both the historical (1985–2005) and future scenario without geoengineering (RCP4.5). The change in total radiation is less negative than the change in direct radiation, and the effect of geoengineering on fixed-angle PV is small: the decrease in radiation is partially offset by the decrease in surface temperature, which increases PV efficiency. 2-axis tracking PV, in which the PV collector is aligned normal to the solar beam, is an intermediate case; increases in output for Europe, the eastern US and east Asia are still seen in the SSI scenario, but are less positive than without geoengineering.

The locations of significant changes in energy output increase and decrease, in the non-geoengineering scenarios, are similar between chapters 6 and 7. This would be expected as the climate model scenarios are from the same family.

8.2 Limitations, and ideas for future work

The work presented in chapters 3, 5, 6 and 7 has been performed on GCM grids, the smallest being $1^\circ \times 1^\circ$ if the MODIS albedo dataset is discounted. The results presented apply to very large areas ($1^\circ \approx 110$ km at the equator). Within a 1° grid square there are likely to be many different regional climates. The results reported are grid-cell averages and there can be much variation within the cell on scales of a few km or even less. In urban areas, the aerosol profile is very different to rural areas and surface radiation will differ as a result, most likely with a reduction in total irradiance and increase in diffuse irradiance as a consequence of aerosol scattering. In chapters 6 and 7, to obtain an estimate for the likely range of future climate outcomes, more regionally-applicable results can be determined using RCMs. This has been performed by a few authors in some locations as detailed in chapter 6. It is not practical to do RCM-scale simulations globally, due to the additional computing time required. Therefore RCM simulations can only be performed for small regions of interest.

More specific chapter-by-chapter suggestions are described below.

8.2.1 Phase change materials

The results in chapter 3 provide an initial assessment of where PV/PCM systems could be worthwhile. To provide more detailed analysis, specific observed weather conditions for the site in question should be obtained. If this is not possible, a longer-term period of data from the ECMWF dataset should be used, and every day of a full year of data rather than the diurnal average.

The validation of the PV/PCM energy balance model with a real-world experiment is desirable. This was attempted with two one-cell PV/PCM systems in India. Due to equipment failures it was not possible to perform a proposed validation in the time available. Thermocouple data obtained from the PV/PCM modules, the bottom of the PCM boxes, and a reference cell, show that the desired thermal regulation effect was observed in the

PV/PCM module over the course of one afternoon. To infer robust conclusions it would be necessary to run the experiment over a longer time period, and ideally to obtain power output data alongside temperature data. Another worthwhile validation technique would be to use a 2D or 3D computational fluid dynamics package to simulate the convection within the phase change layer and the moving boundary of the phase change front.

The simulation in chapter 3 considered an open-mount PV/PCM module on a horizontal panel tilt. If tilt angle was optimised, the increase in plane-of-array irradiance would drive up module operating temperatures, facilitating the need for more cooling. In building-integrated and building-mounted photovoltaics, operating temperatures are higher than in open mounts because of the lack of free convection from the reverse side of the solar module. If these additions to the model were made, it is expected that optimal PCM temperatures would be higher than those reported in the chapter. It is not certain whether the change in power output between PV/PCM and reference modules under these different assumptions would change.

8.2.2 Cloud transmission statistics

The reason for the high number of observations with low clear-sky index during hours of okta 0 at low solar elevation angles would be beneficial to investigate further. One reason that may account for much of the difference relates to whether the observation was made by a human observer or a cloud-base laser recorder (ceilometer). There may be, in addition, combinations of meteorological conditions which cause such results to occur. For example, where pyranometers are not ventilated, dew or ice can build up on the inside of the instrument resulting in lower readings than the actual irradiance level. This can be a particular problem in the morning on clear days. Correlating clear-sky index observations with humidity (to estimate atmospheric absorption due to water vapour), dew point temperature and pressure (to estimate likelihood of fog near ground level that is not thick enough to prevent the sky being obscured, or likely instances of ice and dew buildup), and in weather stations where both a human observer and a cloud-base laser recorder is present, data from the automated device (to determine whether the past hour was fully cloud-free), may provide insight into some of these low observations.

In order to better integrate the statistics of cloud coverage from observation with the work of the rest of the thesis, the statistics of cloud transmission could be extended to reanalysis and climate models. The long-term cloud fraction statistics from climate models, which are often only output on monthly, daily, or occasionally 3-hourly timesteps, could be used to downscale to hourly time periods by correlation with the statistics presented in chapter 4. There are a number of challenges to performing this; firstly cloud fraction in climate and reanalysis models is a continuous value instead of the discrete number of eighths from meteorological observations; secondly climate and reanalysis models use nadir-view cloud fraction whereas human observers are most likely to report hemispherical sky coverage; and thirdly, the grid cells used in GCMs are fairly large and may not represent all of the local variations exhibited in data such as the MIDAS series.

A natural extension would be to consider the effect of cloud type on the atmospheric transmission, which is recorded at MIDAS stations where there is a human observer present. The effect of cloud type on transmission has been investigated by Kasten & Czeplak (1980) and Matszuko (2012) for mean clear-sky index and irradiance by okta respectively, so the distributional approach taken in chapter 4 could be extended to cloud type.

8.2.3 Integrated radiance method for plane irradiance

Currently the largest drawback to the IntRad method in chapter 5 being used more generally is the computational time required to run the calculations, around 6 hours on a 2.3 GHz Linux machine. One way to speed up the calculation would be to use 5-dimensional lookup tables based on pre-calculated radiance fields for differing atmospheric loadings of water vapour and aerosols, cloud optical depths, zenith angle and relative azimuth. Pre-calculating such a lookup table would only need to be done once, but would be a large undertaking, and would need a suitable interpolation scheme. Cloud fraction could be used as a weighting between clear and overcast lookup tables.

The 1D implementation of clouds in the IntRad method is clearly an approximation to reality. Modelling including clouds is problematic, because clouds are difficult to resolve in time and space, and even approximately plane-parallel clouds such as marine stratocumulus can have a wide variety of internal variability in cloud droplet size and optical depth (Marshak & Davis, 2005). However, as previously mentioned, the approach taken is no less accurate than the current methods of broadband cloud adjustment.

A full 3D radiative transfer method to include clouds would be necessary for an accurate comparison. This has been attempted by comparison of the results with the UniSky model which is shown to agree well for low cloud fractions but not well for high cloud fractions. If a suitable 3D code could be used to resolve realistic clouds, it is unlikely that the kind of year-long simulations performed for selected locations as shown in chapter 5 could be performed in a reasonable amount of computing time. Such applications would again be limited to validating certain situations of the 1D model.

Validation of the model with actual observations of sky radiance would be beneficial. Such sky-radiance measuring devices exist, for example the EKO Sky Scanner. One future piece of work will investigate integrating the radiance distributions from the EKO sky scanner hosted at the NREL site and comparing this to the tilted irradiance measurements obtained from the same location. Sky radiance observations were used by Brunger & Hooper (1993) in their diffuse radiation model. A lower-cost alternative may be to set up a fish-eye camera at a location of interest and calibrate pixel brightness from the camera image to radiance values. This is a modern version of the photographic technique used by McArthur & Hay (1981). The calibration could be performed using a horizontally-mounted pyranometer, and ideally at least one tilted pyranometer.

Finally it should be noted that the IntRad method relies on the radiances calculated by the radiative transfer code being relatively free of error, which may not be true if the input data used in the radiative transfer model is not of high quality. Therefore, efforts could also be extended in the direction of obtaining higher-quality input data. This is most likely to rest on the sampling frequency of cloud fields, which are only obtained for 8-day averages twice per day in the method presented in chapter 5. With higher resolution data, it is likely that differences relative to high-quality ground measurements from pyranometers would reduce.

8.2.4 Solar energy resource in a future climate

There are several avenues for investigation in the method presented in chapter 6, and many climate effects of high significance have not been included. Snow, which settles on panels and blocks sunlight, will probably become less prevalent in many temperate, Arctic and high-latitude parts of the world in a warmer climate, likely leading to a small increase in performance during the winter. The atmospheric transmission effect of dust has been explored by its relationship to aerosol, but the effect of dust settling and blocking sunlight on panels is a major problem that has not been included. It was shown in chapter 6 that dry areas of the world such as India, the Sahara, and Australia may get dustier in the future, which may make this problem worse. A further intricacy of dust is that its settlement and transmission properties vary with tilt angle (Garg, 1974), and properly taking into account dust may lead to new relationships for optimal tilt. The frequency and intensity of precipitation affects how effectively settled dust is cleaned away from panels, which is another climate variable that can be built in to a more complex model. From a systems reliability perspective, it has been established for a long time that increased humidity leads to greater degradation in PV operating performance. Finally, as frequency and extremity of weather hazards such as hurricanes and hail storms are likely to change in the future, system downtime from storm damage could be built into the overall PV energy forecast. This may involve the use of probabilistic modelling.

As described in the summary of chapter 6, concentrating multi-junction PV provides an interesting case as each layer will be affected differently by changes in the solar spectrum. The highly concentrated solar irradiance that is focused on spectral cells leads to high operating temperatures, which affects efficiency. This may be mitigated using phase change materials, which as previously discussed due to the small size, high efficiency and high operating temperatures of concentrating multi-junction modules may make using PCMs cost-effective.

A very interesting and worthwhile investigation would be to produce a global map of optimised solar cell semiconductor bandgap, using the detailed balance method, in both present and future climates. The optimal bandgap question creates a good argument to continue to investigate other single-junction materials to c-Si. For example, perovskites ($CH_3NH_3Pb(I_{1-x}Br_x)_3$) are low-cost cells with bandgaps that are tuneable by varying the Br/I ratio (Noh *et al.*, 2012), and could be a promising future material if the problem of rapid degradation can be solved and baseline efficiencies start to approach those of c-Si (Niu *et al.*, 2015). In the short-to-medium term, the abundance, low material cost, and low toxicity of silicon relative to other established PV technologies means that it is unlikely to be overhauled as the dominant PV material.

If more time was available, producing the solar power output in a future climate for more climate models would lead to more robust measures of confidence similar to those performed by Wild *et al.* (2015) for broadband irradiance, and allow statistical measures of uncertainty to be applied.

8.2.5 Applications of geoengineering

The extension to other geoengineering methods besides stratospheric sulphate injection can be investigated. Surface albedo enhancement is interesting as it has potential to both increase the solar energy reflected to space (net cooling) and increase the energy available for solar modules at ground level due to both reflection onto tilted panels and backscattering from the atmosphere. The albedo of solar collectors themselves need to be built into calculations if deployment covers a significant fraction of a GCM/RCM grid cell. Solar PV panels tend to be dark and low albedo. CSP takes advantage of mirrors, which are high albedo. In both cases the conversion of solar radiation to electricity will alter the energy balance. Previous authors have modelled the extraction of energy from solar cells as an adjustment to surface albedo (Millstein & Menon, 2011). This raises the intriguing possibility that large solar arrays themselves could affect the regional climate.

As for chapter 6, uncertainty in climate variables is always one area in which confidence in future results can be questioned when using a single climate model. This could be improved by repeating the experiments for multiple CMIP5 climate models.

8.3 Concluding remarks

The thesis has shown that computational modelling can be a useful and flexible tool for solar energy resource prediction. A heat transfer model of a solar module shows the potential benefit of passive cooling with phase change materials. Radiative transfer models, which are used extensively in this thesis, underpin all of the radiation estimates available in reanalysis and climate models. A range of applications are shown, including clear-sky radiation modelling, multi-stream modelling for calculating tilted irradiance in all-sky atmospheres, and spectral irradiance modelling in different climate scenarios. In terms of applications to solar energy technologies, the output of these radiative transfer models can be combined with the spectral response of PV semiconductors to predict output power.

The effects of climate change on the solar energy resource differ by region and scenario, but are not insignificant. If a change of ±5% is used as a benchmark of significance, then these changes are seen in several places for PV by the end of the 21st Century under RCP8.5. For the middle of the century under RCP4.5, there are fewer regions were a ±5% change is seen for PV as the climate changes are less severe. It may be questioned why some of the marginal changes in PV and CSP energy output shown in chapters 6 and 7 are of great importance. One is that, if solar energy does become as widespread as the IEA predict, at 27% of global electricity supply by 2050, then a change in expected energy output of the order of 5% by 2050 becomes a significant amount in absolute terms. For the "moderate" RCP4.5 scenario, this is seen in a few places for fixed PV, is more widespread for tracking PV, and occurs over much of the world for CSP. Geoengineering does not have a large effect on PV output, but is critical for CSP in tropical areas. Where changes in projected PV output are negative, passive cooling by PCMs can mitigate some of the loss in power output caused by elevated module temperature. The assimilation of all of the separate components presented in this thesis into one model could provide the future solar energy resource for a climate situation of interest.

References

Aas, K., & Haff, I.H. 2006. The generalised hyperbolic skew Student's t-distribution. *Journal of Financial Econometrics*, **4**(2), 275–309.

Allahverdi, Ç., & Yükselici, M.H. 2008. Temperature dependence of absorption band edge of CdTe nanocrystals in glass. *New Journal of Physics*, **10**.

Almorox, J., Benito, M., & Hontoria, C. 2005. Estimation of monthly Ångström-Prescott equation coefficients from measured daily data in Toledo, Spain. *Renewable Energy*, **30**(6), 931–936.

Anderson, G.P., Clough, S.A., Kneizys, F.X., Chetwynd, J.H., & Shettle, E.P. 1986. *AFGL Atmospheric Constituent Profiles (0–120km)*. Air Force Geophysics Laboratory.

Andreas, A., & Stoffel, T. 1981. *NREL Solar Radiation Research Laboratory (SRRL): Baseline Measurement System (BMS)*. Tech. rept. DA-5500-56488. Golden, Colorado. `http://dx.doi.org/10.5439/1052221`.

Ångström, A. 1924. Solar and terrestrial radiation. Report to the international commission for solar research on actinometric investigations of solar and atmospheric radiation. *Quarterly Journal of the Royal Meteorological Society*, **50**(210), 121–126.

Ångström, A. 1929. On the atmospheric transmission of sun radiation and on dust in the air. *Geografiska Annaler*, **11**, 156–166.

Armstrong, S., & Hurley, W. G. 2010a. A thermal model for photovoltaic panels under varying atmospheric conditions. *Applied Thermal Engineering*, **30**(11), 1488–1495.

Armstrong, S., & Hurley, W.G. 2010b. A new methodology to optimise solar energy extraction under cloudy conditions. *Renewable Energy*, **35**, 780–787.

ASTM. 2003. *Standard tables for reference solar spectral irradiances: Direct normal and hemispherical on 37° tilted surface. Standard G173-03*.

Azzalini, A., & Capitanio, A. 2003. Distributions generated by perturbation of symmetry with emphasis on a multivariate skew t distribution. *Journal of the Royal Statistical Society B*, **65**, 367–389.

Badescu, V. 2002. 3D isotropic approximation for solar diffuse irradiance on tilted surfaces. *Renewable Energy*, **26**(2), 221–233.

Barker, G.M., & Christensen, C.B. 2001 (21–25 April). Effects of tilt and azimuth on annual incident solar radiation for United States locations. *In: Solar Forum*. Washington DC, USA.

Baruch, P., de Vos, A., Landsberg, P.T., & Parrott, J.E. 1995. On some thermodynamic aspects of photovoltaic solar energy conversion. *Solar Energy Materials and Solar Cells*, **36**, 201–222.

Baum, B.A., Heymsfield, A.J., Yang, P., & Bedka, S.T. 2005. Bulk scattering properties for the remote sensing of ice clouds. Part I: Microphysical data and models. *Journal of Applied Meteorology*, **44**, 1885–1895.

Baum, B.A., Yang, P., Heymsfield, A.J., Bansemer, A., Cole, B.H., Merrelli, A., & Wang, C. 2014. Ice cloud single-scattering property models with the full phase matrix at wavelengths from 0.2 to 100 μm. *Journal of Quantitative Spectroscopy & Radiative Transfer*, **146**, 123–139.

Bauwens, L., & Laurent, S. 2005. A new class of multivariate skew densities, with application to GARCH models. *Journal of Business and Economic Statistics*, **23**(3), 346–354.

Becker, S. 2001. Calculation of direct solar and diffuse radiation in Israel. *International journal of climatology*, **21**, 1561–1576.

Behrendt, T., Kuehnert, J., Hammer, A., Lorenz, E., Betcke, J., & Heinemann, D. 2013. Solar spectral irradiance derived from satellite data: A tool to improve thin film PV performance estimations? *Solar Energy*, **98**, 100–110.

Bellouin, N., Boucher, O., Haywood, J., Johnson, C., Jones, A., Rae, J., & Woodward, S. 2007. *Improved representation of aerosols for HadGEM2*. Tech. rept. Met Office Hadley Centre for Climate Change, Exeter, UK.

Bellouin, N., Mann, G.W., Woodhouse, M.T., Johnson, C., Carslaw, K.S., & Dalvi, M. 2013. Impact of the modal aerosol scheme GLOMAP-mode on aerosol forcing in the Hadley Centre Global Environmental Model. *Atmospheric Chemistry and Physics*, **13**(6), 3027–3044.

Belward, A., & Loveland, T. 1996. The DIS 1-km land cover data set. *Global Change, the IGBP Newsletter*, **27**.

Bendt, P., Collares-Pereira, M., & Rabl, A. 1981. The frequency distribution of daily insolation values. *Solar Energy*, **27**, 1–5.

Betts, T.R. 2004. *Investigation of photovoltaic device operation under varying spectral conditions*. Ph.D. thesis, Loughborough University.

Bird, R.E., & Hulstrom, R.L. 1981. *A simplified clear sky model for direct and diffuse insolation on horizontal surfaces*.

Bird, R.E., & Riordan, C. 1986. Simple solar spectral model for direct and diffuse irradiance on horizontal and tilted planes at the earth's surface for cloudless atmospheres. *Journal of Climate and Applied Meteorology*, **25**(1), 87–97.

Blanc, P., Espinar, B., Geuder, N., Gueymard, C., Meyer, R., Pitz-Paal, R., Reinhardt, B., Renné, D., Sengupta, M., Wald, L., & Wilbert, S. 2014. Direct normal irradiance related definitions and applications: The circumsolar issue. *Solar Energy*, **110**, 561–577.

Blanco-Muriel, M., Alarcón-Padilla, D. C., López-Moratalla, T., & Lara-Coira, M. 2001. Computing the solar vector. *Solar Energy*, **70**(5), 431–441.

Bluth, G.J.S., Doiron, S.D., Schnetzler, C.C., Krueger, A.J., & Walter, L.S. 1992. Global tracking of the SO_2 clouds from the June, 1991 Mount Pinatubo eruptions. *Geophysical Research Letters*, **19**(2), 151–154.

Boucher, O., Randall, D., Artaxo, P., Bretherton, C., Feingold, G., Forster, P., Kerminen, V.-M., Kondo, Y., Liao, H., Lohmann, U., Rasch, P., Satheesh, S.K., Sherwood, S., Stevens, B., & Zhang, X.Y. 2013. Clouds and Aerosols. *Chap. 7 of:* Stocker, T.F., Qin, D., Plattner, G.-K., Tignor, M., Allen, S.K., Boschung, J., Nauels, A., Xia, Y., Bex, V., & Midgley, P.M. (eds), *Climate Change 2013: The Physical Science Basis. Contribution of Working Group I to the Fifth Assessment Report of the Intergovernmental Panel on Climate Change*. Cambridge University Press, Cambridge, United Kingdom and New York, NY, USA.

BP. 2015. *Statistical review*. `http://www.bp.com/content/dam/bp/pdf/energy-economics/statistical-review-2015/bp-statistical-review-of-world-energy-2015-full-report.pdf`.

Branker, K., Pathak, M.J.M., & Pearce, J.M. 2011. A review of solar photovoltaic levelized cost of electricity. *Renewable and Sustainable Energy Reviews*, **15**(9), 4470–4482.

Bridgman, P. W. 1914. A complete collection of thermodynamic formulas. *Physical Review*, **3**, 273–281.

Bright, J.M., Smith, C.J., Taylor, P.G., & Crook, R. 2015. Stochastic generation of synthetic minutely irradiance time series derived from mean hourly weather observation data. *Solar Energy*, **115**, 229–242.

Brinkworth, B.J., & Sandberg, M. 2006. Design procedure for cooling ducts to minimise efficiency loss due to temperature rise in PV arrays. *Solar Energy*, **80**(1), 89–103.

Brinsfield, R., Yaramanoglu, M., & Wheaton, F. 1984. Ground level solar radiation prediction model including cloud cover effects. *Solar Energy*, **33**(6), 493–499.

Bristow, K.L., & Campbell, G.S. 1984. On the relationship between incoming solar radiation and daily maximum and minimum temperature. *Agricultural and Forest Meteorology*, **31**(2), 159–166.

Brunger, A.P., & Hooper, F.C. 1993. Anisotropic sky radiance model based on narrow field of view measurements of shortwave radiance. *Solar Energy*, **51**(1), 53–64.

Budyko, M.I. 1976. *Climatic Changes*. American Geophysical Union.

Buras, R. 2011. *RODENTS: Robert's Delta-Eddington Two-Stream*. C program included as part of the libRadtran distribution.

Burnett, D., Barbour, E., & Harrison, G.P. 2014. The UK solar energy resource and the impact of climate change. *Renewable Energy*, **71**, 333–343.

Cano, D., Monget, J.M., Albuisson, M., Guillard, H., Regas, N., & Wald, L. 1986. A method for the determination of the global solar radiation from meteorlogical satellite data. *Solar Energy*, **37**(1), 31–39.

Cao, S., & Sirén, K. 2014. Impact of simulation time-resolution on the matching of PV production and household electric demand. *Applied Energy*, **128**, 192–208.

Chandrasekhar, S. 1960. *Radiative transfer*. Dover.

Chang, Y.-P. 2009. Optimal design of discrete-value tilt angle of PV using sequential neural-network approximation and orthogonal array. *Expert systems with applications*, **36**, 6010–6018.

Chang, Y.-P. 2010. Optimal the tilt angles for photovoltaic modules using PSO method with nonlinear time-varying evolution. *Energy*, **35**, 1954–1963.

Cherrington, R., Goodship, V., Longfield, A., & Kirwan, K. 2013. The feed-in tariff in the UK: a case study focus on domestic photovoltaic systems. *Renewable Energy*, **50**, 421–426.

Choudhary, P.K., Sengupta, D., & Cassey, P. 2014. A general skew-t mixed model that allows different degrees of freedom for random effects and error distributions. *Journal of Statistical Planning and Inference*, **147**, 235–247.

Ciulla, G., Lo Brano, V., Cellura, M., Franzitta, V., & Milone, D. 2012. A Finite Difference Model of a PV-PCM System. *Energy Procedia*, **30**, 198–206.

Cohen, A. 2012. Solar Farms. `http://www.thehouseofsolar.com/solar-farms/`. Accessed 04.03.2013.

Crook, J.A., Jones, L.A., Forster, P.M., & Crook, R. 2011. Climate change impacts on future photovoltaic and concentrated solar power energy output. *Energy and Environmental Science*, **4**, 3101–3109.

Crutzen, P. 2006. Albedo enhancement by stratospheric sulfur injections: a contribution to resolve a policy dilemma? *Climatic Change*, **77**(3–4), 211–220.

D'Agostino, R., & Pearson, E.S. 1973. Tests for departure from normality. Empirical results for the distributions of b^2 and $\sqrt{b^1}$. *Biometrika*, **60**(3), 613–622.

D'Agostino, R.B. 1971. An omnibus test of normality for moderate and large size samples. *Biometrika*, **58**(2), 341–348.

Dahlback, A., & Stamnes, K. 1991. A new spherical model for computing the radiation field available for photolysis and heating at twilight. *Planetary and Space Science*, **39**(5), 671–683.

de Jong, R., & Stewart, D.W. 1993. Estimating global solar radiation from common meteorological observations in western Canada. *Canadian Journal of Plant Science*, **73**(2), 509–518.

DECC. 2011. *Planning our electric future: a White Paper for secure, affordable and low-carbon electricity*. `https://www.gov.uk/government/uploads/system/uploads/attachment_data/file/48129/2176-emr-white-paper.pdf`.

DECC. 2013. *Calculating Renewable Obligation Certificates (ROCs)*. `https://www.gov.uk/guidance/calculating-renewable-obligation-certificates-rocs`.

DECC. 2015a. *2010 to 2015 government policy: low carbon technologies*. `https://www.gov.uk/government/publications/2010-to-2015-government-policy-low-carbon-technologies/2010-to-2015-government-policy-low-carbon-technologies`.

DECC. 2015b (27 August). *Consultation on a review of the Feed-in Tariffs scheme*. `https://www.gov.uk/government/uploads/system/uploads/attachment_data/file/467074/Consultation_on_a_review_of_the_feed-in_tariff_scheme.pdf`.

DECC. 2015c. *Contracts for Difference (CFD) Allocation Round One Outcome*. `https://www.gov.uk/government/uploads/system/uploads/attachment_data/file/407059/Contracts_for_Difference_-_Auction_Results_-_Official_Statistics.pdf`.

Dee, D.P., Källén, E., Simmons, A.J., & Haimberger, L. 2011a. Comments on "Reanalyses Suitable for Characterizing Long-Term Trends". *Bulletin of the American Meteorological Society*,

92(1), 65–70.

Dee, D.P., Uppala, S.M., Simmons, A.J., Berrisford, P., Poli, P., Kobayashi, S., Andrae, U., Balmaseda, M.A., Balsamo, G., Bauer, P., Bechtold, P., Beljaars, A.C.M., van de Berg, L., Bidlot, J., Bormann, N., Delsol, C., Dragani, R., Fuentes, M., Geer, A.J., Haimberger, L., Healy, S.B., Hersbach, H., Hólm, E.V., Isaksen, L., Kållberg, P., Köhlera, M., Matricardi, M., McNally, A.P., Monge-Sanz, B.M., Morcrette, J.-J., Park, B.-K., Peubey, C., de Rosnay, P., Tavolato, C., Thépauta, J.-N., & Vitarta, F. 2011b. The ERA-Interim reanalysis: configuration and performance of the data assimilation system. *Quarterly Journal of the Royal Meteorological Society*, **137**, 553–597.

Deneke, H.M., Feijt, A.J., & Roebeling, R.A. 2008. Estimating surface solar irradiance from METEOSAT SEVIRI-derived cloud properties. *Remote Sensing of Environment*, **112**, 3131–3141.

Diedrich, H., Preusker, R., Lindstrot, R., & Fischer, J. 2015. Retrieval of daytime total columnar water vapour from MODIS measurements over land surfaces. *Atmospheric Measurement Techniques*, **8**, 823–836.

Dirnberger, D., Blackburn, G., Müller, B., & Reise, C. 2015. On the impact of solar spectral irradiance on the yield of different PV technologies. *Solar Energy Materials and Solar Cells*, **132**, 431–442.

Dlugokencky, E., & Tans, P. 2015. *Trends in atmospheric carbon dioxide, NOAA/ESRL*. `www.esrl.noaa.gov/gmd/ccgg/trends/`. Accessed 17.11.2015.

Dong, X., Minnis, P., Xi, B., Sun-Mack, S., & Chen, Y. 2008. Comparison of CERES-MODIS stratus cloud properties with ground-based measurements at the DOE ARM Southern Great Plains site. *Journal of Geophysical Research: Atmospheres*, **113**(D3). D03204.

Dubey, S., Sandhu, G.S., & Tiwari, G.N. 2009. Analytical expression for electrical efficiency of PV/T hybrid air collector. *Applied Energy*, **86**(5), 697–705.

Dudley, V.E. 1995. *Test Results Industrial Solar Technology Parabolic Trough Solar Collector*. Tech. rept. Sandia National Laboratories.

Ehnberg, J.S.G., & Bollen, M.H.J. 2005. Simulation of global solar radiation based on cloud observations. *Solar Energy*, **78**, 157–162.

Electricity Company of Ghana Limited. 2013. *Proposal for Tariff Review*. `http://www.ecgonline.info/images/Publication/ECG_STRATEGIC_ISSUES_AND_TARIFF_PROPOSALS.pdf`. Accessed 05.03.2014.

Energy Matters. 2013. Construction Of Mesquite Solar 1 Completed. `http://www.energymatters.com.au/index.php?main_page=news_article&article_id=3545`. Accessed 04.03.2013.

Erbs, D.G., Klein, S.A., & Duffie, J.A. 1982. Estimation of the diffuse radiation fraction for hourly, daily and monthly-average global radiation. *Solar Energy*, **28**(4), 293–302.

European Commission. 2012a. EU energy in figures—pocketbook 2012. Available from `http://ec.europa.eu/energy/publications/doc/2012_energy_figures.pdf`. Accessed 20.02.2014.

European Commission. 2012b. *Photovoltaic Geographical Information System (PVGIS)*. `http://re.jrc.ec.europa.eu/pvgis/index.htm`. Accessed 26.09.2014.

Evans, D. L. 1981. Simplified method for predicting photovoltaic array output. *Solar Energy*, **27**(6), 555–560.

Falls, L.W. 1974. The beta distribution: A statistical model for world cloud cover. *Journal of Geophysical Research*, **79**(9), 1261–1264.

Fan, L., & Khodadadi, J. M. 2011. Thermal conductivity enhancement of phase change materials for thermal energy storage: A review. *Renewable and Sustainable Energy Reviews*, **15**(1), 24–46.

First Solar. 2012. World's Largest Operational Solar PV Project, Agua Caliente, Achieves 250 Megawatts of Grid-Connected Power. Available from `http://investor.firstsolar.com/releasedetail.cfm?ReleaseID=706034`. Accessed 04.03.2013.

Forster, P.M., & Shine, K.P. 1995. A comparison of two radiation schemes for calculating ultraviolet radiation. *Quarterly Journal of the Royal Meteorological Society*, **121**, 1113–1131.

Fraunhofer ISE. 2015 (26 August). *Photovoltaics Report*. `https://www.ise.fraunhofer.de/de/downloads/pdf-files/aktuelles/photovoltaics-report-in-englischer-sprache.pdf`.

Fu, Q. 1996. An accurate parameterization of the solar radiative properties of cirrus clouds for climate models. *Journal of Climate*, **9**, 2058–2082.

Gaetani, M., Huld, T., Vignati, E., Monforti-Ferrario, F., Dosio, A., & Raes, F. 2014. The near-future availability of photovoltaic energy in Europe and Africa in climate-aerosol modeling experiments. *Renewable and Sustainable Energy Reviews*, **38**, 706–716.

Gagnon, L., Bélanger, C., & Uchiyama, Y. 2002. Life-cycle assessment of electricity generation options: The status of research in year 2001. *Energy Policy*, **30**(14), 1267–1278.

Garg, H.P. 1974. Effect of dirt on transparent covers in flat-plate solar energy collectors. *Solar Energy*, **15**, 299–302.

Gasteiger, J., Emde, C., Mayer, B., Buras, R., Buehler, S.A., & Lemke, O. 2014. Representative wavelengths absorption parameterization applied to satellite channels and spectral bands. *Journal of Quantitative Spectroscopy & Radiative Transfer*, **148**, 99–115.

Gil, V., Gaertner, M.A., Sanchez, E., Gallardo, C., Hagel, E., Tejeda, C., & de Castro, M. 2015. Analysis of interannual variability of sunshine hours and precipitation over Peninsular Spain. *Renewable Energy*, **83**, 680–689.

Gooding, J., Smith, C.J., Crook, R., & Tomlin, A.S. 2015 (14–18 September). Solar Resource Estimation using a radiative transfer with shading (RTS) model. *Pages 2800–2805 of: Proceedings of the 31st EU PVSEC Conference*. Hamburg, Germany.

Gottschalg, R., Infield, D.G., & Kearney, M.J. 2003. Experimental study of variations of the solar spectrum of relevance to thin film solar cells. *Solar Energy Materials and Solar Cells*, **79**(4), 527–537.

Gottschalg, R., Betts, T.R., Eeles, A., Williams, S.R., & Zhu, J. 2013. Influences on the energy delivery of thin film photovoltaic modules. *Solar Energy Materials and Solar Cells*, **119**, 169–180.

Gracia-Amillo, A., & Huld, T. 2013. *Performance comparison of different models for the estimation of global irradiance on inclined surfaces*. European Commission, Joint Research Centre, Via Enrico Fermi 2749, TP 450, 21027 Ispra (VA), Italy.

Graham, V.A., & Hollands, K.G.T. 1990. A method to generate synthetic hourly solar radiation globally. *Solar Energy*, **44**(6), 333–341.

Graham, V.A., Hollands, K.G.T., & Unny, T.E. 1988. A time series model for K_t with application to global synthetic weather generation. *Solar Energy*, **40**(2), 83–92.

Green, M.A., Emery, K., Hishikawa, Y., Warta, W., & Dunlop, E.D. 2014. Solar cell efficiency tables (version 44). *Progress in Photovoltaics: Research and Applications*, **22**, 701–710.

Gueymard, C. 1987. An anisotropic solar irradiance model for tilted surfaces and its comparison with selected engineering algorithms. *Solar Energy*, **38**(5), 367–386.

Gueymard, C. 1995. *SMARTS2, A simple model of the atmospheric radiative transfer of sunshine: algorithms and performance assessment*. Florida Solar Energy Center.

Gueymard, C. 2009. Direct and indirect uncertainties in the prediction of tilted irradiance for solar engineering applications. *Solar Energy*, **83**, 432–444.

Gueymard, C.A., & Wilcox, S.M. 2011. Assessment of spatial and temporal variability in the US solar resource from radiometric measurement and predictions from models using ground-based or satellite data. *Solar Energy*, **85**(5), 1068–1084.

Hammer, A., Heinemann, D., Hoyer, C., Kuhlemann, R., Lorenz, E., Müller, R., & Beyer, H.G. 2003. Solar energy assessment using remote sensing technologies. *Remote Sensing of Environment*, **86**, 423–432.

Hardiman, S.C., Butchart, N., Hinton, T.J., Osprey, S.M., & Gray, L.J. 2012. The effect of a well-resolved stratosphere on surface climate: differences between CMIP5 simulations with high and low top versions of the Met Office climate model. *Journal of Climate*, **25**(20), 7083–7099.

Hargreaves, G.L., Hargreaves, G.H., & Riley, J. 1985. Irrigation Water Requirements for Senegal River Basin. *Journal of Irrigation and Drainage Engineering*, **111**(3), 265–275.

Harrison, G.P., & Wallace, A.R. 2005. Sensitivity of wave energy to climate change. *IEEE Transactions on Energy Conversion*, **20**(4), 870–877.

Hassan, A. 2010. *Phase Change Materials for Thermal Regulation of Building Integrated Photovoltaics*. Ph.D. thesis, Dublin Institute of Technology.

Hassan, A., McCormack, S.J., Huang, M.J., & Norton, B. 2010. Evaluation of phase change materials for thermal regulation enhancement of building integrated photovoltaics. *Solar Energy*, **84**, 1601–1612.

Hassan, A., McCormack, S.J., Huang, M.J., & Norton, B. 2014. Energy and cost saving of a photovoltaic-phase change materials (PV-PCM) system through temperature regulation and performance enhancement of photovoltaics. *Energies*, **7**, 1318–1331.

Hassan, A., McCormack, S.J., Huang, M.J., Sarwar, J., & Norton, B. 2015. Increased photovoltaic performance through temperature regulation by phase change materials: Materials comparison in different climates. *Solar Energy*, **115**, 264–276.

Heinz, A., & Streicher, W. 2006 (31 May – 2 June). Application of Phase Change Materials and PCM slurries for thermal energy storage. *In: Ecostock Conference*. Pomona, USA.

Henderson-Sellers, A., Hughes, N.A., & Wilson, M. 1981. Cloud cover archiving on a global scale: a discussion of principles. *Bulletin of the American Meteorological Society*, **62**, 1300–1307.

Hendricks, J. H. C., & van Sark, W. G. J. H. M. 2011. Annual performance enhancement of building integrated photovoltaic modules by applying phase change materials. *Progress in Photovoltaics: Research and Applications*.

HM Government. 2008. *Climate Change Act 2008*. `http://www.legislation.gov.uk/ukpga/2008/27/contents`.

Hollands, K.G.T., & Suehrcke, H. 2013. A three-state model for the probability distribution of instantaneous solar radiation, with applications. *Solar Energy*, **96**, 103–1112.

Hottel, H.C., & Woertz, B.B. 1942. The performance of flat plate solar heat collectors. *Transcripts of the American Society of Mechanical Engineers*, 91–104.

Hu, Y.X., & Stamnes, K. 1993. An accurate parameterization of the radiative properties of water clouds suitable for use in climate models. *Journal of Climate*, **6**, 728–742.

Huang, M. J. 2011. The effect of using two PCMs on the thermal regulation performance of BIPV systems. *Solar Energy Materials and Solar Cells*, **95**(3), 957–963.

Huang, M. J., Eames, P. C., & Norton, B. 2004. Thermal regulation of building-integrated photovoltaics using phase change materials. *International Journal of Heat and Mass Transfer*, **47**(12-13), 2715–2733.

Huang, M. J., Eames, P. C., & Norton, B. 2006. Phase change materials for limiting temperature rise in building integrated photovoltaics. *Solar Energy*, **80**(9), 1121–1130.

Hubanks, P.A., King, M.D., Platnick, S.A., & Pincus, R.A. 2008. *MODIS atmosphere L3 gridded product algorithm theoretical basis document*. `http://modis-atmos.gsfc.nasa.gov/_docs/L3_ATBD_C6.pdf`.

Huld, T., Müller, R., & Gambardella, A. 2012. A new solar radiation database for estimating PV performance in Europe and Africa. *Solar Energy*, **86**, 1803–1815.

IEA. 2014a. *Key World Energy Statistics*.

IEA. 2014b. *Technology Roadmap Solar Photovoltaic Energy*.

IEA. 2014c. *Technology Roadmap Solar Thermal Electricity*.

IEA. 2015a. *Energy and climate change*.

IEA. 2015b. *Excerpt from energy balances of non-OECD countries*.

IEA-PVPS. 2014. *Snapshot of global PV markets*.

Indian Express (The). 2012. *Gujurat Hikes Its Power Tariff*. `http://archive.indianexpress.com/news/gujarat-hikes-its-power-tariff/957299/`. Accessed 04.03.2013.

Ineichen, P., & Perez, R. 2002. A new airmass independent formulation for the Linke turbidity coefficient. *Solar Energy*, **73**, 151–157.

IPCC. 2013. Summary for Policymakers. *In:* Stocker, T.F., Qin, D., Plattner, G.-K., Tignor, M., Allen, S.K., Boschung, J., Nauels, A., Xia, Y., Bex, V., & Midgley, P.M. (eds), *Climate Change 2013: The Physical Science Basis. Contribution of Working Group I to the Fifth Assessment Report of the Intergovernmental Panel on Climate Change*. Cambridge, United Kingdom and New York, NY, USA: Cambridge University Press.

IPCC. 2014. Technical Summary. *In:* Edenhofer, O., Pichs-Madruga, R., Sokona, Y., Farahani, E., Kadner, S., Seyboth, K., Adler, A., Baum, I., Brunner, S., Eickemeier, P., Kriemann, B., Savolainen, J., Schlömer, S., von Stechow, C., Zwickel, T., & Minx, J. C. (eds), *Climate Change 2014: Mitigation of Climate Change. Contribution of Working Group III to the Fifth Assessment Report of the Intergovernmental Panel on Climate Change*. Cambridge, United Kingdom and New York, NY, USA: Cambridge University Press.

IRENA. 2014. *Renewable power generation costs in 2014*. `http://www.irena.org/DocumentDownloads/Publications/IRENA_RE_Power_Costs_2014_report.pdf`.

Ishitani, Y., Minagawa, S., & Tanaka, T. 1994. Temperature dependence of the band-gap energy of disordered GaInP. *Journal of Applied Physics*, **75**, 5326–5331.

Jackson, L.S., Crook, J.A., Jarvis, A., Leedal, D., Ridgwell, A., Vaughan, N., & Forster, P.M. 2015. Assessing the controllability of Arctic sea ice extent by sulfate aerosol geoengineering. *Geophysical Research Letters*, **42**(4), 1223–1231.

Jaeger, C.C., & Jaeger, J. 2010. Three views of two degrees. *Regional Environmental Change*, **11**(Suppl. 1), S15–S26.

Jones, A., Haywood, J., Boucher, O., Kravitz, B., & Robock, A. 2010. Geoengineering by stratospheric SO_2 injection: results from the Met Office HadGEM2 climate model and comparison with the Goddard Institute for Space Studies ModelE. *Atmospheric Chemistry and Physics*, **10**(13), 5999–6006.

Jones, A.D., & Underwood, C.P. 2001. A thermal model for photovoltaic systems. *Solar Energy*, **70**, 349–359.

Jones, C.D., Hughes, J.K., Bellouin, N., Hardiman, S.C., Jones, G.S., Knight, J., Liddicoat, S., O'Connor, F.M., Andres, R.J., Bell, C., Boo, K.-O., Bozzo, A., Butchart, N., Cadule, P., Corbin, K.D., Doutriaux-Boucher, M., Friedlingstein, P., Gornall, J., Gray, L., Halloran, P.R., Hurtt, G., Ingram, W.J., Lamarque, J.-F., Law, R.M., Meinshausen, M., Osprey, S., Palin, E.J., Parsons Chini, L., Raddatz, T., Sanderson, M.G., Sellar, A.A., Schurer, A., Valdes, P., Wood, N., Woodward, S., Yoshioka, M., & Zerroukat, M. 2011. The HadGEM2-ES implementation of CMIP5 centennial simulations. *Geoscientific Model Development*, **4**(3), 543–570.

Jones, E., Oliphant, T., & Peterson, P. 2015. *SciPy: Open source scientific tools for Python*.

Jones, M.C., & Faddy, M.J. 2003. A skew extension of the t-distribution, with applications. *Journal of the Royal Statistical Society B*, **65**(1), 159–174.

Jones, P.A. 1992. Cloud-cover distributions and correlations. *Journal of Applied Meteorology*, **31**, 732–741.

Joseph, J.H., Wiscombe, W.J., & Weinman, J.A. 1976. The Delta-Eddington approximation for radiative flux transfer. *Journal of the Atmospheric Sciences*, **33**, 2452–2459.

Jurado, M., Caridad, J.M., & Ruiz, V. 1995. Statistical distribution of the clearness index with radiation data integrated over five minute intervals. *Solar Energy*, **55**(6), 469–473.

Kalogirou, S.A. 2004. Solar thermal collectors and applications. *Progress in Energy and Combustion Science*, **30**(3), 231–295.

Kasten, F., & Young, A.T. 1989. Revised optical air mass tables and approximation formula. *Applied Optics*, **28**(22), 4735–4738.

Kasten, Fritz, & Czeplak, Gerhard. 1980. Solar and terrestrial radiation dependent on the amount and type of cloud. *Solar Energy*, **24**(2), 177–189.

Kato, S., Ackerman, T.P., Mather, J.H., & Clothiaux, E.E. 1999. The k-distribution method and correlated-k approximation for a shortwave radiative transfer model. *Journal of Quantitative*

Spectroscopy & Radiative Transfer, **62**, 109–121.

Kaufman, Y.J., & Gao, B.C. 1992. Remote sensing of water vapor in the near IR from EOS/MODIS. *IEEE Transactions on Geoscience and Remote Sensing*, **30**(5), 871–884.

Kearney, D. 1989. Solar Electric Generating Stations (SEGS). *Power Engineering Review, IEEE*, **9**(8), 4–8.

Kenisarin, M., & Makhamov, K. 2007. Solar energy storage using phase change materials. *Renewable and Sustainable Energy Reviews*, **11**, 1913–1965.

Key, J.R., Yang, P., Baum, B.A., & Nasiri, S.L. 2002. Parameterization of shortwave ice cloud optical properties for various particle habits. *Journal of Geophysical Research: Atmospheres*, **107**(D13), AAC 7–1–AAC 7–10.

King, M.D., & Harshvarhan. 1986. Comparative Accuracy of Selected Multiple Scattering Approximations. *Journal of the Atmospheric Sciences*, **43**, 784–801.

Klucher, T.M. 1979. Evaluation of models to predict insolation on tilted surfaces. *Solar Energy*, **23**, 111–114.

Köberle, A.C., Gernaat, D.E.H.J., & van Vuuren, D.P. 2015. Assessing current and future techno-economic potential of concentrated solar power and photovoltaic electricity generation. *Energy*, **89**, 739–756.

Kocifaj, M. 2012. Angular distribution of scattered radiation under broken cloud arrays: An approximation of successive orders of scattering. *Solar Energy*, **86**, 3575–3586.

Kocifaj, M. 2015. Unified model of radiance patterns under arbitrary sky conditions. *Solar Energy*, **115**, 40–51.

Kocifaj, M., & Fečko, S. 2014. *UniSky Simulator*. `http://www.unisky.sav.sk`.

Koronakis, P.S. 1986. On the choice of the angle of tilt for south facing solar collectors in the Athens basin area. *Solar Energy*, **36**(3), 217–225.

Kost, C., Mayer, J.N., Thomsen, J., Hartmann, N., Senkpiel, C., Philipps, S., Nold, S., Lude, S., Saad, N., & Schlegl, T. 2013. *Levelized Cost of Electricity Renewable Energy Technologies*.

Krauter, S. 2004. Increased electrical yield via water flow over the front of photovoltaic panels. *Solar Energy Materials and Solar Cells*, **82**(1-2), 131–137.

Kravitz, B., Robock, A., Boucher, O., Schmidt, H., Taylor, K.E., Stenchikov, G., & Schulz, M. 2011. The Geoengineering Model Intercomparison Project (GeoMIP). *Atmospheric Science Letters*, **12**(2), 162–167.

Kylling, A., Stamnes, K., & Tsay, S.-C. 1995. A reliable and efficient two-stream algorithm for spherical radiative transfer: Documentation of accuracy in realistic layered media. *Journal of Atmospheric Chemistry*, **21**, 115–150.

Labouret, A., & Villoz, M. 2010. *Solar photovoltaic energy*. London: Institution of Engineering and Technology.

Lacis, A.A., & Mishchenko, M.I. 1995. Climate forcing, climate sensitivity, and climate response: a radiative model perspective on atmospheric aerosols. *Pages 11–42 of:* Charlson, R.J., & Heintzenberg, J. (eds), *Aerosol forcing of climate*. John Wiley & Sons.

Lamberg, P., Lehtiniemi, R., & Henell, A.M. 2004. Numerical and experimental investigation of melting and freezing processes in phase change material storage. *International Journal of Thermal Sciences*, **43**(3), 277–287.

Lenardic, D. 2011. Large-scale photovoltaic power plants ranking 1–50. `http://www.pvresources.com/PVPowerPlants/Top50.aspx`. Accessed 04.03.2013.

Lenton, T.M., & Vaughan, N.E. 2009. The radiative forcing potential of different climate geoengineering options. *Atmospheric Chemistry and Physics*, **9**, 5539–5561.

Lillo Bravo, I., Pérez, M. Silva, & Gómez-Caminero, M.L. 2011. Use of phase change materials in photovoltaic modules with solar concentration up to 2X. *Pages 634–639 of: 26th European Photovoltaic Solar Energy Conference and Exhibition.*

Liu, B.H.Y., & Jordan, R.C. 1962. Daily insolation on surfaces tilted towards the equator. *Trans ASHRAE*, **53**, 526–541.

Liu, B.Y.H., & Jordan, R.C. 1960. The interrelationship and characteristic distribution of direct, diffuse and total solar radiation. *Solar Energy*, **4**(3), 1–19.

Liu, J., Schaaf, C., Strahler, A., Jiao, Z., Shuai, Y., Zhang, Q., Roman, M., Augustine, J.A., & Dutton, E.G. 2009. Validation of Moderate Resolution Imaging Spectroradiometer (MODIS) albedo retrieval algorithm: Dependence of albedo on solar zenith angle. *Journal of Geophysical Research: Atmospheres*, **114**(D1). D01106.

Liu, X., Hoekman, S.K., Robbins, C., & Ross, P. 2015. Lifecycle climate impacts and economic performance of commercial-scale solar PV systems: A study of PV systems at Nevadas Desert Research Institute (DRI). *Solar Energy*, **119**, 561–572.

Loferski, J.J. 1956. Theoretical considerations governing the choice of the optimum semiconductor for photovoltaic solar energy conversion. *Journal of Applied Physics*, **27**, 777–784.

Lohmann, S., Schillings, C., Mayer, B., & Meyer, R. 2006. Long-term variability of solar direct and global radiation derived from ISCCP data and comparison with reanalysis data. *Solar Energy*, **80**, 1390–1401.

López-Navarro, A., Biosca-Taronger, J., Corberán, J.M., Peñalosa, C., Lázaro, A., Dolado, P., & Payá, J. 2014. Performance characterization of a PCM storage tank. *Applied Energy*, **119**, 151–162.

Lorenzo, E. 2003. Energy collected and delivered by PV modules. *Chap. 20, pages 905–970 of:* Luque, A., & Hegedus, S. (eds), *Handbook of photovoltaic science and engineering*. John Wiley and Sons.

Louche, A., Peri, G., & Iqbal, M. 1986. An analysis of Linke turbidity factor. *Solar Energy*, **37**, 393–396.

Loveday, D. L., & Taki, A. H. 1996. Convective heat transfer coefficients at a plane surface on a full-scale building facade. *International Journal of Heat and Mass Transfer*, **39**(8), 1729–1742.

Ma, J. 2011. On-grid electricity tariffs in China: Development, reform and prospects. *Energy Policy*, **39**, 2633–2645.

Maiti, S., Banerjee, S., Vyas, K., Patel, P., & Ghosh, P. K. 2011. Self regulation of photovoltaic module temperature in V-trough using a metal-wax composite phase change matrix. *Solar Energy*, **85**(9), 1805–1816.

Malvi, C. S., Dixon-Hardy, D. W., & Crook, R. 2011. Energy balance model of combined photovoltaic solar-thermal system incorporating phase change material. *Solar Energy*, **85**(7), 1440–1446.

Markvart, T., & Castañer, L. 2005. IIa-1 - Principles of solar cell operation. *Pages 5–27 of:* Castañer, L., & Markvart, T. (eds), *Solar Cells: Materials, Manufacture and Operation*. Oxford: Elsevier Science.

Marshak, A., & Davis, A.B. (eds). 2005. *3D Radiative Transfer in Cloudy Atmospheres*. Springer.

Martin, G.M., Bellouin, N., Collins, W.J., Culverwell, I.D., Halloran, P.R., Hardiman, S.C., Hinton, T.J., Jones, C.D., McDonald, R.E., McLaren, A.J., O'Connor, F.M., Roberts, M.J., Rodriguez, J.M., Woodward, S., *et al.* 2011. The HadGEM2 family of Met Office Unified Model climate change configurations. *Geoscientific Model Development*, **4**(3), 723–757.

Matszuko, Dorota. 2012. Influence of the extent and genera of cloud cover on solar radiation intensity. *International Journal of Climatology*, **32**, 2403–2414.

Mayer, B., & Kylling, A. 2005. Technical note: The libRadtran software package for radiative transfer calculations – description and examples of use. *Atmospheric Chemistry and Physics*, **5**, 1855–1877.

Mayer, B., Kylling, A., Emde, C., Hamann, U., & Buras, R. 2012. *libRadtran user's guide*. `http://www.libradtran.org`.

McArthur, L.J.B., & Hay, J.E. 1981. A technique for mapping the distribution of diffuse solar radiation over the sky hemisphere. *Journal of Applied Meteorology*, **20**(4), 421–429.

McGlade, C., & Ekins, P. 2015. The geographical distribution of fossil fuels unused when limiting global warming to 2°C. *Nature*, **517**, 187–190.

McLaughlin, M.P. 2014. *Compendium of common probability distributions*. `http://www.causascientia.org/math_stat/Dists/Compendium.pdf`.

McMahon, S. 2012. Gujarat's 214MW solar park named as Asia's largest single PV plant. `http://www.pv-tech.org/news/gujarats_214mw_solar_park_named_as_asias_largest_single_pv_plant`. Accessed 17.11.2015.

McPeters, R.D., Bhartia, P.K., Krueger, A.J., Herman, J.R., Wellemeyer, C.G., Seftor, C.J., Jaross, G., Torres, O., Moy, L., Labow, G., Byerly, W., Taylor, S.L., Swissler, T., & Cebula, R.P. 1998. *Earth Probe Total Ozone Mapping Spectrometer (TOMS) Data Products User's Guide*.

Meeder, A., Jäger-Waldau, A., Tezlevan, V., Arushanov, E., Schedel-Niedrig, T., & Lux-Steiner, M.C. 2003. Temperature dependence of the exciton gap in monocrystalline CuGaSe$_2$. *Journal of Physics: Condensed Matter*, **15**, 6219–6227.

Meinshausen, M., Meinshausen, N., Hare, W., Raper, S.C.B., Frieler, K., Knutti, R., Frame, D.J., & Allen, M.R. 2009. Greenhouse-gas emission targets for limiting global warming to 2°C. *Nature*, **458**, 1158–1162.

Menzel, W.P., Frey, R.A., & Baum, B.A. 2010. *Cloud top properties and cloud phase algorithm theoretical basis document*. `http://modis-atmos.gsfc.nasa.gov/_docs/CTP_ATBD_oct10.pdf`.

Millstein, D., & Menon, S. 2011. Regional climate consequences of large-scale cool roof and photovoltaic array deployment. *Environmental Research Letters*, **6**(3), 034001.

Minemoto, T., Nakada, Y., Takahashi, H., & Takakura, H. 2009. Uniqueness verification of solar spectrum index of average photon energy for evaluating outdoor performance of photovoltaic modules. *Solar Energy*, **83**(8), 1294–1299.

Minnis, P., Garber, D.P., Young, D.F., Arduini, R.F., & Takano, Y. 1998. Parameterizations of Reflectance and Effective Emittance for Satellite Remote Sensing of Cloud Properties. *Journal of the Atmospheric Sciences*, **55**(22), 3313–3339.

Minnis, P., Smith Jr., W.L., Nguyen, L., Murray, J.J., Heck, P.W., & Khaiyer, M.M. 2003 (16–20 June). Near-real-time satellite cloud products for icing detection and aviation weather over the USA. *In: In-Flight Icing/De-icing International Conference*.

Minnis, P., Szedung, S.-M., Young, D.F., Heck, P.W., Garber, D.P., Chen, Y., Spangenberg, D.A., Arduini, R.F., Trepte, Q.Z., Smith, W.L., Ayers, J.K., Gibson, S.C., Miller, W.F., Hong, G., Chakrapani, V., Takano, Y., Liou, K.-N., Xie, Y., & Yang, P. 2011. CERES Edition-2 Cloud Property Retrievals Using TRMM VIRS and Terra and Aqua MODIS Data—Part I: Algorithms. *IEEE Transactions on Geoscience and Remote Sensing*, **49**(11), 4374–4400.

Morcrette, J-J., Barker, H.W., Cole, J.N.S., Iacono, M.J., & Pincus, R. 2008. Impact of a new radiation package, McRad, in the ECMWF integrated forecasting system. *Monthly Weather Review*, **136**, 4773–4798.

Moss, R.H., Edmonds, J.A., Hibbard, K.A., Manning, M.R., Rose, S.K., van Vuuren, D.P., Carter, T.R., Emori, S., Kainuma, M., Kram, T., Meehl, G.A., Mitchell, J.F.B., Nakićenović, N., Riahi, K., Smith, S.J., Stouffer, R.J., Thomson, A.M., Weyant, J.P., & Wilbanks, T.J. 2010. The next generation of scenarios for climate change research and assessment. *Nature*, **463**, 747–756.

Mueller, R.W., Dagestad, K.F., Ineichen, P., Schroedter-Homscheidt, M., Cros, S., Dumortier, D., Kuhlemann, R., Olseth, J.A., Pieravieja, G., Reise, C., Wald, L., & Heinemann, D. 2004. Rethinking satellite-based solar irradiance modelling: The SOLIS clear-sky module. *Remote Sensing of Environment*, **91**, 160–174.

Mueller, R.W., Matsoukas, C., Gratzki, A., Behr, H.D., & Hollman, R. 2009. The CM-SAF operational scheme for the satellite based retrieval of solar surface irradiance – a LUT based eigenvector hybrid approach. *Remote Sensing of Environment*, **113**, 1012–1024.

Mueller, R.W., Behrendt, T., Hammer, A., & Kemper, A. 2012. A new algorithm for the satellite-based retrieval of solar surface irradiance in spectral bands. *Remote Sensing*, **4**, 622–647.

Muhammad-Sukki, F., Ramirez-Iniguez, R., Munir, A.B., Yasin, S.H.M., Abu-Bakar, S.H., McMeekin, S.G., & Stewart, B.G. 2013. Revised feed-in tariff for solar photovoltaic in the United Kingdom: A cloudy future ahead? *Energy Policy*, **52**, 832–838.

Muneer, T. 1990. Solar radiation model for Europe. *Building Services Engineering Research and Technology*, **11**(4), 153–163.

Muneer, T., & Gul, M.S. 2000. Evaluation of sunshine and cloud cover based models for generating solar radiation data. *Energy Conversion & Management*, **41**, 461–482.

Muneer, T., Gul, M., & Kambezedis, H. 1998. Evaluation of an all-sky meteorological radiation model against long-term measured hourly data. *Energy Conversion and Management*, **19**(3/4), 303–317.

Murphy, D. 2009. Effect of stratospheric aerosols on direct sunlight and implications for concentrating solar power. *Environmental Science and Technology*, **43**, 2784–2786.

Nakićenović, N., Davidson, O., Davis, G., Grübler, A., Kram, T., Lebre La Rovere, E., Metz, B., Morita, T., Pepper, W., Pitcher, H., Sankovski, A., Shukla, P., Swart, R., Watson, R., & Dadi, Z. 2000. *IPCC special report: emissions scenarios*. `https://www.ipcc.ch/pdf/special-reports/spm/sres-en.pdf`.

Nann, S., & Emery, K. 1992. Spectral effects on PV-device rating. *Solar Energy Materials and Solar Cells*, **27**, 189–216.

Nell, M.E., & Barnett, A.M. 1987. The spectral *p-n* junction model for tandem solar cell design. *IEEE Transactions on electron devices*, **ED34**(2), 257–266.

Ngoko, B.O., Sugihara, H., & Funaki, T. 2014. Synthetic generation of high temporal resolution solar radiation data using Markov models. *Solar Energy*, **103**, 160–170.

Nielsen, L.B., Prahm, L.P., Berkowicz, R., & Conradsen, K. 1981. Net incoming radiation estimated from hourly global radiation and/or cloud observations. *Journal of Climatology*, **1**(3), 255–272.

Niu, G., Guo, X., & Wang, L. 2015. Review of recent progress in chemical stability of perovskite solar cells. *Journal of Materials Chemistry A*, **3**(17), 8970–8980.

Nofuentes, G., García-Domingo, B., Muñoz, J.V., & Chenlo, F. 2014. Analysis of the dependence of the spectral factor of some PV technologies on the solar spectrum distribution. *Applied Energy*, **113**, 302–309.

Noh, J.H., Im, S.H., Heo, J.H., Mandal, T.N., & Seok, S.I. 2012. Chemical Management for Colorful, Efficient, and Stable Inorganic-Organic Hybrid Nanostructured Solar Cells. *Nano Letters*, **13**, 1764–1769.

Notton, G., Cristofari, C., Mattei, M., & Poggi, P. 2005. Modelling of a double-glass photovoltaic module using finite differences. *Applied Thermal Engineering*, **25**(17), 2854–2877.

Nou, J., Chauvin, R., Thil, S., Eynard, J., & Grieu, S. 2015. Clear-sky irradiance model for real-time sky imager application. *Energy Procedia*, **69**, 1999–2008. International Conference on Concentrating Solar Power and Chemical Energy Systems, SolarPACES 2014.

NREL. 1993. *Users Manual for SERI QC Software. Assessing the quality of solar radiation data*. Tech. rept. National Renewable Energy Laboratory, Golden, Colorado, USA. `http://www.nrel.gov/docs/legosti/old/5608.pdf`.

Ofgem. 2015. *The Renewables Obligation (RO) buy-out price (£44.33) and mutualisation ceilings 2015-16*. `https://www.ofgem.gov.uk/publications-and-updates/renewables-obligation-ro-buy-out-price-44-33-and-mutualisation-ceilings-2015-16`.

Ofgem. 2016. *Tariff Tables*. `https://www.ofgem.gov.uk/environmental-programmes/feed-tariff-fit-scheme/tariff-tables`.

Olseth, J.A., & Skartveit, A. 1984. A probability density function for daily insolation within the temperate storm belts. *Solar Energy*, **33**(6), 533–542.

Olseth, J.A., & Skartveit, A. 1987. A probability density model for hourly total and beam irradiance on arbitrarily orientated planes. *Solar Energy*, **39**(4), 343–351.

Oppenheimer, M., Campos, M., Warren, R., Birkmann, J., Luber, G., O'Neill, B., & Takahashi, K. 2014. Emergent risks and key vulnerabilities. *Chap. 19, pages 1039–1099 of:* Field, C.B., Barros, V.R., Dokken, D.J., Mach, K.J., Mastrandrea, M.D., Bilir, T.E., Chatterjee, M., Ebi, K.L., Estrada, Y.O., Genova, R.C., Girma, B., Kissel, E.S., Levy, A.N., MacCracken, S., Mastrandrea, P.R., & White, L.L. (eds), *Climate Change 2014: Impacts, Adaption, and Vulnerability. Part A: Global and Sectoral Aspects. Contribution of Working Group II to the Fifth Assessment Report of the Intergovernmental Panel on Climate Change*. Cambridge, United Kingdom and

New York, NY, USA: Cambridge University Press.

Öttinger, O. 2004. PCM/Graphitverbund-Produkte für Hochleistungswärmespeicher. *In: ZAE Symposium: Wärme- und Kältespeicherung mit Phasenwechselmaterialien (PCM)*.

Oumbe, A., Wald, L., Blanc, P., & Schroedter-Homscheidt, M. 2008 (7–10 October). Exploitation of radiative transfer model for assessing solar resource radiation: the relative importance of atmospheric constituents. *In: EUROSUN2008, 1st International Congress on Heating, Cooling and Buildings*. Lisbon, Portugal.

Pan, Z., Segal, M., Arritt, R.W., & Takle, E.S. 2004. On the potential change in solar radiation over the US due to increases of atmospheric greenhouse gases. *Renewable Energy*, **29**, 1923–1928.

Panagea, I.S., Tsanis, I.K., Koutroulis, A.G., & Grillakis, M.G. 2014. Climate change impact on photovoltaic energy output: the case of Greece. *Advances in Meteorology*, **2014**, 1–11.

Pašičko, R., Č. Branković, & Šimić, Z. 2012. Assessment of climate change impacts on energy generation from renewable sources in Croatia. *Renewable Energy*, **46**, 224–231.

Pehnt, M. 2006. Dynamic life cycle assessment (LCA) of renewable energy technologies. *Renewable Energy*, **31**(1), 55–71.

Perez, R., Ineichen, P., Seals, R., & Zelenka, A. 1990a. Making full use of the clearness index for parameterising hourly insolation conditions. *Solar Energy*, **40**(2), 111–114.

Perez, R., Ineichen, P., Seals, R., Michalsky, J., & Stewart, R. 1990b. Modeling daylight availability and irradiance components from direct and global irradiance. *Solar Energy*, **44**(5), 271–289.

Pincus, R. 2011. Radiation: fast physics with slow consequences in an uncertain atmosphere. *Pages 65–76 of: Workshop on Representing Model Uncertainty and Error in Numerical Weather and Climate Prediction Models, 20-24 June 2011*. Shinfield Park, Reading: ECMWF, for ECMWF.

Pincus, R., Mlawer, E.J., Oreopoulos, L., Ackerman, A.S., Baek, S., Brath, M., Buehler, S.A., Cady-Pereira, K.E., Cole, J.N.S., Dufresne, J.-L., Kelley, M., Li, J., Manners, J., Paynter, D.L., Roehrig, R., Sekiguchi, M., & Schwarzkopf, D.M. 2015. Radiative flux and forcing parameterization error in aerosol-free clear skies. *Geophysical Research Letters*, **42**(13), 5485–5492. 2015GL064291.

Platnick, S., & Valero, F.P.J. 1995. A Validation of a Satellite Cloud Retrieval during ASTEX. *Journal of the Atmospheric Sciences*, **52**(16), 2985–3001.

Prescott, J.A. 1940. Evaporation from water surfaces in relation to solar radiation. *Transactions of the Royal Society of South Australia*, **64**, 114–118.

Ramanathan, V., Crutzen, P.J., Kiehl, J.T., & Rosenfeld, D. 2001. Aerosols, climate and the hydrological cycle. *Science*, **294**, 2119–2124.

Ramaswamy, V., Boucher, O., Haigh, J., Hauglustaine, D., Haywood, J., Myhre, G., Nakajima, T., Shi, G.Y., Solomon, S., *et al.* 2001. Radiative forcing of climate change. *Chap. 6, pages 349–416 of:* Houghton, J.T., Ding, Y., Griggs, D.J., Noguer, M., van der Linden, P.J., Dai, X., Maskell, K., & Johnson, C.A. (eds), *Climate Change 2001: The Scientific Basis. Contribution of Working Group I to the Third Assessment Report of the Intergovernmental Panel on Climate Change*. Cambridge, United Kingdom and New York, NY, USA: Cambridge University Press.

Rasch, P.J., Tilmes, S., Turco, R.P., Robock, A., Oman, L., Chen, C.-C., Stenchikov, G.L., & Garcia, R.R. 2008. An overview of geoengineering of climate using stratospheric sulphate aerosols. *Philosophical transactions. Series A, Mathematical, physical, and engineering sciences*, **366**(1882), 4007–4037.

Razykov, T.M., Ferekides, C.S., Morel, D., Stefanakos, E., Ullal, H.S., & Upadhyaya, H.M. 2011. Solar photovoltaic electricity: Current status and future prospects. *Solar Energy*, **85**(8), 1580–1608.

Reindl, D.T., Beckman, W.A., & Duffie, J.A. 1990. Evaluation of hourly tilted surface radiation models. *Solar Energy*, **45**, 9–17.

Remund, J., Wald, L., Lefèvre, M., Ranchin, T., & Page, J. 2003 (June). Worldwide Linke turbidity information. *In: Proceedings of ISES Solar World Congress*.

Rhead, C. 2012. Africa's largest solar PV plant. `http://www.blue-energyco.com/news/`

`africas-largest-solar-pv-plant/`. Accessed 04.03.2013.

Riahi, K., Rao, S., Krey, V., Cho, C., Chirkov, V., Fischer, G., Kindermann, G., Nakicenovic, N., & Rafaj, P. 2011. RCP 8.5—A scenario of comparatively high greenhouse gas emissions. *Climatic Change*, **109**, 33–57.

Rigollier, C., Bauer, O., & Wald, L. 2000. On the clear sky model of the ESRA European Solar Radiation Atlas with respect to the HELIOSAT method. *Solar Energy*, **68**(1), 33–48.

Rincón, C., González, J., & Sánchez-Pérez, G. 1983. Temperature dependence of the energy gap in $\mathrm{CuInSe_2}$. *Physica Status Solidi (b)*, **117**, K123–K126.

Robock, A., Oman, L., & Stenchikov, G.L. 2008. Regional climate responses to geoengineering with tropical and Arctic SO_2 injections. *Journal of Geophysical Research: Atmospheres*, **113**(D16), D16101.

Robock, A., Marquardt, A., Kravitz, B., & Stenchikov, G. 2009. Benefits, risks and costs of stratospheric geoengineering. *Geophysical Research Letters*, **36**, L19703.

Roesch, A., Wild, M., Ohmura, A., Dutton, E.G., Long, C.N., & Zhang, T. 2011. Assessment of BSRN radiation records for the computation of monthly means. *Atmospheric Measurement Techniques*, **4**(2), 339–354.

Rogelj, J., Meinhausen, M., & Knutti, R. 2012. Global warming under old and new scenarios using IPCC climate sensitivity range estimates. *Nature Climate Change*, **2**(4), 248–253.

Rossow, W.B., Walker, A.W., Beuschel, D.E., & Roiter, M.D. 1996. *International Satellite Cloud Climatology Project (ISCCP) documentation of new cloud datasets*. World Climate Research Programme. `http://isccp.giss.nasa.gov/pub/documents/d-doc.pdf`.

Rozwadowska, A. 2004. Optical thickness of stratiform clouds over the Baltic inferred from on-board irradiance measurements. *Atmospheric Research*, **72**, 129–147.

Scharmer, K., & Greif, J. 2000. *The European Solar Radiation Atlas: Volume 2, Database and Exploitation Software*.

Scott, C. E., Rap, A., Spracklen, D. V., Forster, P. M., Carslaw, K. S., Mann, G. W., Pringle, K. J., Kivekäs, N., Kulmala, M., Lihavainen, H., & Tunved, P. 2014. The direct and indirect radiative effects of biogenic secondary organic aerosol. *Atmospheric Chemistry and Physics*, **14**(1), 447–470.

Seemann, S.W., Li, J., Menzel, W.P., & Gumley, L.E. 2003. Operational Retrieval of Atmospheric Temperature, Moisture, and Ozone from MODIS Infrared Radiances. *Journal of Applied Meteorology*, **42**, 1072–1091.

Seljom, P., Rosenberg, E., Fidje, A., Haugen, J.E., Meir, M., Rekstad, J., & Jarlset, T. 2011. Modelling the effects of climate change on the energy system—A case study of Norway. *Energy Policy*, **39**, 7310–7321.

Shettle, E.P. 1989. Models of aerosols, clouds and precipitation for atmospheric propagation studies. *In: Proceedings of AGARD Conference No. 454: Atmospheric, UV, visible, IR and mm-region and related system aspects*.

Shockley, W., & Queisser, H.J. 1961. Detailed balance limit of efficiency of *p-n* junction solar cells. *Journal of Applied Physics*, **32**(3), 510–519.

Singh, P., & Ravindra, N.M. 2012. Temperature dependence of solar cell performance—an analysis. *Solar Energy Materials and Solar Cells*, **101**, 36–45.

Singh, P., Singh, S.N., Lal, M., & Husain, M. 2008. Temperature dependence of *I-V* characteristics and performance parameters of silicon solar cell. *Solar Energy Materials and Solar Cells*, **92**, 1611–1616.

Skartveit, A., & Olseth, J.A. 1986. Modelling slope irradiance at high latitudes. *Solar Energy*, **36**(4), 333–344.

Skartveit, A., & Olseth, J.A. 1992. The probability density and autocorrelation of short-term global and beam irradiance. *Solar Energy*, **49**(6), 477–487.

Skoplaki, E., & Palyvos, J. A. 2009. On the temperature dependence of photovoltaic module electrical performance: A review of efficiency/power correlations. *Solar Energy*, **83**(5), 614–624.

Skoplaki, E., Boudouvis, A.G., & Palyvos, J.A. 2008. A simple correlation for the operating temperature of photovoltaic modules of arbitrary mounting. *Solar Energy Materials and Solar Cells*, **92**, 1393–1402.

Smith, C.J., Crook, R., & Forster, P.M. 2015 (14–18 September). Changes in solar PV output due to water vapour loading in a future climate scenario. *Pages 2102–2105 of: 31st European Photovoltaic Solar Energy Conference*. Hamburg, Germany.

Snedecor, G.W., & Cochran, W.G. 1989. *Statistical Methods, Eighth Edition*. Iowa State University Press.

Spracklen, D.V., Pringle, K.J., Carslaw, K.S., M.P., Chipperfield, & Mann, G.W. 2005. A global off-line model of size-resolved aerosol microphysics: I. Model development and prediction of aerosol properties. *Atmospheric Chemistry and Physics Discussions*, **5**(1), 179–215.

Stacy, E.W. 1962. A Generalization of the Gamma Distribution. *The Annals of Mathematical Statistics*, **33**(3), 1187–1192.

Stamnes, K., Tsay, S.-C., Wiscombe, W., & Jayaweera, K. 1988. Numerically stable algorithm for discrete-ordinate-method radiative transfer in multiple scattering and emitting layered media. *Applied Optics*, **27**(12), 2502–2509.

Stamnes, K., Tsay, S.-C., Wiscombe, W., & Laszlo, I. 2000. *DISORT, a General-Purpose Fortran Program for Discrete-Ordinate-Method Radiative Transfer in Scattering and Emitting Layered Media: Documentation of Methodology*. Dept. of Physics and Engineering Physics, Stevens Institute of Technology, Hoboken, NJ, USA. `ftp://climate1.gsfc.nasa.gov/ridgway/Multiple_Scatt/DISORTReport1.1.pdf`.

Stephens, G.L. 1976. The transfer of radiation through vertically nonuniform Sc clouds. *Contrib. Phys. Atmos.*, **49**, 237–253.

Suehrcke, H., & McCormick, P.G. 1988. The frequency distribution of instantaneous insolation values. *Solar Energy*, **40**(5), 413–422.

Supit, I., & van Kappel, R.R. 1998. A simple method to estimate global radiation. *Solar Energy*, **63**(3), 147–160.

Šúri, M., & Hofierka, J. 2004. A New GIS-based solar radiation model and its application to photovoltaic assessments. *Transactions in GIS*, **8**, 175–190.

Swinbank, W. C. 1963. Long-wave radiation from clear skies. *Quarterly journal of the Royal Meterological Society*, **89**, 339–348.

Talebizadeh, P., Mehrabian, M.A., & Abdolzadeh, M. 2011. Prediction of the optimum slope and surface azimuth angles using the Genetic Algorithm. *Energy and Buildings*, **43**(11), 2998–3005.

Temps, Ralph C., & Coulson, K.L. 1977. Solar radiation incident upon slopes of different orientations. *Solar Energy*, **19**(2), 179–184.

Teo, H.G., Lee, P.S., & Hawlader, M.N.A. 2011. An active cooling system for photovoltaic modules. *Applied Energy*, **90**, 309–315.

Thomas, G.E., & Stamnes, K. 2002. *Radiative transfer in the atmosphere and ocean*. Cambridge University Press.

Thomson, A.M., Calvin, K.V., Smith, S.J., Kyle, G. Page, Volke, A, Patel, P., Delgado-Arias, S., Bond-Lamberty, B., Wise, M.A., Clarke, L.E., & Edmonds, J.A. 2011. *RCP4.5: A Pathway for Stabilization of Radiative Forcing by 2100*.

Thorne, P.W., & Vose, R.S. 2010. Reanalyses Suitable for Characterizing Long-Term Trends. *Bulletin of the American Meteorological Society*, **91**(3), 353–361.

Tilmes, S., Müller, R, & Salawitch, R. 2008. The sensitivity of polar ozone depletion to proposed geoengineering schemes. *Science*, **320**(5880), 1201–1204.

Tovar, J., Olmo, F.J., & Alados-Arboledas, L. 1998. One minute global irradiance probability density distributions conditioned to the optical air mass. *Solar Energy*, **62**, 387–393.

Trenberth, K.E., Fasullo, J.T., & Kiehl, J. 2009. Earth's Global Energy Budget. *Bulletin of the American Meteorological Society*, **90**(3), 311–323.

Triami Media BV. 2015. *inflation.eu worldwide inflation data*. `http://www.inflation.eu/inflation-rates/germany/historic-inflation/cpi-inflation-germany.aspx`.

Accessed 30.07.2015.

UK Met Office. 2010. *Observations: National Meteorological Library and Archive Fact sheet 17 — Weather observations over land*. Tech. rept. `http://www.metoffice.gov.uk/media/pdf/p/6/10_0230_FS_17_Observations.pdf`.

UK Met Office. 2015a. *Met Office surface data users guide*. `http://badc.nerc.ac.uk/data/ukmo-midas/ukmo_guide.html`. Accessed 31.07.2015.

UK Met Office. 2015b. *UK climate*. `http://www.metoffice.gov.uk/public/weather/climate/`. Accessed 18.11.2015.

UNFCCC. 2009. *Report of the Conference of the Parties on its fifteenth session, held in Copenhagen from 7 to 19 December 2009*. `http://unfccc.int/resource/docs/2009/cop15/eng/11a01.pdf`.

UNFCCC. 2012. *Doha amendment to the Kyoto Protocol*. `https://treaties.un.org/doc/Publication/CN/2012/CN.718.2012-Eng.pdf`.

U.S. Energy Information Administration. 2014. *Table 5.6.A. Average Retail Price of Electricity to Ultimate Customers by End-Use Sector*. `http://www.eia.gov/electricity/monthly/epm_table_grapher.cfm?t=epmt_5_06_a`. Accessed 05.03.2014.

van Vuuren, D.P., Edmonds, J., Kainuma, M., Riahi, K., Thomson, A., Hibbard, K., Hurtt, G.C., Kram, T., Krey, V., Lamarque, J.F., Masui, T., Meinshausen, M., Nakićenović, N., Smith, S.J., & Rose, S.K. 2011. The representative concentration pathways: an overview. *Climatic change*, **109**, 5–31.

Varshni, Y.P. 1967. Temperature dependence of the energy gap in semiconductors. *Physica*, **34**, 149–154.

Velraj, R., Seeniraj, R. V., Hafner, B., Faber, C., & Schwarzer, K. 1999. Heat transfer enhancement in a latent heat storage system. *Solar Energy*, **65**(3), 171–180.

Vignola, F., Michalsky, J., & Stoffel, T. 2012. *Solar and infrared radiation measurements*. CRC Press.

Wand, R., & Leuthold, F. 2011. Feed-in tariffs for photovoltaics: Learning by doing in Germany? *Applied Energy*, **88**(12), 4387–4399.

Wauben, W., Baltink, H.K., de Haij, M., Maat, N., & The, H. 2006. Status, evaluation and new developments of the automated cloud observations in the Netherlands. *In:* World Meteorological Organization (ed), *TECO-2006 — WMO Technical Conference on Meteorological and Environmental Instruments and Methods of Observation*. Geneva, Switzerland.

Wild, M. 2009. Global dimming and brightening: A review. *Journal of Geophysical Research*, **114**(D00D16).

Wild, M., Folini, D., Henschel, F., Fischer, N., & Müller, B. 2015. Projections of long-term changes in solar radiation based on CMIP5 climate models and their influence on energy yields of photovoltaic systems. *Solar Energy*, **116**, 12–24.

Wiscombe, W.J. 1980. Improved Mie scattering algorithms. *Applied Optics*, **19**(9), 1505–1509.

WMO. 2014. *Guide to meteorological instruments and methods of observation (WMO-No. 8)*. World Meterological Association. `https://www.wmo.int/pages/prog/www/IMOP/publications/CIMO-Guide/Provisional2014Edition.html`. Provisional 2014 edition. Accessed 31.07.2015.

Woodman, B., & Mitchell, C. 2011. Learning from experience? The development of the Renewables Obligation in England and Wales 2002-2010. *Energy Policy*, **39**(7), 3914–3921. Special Section: Renewable energy policy and development.

Wörner, H. 1967. Zur Frage der Automatisierbarkeit der Bewölkungsangaben durch Verwendung von Strahlungsgrößen. *Abh. Met. Dienst DDR*, **11**(82).

Xie, Y., Yang, P., Gao, B.-C., Kattawar, G.W., & Mishchenko, M.I. 2006. Effect of ice crystal shape and effective size on snow bidirectional reflectance. *Journal of Quantitative Spectroscopy and Radiative Transfer*, **100**(1–3), 457–469.

Xie, Y., Yang, P., Kattawar, G.W., Minnis, P., Hu, Y., & Wu, D.L. 2012. Determination of ice cloud models using MODIS and MISR data. *International Journal of Remote Sensing*, **33**(13), 4219–4253.

Yadav, Amit Kumar, & Chandel, S.S. 2013. Tilt angle optimization to maximize incident solar radiation: A review. *Renewable and Sustainable Energy Reviews*, **23**, 503–513.

Yamaguchi, M., Nishimura, K.-I., Sasaki, T., Suzuki, H., Arafune, K., Kojima, N., Ohsita, Y., Okada, Y., Yamamoto, A., Takamoto, T., & Araki, K. 2008. Novel materials for high-efficiency IIIV multi-junction solar cells. *Solar Energy*, **82**(2), 173–180.

Zalba, B., Marín, J. M., Cabeza, L. F., & Mehling, H. 2003. Review on thermal energy storage with phase change: materials, heat transfer analysis and applications. *Applied thermal engineering*, **23**(3), 251–283.

Zdanowicz, T., Rodziewicz, R., & Zabkowska-Waclawek, M. 2005. Theroetical analysis of the optimum energy band gap of semiconductors for fabrication of solar cells for applications in higher latitudes locations. *Solar Energy Materials and Solar Cells*, **87**, 757–769.

Zelen, N., & Severo, M.C. 1964. Student's *t* distribution. *Chap. 26, page 948 of:* Abramowitz, M., & Stegun, I. (eds), *Handbook of Mathematical Functions*. Dover.

Zib, B.J., Dong, X., Xi, B., & Kennedy, A. 2012. Evaluation and Intercomparison of Cloud Fraction and Radiative Fluxes in Recent Reanalyses over the Arctic Using BSRN Surface Observations. *Journal of Climate*, **25**(7), 2291–2305.

Zondag, H.A. 2008. Flat-plate PV-Thermal collectors and systems: A review. *Renewable and Sustainable Energy Reviews*, **12**, 891–959.

Zukowski, M. 2007. Mathematical modeling and numerical simulation of a short term thermal energy storage system using phase change material for heating applications. *Energy Conversion and Management*, **48**, 155–165.